Synthesis, structural and magneto-electric properties of compounds belonging to the pyroxene family

Lei Ding

UNIVERSITÉ GRENOBLE ALPES

THÈSE

Pour obtenir le grade de

DOCTEUR DE L'UNIVERSITÉ GRENOBLE ALPES

Spécialité : **Physique des matériaux**

Arrêté ministériel : 7 août 2006

Présentée par

Lei DING

Thèse dirigée par **Pierre BORDET** et Co-encadrée par **Claire V. COLIN**

préparée au sein de l'**Institut Néel**
dans **l'École Doctorale de physique de Grenoble**

Synthèse et étude structurale et magnétoélectrique de composés multiferroïques de la famille des pyroxènes

Thèse soutenue publiquement le **11 Septembre 2015**,
devant le jury composé de :

Françoise DAMAY
Chargée de Recherche au Laboratoire Léon Brillouin (Saclay), Rapporteur
Etienne JANOD
Chargé de Recherche à l'Institut des Matériaux Jean Rouxel (Nantes), Rapporteur
Françoise HIPPERT
Professeur à Grenoble INP (Grenoble), Président, Examinateur
Olivier MENTRE
Directeur de Recherche à l'Unité de Catalyse et de Chimie du Solide (Lille), Examinateur
Pierre BORDET
Directeur de Recherche à l'Institut Néel (Grenoble), Directeur de thèse
Claire V. COLIN
Maitre de Conférences à l'Université Joseph Fourier (Grenoble), Co-Encadrante de thèse
Céline DARIE
Maitre de Conférences à l'Université Joseph Fourier (Grenoble), Invitée
Juan RODRIGUEZ-CARVAJAL
Chercheur à l'Institut Laüe-Langevin (Grenoble), Invité

Acknowledgements

First of all, I am grateful to China Scholarship Council (CSC) for the scholarship support, allowing me to accomplish this work. There are many people I would like to thank, who have contributed to some extent to prepare this thesis. I would like to express my sincere gratitude to my supervisors, Pierre Bordet and Claire V. Colin, for their guidance and encouragement throughout this work. Their rigorous working attitude, creative and logical research ways will always invoke and motivate me in my future research career. The most invaluable things what I learned from them, beyond science knowledge, are the passion to fundamental research and the attitude of slow science. I express my special thanks to Celine Darie for her kind care and guidance during these three years. I want to thank my committee members for their helpful comments and constructive advices which have improved my work: Françoise Damay, Etienne Janod, Françoise Hippert, Olivier Mentre, Juan Rodriguez-Carvajal. I also want to acknowledge Julien Robert from Institut Néel, for his theoretical support.

Many thanks to the instrument scientists in the Institut Néel and the Institut Laue Langevin, for the help I received: Céline Goujon, Muriel Legendre, Bertrand Menaert, Pascal Lejay, Abdellali Hadj-Azzem, Marine Liotaud, Olivier Leynaud, Sebastien Pairis, Holger Klein, Philippe Plaindoux, Eric Eyraud, Didier Dufeu, Pierre Lachkar, Frederic Gay, Vivian Nassif, Laetitia Laversenne and Sofien Djellit. I also thank Virginie Simonet from Institut Néel who has provided many useful discussions.

Finally, I would like to thank my parents and my sister.

Contents

1 Introduction **7**

1.1 What holds solids together: atoms and forces . . . 7

1.1.1 Crystal structure: symmetry, reality's riddle . . . 7

1.1.2 Chemical bonding . . . 9

1.2 Magnetism in solids . . . 11

1.2.1 Magnetism . . . 11

1.2.1.1 Origins of magnetism . . . 11

1.2.1.2 Order and magnetic structure . . . 12

1.2.2 Broken symmetry in magnetism . . . 18

1.2.2.1 Models . . . 18

1.2.2.2 Consequences of broken symmetry . . . 20

1.2.3 Competing interactions and one dimensional magnets . . . 20

1.2.3.1 Frustration . . . 20

1.2.3.2 Spin-glass . . . 21

1.2.3.3 One-dimensional magnets . . . 22

1.3 Structure-property relationships . . . 23

1.3.1 Polar and axial tensors . . . 23

1.3.2 Neumann's principle . . . 24

1.3.3 Symmetry consideration . . . 24

1.4 Multiferroics . . . 29

1.4.1 Primary orders and multiferroics . . . 29

1.4.1.1 Primary orders in dielectrics . . . 29

1.4.1.2 Multiferroics . . . 29

1.4.1.3 Ferrotoroidic order vs magnetoelectric effect . . . 30

1.4.2 Recent progress in multiferroics . . . 31

1.4.2.1 Independence between magnetism and ferroelectricity (type-I) 32

1.4.2.2 Multiferroics of spin origin (type-II) . . . 33

1.4.3 Potential applications . . . 36

1.5 Pyroxenes . . . 37

1.5.1 What are pyroxenes: structural viewpoint . . . 38

1.5.2 Nontrivial magnetic properties . . . 41

1.5.3 Motivations and outline . . . 45

2 Experimental methods 57
2.1 Synthesis methods . . . 57
2.1.1 Solid state reaction[1] . . . 57
2.1.2 High pressure and high temperature . . . 58
2.1.2.1 Syntheses requiring high pressure . . . 58
2.1.2.2 HP-HT systems . . . 59
2.1.3 Sol-gel processing . . . 60
2.1.4 Single crystal growth . . . 62
2.2 Thermal analysis . . . 63
2.3 Morphology and microstructural analysis . . . 64
2.3.1 Electron microscopy: Electrons interact with specimen . . . 64
2.4 Structural characterization . . . 66
2.4.1 Comparison of the characteristics of X-ray and neutron beams . . . 67
2.4.2 X-ray instruments and operations . . . 68
2.4.2.1 X-ray powder diffractometer . . . 68
2.4.2.2 X-ray single crystal diffractometer . . . 71
2.4.3 Determination of crystal structure from powder diffraction . . . 71
2.4.4 Neutron scattering and magnetic structure . . . 72
2.4.4.1 Neutron diffractometer[20] . . . 72
2.4.4.2 Magnetic structure determination . . . 72
2.5 Magnetization measurement . . . 74
2.5.1 MPMS_XL . . . 74
2.5.2 SQUID-VSM . . . 76
2.6 Heat capacity measurement . . . 76
2.7 Magneto-electric measurement . . . 77

3 Synthesis strategy 83
3.1 Solid state reaction . . . 83
3.2 High pressure high temperature method(HPHT) . . . 86
3.3 Soft chemistry method . . . 86
3.4 Single crystal growth . . . 88

4 A copper-bearing silicate with the low clinopyroxene structure 91
4.1 Introduction . . . 91
4.2 Experimental . . . 92
4.2.1 Sample preparation and characterization . . . 92
4.2.2 X-ray powder diffraction . . . 92
4.3 Results and discussion . . . 93
4.3.1 Synthesis and characterization . . . 93
4.3.2 Structural study . . . 95

4.3.3 Magnetic Properties . . . 98
4.4 Discussion . . . 99
4.5 Conclusions . . . 102

5 $CaMnGe_2O_6$: magnetoelectricity and one-dimensional short range magnetic correlations 107
5.1 Introduction . . . 107
5.2 Experimental details . . . 109
5.2.1 Sample preparation . . . 109
5.2.2 X-ray and neutron powder diffraction . . . 109
5.2.3 Magnetic susceptibility measurement . . . 109
5.2.4 Specific heat measurement . . . 110
5.2.5 Electrical properties . . . 110
5.3 Results and discussion . . . 110
5.3.1 Crystal structure . . . 110
5.3.2 Magnetic properties . . . 113
5.3.3 Magnetic structure . . . 117
5.3.4 Short range spin correlations . . . 118
5.3.5 Linear magnetoelectric effect . . . 122
5.3.6 Ferrotoroidicity . . . 127
5.4 Discussion . . . 129
5.5 Conclusion . . . 131

6 Short-range magnetic correlations and magnetoelectric properties in high-pressure synthesized $CaMnSi_2O_6$ 137
6.1 Introduction . . . 137
6.2 Experimental details . . . 138
6.2.1 Sample preparation . . . 138
6.2.2 X-ray and neutron powder diffraction . . . 138
6.2.3 Magnetic susceptibility measurement . . . 138
6.2.4 Specific heat measurement . . . 139
6.2.5 Electrical properties . . . 139
6.3 Results and discussion . . . 139
6.3.1 Crystal structure . . . 139
6.3.2 Magnetic properties . . . 144
6.3.3 Magnetic structure . . . 147
6.3.4 One dimensional short range spin correlations . . . 149
6.3.5 Linear magnetoelectric effect of $CaMnSi_2O_6$ . . . 154
6.4 Discussion . . . 154
6.5 Conclusion . . . 156

7 Structure and magnetic properties in $CaCo_{1-x}Mn_xGe_2O_6$ 159
7.1 Introduction . . . 159
7.2 Experimental detail . . . 160
7.2.1 Sample preparation . . . 160
7.2.2 X-ray and neutron powder diffraction . . . 160
7.2.3 Magnetic susceptibility measurement . . . 160
7.2.4 Specific heat measurement . . . 161
7.3 Results and discussion . . . 161
7.3.1 Crystal structure of $CaCo_{1-x}Mn_xGe_2O_6$ . . . 161
7.3.2 Magnetic properties of $CaCo_{1-x}Mn_xGe_2O_6$ . . . 168
7.3.3 Magnetic structure of $CaCo_{1-x}Mn_xGe_2O_6$ . . . 175
7.3.3.1 Diffuse scattering of $CaCo_{1-x}Mn_xGe_2O_6$ . . . 180
7.3.4 Bilinear magnetoelectric effect . . . 180
7.3.5 Magnetic properties of $CaMn_{0.5}Ni_{0.5}Ge_2O_6$ and $CaCo_{0.5}Ni_{0.5}Ge_2O_6$ . . . 185
7.4 Discussion . . . 186
7.5 Conclusion . . . 189

8 $SrMGe_2O_6$(M=Mn, Co): a new family of pyroxenes 193
8.1 Introduction . . . 193
8.2 Experimental details . . . 194
8.2.1 Sample preparation . . . 194
8.2.2 X-ray and neutron powder diffraction . . . 195
8.2.3 Single crystal x-ray diffraction . . . 195
8.2.4 Magnetic susceptibility measurement . . . 195
8.2.5 Specific heat measurement . . . 196
8.2.6 Electrical properties . . . 196
8.3 Results and discussion . . . 196
8.3.1 Crystal structure . . . 196
8.3.1.1 Crystal structure determination for $SrMnGe_2O_6$ and $SrCoGe_2O_6$ . . . 196
8.3.1.2 A structural comparison between $SrMnGe_2O_6$, $SrCoGe_2O_6$, $CaMnGe_2O_6$ and $CaCoGe_2O_6$ . . . 201
8.3.2 Magnetic properties . . . 204
8.3.2.1 $SrCoGe_2O_6$ . . . 204
8.3.2.2 $SrMnGe_2O_6$ . . . 207
8.3.3 Magnetic structure . . . 209
8.3.3.1 $SrCoGe_2O_6$ . . . 209
8.3.3.2 $SrMnGe_2O_6$ . . . 211
8.3.4 Magnetoelectric properties . . . 220
8.3.4.1 . . . 220
8.3.4.2 Multiferroic properties in $SrMnGe_2O_6$ . . . 220

8.4 Discussion 222
8.5 Conclusion 224

9 Summary and Outlook **229**
9.1 Summary 229
9.2 Perspectives 231

Chapter 1

Introduction

This chapter is intended to give a short overview on fundamental concepts and principles used within this thesis. We will start from the basal principles of solids, whether physical or chemical, to the central theme of this dissertation-Multiferroics. Crystals are intrinsically symmetric, and the symmetry plays a very important role in determining their properties. For materials containing transition metal atoms, long range ordering of magnetic moments can be constructed by their exchange interactions. In order to explore the coupling between magnetic and electric orders in crystals, symmetry consideration, including interactions between polar and axial tensors, is tackled in this chapter. We will see that symmetry will be often employed throughout this dissertation in constructing the structure-property relationships. The next chapter will concern the synthesis methods of materials as well as the experimental aspects used to characterize microscopic and macroscopic properties of solids that were used in this work.

1.1 What holds solids together: atoms and forces

Most macroscopic properties of solids are linked to their atomic arrangement (structure) and the forces between the atoms (electromagnetic). In this opening section, we will hence first discuss the crystal structure as well as the geometrical symmetry which underpins the fundamental of crystallography, followed by considering what holds the solids together from the point of view of chemical bonding.

1.1.1 Crystal structure: symmetry, reality's riddle

Crystals are the most structurally ordered solids. By the translational periodicity, the unit cell, formed by an atom or group of atoms, will be repeated translationally in a periodic way generating the three dimensional lattice in which crystal is defined. Atoms can be packed together to form distinct crystal structures by some main principles which are geometric in origin, depending on packing atoms of various sizes or specific chemical bonding. This leads to a great diversity of crystal structures. From the viewpoint of art, this is very beautiful

as if entering an art gallery. Nevertheless, we will have to pay our attention to a particular formalism: symmetry.

Not only is crystal structure formalized by symmetry but also the concomitant physical properties addressed in section 1.1.3 can be better understood. We already mentioned that the unit cell itself presents symmetry properties. In addition to simple translations, there are other important symmetries that perform a certain transformation to the environment leaving a point invariant, which are called point symmetries. There are four point symmetry operations: rotation, inversion, reflection, and roto-inversion. Symmetry elements and operations combine with each other, giving rise to new symmetry elements and operations, respectively. By three dimensional combinations of symmetry operations, the generation of all symmetry elements can be attained. Each of these complete sets of symmetry elements is defined as a crystallographic point group. Considering the point symmetry elements and all valid combinations among them, 32 point groups can be constructed.

So far, the discussion of symmetry of crystal was confined to point symmetry. The translational symmetry will be immediately taken into account when considering the periodicity of crystal. The first idea is to combine the point groups with the 14 Bravais lattices by considering the combination of their symmetry elements. This yields 61 space groups. By combining the rotation and reflection symmetries with a translation, two new types of symmetry operations, screw axes and glide planes, can be produced. In total, 230 crystallographic space groups will be reached via combining these new symmetry operations with those already existing in the point groups described above.

Diffraction of x-rays or neutron involves constructive reflections from planes of atoms. And vibrations of the crystal involve motions of planes of atoms. With such a prominent importance of planes of atoms, a consistent and general representation of crystals can be given through the geometric relations between atomic planes, which is formalized by the reciprocal lattice. Usually, the volume of unit cell is given by

$$V_{cell} = \vec{a} \cdot (\vec{b} \times \vec{c}) \tag{1.1}$$

Accordingly, we have three vectors in reciprocal space

$$\vec{a}^* = \frac{2\pi}{V_{cell}} \vec{b} \times \vec{c}, \vec{b}^* = \frac{2\pi}{V_{cell}} \vec{c} \times \vec{a}, \vec{c}^* = \frac{2\pi}{V_{cell}} \vec{a} \times \vec{b} \tag{1.2}$$

We can formally define the vector of reciprocal lattice $\vec{d}^*_{hkl}$ in terms of basis vectors $\vec{a}^*$, $\vec{b}^*$, and $\vec{c}^*$

$$\vec{d}^*_{hkl} = h\vec{a}^* + k\vec{b}^* + l\vec{c}^* \tag{1.3}$$

where the set of integers h,k,l are called the Miller indices. Usually, the plane normal to $\vec{d}^*_{hkl}$ is represented by the notation (hkl).

The concept of reciprocal lattice is not only very helpful in interpreting diffraction patterns (even if it arises from the need to have a formal mathematical representation of the planes of

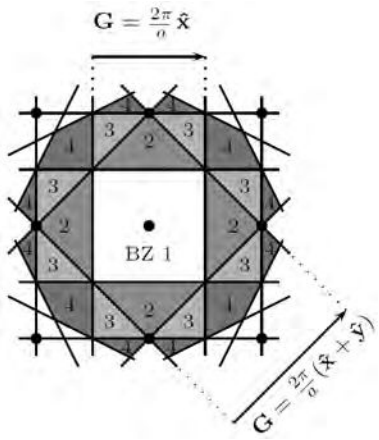

Figure 1.1: First, second, third, and fourth Brillouin zones of the square lattice.[2]

atoms within a crystal) but, more importantly, used in understanding the physics of waves, whether they are vibrational waves (respect to lattice dynamics) or electron waves (respect to electronic structure), in solids[1]. To properly describe the dispersions of phonons and electrons in lattice, another concept, Brillouin zone, related to reciprocal space should be adopted. A Brillouin zone is any primitive unit cell of the reciprocal lattice. We may construct the first Brillouin zone in reciprocal space by the way of construction of the Wigner-Seitz cell for the direct lattice, i.e. drawing the perpendicular bisector between the original point and each of the reciprocal lattice vectors. These bisectors form the Brillouin zone boundaries. The Brillouin zones of a section square lattice were shown in figure 1.1.

Two waves whose wave vectors differ from a reciprocal vector have an identical effect on a crystal lattice point. Thus, the set of wave vectors within first Brillouin zone are sufficient to describe the lattice vibrations waves and electronic waves in the whole crystal. Waves are therefore physically equivalent under shifts of the wavevector k by a reciprocal lattice vector $2\pi/a$, and we can always describe excitations within the first Brillouin zone.

1.1.2 Chemical bonding

In the previous subsection, we first mentioned that solids are made up of individual atoms arranged in periodic structures and introduced the concept of space group on the basis of symmetry of crystal structure. However, symmetry considerations are insufficient to determine the physical properties of solids. It is the balance of the attractive and repulsive forces acting on atoms that leads to the various structural parameters such as bond length, bong angle, coordination numbers and so on. Hence, producing various physical and chemical properties. Drawing upon the configuration of valence electrons, we are able to distinguish metals from insulators, and then a less rigorous classification of solids according to bonding can be reached on emphasizing their physical properties.

Depending on the types of atoms involved in solids, several types of chemical bonds can be defined. These include ionic bonds, covalent bonds, metallic bonds, Van der Waals bonds

and hydrogen bonds. Any given material may exhibit several aspects of these types of bonding. Nevertheless, we are able to qualitatively characterize the physical properties by simply considering these bonds.

Ionic bond is that for certain compounds, it is energetically favorable for an electron to be physically transferred from one atom to the other, resulting in two oppositely charged ions. These ions will attract each other, through long range electrostatic interactions. Most of the materials belonging to ionic solids are typically hard and have high melting points. They generally are electrical insulators.

The second type of bonding is covalent bonds in which one or more pairs of electrons are shared by two neighboring atoms. The overlap of partially occupied electron orbitals on each atoms results in a lowering of the overall electronic energy, and gives rise to covalent bonds. Materials with covalent bonds tend to be strong and electrical semiconductors or insulators. However, covalent bonds are very directional, this makes these materials non-ductile. The bonding occuring in a metal is called metallic bonding. The electrons form a delocalized electron gas throughout the whole crystal within which the ion cores are dispersed. Since the electrons are completely delocalized, metals are hence often ductile and malleable, and of course, they are good conductors of electricity as well as heat.

A relatively weak attractive interaction, so-called van der Waals bonds, results from induced electric dipole-dipole effects. Within this interaction, there is no charge transfer between atoms, and the charge distribution of each atom is spherically symmetric. It is responsible for the cohesion of rare-gas solids such as crystalline argon, and most molecular solids consist of organic molecules. This interaction is short-ranged and concerns essentiallynearest-neighbour atoms [3]. A weak hydrogen bond, for example in water, can be formed by the attraction between hydrogen on one water molecule and oxygen on another molecule.

By chemical bonding, we mean that the atoms are held in position by mutual forces. In addition to this internal forces, there are external forces, some of them we may consider in section 1.3, which will influence on the properties of crystals. First of all, external forces, such as mechanical stresses, magnetic fields, electric fields, can be applied to solids, resulting in microscopic distortions of the crystal structure or electronic state. This may in turn lead to some exotic properties, and as a result external forces are taken into account as an important way to stimulate or suppress special physical quantities in order to understand solids. In crystals, temperature will characterize the vibration of atoms, which produces displacements of atoms with magnitude comparable to static displacements that can be induced by those external forces. When the temperature is high enough, all materials will melt or sublime, but phase transition will occur in some materials, this can be observed through changes in physical properties macroscopically, and via the detections of microscopic characteristics (see the experimental techniques developed in chapter 2).

1.2 Magnetism in solids

In the previous section, we introduced that the solids are periodic arrangement of atoms. We will now introduce a collective phenomenon in solids, which is of electronic origin, called magnetism.The first question we will answer in this section is why atoms have magnetic moments, and then how magnetic moments sometimes align. Then, we discuss the basic ideas of broken symmetry, followed by some simple models which will be very useful in discussing the consequence of broken symmetry. Magnetic phenomena associating with competing interactions, as well as the low dimensionality will be finally introduced since they were investigated by means of experimental observations and theoretical calculations throughout this dissertation.

1.2.1 Magnetism

1.2.1.1 Origins of magnetism

Apart from the direct manifestation of magnetism of attraction or repulsion between magnets, as people know, magnetic phenomena ascribe from the quantum mechanical behavior of electrons. We start with the magnetic moment of an isolated atom. Generally speaking, the magnetic moment of an isolated atom consists of two contributions. The first one is the orbital angular momentum which is associated with the orbital motion of an electron around the nucleus. The quantum number, l, called orbital quantum number, determines the magnitude of the orbital angular momentum (denoted with |L|) of the electron. For an individual electron, |L| is related to l by $|L| = \sqrt{l(l+1)}\hbar$. The magnetic quantum number, m_l, represents the quantized orientation of the orbital angular momentum with respect to a magnetic field. As a result, the component of orbital angular momentum along a field direction is equal to $m_l\hbar$. This means that any component of orbital angular momentum along the field direction is smaller than total orbital angular momentum. Therefore, the corresponding contribution from the orbital part is $m = \sqrt{l(l+1)}\mu_B$. The second contribution is related to the intrinsic magnetic moment of an electron, which is associated with spin quantum momentum |S|. The spin quantum number s, which has the value $\frac{1}{2}$, giving rise to the spin quantum momentum by $|S| = \sqrt{s(s+1)}\hbar = \frac{\sqrt{3}}{2}\hbar$. The analogous term to the magnetic quantum number m_l is spin magnetic quantum number m_s, which is allowed to only take values of $\pm\frac{1}{2}$. Accordingly, the component of spin angular momentum along magnetic fields is then $m_s\hbar$. The spin contribution to magnetic moment is given by $m = \sqrt{s(s+1)}g\mu_B$with a component along a fixed axis equals to $-g\mu_B m_s$.

In fact, in real magnetic materials, many interesting phenomena and properties, such as magnetostriction and magnetoresistance, are generated or related by spin-orbit coupling. Spin-orbit coupling is produced by spin and orbital angular momenta. The magnetic moments from spin of electrons interact with the magnetic field induced by electron's orbital motions. The magnitude of the spin-orbit coupling depends on the charge on the atomic nucleus, in other words, determined by the atomic numbers Z. For light atoms, the total angular momentum associated with the magnetic moment of a many electron atom can therefore be estimated

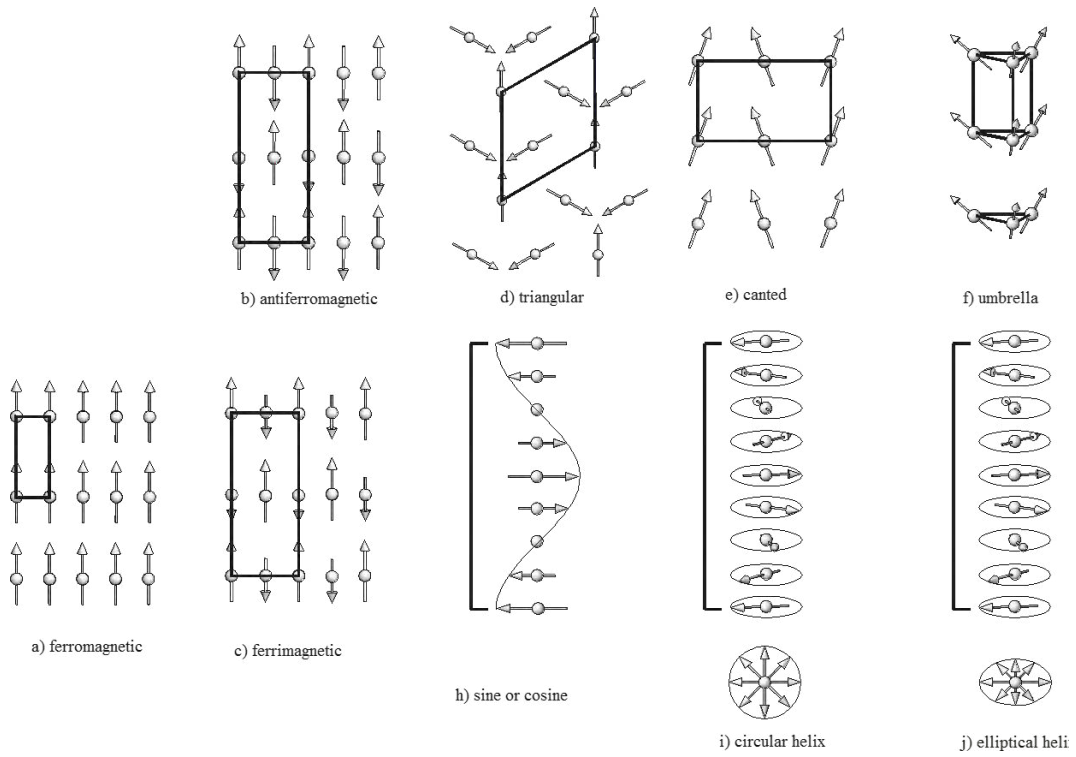

Figure 1.2: Various spin arrangements in ordered systems[8]

by combining the total orbital and spin momenta, so that $J = L + S$. The magnitude of total angular momentum is then given by $\sqrt{J(J+1)}\hbar$, and the projection onto the magnetic field direction is equal to $M_J\hbar$. This scheme is described by Russell-Saunders coupling. This coupling leads to the energy differences between states with different J values. By the Hund's rules, one can estimate the lowest-energy configuration for the electrons in a partially filled shell, namely, the ground state of an ion.

It is worth noting that for complete shells of electrons, L, S and J are equal to zero, so there is no net angular momentum and hence no contribution to the permanent magnetic dipole moment. Such atoms are called diamagnetic. Diamagnetism is generated by the change in orbital motion of the electrons when an external magnetic field is applied. Indeed, diamagnetism is present in all materials, but it is a weak effect which can be overshadowed by much stronger interactions such as ferromagnetism or paramagnetism.

1.2.1.2 Order and magnetic structure

When magnetic ions or atoms are embedded into solids, the spin arrangements can be ordered in many ways, as illustrated in figure 1.2. The reasons for the different orderings, and the resulting magnetic properties will be discussed in this section. But first the immediate surroundings and possible moment interactions will be addressed. In fact it is these types of magnetic interactions in different crystals which account for various types of magnetic ground states.

Crystal field and Jahn-Teller effect

In general, $4f$ electrons of rare earth ions are largely localized in solids, and $3d$ electrons of transition metals are delocalized in metals, but localized in oxides and other ionic compounds, where they adopt commonly the six-fold (octahedral) or four-fold (tetrahedral) coordination. Normally, for a free atom the five 3d orbitals have equal energy, but when a transition-metal atom is surrounded by anions in a solid this does not hold anymore. An electrostatic environment, deriving from the surrounding anions, called the crystal field, will exert on transition metal atom. The role of the d orbitals on the central ion and their overlap with orbitals on surrounding ions can be described by ligand field theory. In the common octahedral crystal field provided by the oxygen on each corner, the d_{z^2} and $d_{x^2-y^2}$ orbitals are raised in energy relative to other orbitals, as illustrated in figure 1.3. The opposite manner will be introduced when one considers the tetrahedral environment in which the two-fold e_g levels lower in energy. Accordingly, the spin configurations, relative to the orbital fillings, depend strongly on the competition between the crystal field energy and the energy expense of putting two electrons in the same orbital (pairing energy). The high-spin configuration, appearing in the weak-field case, is formed when the crystal field energy is lower than the pairing energy. On the contrary, the low-spin configuration (in the strong-field case) can be obtained if the crystal field energy is higher than the pairing energy.

In fact, both the orbital quenching and the Jahn-Teller effect are the results of crystal field effect. Orbital quenching means that the orbital angular momentum is equal to zero, deviating from the Hund's rules. The reason is that for 3d ions the crystal field interaction is much stronger than the spin-orbit interaction. Another consequence of crystal field effect occurs when the e_g or t_{2g} orbitals are partially occupied. Taking Mn^{3+} ion in an octahedral environment as an example, we will see that sometimes, the magnetic properties themselves can affect the symmetry of the local environment due to the energetically favorable cause. As shown in figure 1.4, distorted octahedron is often observed in practice, which lowers the energy of one of e_g orbitals at the cost of raising the energy of the other. Since the raised orbital is unoccupied, a net lowering of electronic energy is obtained. This phenomenon is known as the Jahn-Teller effect. This effect is an elongation of the octahedron that makes the energy of the d_{z^2} orbital lower. Consequently, the arrangement of the local structural distortions in the material can have a obvious influence on the magnetic properties. For example, the orbital ordering has been found in $NaMnGe_2O_6$, a Jahn-Teller active compound, and leading to the up-up-down-down spin configuration which is totally different to the theoretical prediction[84]. The orbital ordering phenomenon in $NaTiSi_2O_6$ is used to explain the spin-Peierls transition[104].

Exchange interactions

To account for the ordering in most magnetic materials, it is necessary to consider the exchange interactions which lie at the heart of the phenomenon of long range magnetic ordering. Exchange interactions are very important in explaining the origin of Weiss molecular field

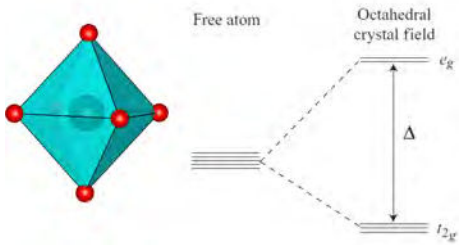

Figure 1.3: The crystal field in an octahedral environment.

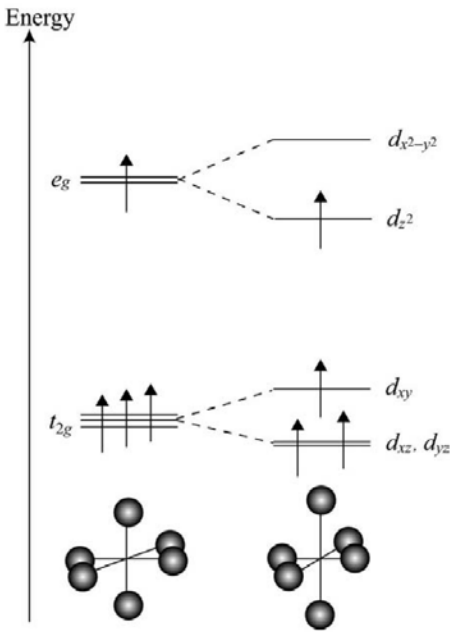

Figure 1.4: The Jahn-Teller effect for$Mn^{3+}(3d^4)$. Elongation of the oxygen octahedron along the z axis, and its consequent compression in the x-y plane, lowers the energy of the d_{z^2}orbital relative to the the $d_{x^2-y^2}$, and of the $d_{xz}$and d_{yz} relative to the d_{xy}. [9]

(responsible for the spontaneous magnetization), as a result of quantum mechanics. Exchange interaction actually reflects the consequence of the competition between the Coulomb repulsion of two neighbouring atoms and the Pauli exclusion principle. The relevant result which emerges from the quantum mechanics is that there is a term of electrostatic origin in the energy of interaction between neighboring atoms which tends to orient the electron spins parallel to each other. This term is called the exchange integral. Deriving from the two-electron model, the Hamiltonian of Heisenberg model, accounting for the exchange interactions in many-body system, will be described as[4]:

$$H = -\sum_{i>j} J_{ij} S_i \cdot S_j \tag{1.4}$$

where $J_{ij}$is the exchange integral between the i^{th} and j^{th} spins. The interatomic exchange interactions described by the Heisenberg Hamiltonian can be ferromagnetic (J>0) or antiferromagnetic (J<0). Competing exchange interactions may coexist with different signs of exchange integral. Thus in many magnetic materials it is necessary to combine direct interactions and some kinds of indirect exchange into the interpretation of magnetic phenomena.

Superexchange is defined as an indirect exchange interaction in which a non-magnetic anion (often oxygen, placed in between the magnetic ions) mediates the magnetic interaction between non-neighbouring magnetic cations. According to the localized nature of transition-metal oxides, there is little direct 3d-3d overlap, however, the 3d-orbitals are largely hybridized with oxygen 2p-orbitals. The superexchange arises from the partial covalent bond formation between the electrons on the magnetic ions and those on the anions(O^{2-}). The occupancy and orbital degeneracy of 3d ground states are the vital factors in determining the strength and sign of exchange constant for superexchange. As a result, superexchange is usually antiferromagnetic, and in some circumstances, it can actually be ferromagnetic. Whether the interaction will be antiferromagnetic or ferromagnetic can be considered from the empirical Goodenough-Kanamori rules.

As an indirect exchange interaction in metals, the **RKKY** (named by the discoverers of this effect, Ruderman, Kittel, Kasuya and Yosida) interaction describes the interaction between a localized magnetic moment and an conduction electron. A localized magnetic moment polarizes the conduction electrons so as to couple to a neighboring localized magnetic moment. The sign of the coupling is oscillatory, and can lead to either ferromagnetism or antiferromagnetism, depending on the separation between the localized magnetic moments.

Double exchange occurs in mixed-valent oxides, in which the hopping of delocalized electrons from high to low valent ions is energetically favorable because this lowers the kinetic energy of the system. In order to keep the high-spin states on both the high-valent ions and low-valent ions, ferromagnetic alignment of neighbouring magnetic cations are therefore formed. Furthermore, the ferromagnetic alignment allows the e_g electrons to hop throughout the crystal, as a result, the material becomes conductor.

Anisotropic exchange comes about in a few materials with low symmetry and reflects the mediated role of spin-orbit interaction. This kind of indirect interaction is known

as Dzyaloshinsky-Moriya interaction[5], which involves the exchange interactin between two neighboring magnetic spins, S_i and S_j. It can be written as $H_{DM}=D\cdot(S_i\times S_j)$ where D is a constant vector. This term in the Hamiltonian favors the canted spin arrangement rather than the antiferromagentic one and therefore is essential to the weak ferromagnetism observed in some antiferromagnets, e.g. $MnCO_3$ and Fe_2O_3[6]. The constant vector D is constrained by local symmetry. Considering the case that the magnetic interaction between two neighboring ions is mediated via a third ion (ligand) by the superexchange mechanism. The interaction forces S_i and S_j to be at right angles in a plane which is perpendicular to the vector D, in such an orientation the energy of system is the lowest.

The anisotropic exchange is of great importance in understanding the multiferroism of spin origin. This mechanism is called "inverse Dzyaloshinskii-Moriya effect", i.e., displacements of the ligand ions (like O^{2-}) can be induced by magnetic ordering, leading to a net electric polarization. This will be addressed in the following section.

Types of magnetic ordering

In the previous subsection, the different types of magnetic interaction which drive magnetic moments to adopt particular orderings have been presented. Now let us consider the various magnetic ground states which can be generated by these interactions.

When it comes to the atoms with unpaired shells, a positive magnetic susceptibility of **paramagnet** can be observed. In paramagnets, the magnetic moments are weakly coupled to each other, and any thermal agitation makes the alignment of these magnetic moments at random. At low magnetic field, a small fraction of moments are aligned into the field direction, and the susceptibility is almost constant. In many paramagnetic materials, the susceptibility is inversely proportional to the temperature, as shown in figure 1.5, and this can be explained by the Langevin theory. According to the Brillouin function, one can deduce the famous Curie law $\chi = C/T$ which describes the relationship between magnetic susceptibility and temperature. In metallic paramagnetic materials, the susceptibility is temperature-independent and weak, namely, the Pauli paramagnets. The Pauli paramagnetism originates from the conduction electrons and therefore can be explained by the band structure theory. Many compounds containing transition-metal elements are paramagnetic. In some transition-metal oxides, each transition metal cation has a net magnetic moment, and the anions O^{2-} make spatial separation between cations. Thus the interactions between the magnetic moments of neighbouring cations are weak. An example will be given in Chapter 4.

For some paramagnetic materials, the magnetization will be enhanced from initial zero to a saturation value even under a rather small magnetic field below a critical temperature T_C. This is called **ferromagnetism**, characterized by magnetic hysteresis loop. In fact the initial zero magnetization can be explained by the Weiss theory of magnetic domain. In ferromagnet, there is a strong internal interaction between magnetic moments, namely, molecular field, which leads them to align in parallel and gives rise to a spontaneous magnetization even if the existence of thermal fluctuation. Molecular field theory tells us that the temperature dependence of a

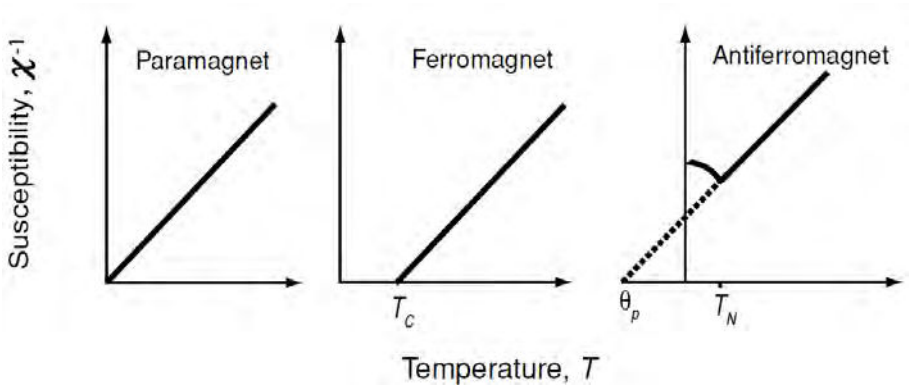

Figure 1.5: Comparison of the inverse susceptibility of a paramagnet, a ferromagnet and an antiferromagnet[7]

ferromagnet follows the Curie-Weiss law $\chi = \frac{C}{T-\theta}$ above the Curie temperature T_C, as shown in figure 1.5. The spontaneous ordering will develop and yields the ferromagnetic phase below the critical temperature.

Another long range ordered magnet can be produced if the exchange interaction is negative, and the molecular field is oriented so that it is preferred for adjacent magnetic moments to align antiparallel to each other. This is **antiferromagnetism.** Although, like the case of paramagnet, antiferromagnet has no net magnetization and a small positive susceptibility, it is a result of long range ordering of magnetic moments. Actually, they are quite different at the microscopic level. It was Louis Néel who first pointed out that antiferromagnet can be regarded as consisting of two interpenetrating and identical sublattices of magnetic ions, as illustrated in figure 1.2(b). Then the first direct observation of the magnetic structure of antiferromagnets was obtained by neutron diffraction. Even though one of the magnetic sublattices is spontaneously magnetized below a critical temperature, T_N (the Neel temperature), the second sublattice is spontaneously magnetized by the same internal field in the antiparallel direction. Therefore, the temperature dependence of the susceptibility above T_N is similar to that of a paramagnet, but below T_N it reduces with decreasing temperature. As shown in figure 1.5, the magnetic susceptibility of antiferromagnet in the paramagnetic state can be fitted to a Curie-Weiss curve, but unlike the case of ferromagnet, here the Weiss temperature θ is negative. We expect that $\theta = -T_N$, although experimentally determined Weiss temperature in antiferromagnet is often a long way from $-T_N$. This derivation is largely attributed to the assumption that the molecular field on one sublattice relies only on the magnetization of the other sublattice.

The **ferrimagnets** are somewhat similar to antiferromagnets, in which the magnetic moments from two magnetic sublattices align antiparallel to one another, however, the magnitudes of the moments on the two magnetic sublattices are different. This is allowed if the atoms on the two subllattices are different in nature or/and the two sublattices are crystallographically inequivalent. As a result, ferrimagnets have net overall magnetization. Most ferrimagnets are in fact ionic solids, meaning that they are electrically insulating, whereas most ferromagnets

are metals. This leads to a wide range of practical applications for ferrimagnets, in circumstances requiring magnetic insulators. Most pyroxene compounds containing transition-metal atoms are antiferromagnets, whereas only one ferromagnet $NaCrGe_2O_6$ is reported at present. We will give an overview of the relevant pyroxene compounds in the last section of current chapter, and then open up the theme of this dissertation.

1.2.2 Broken symmetry in magnetism

At low temperature, the presence of spontaneous ordering is a common and fundamental phenomenon of solid state physics. We know that ferromagnets, ferrimagnets, antiferromagnets, ferroelectrics, antiferroelectrics and superconductors are ordered phases, as well as solid state itself. It is worth noting that all these phenomena give rise to somehow similar fundamental properties and characteristics. One of the apparent characteristics is that their corresponding physical properties undergo very different temperature-dependent behavior above and below a **critical temperature** T_C. One can design an **order parameter** as a term to describe these ordered fundamental phenomena, i.e., the order parameter is zero for $T>T_C$, and non-zero for $T<T_C$.

Broken symmetry can be depicted when we consider the liquid-solid phase transition[4]. The matter at high temperature state possesses complete transitional and rotational symmetries. Below the critical temperature, the periodic crystals at low temperature have residual symmetries, as a result of breaking the high symmetry of liquid phase. This argument also holds when it comes to ferromagnets. The lower temperature long range order state of magnetic moment has a reduced symmetry because the system chose a unique direction for all the moments to line up.

1.2.2.1 Models

Some models are devoted to understanding the consequences of broken symmetry. A magnetic model system is one with a simple lattice structure, occupied by spins with one, two or three dimensions, which is convenient to describe the spin configurations in materials.

Landau theory of ferromagnetism

Very often, the immediate consequence of breaking symmetry is phase transition. A common model which simply describes a phase transition was given by Lev Landau. The relationship between free energy of a ferromagnet and magnetization M is provided by the expression:[4]

$$F(M) = F_0 + a(T)M^2 + bM^4 \tag{1.5}$$

where F_0 and b are constants and a(T) is written as $a(T) = a_0(T - T_C)$ near the transition, and a_0 is a positive constant. The ground state of the system can be gained by derivating F with respect to M and equating to 0. Then we obtain:

$$M = 0 or M = \pm \left[\frac{a_0(T_C - T)}{2b}\right]^{1/2} \tag{1.6}$$

the minimal energy of the system is only given when $T<T_C$. Consequently, the magnetization is non-zero and proportional to $(T_C - T)^{1/2}$ when $T<T_C$, otherwise, M=0. The mechanism underlying the Landau's theory of phase transition is one type of mean-field theory, which has been encountered in understanding the origin of the paramagnetism. Near the critical temperature, the correlations and fluctuations, which are not considered in mean-field theory, become more significant. The fluctuations are characterized by the correlation length, which is the dominant length scale. The pair correlation function $\Gamma(r)$ between two spins i and j is defined as:[7]

$$\Gamma(r_{ij}) = < S_i \cdot S_j > - < S_i > \cdot < S_j > \tag{1.7}$$

The correlations decay exponentially, and the correlation length ξ can be defined by $\lim_{r\to\infty} \Gamma(r) \sim exp(-\frac{r}{\xi})$. The correlation length becomes infinite at the critical temperature.

Heisenberg and Ising Models

As an important magnetic model, the nearest-neighbor Heisenberg model is to consider particular microscopic behaviors of the magnetic interaction. The Hamiltonian of Heisenberg model has been shown when we talked about the exchange interactions, see 1.4. It may be rewritten in terms of their x, y, z, components for interactions of two spins:

$$H = -J(S_1^x S_2^x + S_1^y S_2^y + S_1^z S_2^z) \tag{1.8}$$

with good reason that the spins $\mathbf{S}_i$ are allowed to align in three-dimensional space (dimensionality of spins D=3). However, when a lattice is involved, the sum of interactions can be taken over a lattice of 1, 2, or 3 dimensions (dimensionality of lattice d=1,2,3). An alternative model can be envisaged when the two-dimensional spins are confined to a plane-the xy model. An even simpler model is concerned with one-dimensional spins. This is called Ising model in which the spins are only allowed to point along the z-axis. The Hamiltonian of this model for two spins is given by:

$$H = -JS_1^z S_2^z \tag{1.9}$$

Whereas the dimensionality of the order parameter D is equal to 1, these one dimensional spins can be arranged in any dimensional lattice. In fact, no long range order occurs in one-dimensional Ising system (D=1, d=1) for T>0. Nevertheless, quasi-one-dimensional characteristic was observed and investigated in pyroxene related compounds, e.g. $CaCuGe_2O_6$ and $CuGeO_3$. We will move on this topic in next section.

Magnetic ordering at a finite phase transition temperature becomes preferred for lower spin dimensionality D, for the spins then have fewer degrees of freedom, and is often formed

in higher spatial dimension d, because fluctuations are then less likely to destroy the order. As a result, only a few systems show the low-dimensional long range order, and that is one of the motivations for this dissertation.

1.2.2.2 Consequences of broken symmetry

The direct result of broken symmetry is **phase transition**. The temperature at which occurs the disorder-order transition is called the critical temperature. The region near the phase transition is called the critical region. A number of exponents describing the temperature evolution of the order parameter, known as critical exponents, are defined to give the information about the nature of the phase transition.

It is known that ferromagnets show permanent magnetism, and crystals have rigidity. They are results of breaking symmetry. This is called **rigidity phenomenon** which behaves like resistance to keep the broken-symmetry state (phase) with energetic preference. **Excitation** is produced because of the thermal fluctuations. In ferromagnets these excitations are called spin waves, quantized into magnons, which can be detected by neutron scattering measurement. **Defects** are inevitable results, even if they are very often unexpected, for example, the grain boundaries in crystals and domain walls in ferromagnets.

1.2.3 Competing interactions and one dimensional magnets

When atoms or ions are made up into lattice, in some special crystal circumstances, the magnetic moments may couple so as to give rise to competitions between different interactions and low dimensionality. In some cases, the magnetic moments occupy sites on specific lattices, the topology of which can result in geometrical frustration. These phenomena may lead to some extremely complex, and novel magnetic properties in solids. At least, we see that they are all crystal-structure-dependent. We start with frustration, which can lead to many different ground states, and then by combining somehow disorder, spin glass behavior will be introduced. At the end of this subsection, we will show the interesting one-dimensional magnets in three-dimensional lattice, therein some examples of pyroxene compounds will be taken.

1.2.3.1 Frustration

It is known that ferromagnetic interactions are satisfied by a parallel alignment of magnetic moments. But it is not likely that antiferromagnetic interactions are also satisfied in some lattices. In crystal lattice with odd-membered rings, it is impossible to satisfy all the antiferromagnetic interactions to find the ground state, as shown in figure 1.6. In this situation, the system is said to be frustrated. For perfectly frustrated systems , this leads to a high degeneracy of the magnetic ground state and prevents the system from ordering at long range. This is called a spin liquid state, characterized by the absence of long range order and the persistence of magnetic fluctuations down to the lowest temperatures. In many real systems, complex magnetic orderings are achieved at low temperature and the Néel temperature T_N

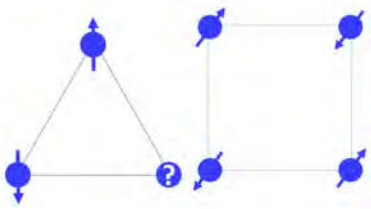

Figure 1.6: Antiferromagnetic nearest neighbouring interactions on the triangular and square lattices

may be much smaller than the experimentally determined Weiss temperature.Accordingly, the frustrated system exhibit metastability, hysteresis effects, and time-dependent relaxation towards equilibrium[4]. Some particular lattices are well-known to yield geometrical frustration. For example, it can be observed in two-dimensional triangular and corner sharing kagome lattices. The pyrochlore family, as one example of three-dimensional frustrated systems, has been extensively studied, in which the magnetic moments form a lattice of corner-sharing tetrahedra. It shows a cooperative paramagnetism behavior in which only short-range correlations between moments are formed for all temperatures. Related features occur in magnets with competing interactions, such as the pyroxene compounds we will discuss in detail, where both ferromagnetic and antiferromagnetic couplings between pairs of spins are present, with the sign of interaction depending on the spatial distance of the spins.

1.2.3.2 Spin-glass

Another complex situation, resulting from competing interactions, can be found in some materials, which incorporates both magnetic frustration and disorder in their spin systems. As a result, a spin glass is described as a random, mixed-interacting magnetic system characterized by a random, yet cooperative, freezing of spins at a fixed temperature T_f below which a frozen state appears without the common magnetic long range ordering.[4] The disorder can be introduced by site-randomness in which the magnetic ions or atoms will be distributed randomly in the crystal structure, as well as by bond-randomness in which the exchange interactions between the nearest magnetic ions or atoms vary between +J and -J. As a consequence of disorder, the distribution of distances between magnetic moments in a site-random spin glass gives rise to competing interactions since the RKKY interactions, for example, depend largely on the spatial distribution of magnetic ions or atoms. In addition to the effect of site-randomness, bond-randomness naturally leads to the formation of competition between exchange interactions. The system thus remains in a frustrated state.

Consequently, the interactions between the magnetic moments are "in conflict" with each other due to some frozen-in structure disorder. On the basis of the spin dimensionality, three microscopic models, with respect to the mentioned models in previous subsection, can be used to describe the materials with spin glass behavior. The diluted alloys, such as Cu(Mn), formed by non-magnetic noble metals and transition metals, is a classical **Heisenberg-like spin glass**. A layered manganite $Eu_{0.5}Sr_{0.5}MnO_4$ can be described by **XY spin glass** model.

The **Ising-like spin glass** model can be used to explain the spin glass transition in recent reported $Ni_xMn_{1-x}TiO_3$ series compounds in which an evident magnetoelectric effect were observed.[10]

1.2.3.3 One-dimensional magnets

According to the discussion of magnetic models in last subsection, it is evident that isolated magnetic chains can never be long range ordered. Apart from the non-long range order, a one-dimensional magnet shows possible magnetic excitations, and they are complex, interesting and incompletely understood.

A spin chain (d=1, D=1, 2 or 3) is known as a one-dimensional line of spins. In the chain, the spin can be confined to align parallel or antiparallel to a particular axis (Ising spins), or constrained into a specifying plane (XY spins), or may be free to order in any direction (Heisenberg spins). Spin chains can be approximately obtained in three-dimensional crystals, when the structure is crystallized with approximately isolated chains. We said that what makes these chains interesting is their excitations rather than their orderings. In an Ising spin chain, the excitation is associated with domain walls, and there is no wave vector dependence. The excitations of Heisenberg spin chains are known as gapless spinons which have half spin quantum number and belong to ferminons. Spinons were indeed observed in some one-dimensional antiferromagnetic materials. The excitation behavior of integer spin chains is quite different from spinons. A one-dimensional chain with integer spins is known as Haldane chain which has no gapless excitations. In the pyroxene family, for example, the V-based pyroxenes have been considered as a promising Haldane-chain system with S=1.[11]

Another interesting phenomenon of spin-1/2 antiferromagnetic chain is related to the well-known Peierls distortion. This is known as spin-Peierls transition which can open a gap in the excitation spectrum. The magnetoelastic coupling between the one-dimensional electronic structure and the three-dimensional lattice vibrations drives this intrinsic lattice distortion. Actually, above the transition temperature, there is a uniform antiferromagnetic exchange in each chain, but below the transition temperature, two unequal alternating exchanges are produced by forming dimerization for adjacent lattice sites. Because antiferromagentic chains often become three-dimensionally ordered at low temperature, there are only a few materials which show a spin-Peierls transition. The well-known example for inorganic material is $CuGeO_3$ with a spin-Peierls transition at 14 K. As a system with half-spin chains, Ti-based silicate pyroxenes were found to show this spin-Peierls transition.

A system somewhere in between a one-dimensional magnet and a two-dimensional magnet can be considered when the coupling between nearest chains is of comparable strength as the coupling within the chains. Such a system is known as a two-leg spin ladder.

1.3 Structure-property relationships

The physical and chemical properties of materials often depend on direction. Anisotropy effect is therefore of significance when physical properties of materials is demanded in technological applications. In this section, we will show that tensors and matrices provide the mathematical framework to study the structure-property relationships, and again symmetry is very useful in determining which coefficient of property is absent, and which must be equivalent. Neumann's principle will guide us how to properly measure distinct physical properties in specific materials. At the end of this section, two examples, which are related to two different rank and type of tensors, will be treated to illustrate how to apply the laws to various classes of physical properties. This is also one of the most important themes of this dissertation.

1.3.1 Polar and axial tensors

The physical properties of crystals are defined by relations between measurable quantities. Crystal physics is mainly concerned with the relationships between symmetry and the directional properties of crystals. By symmetry arguments, we may fundamentally understand the mechanisms underlying the useful physical properties and how to correctly measure these physical properties.

Tensors are the mathematical form of the anisotropic physical properties of crystals. In fact, vectors, such as those used to represent the pyroelectricity, and matrices, such as those used to describe the thermal expansion, are special forms of tensors. All tensors can be defined as the way which transforms from one coordinate system to another. The transformations involve a set of direction cosines a_{ij}, where i,j=1, 2, 3. In general, there are two kinds of tensors: polar tensors and axial tensors. Axial tensor properties appear when magnetic phenomenon is involved. Axial tensors change sign when the handedness varies, whereas polar tensors do not. For a **polar tensor**, the general transformation for a tensor with rank N is described by:

$$T'_{ijk...} = a_{il}a_{jm}a_{kn}...T_{lmn...} \tag{1.10}$$

where the left term is the tensor component in the new coordinate system, T_{lmn} is a tensor component in the old system, and the rest coefficients are the direction cosines linking the two coordinate systems. In this equation, each tensor component has N subscripts and there are N direction cosines which are denoted by those coefficients. The rank of tensor is defined as the number of directions considered in measuring the property. As a result, tensors are classified into different ranks according to how they transform from one coordinate system to another, as summarized in table 1.1.

For example, the thermal conductivity k relates the heat flow h to the temperature gradient by: $h_i = -k_{ij}\frac{dT}{dZ_j}$. There are three tensors: h_i and $\frac{dT}{dZ_j}$ are vectors. However, the thermal conductivity is a second rank tensor property: $k_{ij} = a_{il}a_{jm}k_{lm}$. It is worth noting that the two vectors are not properties of the materials, while the thermal conductivity is a property that belongs to the material. Therefore, only k_{ij} depends on the symmetry of the material.

Rank	Polar	Axial
zero	Specific heat	Rotatory power
First	Pyroelectricity	Pyromagnetism
Second	Thermal expansion	Magnetoelectricity
Third	Piezoelectricity	Piezomagnetism

Table 1.1: Some examples of Polar and axial tensors.

Properties such as pyromagnetism, optical activity, and the Hall effect are all **axial tensors** that are determined by the handedness. Slightly similar to polar tensors, axial tensors transform in the following expression:

$$T'_{ijk...} = \mid a \mid a_{il}a_{jm}a_{kn}...T_{lmn...} \tag{1.11}$$

It is obvious that this expression is almost identical to that of a polar tensor except the determinant of the direction cosine matrix. The determinant is equal to +1 or -1, depending on if or not the handedness of the axial system changes during the transformation. Any symmetry operation related to mirror planes or inversion centers will give $\mid a \mid = -1$. After applying the Neumann's principle, we will see later that magnetoelectricity is a good example of an axial tensor property.

1.3.2 Neumann's principle

It is the Neumann's principle that builds up the symmetric relationship between crystals and their relevant physical properties. It states: " The symmetry of any physical property of a crystal must include the symmetry elements of the point group of the crystal." [13] In other words, the measurements performed in symmetry-related directions will give the same property coefficients. In the expression of tensor 1.10, we see that the direction cosine matrix for any symmetry operation is expressed via the (a) matrix. It is employed to transform the tensors under the relevant symmetry operator. If the crystal possesses this symmetry element, then the property coefficient must be left unchanged according to Neumann's principle.

1.3.3 Symmetry consideration

Pyroelectricity

The prefix pyro- in the term pyroelectrics means heat in Greek, so as in pyroxenes. A change in the spontaneous polarization of a material in response to a change in temperature is called pyroelectricity. Thus pyroelectricity is a first rank tensor property. The defining relation can also be written in terms of the electric displacement D since no external field is applied: $P_i = D_i = p_i \triangle T$. Because D_i is a polar vector, and temperature variation transforms as a zero rank tensor, we get:

$$D'_i = a_{ij}D_j = a_{ij}p_j\triangle T = a_{ij}p_j\triangle T' = p'_i\triangle T' \tag{1.12}$$

As a result, the property relating transformed $D_i^{'}$ to transformed $\triangle T^{'}$ is the transformed pyroelectric coefficient: $p_i^{'} = a_{ij}p_j$. This is a polar first rank tensor property. Actually, pyroelectricity is absent in all centrosymmetric materials. We will show this argument using Neumann's principle. For any first rank tensor, there are three non-zero cofficients p_1,p_2 and p_3 that represent the directional pyroelectric coefficients. So the tensor coefficients are often given in matrix form: $(p^{'})$ is a 3×1matrix, (a) is a 3×3matrix, and (p) is also a 3×1matrix. When considering the direction cosine matrix as a symmetry element of crystal, by Neumann's principle, we should finally have $\left(p^{'}\right) = (p)$. We treat this with a center of symmetry operator, given:

$$\left(p^{'}\right) = \begin{pmatrix} p_1^{'} \\ p_2^{'} \\ p_3^{'} \end{pmatrix} = \begin{pmatrix} -1 & 0 & 0 \\ 0 & -1 & 0 \\ 0 & 0 & -1 \end{pmatrix} \begin{pmatrix} p_1 \\ p_2 \\ p_3 \end{pmatrix} = \begin{pmatrix} -p_1 \\ -p_2 \\ -p_3 \end{pmatrix} = -(p) \tag{1.13}$$

Using Neumann's principle, we have: $\left(p^{'}\right) = -(p) = (p)$. Finally, the only solution for this equation is that all three pyroelectric coefficients are zero. Therefore, pyroelectricity is presented only in 10 of the 32 crystal point groups, which do not possess inversion symmetry. By similar treatment, we can predict that the first discovered pyroelectric tourmaline with point group 3m has non-zero pyroelectric coefficients only along the *b*-axis.

Magnetic structures and time reversal: Axial tensors

Before working out the magnetoelectricity, we first answer some questions about magnetic structures in the viewpoint of symmetry. A number of ordered magnetic structures have been determined by neutron diffraction and various resonance techniques, as shown in figure 1.2. The question of interest is how these magnetic moments transform under various symmetry operations. As we known that the magnetic structures are often represented as a set of arrows, associated to the magnetic atoms, with magnitudes and orientations. However, this is misleading or inconvenient when considering the symmetric effects. A current loop is, equivalent with magnetic moment, helpful to retain the arrow indicating the magnetization direction as an aid in visualizing the orientation of the current loop.

Figure 1.7 shows some examples of the transformations of a current loop under various symmetry operations. Although a twofold axis reverses the direction of magnetic moments oriented perpendicular to the axis, it does not vary the parallel components. Similar relations are observed under mirror plane symmetry: magnetic moments parallel to the mirror are reversed by the reflection operation, while perpendicular components are invariant. A very important symmetry operation, center of inversion, is often considered in magnetoelectric effect. A polar vector, such as electric field and electric polarization, breaks the inversion symmetry, whereas an inversion center retain the magnetic moments unaffected.

Time reversal or spin reversal is an often used operator in describing magnetic configurations. This operator changes the direction of current loop so as to reverse the direction of magnetic moment. In magnetically ordered systems the time reversal can be combined into

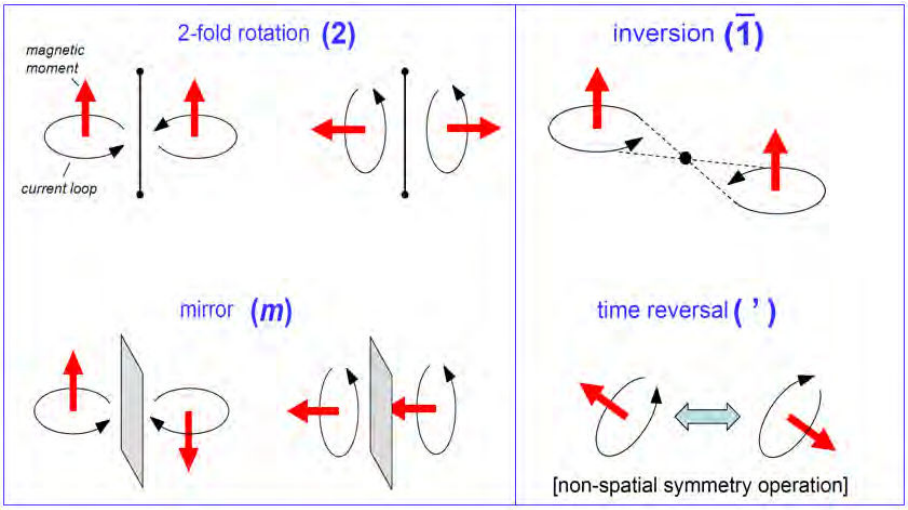

Figure 1.7: Transformation of a current loop under twofold rotation, reflection, inversion, and time reversal.

the conventional symmetry operations. The operator is called "primed" to indicate that we have to reverse the spin after applying the conventional symmetry operations. Magnetic point groups are constructed by combining crystallographic point groups and time reversal symmetry. There are 32 trivial magnetic groups, called "grey" magnetic point groups, which are the ordinary crystallographic point groups supplemented by the time reversal. Other magnetic point groups, called white magnetic point groups, only contain all the 32 crystallographic point groups. The third type of magnetic point groups, the only nontrivial one, consists of the point groups in which time reversal selectively combines with rotations or reflections. This gives rise to 58 point groups, called black and white groups.

Electric and magnetic phenomena are related to each other through Maxwell equations. It is evident that electric and magnetic variables are coupled by vector products (cross). In tensor formation, the vector products are denoted as the rotation tensor ε_{ijk}which is equal to zero unless all three subscripts are unequal. And the rotation tensor changes sign when the handedness varies. As a result, when the time reversal is considered in the transformation, there are two possible sign variations, one for the handedness change and the other for time reversal.

Magnetoelectric effect

In solids, the electric and magnetic orderings are often considered incompatible due to their distinguishing origins. Electric order is the result of ordering of local electric dipoles (charges), while magnetic order conventionally originates from exchange interactions between magnetic dipoles (spins). However, the strong coupling of these degrees of freedom can be ascertained in magnetoelectric materials, that is, the cross coupling of magnetization and polarization, to their conjugate fields, E and H, which is known as magnetoelectric (ME) effect. Date back to 1894, Pierre Curie first proposed that the coupling between magnetic and electric orders

is possible in insulators on symmetry grounds. A more rigorous prediction of a linear coupling between electric polarization and magnetization was shortly formulated by L.D. Landau and E. Lifshitz in one book of their famous series on theoretical physics.[14] In 1960, I.E. Dzyaloshinskii[16] showed that Cr_2O_3 has a magnetic symmetry which allows ME effect, and then the first experimental verification came up by D.N. Astrov.[15] These findings reveal that specific symmetry requirements must be fulfilled for the tensor to be non-zero in order to gain ME effect in materials.

The expansion of free energy for a system which describes the interactions between magnetism and electricity is given by:

$$F(E,H) = F_0 - P_i^s E_i - M_i^s H_i - \frac{1}{2}\varepsilon_0\varepsilon_{ij}E_iE_j - \frac{1}{2}\mu_0\mu_{ij}H_iH_j - \alpha_{ij}E_iH_j \tag{1.14}$$

$-\frac{1}{2}\beta_{ijk}E_iH_jH_k - \frac{1}{2}\gamma_{ijk}H_iE_jE_k$

where ε_0 and μ_0 are the free space permittivity and permeability, respectively; P^s and M^s denote the spontaneous polarization and spontaneous magnetization, respectively; α is used to represent the tensor of the linear ME effect, while $\beta$and γ are used to design the two kinds of bilinear ME effect.

The linear magnetoelectric effect is defined as the first-order electric polarization response of a system to an applied magnetic field, or equivalently the magnetization induced by an applied electric field. By the differentiation of above equation, we have, to first order:

$$P_i = \alpha_{ij}H_j \tag{1.15}$$

$$M_i = \alpha_{ij}E_j \tag{1.16}$$

Considering the symmetry restriction which we discussed in previous section, in a magnetoelectric material, both space inversion and time reversal must be broken. Since electric field E is a polar first rank tensor and magnetization M is an axial first rank tensor, the magnetoelectric effect is an axial second rank tensor which thus transform as follows:

$$M_i = \pm \mid a \mid a_{ij}M_j = \pm \mid a \mid a_{ij}\alpha_{jk}E_k = \pm \mid a \mid a_{ij}\alpha_{jk}a_{lk}E_l = \alpha_{il}^{'}E_l^{'} \tag{1.17}$$

This equation yields $\alpha_{il}^{'} = \pm \mid a \mid a_{ij}\alpha_{jk}a_{lk}$. In matrix form, the linear magnetoelectric effect transforms in a similar way from the old system to the new system. Hence we have $(\alpha^{'}) = \pm \mid a \mid (a)(\alpha)(a)_t$. For a system containing time reversal symmetry $(1^{'})$, the ME effect is absent by the Neumann's principle: $(\alpha^{'}) = (-1)(+1)(+1)(\alpha)(+1) = (-\alpha) = (\alpha) = 0$. Similarly, for conventional space inversion operation, the ME effect also disappears, whereas ME effect can be present in special operations of space inversion accompanied by time inversion. We will take pyroxene compounds to demonstrate how useful the symmetry consideration is, in chapter 5.

Magnetoelectric matrices for relevant magnetic point groups are listed in table 1.5.8.1 in

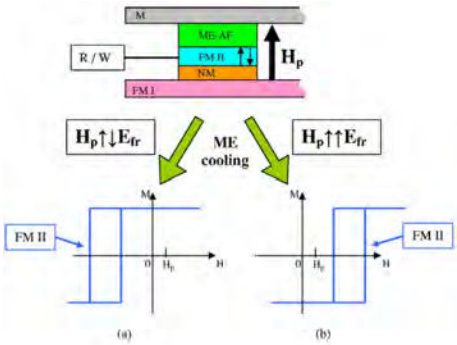

Figure 1.8: Schematics of a ME-RAM cell. [17]

IUCr International Tables for Crystallography. Only 58 magnetic point groups are magnetoelectric. According to the magnetoelectric tensors, the measurement of magnetoelectric effect in single crystal may be the ideal choice, since it is easy to predict and easy to evaluate. However, very often, a single crystal with suitable size and quality are unavailable, and it does not provide macroscopic properties on the bulk material. Alternatively, the possibility to measure the ME effect in polycrystalline samples are expected. To realized this measurement, the so-called magnetoelectric poling, also known as magnetoelectric annealing, is indispensible.

The fields H and E are simultaneously applied to the sample as it cools through the Neel temperature. Then the poling fields are removed and the magnetoelectric coefficients are measured. For a symmetry allowed magnetoelectric polycrystalline material, all ME tensors will vanish by cooling below its transition temperature in the absence of any field. The reason is that most magnetoelectric materials are antiferromagnetic, and therefore have two variables with opposite magnetoelectric coefficients related by time reversal. In the absence of external field, accordingly, there are two types of antiferromagnetic domains with equal volume fraction, and their ME effect cancels each other out, showing no macroscopic ME effect. To alter the domain distributions in the material, electric and magnetic fields have to be applied simultaneously during the cooling through Neel point, which favors one over the other and hence gives rise to macroscopic ME effect.

Unlike the electric polarization yielded in typical multiferroics, linear ME materials is characterized with weak polarization. However, this did not impede its possible applications on random access memory device since the small linear ME effect has recently been shown to control spintronic devices very efficiently in a magnetoelectric exchange bias system[17], as shown in figure 1.8. The underlying mechanism leading to a linear ME coupling is still unclarified, but apparently, it is strongly material-dependent. Therefore, neutron diffraction technique, employed to reveal the magnetic and crystal structuresymmetry, is vital for the study of linear ME effect as well as evaluating new materials exhibiting linear ME effect.

1.4 Multiferroics

In the previous sections, we have came up with how atoms get stack into solids, discussed the fundamental of magnetism and the interesting one dimensional magnets, and showed how structure and property are strongly related by symmetry. In this section, we will move on the main topic of this thesis: multiferroics.

1.4.1 Primary orders and multiferroics

1.4.1.1 Primary orders in dielectrics

Materials can be defined as multiferroics (MF) when two or more of the primary ferroic orders are unified in the same phase.[18] So we will confine our discussion into single phase multiferroics, excluding composites such as heterostructures of ferroelectrics interlayered with magnetic materials. The primary ferroic states can be classified in terms of space inversion and time reversal symmetry of their order parameters. Four established primary ferroic orders are known up to now. The analogous characteristics of the four types of primary ferroics are spontaneous ordering and the formation of domains, as we have discussed in previous section, they are the consequence of broken symmetry. However, they have very distinct transformations according to the symmetry operations of space inversion and time reversal, showing the nature of polar or axial tensor property. Ferroelectric order is characterized by a spontaneous polarization, the sign of polarization changes under space inversion operator but remaining invariant under time reversal. On the contrary, ferromagnetic or antiferromagnetic order is determined by a spontaneous magnetization, its sign changes under time reversal operator but remaining unaltered under space inversion. Ferroelastic order is accompanied by a spontaneous strain for which both space inversion and time reversal are all symmetric. Either space inversion or time reversal can change the sign of toroidal moment.

1.4.1.2 Multiferroics

The term "multiferroics" was first used in 1994 by H. Schmid,[19] but, as we mentioned in previous section, systems exhibiting the magnetoelectric coupling between electric and magnetic properties have been studied since 1894. A new twist of conventional ME was the idea that not only can strong cross-coupling of responses exist in solids, such as the appearance of ME coupling, but also that there may exist systems in which two types of ferroics, magnetism corresponding to the spontaneous ordering of magnetic moments, and ferroelectricity corresponding to the spontaneous ordering of electric dipole moments, can coexist in material without any external field (see figure 1.9).[66, 67] The longing and search for such multiferroics which combines magnetism and ferroelectricity, is driven by the prospect of controlling charges by applied magnetic fields and spins by external electric fields towards new multifunctional devices. At the beginning of 21^{st} century, there was a renaissance of magnetoelectrics and multiferroics due to the improved fundamental understanding of the contraindication between magnetism and ferroelectricity as well as the experimental achievements.

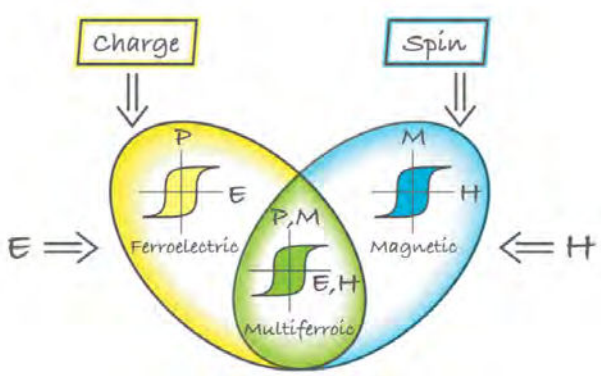

Figure 1.9: Multiferroics combine the properties of ferroelectrics and magnets.[65]

But it has been a challenge to find materials exhibiting strong coupling of electricity and magnetism.[30] The first obvious restriction is that ferroelectrics must be insulators to sustain a polarization, while most ferromagnetic materials are electrical conductors. The second problem is the difference in the microscopic nature of magnetic and electrical dipole orderings. Normally, magnetism requires that materials have unpaired localized electrons, such as those in the partially filled d orbital of a transition metal. In contrast, the electric charges of electrons and ions are responsible for the electric dipole ordering. As a result, ferroelectricity and ferromagnetism are somewhat separate and even mutually exclusive. The way to overcome this contraindication is the incorporation of two different cation types in one compound. Following this way, multiferroicity can be reached in materials here one cation sublattice provides the magnetism, and another one is responsible for the ferroelectricity (prototypal compound is $BiFeO_3$ perovskite). In addition to these magnetic ferroelectric MF, another type of magnetoelectric multiferroics is symmetry restricted with spin order induced ferroelectricity (prototypal compound is $TbMnO_3$). We will come to different MF in more detail in following subsection.

1.4.1.3 Ferrotoroidic order vs magnetoelectric effect

This subsubsection is dedicated to ferrotoroidic ordering. A magnetic toroidal moment is represented by a time-odd polar vector,[23, 24] which changes sign under both space inversion and time reveral, and is generally associated with a circular or ring-like arrangement of spins.[20] Materials in which the toroidal moments are spontaneously aligned are so-called ferrotoroidics,[21, 68] as shown in figure 1.10. The spontaneous toroidal moment in such ferrotoroidics should be tuned by crossed E and H fields. The reason why it is so interesting is because the toroidal moment is related to the antisymmetric part of the linear magnetoelectric tensor, in other words, an applied E field induces a perpendicular magnetization and vice versa.[22, 28]

A number of theoretical and experimental researches have been performed to explore and confirm the nature and existence of ferrotoroidic order. The microscopic sources of ferrotoroidic ordering can be considered in the magnetic multipole expansion as well as the expansion of free energy in terms of gradients of a magnetic field, the detailed discussion can be found in

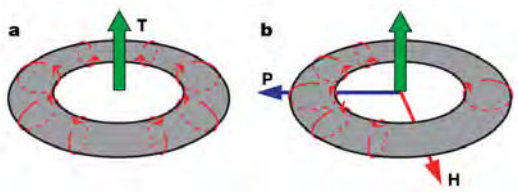

Figure 1.10: Toroidic moment and magnetoelectric effect. (a) Torus with an even number of current windings forming a toroidic moment, T. (b) The magnetoelectric effect α is illustrated by the current loops being shifted by the magnetic field (H), thus inducing an electric polarization (P). By rotating the figure by 90°, the asymmetry ($\alpha_{ij} = -\alpha_{ji}$) becomes obvious. Note that α_{ij} corresponds to a toroidal moment T_k(i≠j≠k).[68]

ref. [20, 28]. From the macroscopic symmetry consideration, the ferrotoroidic order parameter gives rise to antisymmetric contributions to the ME effect, indicating that the indirect evidence for the presence of a spontaneous toroidal moment in a system can be obtained by measuring the linear ME effect. A variety of candidate materials, such as pyroxene $NaFeSi_2O_6$ and $LiFeSi_2O_6$ compounds, were identified by measuring their linear ME properties.[25, 26, 27]

To properly evidence the ferroic nature of an ordered state, two verifications are obligatory[22, 29]: (a) the existence of domains as regions with different orientation of the order parameter; (b) hysteric orientation of these domains between opposite single-domain states in the conjugate field. In 2007, the first criterion was satisfied by observation of domain structure of ferrotoroidics in $LiCoPO_4$.[68] Very recently, the hysteretic poling of ferrotoroidic domains in the conjugate toroidal field was also investigated in $LiCoPO_4$.[22] All these experimental observations confirm that ferrotoroidicity is the fourth form of ferroic order.

1.4.2 Recent progress in multiferroics

A variety of materials exhibiting the multiferroic behavior with strong cross-coupling have been studied, as shown in figure 1.11. Within this figure, the intersection area formed by bold green and red solid lines represents materials that are multiferroic. More importantly, the blue regime shows materials presenting magnetoelectric effect. It is immediately indicative that there are only few materials which exhibit magnetoelectric multiferroism. In the following, we present a more detailed classification of multiferroics.

Since there are several different microscopic causes for ferroelectricity, one can have various types of multiferroics.[65] Generally, multiferroics are classified in two groups. Materials in the first group, called type-I multiferroics, in which ferroelectricity and magnetism have different origins and are essentially independent of each other, though there is finite coupling between them. As shown in table 1.2, these materials are characterized by rather large spontaneous polarization, and quite different ordering temperature between magnetism and ferroelectricity. The second group, namely type-II multiferroics, comprises materials in which the electrical ordering arises from the magnetic ordering, implying a strong coupling between the two orders. We will pay attention to the microscopic picture based on the properties of multiferroics.

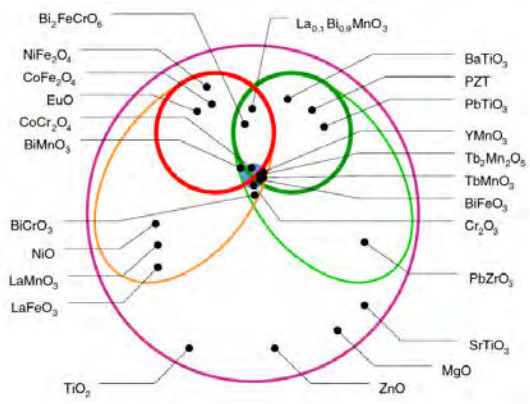

Figure 1.11: Classification of insulating oxides. The largest circle represents all insulating oxides among which one finds electrically polarizable materials (green ellipse) and magnetically polarizable materials (orange ellipse). Within each ellipse, the circle represents materials with a finite polarization (ferroelectrics) and/or a finite magnetization (ferro- and ferrimagnets). Depending on the definition, multiferroics correspond to the intersection between the ellipses or the circles. The small circle in the middle denotes systems exhibiting a magnetoelectric coupling.[69]

1.4.2.1 Independence between magnetism and ferroelectricity (type-I)

Materials belonging to Type-I multiferroics are usually good ferroelectrics with large electrical polarization in the order of 0.1∼1C/m^2. Besides, the critical temperature of the magnetic and ferroelectric transitions are often far above room temperature, allowing technological applications. Unfortunately, because of the different source of magnetic ordering and electric dipole moment ordering, the coupling between magnetism and ferroelectricity in these materials is thus rather weak. Several subclasses of type-I multiferroics are known and the three main subclasses are as follows.

Lone-pair multiferroics

Perovskite-type ABO_3 compounds are a natural choice for searching new multiferroics, since they are known to accommodate a large range of cations and display magnetic (ex/$AMnO_3$ manganites) or ferroelectric properties (ex: $BaTiO_3$, $PbTiO_3$...). One way to stabilize a ferroelectric distortion in perovskite compounds containing d^n cations on site B, is to introduce a cation with a lone $6s^2$ electron pair on site A. Perovskites compounds such as $BiFeO_3$[32] and $BiMnO_3$[33], in which the ferroelectric ordering is attributed to the structural distortion brought about by the lone pairs of Bi cations, whereas the magnetic ordering is due to the transition metal cations, are by far the most studied multiferroics. The temperature of magnetic ordering is different from that of ferroelectric ordering in these materials even if they possess very large polarization coefficient, as shown in table 1.2.

Compound	T_{FE}/T_N(K)	P(μC/cm^2)	Comment
$BiFeO_3$	1100/643	90(film)6(crystal)	MF-type I_Lone pairs
$LuFe_2O_4$	320	26	MF-type I_Charge ordering
$YMnO_3$	914/76	6	MF-type I_Geometric
$TbMnO_3$	27	0.08	MF-type-II
$MnWO_4$	12	0.005	MF type-II

Table 1.2: Comparison of two types of multiferroics.

Charge-ordering multiferroics

Another mechanism that can result in ferroelectric ordering and magnetic ordering can be found in charge-ordering multiferroics. It is often observed in compounds containing transition metal ions with different valences. Examples are $Pr_{0.5}Ca_{0.5}MnO_3$ [35]and $LuFe_2O_4$.[34] In charge ordering systems, the charge ordering of magnetic ions with different valence at different sites gives rise to inequivalent bonds and further ferroelectricity in the absence of ionic displacement.

Geometric ferroelectrics

In addition, multiferroic can be realized in some materials with lattice distortion, such as hexagonal manganite $YMnO_3$, in which the ferroelectric phase is induced by a tilting of the layered MnO_5 polyhedra, accompanied by displacements of the Y ions, which lead to a net electric dipole moment. It is evident that the mechanism is driven entirely by electrostatic and size effects, rather than the usual changes in chemical bonding associated with ferroelectric phase transitions in perovskite oxides.[36]

1.4.2.2 Multiferroics of spin origin (type-II)

From previous discussion about symmetry consideration, we know that both space inversion and time reversal must be broken in order to obtain magnetoelectric coupling. In general, this rule works also in type-II multiferroics because the complex spin configurations, such as cycloidal and conical magnetic structures(see table 1.3), allow the coupling between magnetism and ferroelectricity by symmetry argument. In type-II multiferroic materials, ferroelectric ordering is induced directly by magnetic long range ordering which breaks the space inversion symmetry and therefore the coupling between magnetism and electrical properties is intrinsically stronger than type-I MF. In other words, the tuning of ferroelectric (magnetic) order by the conjugate electric (magnetic) field in these MF should associate with a variation of magnetic (ferroelectric) property. However, the magnetically induced ferroelectric polarization is usually weak and several orders of magnitude smaller than in type-I MF, and this can be seen from table 1.2. Usually, the microscopic mechanisms of ferroelectricity of spin origin can be classified into three types. In order to describe properly these three mechanisms, a model of two transition metal ions with an ligand oxygen in between with generic electronic

Table 1.3: Representative MF of spin origins.

Mechanism	Compound	point group	Magnetic structure	T_N(K)
$\mathbf{P}^{SC}$	$TbMnO_3$	mmm	cycloidal	28
$\mathbf{P}^{SC}$	$Ni_3V_2O_8$	mmm	cycloidal	3.9~6.3
$\mathbf{P}^{p-d}$	$CuFeO_2$	-3m	collinear (H=0); screw(H>0)	11
$\mathbf{P}^{SC}$	$(BaMg)_2Fe_{12}O_{22}$	-3m	screw, L-conical (H=0), T-conical (H>0)	30
$\mathbf{P}^{SC}$	$CoCr_2O_4$	m3m	T-conical	26
$\mathbf{P}^{SC}$	$MnWO_4$	2/m	cycloidal	7~12.5
$\mathbf{P}^{ES}$	$TbMn_2O_5$	pbnm	collinear AFM	2.5

configurations has been studied, giving rise to the polarization P on the bond between the sites i and j by:[70, 71]

$$\mathbf{P} = \mathbf{P}^{ES}(\mathbf{s}_i \cdot \mathbf{s}_j)\mathbf{e} + \mathbf{P}^{SC}\mathbf{e}(\mathbf{s}_i \times \mathbf{s}_j) \times \mathbf{e} + \mathbf{P}^{p-d}\left[(\mathbf{e} \cdot \mathbf{s}_i)\mathbf{s}_i - (\mathbf{e} \cdot \mathbf{s}_j)\mathbf{s}_j\right] \tag{1.18}$$

where $\mathbf{s}_i$ means the spin direction at site i, and $\mathbf{e}$ is the unit vector connecting the two magnetic ions. Accordingly, we have three mechanisms: (a) exchange striction model ($\mathbf{P}^{ES}$), (b) spin current model ($\mathbf{P}^{SC}$), (c) spin-depedent p-d hybridization model ($\mathbf{P}^{p-d}$). These mechanisms are illustrated along with some corresponding examples in table 1.3.

Exchange striction model

The multiferroic property originating from the exchange striction mechanism requires special stacking of crystal lattice.[31] Usually, the exchange striction predicts the presence of polarization along the bond direction for the AB lattice, as shown in figure 1.12 (a-c). The symmetric exchange interaction between the neighboring spins may lead to striction along a specific crystallographic direction. To have net polarization, the propagation vector of spins should be commensurate with the crystal lattice and the resulting striction should show net displacement over the crystal lattice. For instance, considering the A-B aligned chain, as shown in figure 1.12 (b), it consists of up-up-down-down spin alignment, and the electric polarization can be induced and enhanced by the formation of dimerizations between neighboring atoms through the exchange striction. Another aligned configuration of atoms or bonds can be considered when the M-O-M bond is not straight chain but zigzag arrangement with up-up-down-down spin configuration. Examples are perovskite-type rare earth manganites $RMnO_3$ (R=Ho, Er, Tm, Yb and Lu)[38, 39]. Sometimes, multiferroicity due to exchange striction model can be realized in mixed-valence manganese oxide family, such as RMn_2O_5(R=Y, Tb, Ho, Er and Tm)[40, 41, 43, 42]. Magnetically induced ferroelectricity according to the exchange striction model is typically observed in a family of orthoferrites with distorted perovskite structure, $RFeO_3$(R=Gd, Tb and Dy).[46, 44, 45] In these materials, the exchange interaction between the R 4f and Fe 3d electrons plays a crucial role in the multiferroicity. The up-up-down-down spin configuration can be formed in the Ising spin chains in $Ca_3Co_{2-x}Mn_xO_6$, in which the polarization can be induced along the c-axis. [47] As presented in figure 1.12 (c), spin-driven

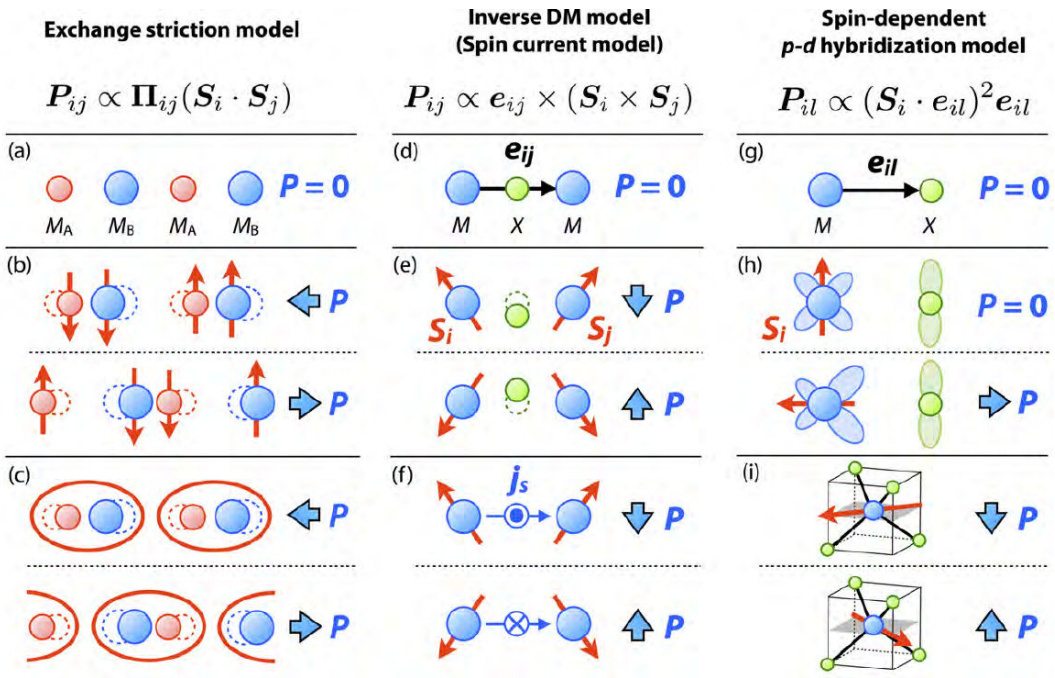

Figure 1.12: Three major mechanisms of ferroelectricity of spin origin: (a)–(c) exchange-striction mechanism arising from the symmetric spin exchange interaction; (d)–(f) spin-current model arising from the antisymmetric spin exchange interaction or inverse DM model; and (g)–(i) spin dependent p–d hybridization mechanism due to the relativistic SOC.[31]

ferroelectricity can be reached on this crystal lattice with spin-Peierls transition.

Spin current model

Spiral magnetic ordering, as shown in figure 1.13, is usually a consequence of magnetic frustration caused by electronic and crystal structures. The occurrence of ferroelectric polarization in this system can be understood in the spin-current model.[48, 49, 50] In the antisymmetric exchange interaction, the spin current is understood as flowing between the canted spin sites s_i and s_j(with e_{ij} being an unit vector connecting these two sites),[31] which forms effective electric field, and further induces the polarization P under the influence of spin-orbit coupling (see figure 1.12 (f)). In fact, the exchange striction plays an important role in determining the magnitude of polarization. This model is often called the inverse Dzyaloshinskii-Moriya (DM) interaction, in which the mediated ligand atom can displace so as to favor the DM interaction, as shown in figure 1.12 (e). The spin-current model has been very useful in recent exploration of new multiferroic materials, as transverse screw spin arrangements (figure 1.13), such as cycloidal and conical spin orders, can always induce spontaneous polarization in respective materials. For a cycloidal spin order the electrical polarization is perpendicular to the spiral propagation vector and lies in the spiral plane. Representative multiferroics belonging to spin current model are perovskite manganites $RMnO_3$ (R=Tb and Dy) which exhibit cycloidal spin order[37, 51]. Other materials showing coupled cycloidal spin order and ferroelectricity include $Ni_3V_2O_8$,[53] pyroxene $NaFeGe_2O_6$ [58, 59, 60, 61, 62, 63, 64]and $MnWO_4$[52]. They present

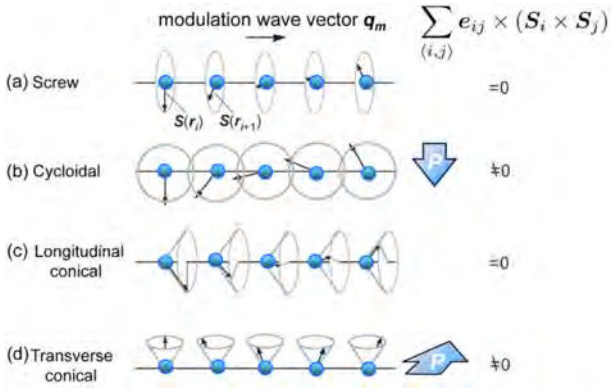

Figure 1.13: Schematic illustrations of types of spiral magnetic structure on a one-dimensional array of magnetic moments.[31]

magnetic frustration as the origin of helimagnetism. As a general characteristic for the materials with cycloidal spin order, the direction of electric polarization can be tuned by external magnetic field. Transverse conical spin order can be obtained when applying magnetic field normal to the spiral plane of cycloidal order. In this spin ordered system, ferromagnetic multiferroics can be realized, examples are $CoCr_2O_4$[57] and $Ba_2Mg_2Fe_{12}O_{22}$[56]. It is worth noting that the latter is an originally longitudinal conical magnet but transformed into a transverse state under a low magnetic field.

Spin dependent p-d hybridization

According to the equation 1.18, exchange striction and spin current models are not the only two mechanisms in explaining the multiferroic phenomenon. The last one employed to describe the mechanisms of multiferroics is spin-dependent p-d hybridization model.[31] This model considers a single pair of M and X sites, as shown in figure (g), in which the locally polar bond can be modulated by the spin-dependent hybridization between the magnetic ions d orbital and ligand p orbital, stemming from the spin-orbit coupling. Therefore, the resulting electric polarization is along the bond direction. Within some appropriate crystal structure such as the noncentrosymmetric $Ba_2CoGe_2O_7$,[55] this result can be demonstrated with macroscopic polarization measurements. This spin-dependent p-d hybridization model is also used to explain the electric polarization in triangular lattice antiferromagnets, such as $CuFeO_2$.[54]

1.4.3 Potential applications

The applications of multiferroics have been expected since the beginning of research. They could be used in sensors, switches, or memory devices. In fact, there are two main potential applications, depending on the strength of coupling between magnetism and ferroelectricity. Materials with weak coupling between the order parameters could be applied to fabricate the "advanced memory", in which both ferroelectric and ferromagnetic orientations could be used as data bits simultaneously, giving rise to dense, fast, and less energy expensive devices. Some effort has been made towards this application, such as the four-logic states cell in figure

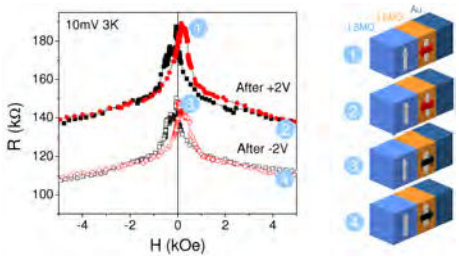

Figure 1.14: Variation of the resistance of an Au/LBMO(2 nm)/LSMO junction as a function of the magnetic field and the applied bias displaying four resistance states whose magnetic and electric configurations are represented on the right-hand side. [69]

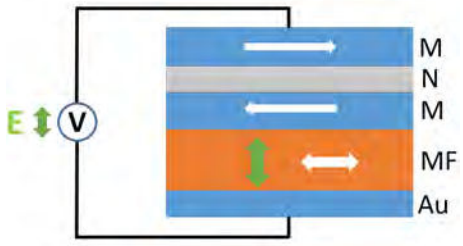

Figure 1.15: Model of storage media with electric field write and magnetic field read.

1.14. The most interesting potential applications come from the strong coupling between the magnetic ordering and electric ordering. One could then write or read bits with either electric or magnetic fields. Materials bearing this strong coupling can be used to improve the storage media. Especially, the technique of magnetically storing information by applying an electric field will improve the products in miniaturization and power consumption, see the E write and H read model in figure 1.15.

1.5 Pyroxenes

Complex oxides containing magnetic transition metal cations are a class of materials which exhibit strong correlation between the charge, spin, orbital and lattice degrees of freedom. From this viewpoint, there can arise diverse, interesting and useful phenomena such as multiferroicity, colossal magnetoresistance, and half-metallicity, among others. Within complex oxides, the intermediate ionic–covalent nature of transition-metal-oxygen bonds results in strong polarizability (a desirable property in ferroelectrics) and the largely localized transition-metal 3d electrons give rise to the strong correlation physics associated with exotic magnetic behaviors. In this context, pyroxenes containing transition metal are considered to be good candidates in studying the strong correlation due to the large variety of compounds and intriguing magnetic properties. In this section, we will begin with the description of crystal structures of pyroxene compounds, which is of significance in determining their physical properties, and then overview the recent progress in pyroxenes concerning their physical properties.

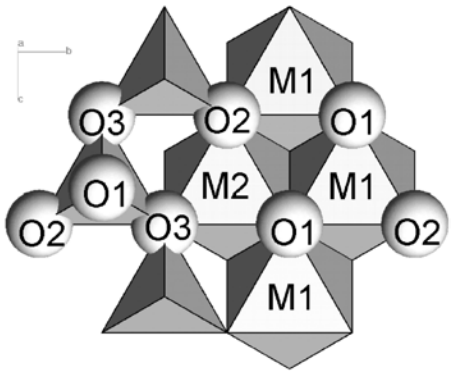

Figure 1.16: A portion of an ideal pyroxene structure viewed along the a axis. M2 and M1 cation sites are marked. Representative O atoms are illustrated as spheres and are labeled to indicate nomenclature[73].

1.5.1 What are pyroxenes: structural viewpoint

The term "pyroxene" refers to a group of minerals that have been studied extensively since the late 1960's from the perspective of crystal chemistry in geology and mineralogy.[72, 73, 75] Compounds of the pyroxene family form one of the most abundant mineral species in the earth crust and upper mantle, and are also important components of lunar, Martian rocks and meteorites, and have therefore been subject to a wealth of detailed studies investigating their structures and crystallo-chemistry depending on composition, forming conditions, etc... According to the previous reports, most documented pyroxenes are naturally occuring silicate. In the past several decades, many pyroxene compounds not found in nature, such as most germanate pyroxenes, have been synthesized and their crystal structures were usually determined by x-ray diffraction.[78, 79, 80, 81, 82, 83, 96]

We are going to recall some ideal pyroxene topology models because they are very helpful in understanding the structure of observed pyroxenes. Ideal pyroxenes are hypothetical structures based on ideal closest-packed stacking of O anions. Pyroxene compounds with chemical formulas $M2M1T_2O_6$ (M1=di- or trivalent transition metal, M2=mono- or divalent metal) are documented under three main forms : orthopyroxene, high clinopyroxene and low clinopyroxene, with space groups Pbca, C2/c and P21/c, respectively. In the perspective of ideal pyroxene topologies, typically, M2 and M1 represent octahedrally coordinated cations, and T represents tetrahedrally coordinated cations such as Si^{4+} and Ge^{4+}. Their structures are commonly built up by chains of edge-sharing M1 and M2 octahedra aligned along the c-axis, linked by chains of TO_x tetrahedra and considerable effort has been used to understand the relation between the pyroxene composition and their structural topology [73, 75, 76, 77]. These chains can be constructed by siting cations in the interstitial voids between closest-packed monolayers of anions (oxygen) arranged along the a axis. Then, the cation sites in a specific chain are associated to each other by a c-glide perpendicular to the b axis.

The conventional nomenclature for oxygen anions in investigated structures has to be introduced. The basal face of the tetrahedra is defined as the faces parallel to (100) according

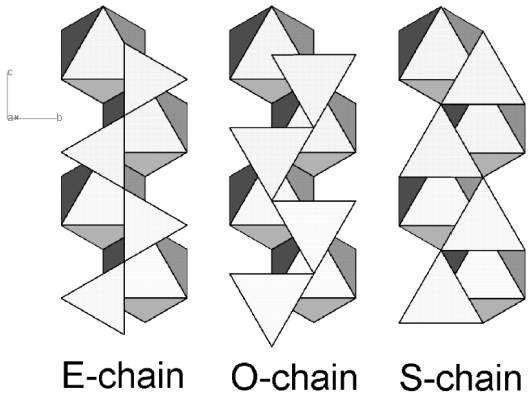

Figure 1.17: Portions of three different model pyroxene structures viewed along the a axis to illustrate chain configurations[73].

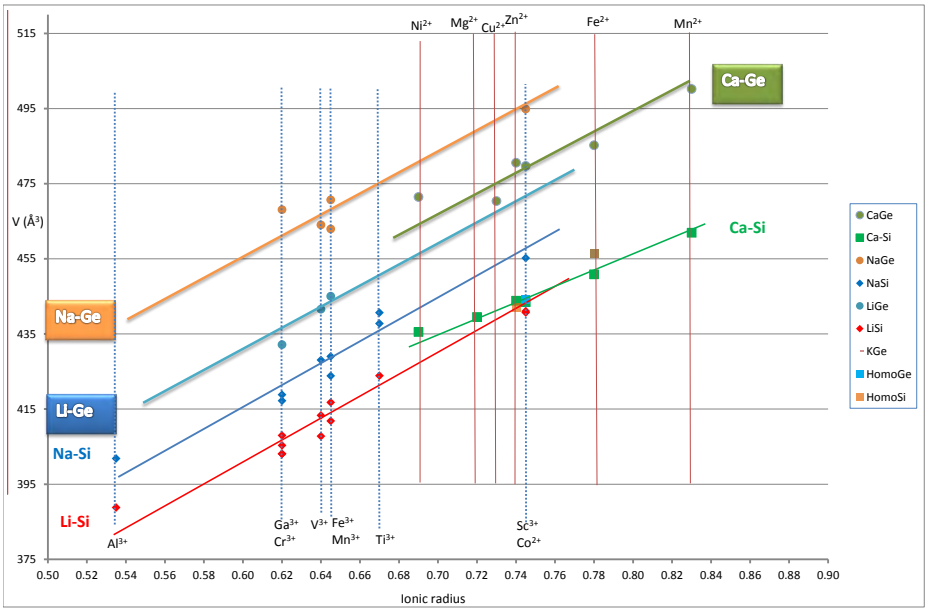

Figure 1.18: Summary of M2M1T_2O_6(T=Ge,Si) pyroxenes.

to the Ref. [73, 76, 77]. The two oxygens that are shared with other tetrahedra at the corners of the basal face are termed as the bridging O3 anion. The non-bridging basal oxygens are referred to as O2. The apical oxygen is O1, as shown in figure 1.16. The chain-forming symmetrically equivalent edge-sharing octahedral sites are called M1, and are related to each other by the c-glide running along the middle of the chain. M2 cations sites are embedded into the kinks of the M1 chains, which are also aligned to each other by the c-glide but without the formation of continuous chains. The electronic density analysis of observed structures of pyroxenes showed that M2 can have four, five, six or eight coordination. [74]

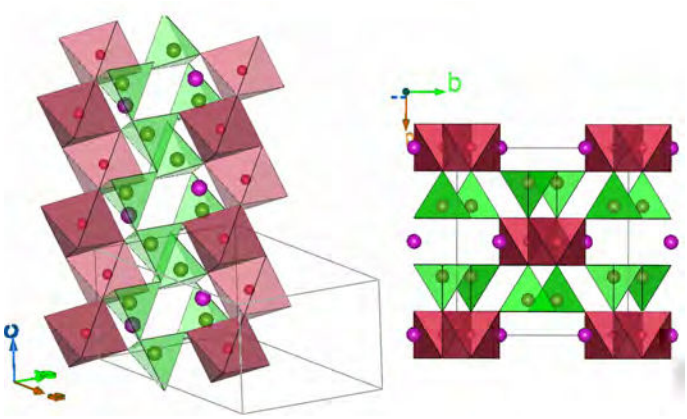

Figure 1.19: Typical crystal structure of clinopyroxene with C2/c symmetry.

Another concept from ideal topology of pyroxene is the so-called extended structures (E-chain), which is concerned with the tetrahedral chains. The model of E-chain made by Thompson is shown in figure 1.17. Two possible model relationships between the tetrahedral chain and the adjacent octahedral chain can be constructed: In S-rotation, referring to S-chain with O3-O3-O3 angle of 240°, tetrahedra in the chain rotates resulting in the hexagonal closest-packed oxygen atoms, while in O-rotation, referring to O-chain with O3-O3-O3 angle of 120°, tetrahedra in the chain rotate leading to the cubic closest-packed oxygen atoms. These are just ideal models in describing pyroxenes. Indeed, the natural and synthetic pyroxenes have O3-O3-O3 angles which lie between these ideal values.

Since we will be working with clinopyroxenes with C2/c (high) and $P2_1/c$ (low) symmetries, we will discuss some common structural features related to these two symmetries with respect to the ideal model of pyroxenes, and then give relevant examples. Generally speaking, the documented pyroxene compounds can be classified into six groups: Li-based silicate, Li-based germanate, Na-based silicate, Na-based germanate, Ca-based silicate, and Ca-based germanate, depending on the species of M2 cation (alkali-based or alkaline-based) and if it is silicate or germanate compounds. The volume of unit cell as a function of M1 ionic radius for each pyroxene is presented in figure 1.18. It is clear that the volume for each compound concordantly raises with the increased ionic radius. In the pyroxenes with space group C2/c (as seen in figure 1.19), the tetrahedral chains either all have O-rotation or all S-rotation but cannot hold both. This is because in this clinopyroxene the tetrahedral chains above and below the octahedral chains are symmetrically equivalent. Many pyroxenes crystallize with C2/c symmetry, for example, most Ca-based pyroxenes, and almost half of Li- and Na-based pyroxenes belong to this group. Compounds crystallizing in space group $P2_1/c$ have the analogous octahedral stacking style as in the C2/c pyroxenes, but they have significant differences in the arrangement of tetrahedra. Because of the absence of twofold symmetry axes in $P2_1/c$ structure, the two tetrahedral chains above and below a neighboring octahedra chains are symmetrically nonequivalent, which leads to the different rotation schemes. Pyroxenes with $P2_1/c$ structure therefore have both S-chains and O-chains, for example, as shown in figure1.20,

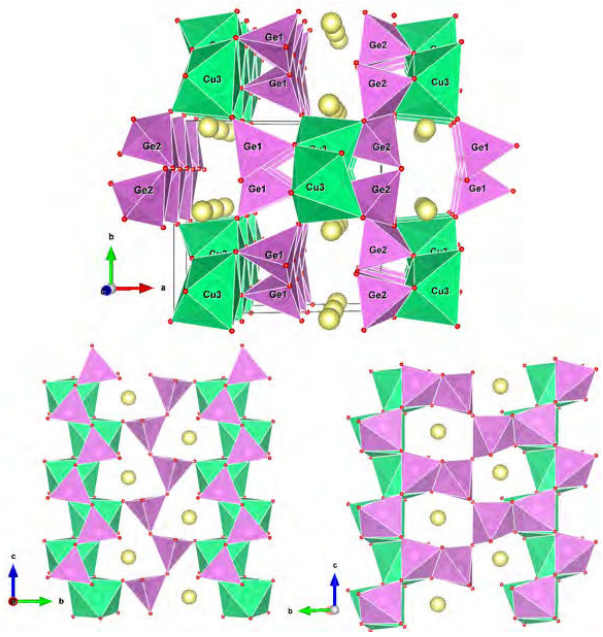

Figure 1.20: Crystal structure of clinopyroxene $CaCuGe_2O_6$ as an example of $P2_1/c$ symmetry.

$CaCuGeO_6$ accounts for this arrangement. Other compounds with this kind of symmetry are $LiCrSi/Ge_2O_6$, $LiVGe_2O_6$[97], $LiFeGe_2O_6$, and $NaCrSi_2O_6$, as summarized in table 1.4.

1.5.2 Nontrivial magnetic properties

In recent years, pyroxenes containing magnetic cations have attracted revitalized interest from a different viewpoint because some of them have been found to present intriguing quasi-one-dimensional (Q1D) magnetic behavior, multiferroic properties[58, 59, 88] and magnetoelectric effect. These physical properties mainly ascribe from their unique crystal structure. As we mentioned in previous subsection, their structures consist of isolated quasi-one-dimensional chains of edge-sharing $M1O_6$ octahedra, separated by the corner-sharing tetrahedra. As a result, the magnetic interchain interaction is considered to be much weaker than the intrachain interaction, giving rise to a typical one-dimensional magnet. Within the zigzag chains of $M1O_6$ octahedra, the edge-sharing octahedra provide a 90° M1-O1-M1 pathway for superexchange interactions, as shown in figure 1.21. More interestingly, the magnetic coupling in pyroxenes can be tuned by either the orbital occupancy on the M1 site or a chemical substitution on the M2 site. The continuous variation of the d-orbital occupancy by replacing different transition metal cations on the M1 site leads to the extremely rich magnetic properties, while the various chemical substitution on the M2 site involves the variation of crystal structure which in turn affects the magnetic properties in this strongly correlated system.[110]

The magnetic moments in pyroxenes arise from the transition metal M1 cation with a value that depends on the ionic state (for example, Ti^{3+} or Cu^{2+} corresponds to S=$\frac{1}{2}$, V^{3+}or Ni^{2+} to S=1, Cr^{3+} or Co^{2+} to S=$\frac{3}{2}$, Mn^{3+} or Fe^{2+} to S=2, Fe^{3+}or $Mn^{2+}$to S=$\frac{5}{2}$). Streltsov and Khomskii[89] have performed theoretical analysis and ab initio calculations on the elec-

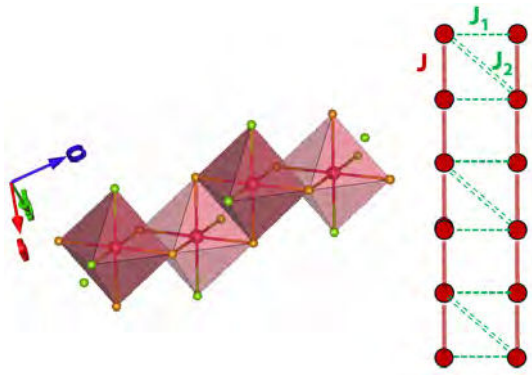

Figure 1.21: Left: A fragment of the crystal structure showing the geometry of the $M1O_6$ chain. Right: Triangularlike topology of the M1 network in pyroxenes.

tronic structures and magnetic properties for Li- and Na-based magnetic pyroxenes by only considering the intrachain interactions with 90° bonds. This work shows that two aspects are especially significant. First, there is a competition between different contributions to the superexchange due to the not exact 90° M1-O1-M1 bond in the chain. Second, two super-super-exchange interactions should be considered because every M1 cation is connected with two M1 ions in neighbouring chain via the O anions of TO_4 tetrahedra. Therefore, the general topology of competing exchange interactions is triangularlike, as shown in figure 1.21, which may lead to magnetic frustration and the appearance of various exotic magnetic properties such as orbit-ordering in $NaMnGe_2O_6$[84], spin singlet ground state[12, 100, 101], spin-Peierls transition[102, 103, 104, 105] and Haldane chains[11, 106, 107, 108, 109].

Both these characteristics make the magnetic properties of pyroxenes nontrivial. As shown in table 1.4, most magnetic pyroxenes show antiferromagnetic phase transition at low temperature, and some pyroxenes were found to be ferromagnetic insulators ($NaCrGe_2O_6$)[90], whereas some magnets exhibit a typical quasi-one-dimensional characteristic instead of showing a long range ordering such as $NaTiSi_2O_6$ and $CaCuGe_2O_6$ pyroxenes with spin S=$\frac{1}{2}$.

It is known that the quantum effects on spin fluctuation and spin-lattice coupling will be more evident in 1D chain system with S=$\frac{1}{2}$. Some quantum spin phenomena of interest such as spin-dimer, spin-Peierls and possible transition to a Haldane state have been studied in Q1D pyroxene magnets. We first see the Q1D magnetism in Li- or Na-based pyroxenes, then series of Ca-based will be followed.

As a spin-half system, $NaTiSi_2O_6$ has attracted a huge interest because of its spin-Peierls-like phase transition at 210K[102]. The magnetic susceptibility measurements, x-ray and neutron diffraction data [102, 103] show that $NaTiSi_2O_6$ undergoes a spin-Peierls transition at 210K, which is accompanied by the formation of alternation of the Ti-Ti distance within the chain of edge-sharing TiO_6 octahedra. Later on, the Raman scattering and theoretical calculations [104] demonstrated that this transition can be described as an orbital analogue of the spin-Peierls transition, in which the high temperature dynamical Jahn-Teller phase

Table 1.4: Summary of crystal structure and magnetic properties of (Li,Na, Ca)M1(Si,Ge)$_2$O$_6$. Data were taken from the references listed in bibliography.

Compound	Spin	SG (RT)	Eff. Mom. (μ_B)	Refined Mom. (μ_B)	Propag.Vector	MSG	Physical properties
$LiTiSi_2O_6$	1/2	C2/c	1.73	-	-	-	Spin-Peierls, Ts=230K
$NaTiSi_2O_6$	1/2	C2/c	1.73	-	-	-	Spin-Peierls, Ts=210K
$LiVSi_2O_6$	1	C2/c	2.83	-	-	-	AFM<22K
$NaVSi_2O_6$	1	C2/c	2.83	-	-	-	AFM<17K
$LiVGe_2O_6$	1	$P2_1/c$	2.83	1.14	-	-	AFM<24K
$NaVGe_2O_6$	1	C2/c	2.83	-	-	-	AFM<16K
$LiCrSi_2O_6$	3/2	$P2_1/c$	3.87	2.06	[0,0,0]	$P2'_1/c$	AFM<11K, ME
$NaCrSi_2O_6$	3/2	C2/c	3.87	2.31	[0,0,0]	C-1'	AFM<3K, ME
$LiCrGe_2O_6$	3/2	$P2_1/c$	3.87	2.33	[0,0,0]	$P2'_1/c$	AFM<3.7K, ME
$NaCrGe_2O_6$	3/2	C2/c	3.87	1.85	[0,0,0]	C2'/c'	FM<6K
$NaMnSi_2O_6$	2	C2/c	4.9	-	-	-	-
$NaMnGe_2O_6$	2	C2/c	4.9	1.92	[0,0,0.5]	-	AFM<7K, orbital ordering
$LiFeSi_2O_6$	5/2	$P2_1/c$	5.92	4.68	[0,0,0]	$P2_1/c'$	AFM<18K, ME
$NaFeSi_2O_6$	5/2	C2/c	5.92	3.3	[0.13,0.86,0.7]		AFM<8K, MF
$LiFeGe_2O_6$	5/2	$P2_1/c$	5.92	4.27	[0.5,0,0]	$P2'_1/c$	AFM<20K
$NaFeGe_2O_6$	5/2	C2/c	5.92	4.05	[0.32,1,0.08]	-	AFM<13K, MF<12K
$CaCuGe_2O_6$	1/2	$P2_1/c$	1.73	-	-	-	Spin-singlet<40K
$CaNiSi_2O_6$	1	C2/c	2.83	-	[1,0,0]	C2'/c'	22K
$CaNiGe_2O_6$	1	C2/c	2.83	1.95	[1,0,0]	C2'/c'	AFM<22K
$CaCoSi_2O_6$	3/2	C2/c	3.87	3.30	[1,0,0]	C2'/c'	10K
$CaCoGe_2O_6$	3/2	C2/c	3.87	3.28	[1,0,0]	C2'/c'	18K
$CaFeSi_2O_6$	2	C2/c	4.90	4.29	[1,0,0]	C2'/c'	AFM<34K
$CaFeGe_2O_6$	2	C2/c	4.90	4.46	[1,0,0]	C2'/c'	AFM<43K
$CaMnSi_2O_6$	5/2	C2/c	5.92	-	-	-	-
$CaMnGe_2O_6$	5/2	C2/c	5.92	4.33	[0,0,0]	C2'/c	12K

exhibits a spontaneous breaking of translational symmetry into a dimerized, JT distorted, orbital ordered state under the formation of spin valence bonds. Apart from this interpretation, a new argument was proposed based on the spin polarized generalized gradient approximation calculations[105], in which the transition was explained with a formation of one-dimensional S=1 chains, namely Haldane state. Thus, a qualitatively different description of magnetic properties can be reached, i.e. $NaTiSi_2O_6$ can be considered as a spin-dimer compound or as a net of Haldane chains depending on the strength of the on-site Hubbard repulsion. $LiTiSi_2O_6$ was found to undergo the spin-Peierls transition at 230K.[102] In contrast to these half-integer spin chain systems, V-bearing pyroxenes have been proposed as a promising 1D Haldane chain system with integer spin S=1.[11, 107, 106, 108] Their magnetic susceptibility curves all exhibit a Bonner-Fisher-like broad maximum at 230K, far above the long-range ordering temperature, which is characteristic of Q1D magnetism.[98] More interestingly, the magnetic ground state for Cr-bearing pyroxenes varies from the long-range AFM for $LiCr(Si, Ge)_2O_6$ to unusual FM ordered $NaCrGe_2O_6$ due to the competition between FM t_{2g}-e_g and AFM t_{2g}-t_{2g} superexchange interactions. [90, 91, 93] Moreover, spin-flip transition from ground state AFM to FM state was found in $NaCrSi_2O_6$. This spin-flip transition was also found in $NaMnGe_2O_6$, a high-pressure synthesized pyroxene with strong Jahn-Teller distortion, in which spin configuration with up-up-down-down along the c axis was determined via neutron diffraction measurement.[83, 84]

In fact, the renewed interest of pyroxenes primely arises from the recent discovery for which pyroxenes was shown to be a new class of multiferroics in 2007 by S. Jodlauk et al.[88]. They showed that the natural $NaFeSi_2O_6$ becomes ferroelectric order in a magnetically ordered state below 6K, while magnetically driven ferroelectricity emerges in $LiFeSi_2O_6$ and $LiCrSi_2O_6$ under an external magnetic fields at 18 K and 11 K, respectively. They proposed that the Q1D spin chain of transition metal cations should be responsible for magnetic competition between intrachain and interchain interactions, giving rise to possible spiral magnetic spin ordering. This tentative incommensurate magnetic structure may be the origin of multiferroics. They suggested finally that other pyroxenes may also be multiferroic. However, subsequent neutron diffraction and electric polarization measurements reveal[60, 80, 99] that only $NaFeSi_2O_6$ has a spiral spin structure and consequent ferroelectric order, while $LiFeSi_2O_6$ and $LiCrSi_2O_6$ are confirmed to be magnetoelectric materials.[94, 95] Since 2007, more magnetoelectric materials have been reported. For example, Nenert et al. found that magnetic symmetries for $LiCrGe_2O_6$[95] and $NaCrSi_2O_6$ [92]were determined as P2'$_1$/c and C-1', respectively, both of them allows for linear magnetoelectric effect. Multiferroic property was found in other Fe-bearing pyroxene $NaFeGe_2O_6$[59], in which a ferroelectric order was observed below 11.8K, supporting the helical spin configurations in $NaFeGe_2O_6$.[61, 62] Consequently, in this versatile Li- or Na-based pyroxene family, only $NaFeSi_2O_6$ and $NaFeGe_2O_6$ are definitely multiferroics.

Recent studies of pyroxenes usually focus on the physical properties of Li-and Na-based pyroxenes, therefore, less attention has been paid to Ca-based pyroxenes. Actually, the Ca-based copper containing pyroxenes are of foremost interest due to the spin-$\frac{1}{2}$ of Cu^{2+}cations which could lead to enhanced quantum effects. Sasago et al.[12] have investigated the magnetic

properties of $CaCuGe_2O_6$, the magnetic susceptibility shows the existence of a spin-singlet ground state and a finite energy gap between the ground state and excited states. Then Zheludev et al. [12]found that even though $CaCuGe_2O_6$ has one-dimensional arrangement of CuO_6 octahedra, inelastic neutron scattering results support the physical picture that the dimerized ground state composed of weak antiferromagnetic interactions between neighboring chains, rather than forming of Cu^{2+} pairs within the one-dimensional chain. Recently, the ab initio electronic structure analysis and quantum Monte-Carlo calculations by Valneti et al. [101]reveal that the spin-singlet behavior in $CaCuGe_2O_6$ is caused by third nearest-neighboring Cu^{2+}pairs. As a result, we see that both $NaTiSi_2O_6$ and $CaCuGe_2O_6$ have the ground state with spin gap, although the physical nature of such a state is totally different: the formation of interchain dimers in $CaCuGe_2O_6$ leads to spin-singlet state, whereas the spin-Peierls transition in $NaTiSi_2O_6$ is attributed to the intrachain dimerization. All of the reported Ca-based pyroxenes are summarized into table 1.4, it is obvious that most of them have same magnetic symmetry (C2'/c') except that the magnetic structure of $CaMnGe_2O_6$ is made of AFM chains coupled ferromagnetically[78, 85, 86, 87, 111].

1.5.3 Motivations and outline

So far, we have a very brief survey of the background knowledge for understanding crystalline materials and for interpreting the magnetic phenomena which will be encountered throughout this work. To build the relationship between structure and property, we have introduced the Neumann's principle and have deduced mathematically how to apply this rule to predict and reveal physical properties in materials, in particular, on magnetoelectric effect. The ideal pyroxene topology as well as the natural and synthetic pyroxenes have been demonstrated, particular highlights were given on Q1D and multiferroic properties. In the regards, the motivation of this thesis is as follows.

Pyroxenes have been shown to exhibit diverse physical properties, and can be seen as a nontrivial magnetic system. Even though the trivalent transition metal bearing pyroxenes have been extensively investigated experimentally, less attention has been paid to divalent bearing magnetic pyroxenes. The interesting magnetic properties in pyroxenes can be tuned by either the orbital occupation on the M1 site or a chemical substitution on the nonmagnetic M2 or T sites. We aim to study the influences of different orbital occupancies and replacement of Ge by Si on the magnetic properties in Ca-bearing pyroxenes. The exploration of new multiferroics is also one of the tasks of this thesis, therefore, synthesis and study of magnetoelectric properties of other new pyroxene family is of great interest.

Accordingly, studies of several different pyroxenes which display strong electron correlation will be presented in this thesis. Most of the work has been experimental, mainly including materials synthesis, microscopic characteristic detections, and bulk measurements. Thus, Chapter 2 covers all experimental methods used in this work. High pressure and high temperature method is considered to be an invaluable synthesis way in exploring new materials which cannot be prepared with ambient pressure and temperature. Neutron diffraction is a microscopic

probe and can be used to detect the atomic position of O atom, and more importantly, it can be employed to determine magnetic structure. We will give the comparison between neutron and x-ray diffraction techniques, and introduce the determination of magnetic structures in some detail. These respects fill up most of the space of Chapter 2. With respect to the motivations, synthesis of several new materials and interesting known materials were carried out, the synthetic strategy is described in Chapter 3. The characterizations and physical properties for some interesting materials are developed individually in following chapters (Chapter 4-8).

1. Although the $CaCuGe_2O_6$ compound has been studied extensively, the isostructural $CaCuSi_2O_6$ has not yet been reported. The results of our study of a new Cu-bearing clinopyroxene silicate are given in Chapter 4.

2. Most of the Ca-based pyroxenes show strong FM interactions within the M chains which dominates the AFM coupling between the chains whereas the magnetic structure of $CaMnGe_2O_6$ is made of AFM chains coupled ferromagnetically. It seems that Mn^{2+}-bearing pyroxene is quite particular. In addition, this commensurate magnetic structure allows for linear magnetoelectric effect. Chapter 5 shows our extensive studies of the magnetic and magneto-electric properties in $CaMnGe_2O_6$.

3. Refer to the table 1.4, there is to date no report of the investigation of the magnetic properties of $CaMnSi_2O_6$. As an isostructural compound to $CaMnGe_2O_6$, some interesting physical properties from the substitution of Ge by Si are expected. We are going to show the sample synthesis under high pressure and high temperature, magnetic and magneto-electric properties in this compound in Chapter 6.

4. A compound involving extremely different spin configurations would be expected to exhibit competing interactions which further give rise to interesting physical properties. We extensively studied the Co/Mn solid solution, in which a competition occurs between FM and AFM coupling within and between the chains. Chapter 7 provides the detailed study of the evolution of magnetic propertiesaccross this solid solution, and the magnetic phase diagram is finally drawn.

5. Chapter 8 is devoted to a new pyroxene family $SrMGe_2O_6$ where M=Co, Mn. We investigated the crystal structure, magnetic structures and magneto-electric properties of this new family. Comparing their structures to those of their Ca-based analogues allows us to gain further insight into the structure-property relationships in pyroxenes by observing the effects of substitution on the M2 site.

Bibliography

[1] Martin T. Dove, Structure and dynamics: an atomic view of materials. Oxford University Press, 2003. 9

[2] Steven H. Simon, The Oxford solid state basics, Oxford University Press, 2013, P135. 9

[3] S. R. Elliott, The physics and chemistry of solids, Wiley, 1998. 10

[4] Stephen Blundell, Magnetism in condensed matter, Oxford University Press, 2001. 15, 18, 21

[5] I.Dzyaloshinsky, A thermodynamic theory of weak ferromagnetism of antiferromagnetics, J.Phys.Chem. Solids, 4, 1958, 241. 16

[6] T.Moriya, Anisotropic superexchange interaction and weak ferromagnetism, Phys. Rev. 120, 1960, 91. 16

[7] J. M. D. Coey, Magnetism and magnetic materials, Cambridge University Press, 2009. 17, 19

[8] A.Wills, Magnetic structures and their determination using group theory, J. Phys. IV France 11, 2001, Pr9-133-Pr9-158. 12

[9] Nicola A. Spaldin, Magnetic mateirals: fundamental and applications, Cambridge University Press, second edition, 2011. 14

[10] Y. Yamaguchi, T. Nakano, Y. Nozue, and T. Kimura, Magnetoelectric effect in an XY-like spin glass system $Ni_xMn_{1-x}TiO_3$, Phys. Rev. Lett., 108, 2012, 057203. 22

[11] J. Lou, T. Xiang, Z. Su, Thermodynamics of the bilinear-biquadratic spin-one Heisenberg chain, Phys. Rev. Lett., 85, 2000, 2380. 22, 42, 44

[12] A. Zheludev, G. Shirane, Y. Sasago, M. Hase, K. Uchinokura, Dimerized ground state and magnetic excitations in $CaCuGe_2O_6$, Phys. Rev. B, 53, 1996, 11642. 42, 44, 45

[13] Robert E. Newnham, Properties of materials: anisotropy, symmetry, structure, Oxford University Press, 2005. 24

[14] L. D. Landau and E.M. Lifshitz, Electrodynamics of continous media, Addison-Wesley Publishing Company, 1960, P119. 27

[15] D.N. Astrov, Magnetoelectric effect in chromium oxide, Soviet Phys. -JETP, 13, 1961, 729. 27

[16] I. E. Dzyaloshinskii, On the magneto-electrical effect in antiferromagnets, Soviet Phys.-JETP, 10, 1961, 628. 27

[17] Xi Chen, Andreas Hochstrat, Pavel Borisov, and Wolfgang Kleemann, Magnetoelectric exchange bias systems in spintronics, Appl. Phys. Lett., 89, 2006, 202508. 28

[18] Hans Schmid, Some symmetry aspects of ferroics and single phase multiferroics, J.Phys. : Condens. Matter, 20, 2008, 434201. 29

[19] Hans Schmid, Multiferroic magnetoelectrics, Ferroelectrics, 162, 1994, 317. 29

[20] V.M. Dubovik, V.V. Tugushev, Toroid moments in electrodynamics and solid-state physics, Physics Reports, 187, 1990, 145. 30, 31

[21] Gorbatsevich A. A., Kopaev, Y.V., Toroidal order in crystals, Ferroelectrics, 161, 1994, 321. 30

[22] Anne S. Zimmermann, Dennis Meier, Manfred Fiebig, Ferroic nature of magnetic toroidal order, Nat. Commun., 5:4796, 2014, 1-6. 30, 31

[23] Ascher E., Some properties of spontaneous currents, Helv. Phys. Acta 39, 1966, 40–48. 30

[24] Claude Ederer, Nicola A. Spaldin, Towards a microscopic theory of toroidal moments in bulk periodic crystals Claude, Phys. Rev. B, 76, 2007, 214404. 30

[25] E. Ressouche, M. Loire, V. Simonet, R. Ballou, A. Stunault, A. Wildes, Magnetoelectric $MnPS_3$ as a candidate for ferrotoroidicity, Phys. Rev. B, 82, 2010, 100408(R). 31

[26] Bruno Mettout, Pierre Tolédano, Manfred Fiebig, Symmetry replication and toroidic effects in the multiferroic pyroxene $NaFeSi_2O_6$, Phys. Rev. B, 81, 2010, 214417. 31

[27] M. Baum, K. Schmalzl, P. Steffens, A. Hiess, L. P. Regnault, M. Meven, P. Becker, L. Bohaty, M. Braden, Controlling toroidal moments by crossed electric and magnetic fields, Phys. Rev. B, 88, 2013, 024414. 31

[28] Spaldin N. A., Fiebig N., Mostovoy M., The toroidal momnet in condensed matter physics and its relation to the magnetoelectric effect, J. Phys.: Condens. Matter, 20, 2008, 434203. 30, 31

[29] Wadhawan V.K., Introduction to Ferroic Materials (Gordon and Breach, 2000). 31

[30] Nicola A. Spaldin, Sangwook Cheong, Ramamoorthy Ramesh, Mutiferroics: past, present, and future, Physics Today, 10 ,2010, 38 30

[31] Y. Tokura, S. Seki, N. Nagaosa, Multiferroics of spin origin, Rep. Prog. Phys., 77, 2014, 076501. 34, 35, 36

[32] J. Wang, J.B. Neaton, H. Zheng, V. Nagarajan, et. al., Epitaxial $BiFeO_3$ multiferroic thin film heterostructures, Science, 299, 2003, 1719. 32

[33] Ram Seshadri, Nicola A. Hill, Visualizing the Role of Bi 6s "Lone Pairs" in the Off-Center Distortion in Ferromagnetic $BiMnO_3$, Chem. Mater., 13, 2001, 2892. 32

[34] Naoshi Ikeda, Hiroyuki Ohsumi, Kenji Ohwada, Kenji Ishii, Toshiya Inami, Kazuhisa Kakurai, et. al. Ferroelectricity from iron valence ordering in the charge-frustrated system $LuFe_2O_4$, 436, 2005, 1136. 33

[35] Dmitry V. Efremov, Jeroen van den Brink, Daniel I. Khomskii, Bond- versus site-centred ordering and possible ferroelectricity in manganites, Nature Materials, 3, 2004, 853. 33

[36] Bas B. Van Aken, Thomas T.M. Palstra, Alessio Filippetti, Nicola A. Spaldin, The origin of ferroelectricity in magnetoelectric $YMnO_3$, Nature Materials, 3, 2004, 164. 33

[37] T. Kimura1, T. Goto, H. Shintani, K. Ishizaka, T. Arima, Y. Tokura, Magnetic control of ferroelectric polarization, Nature, 426, 2003, 55. 35

[38] Shintaro Ishiwata, Yoshio Kaneko, Yusuke Tokunaga, Yasujiro Taguchi, Taka-hisa Arima, and Yoshinori Tokura, Perovskite manganites hosting versatile multiferroic phases with symmetric and antisymmetric exchange strictions, Phys. Rev. B 81, 2010, 100411(R). 34

[39] V Yu Pomjakushin, M Kenzelmann, A Dönni, A B Harris, T Nakajima, S Mitsuda, M Tachibana, L Keller, J Mesot, H Kitazawa, E Takayama-Muromach, Evidence for large electric polarization from collinear magnetism in $TmMnO_3$, New J. Phys., 11, 2009, 043019. 34

[40] Hur N, Park S, Sharma P, Ahn J, Guha S and Cheong S, Electric polarization reversal and memory in a multiferroic material induced by magnetic fields, Nature, 429, 2004, 392. 34

[41] Noda Y, Kimura H, FukunagaM, Kobayashi S, Kagomiya I and Kohn K, Magnetic and ferroelectric properties of multiferroic RMn_2O_5, J. Phys. :Condens. Matter, 20, 2008, 434206. 34

[42] Satoru Kobayashi, Toshihiro Osawa, Hiroyuki Kimura, Yukio Noda, Isao Kagomiya, Kay Kohn, Reinvestigation of Simultaneous Magnetic and Ferroelectric Phase Transitions in YMn_2O_5, J. Phys. Soc. Jpn., 73, 2004, 1593. 34

[43] M. Fukunaga, Y. Sakamoto, H. Kimura, Y. Noda, N. Abe, K. Taniguchi, T. Arima, S. Wakimoto, M. Takeda, K. Kakurai, and K. Kohn, Magnetic-Field-Induced Polarization Flop in Multiferroic $TmMn_2O_5$, Phys. Rev. Lett., 103, 2009, 077204. 34

[44] Tokunaga Y, Furukawa N, Sakai H, Taguchi Y, ArimaThand Tokura Y, Composite domain walls in a multiferroic perovskite ferrite, Nature Mater. , 8, 2009, 558. 34

[45] Tokunaga Y, Taguchi Y, Arima T h and Tokura Y, Electric-field-induced generation and reversal of ferromagnetic moment in ferrites, Nature Phys., 8, 2012, 838. 34

[46] Tokunaga Y, Iguchi S, Arima T and Tokura Y, Magnetic-Field-Induced Ferroelectric State in $DyFeO_3$, Phys. Rev. Lett., 101, 2008, 097205. 34

[47] Choi Y, Yi H, Lee S, Huang Q, Kiryukhin V and Cheong SW, Ferroelectricity in an Ising Chain Magnet, Phys. Rev. Lett. 100, 2008, 047601. 34

[48] Hosho Katsura, Naoto Nagaosa, and Alexander V. Balatsky, Spin Current and Magnetoelectric Effect in Noncollinear Magnets, Phys. Rev. Lett. 95, 2005, 057205. 35

[49] Maxim Mostovoy, Ferroelectricity in Spiral Magnets, Phys. Rev. Lett. 96, 2006, 067601. 35

[50] I. A. Sergienko and E. Dagotto, Role of the Dzyaloshinskii-Moriya interaction in multiferroic perovskites, Phys. Rev. B 73, 2006, 094434. 35

[51] T. Goto, T. Kimura, G. Lawes, A. P. Ramirez, and Y. Tokura, Ferroelectricity and Giant Magnetocapacitance in Perovskite Rare-Earth Manganites, Phys. Rev. Lett. 92, 2004, 257201. 35

[52] K. Taniguchi, N. Abe, T. Takenobu, Y. Iwasa, and T. Arima, Ferroelectric Polarization Flop in a Frustrated Magnet $MnWO_4$ Induced by a Magnetic Field, Phys. Rev. Lett. 97, 2006, 097203 35

[53] G. Lawes, A. B. Harris, T. Kimura, N. Rogado, R. J. Cava, A. Aharony, O. Entin-Wohlman, T. Yildirim, M. Kenzelmann, C. Broholm, and A. P. Ramirez, Magnetically Driven Ferroelectric Order in $Ni_3V_2O_8$, Phys. Rev. Lett. 95, 2005, 087205. 35

[54] T. Kimura, J. C. Lashley, and A. P. Ramirez, Inversion-symmetry breaking in the noncollinear magnetic phase of the triangular-lattice antiferromagnet $CuFeO_2$, Phys. Rev. B 73, 2006, 220401(R) . 36

[55] H. Murakawa, Y. Onose, S. Miyahara, N. Furukawa, and Y. Tokura, Ferroelectricity Induced by Spin-Dependent Metal-Ligand Hybridization in $Ba_2CoGe_2O_7$, Phys. Rev. Lett. 105, 2010, 137202. 36

[56] Ishiwata S, Taguchi Y, Murakawa H, Onose Y and Tokura Y, Low-Magnetic-Field Control of Electric Polarization Vector in a Helimagnet, Science, 319, 2008, 1643. 36

[57] Y. Yamasaki, S. Miyasaka, Y. Kaneko, J.-P. He, T. Arima, and Y. Tokura, Magnetic Reversal of the Ferroelectric Polarization in a Multiferroic Spinel Oxide, Phys. Rev. Lett. 96, 2006, 207204. 36

[58] M. Ackermann, L. Andersen, T. Lorenz, L. Bohatý, P. Becker, Anisotropy study of multiferroicity in the pyroxene $NaFeGe_2O_6$, New J. Phys., 17, 2015, 013045. 35, 41

[59] Ingyu Kim, Byung-Gu Jeon, Deepak Patil, Seema Patil, Gwilherm Nénert, Kee Hoon Kim, Observation of multiferroic properties in pyroxene $NaFeGe_2O_6$, J. Phys.: Condens. Matter, 24, 2012, 306001. 35, 41, 44

[60] Günther J. Redhammer, Anatoliy Senyshyn, Martin Meven, Georg Roth, Sebastian Prinz, Astrid Pachler, et al., Nuclear and incommensurate magnetic structure of $NaFeGe_2O_6$ between 5 K and 298 K and new data on multiferroic $NaFeSi_2O_6$, Phys. Chem. Minerals, 38, 2011, 139-157. 35, 44

[61] T. V. Drokina, G. A. Petrakovskii, L. Keller, J. Schefer, A. D. Balaev, A. V. Kartashev, D. A. Ivanov, Modulated magnetic structure in quasi-one-dimensional clinopyroxene $NaFeGe_2O_6$, JETP, 112, 2011, 121. 35, 44

[62] T. V. Drokina, O. A. Bayukov, G. A. Petrakovskiĭ, D. A. Velikanov, A. F. Bovina, G. N. Stepanov, D. A. Ivanov, Synthesis and properties of $NaFeGe_2O_6$ polycrystals, Phys. Solid State, 50, 2008, 2141. 35, 44

[63] T. V. Drokina, O. A. Bajukov, G. A. Petrakovskiy, D. A. Velikanov, Magnetic properties of a quasi-one-dimensional $NaFeGe_2O_6$ polycrystal, Bull. Russ. Acad. Sci. Phys., 73, 2009, 1054. 35

[64] Drokina T V, Petrakovskii G A, Keller L and Schefer J, Investigation of the magnetic structure in $NaFeGe_2O_6$ using neutron powder diffraction, J.Phys.: Conf. Ser., 251, 2010, 012016. 35

[65] Daniel Khomskii, Classifying multiferroics: Mechanisms and effects, Physics, 2, 2009, 20. 30, 31

[66] W.Eerenstein, N. D. Mathur, J.F. Scott, Multiferroic and magnetoelectric materials, Nature, 442, 2006, 759. 29

[67] Sang-wook Cheong, Maxim Mostovoy, Multiferroics: a magnetic twist for ferroelectricity, Nature Materials, 6, 2007, 13. 29

[68] Bas B.Van Aken, Jean-Pierre Rivera, Hans Schmid, Manfred Fiebig, Observation of ferrotoroidic domains, Nature, 449, 2007, 702. 30, 31

[69] H. Bea, M. Gajek, M. Bibes, A. Barthelemy, Spintronics with multiferroics, J. Phys. :Condens. Matter, 20, 2008, 434221. 32, 37

[70] Jia C, Onoda S, Nagaosa N, Han J. H., Bond electronic polarization induced by spin, Phys. Rev. B, 74, 2006, 224444. 34

[71] Jia C, Onoda S, Nagaosa N., Han J. H. , Microscopic theory of spin-polarization coupling in multiferroic transition metal oxides, Phys. Rev. B, 76, 2007, 144424. 34

[72] W.A. Deer, R.A. Howie, J. Zussman, Rock-forming Minerals, Volume 2A, Second Edition, Single Chain Silicates, Wiley, New York, 1978. 38

[73] R.M. Thompson, R.T.Downs, Model pyroxenes I: Ideal pyroxene topologies, American Mineralogist, 88, 2003, 653. 38, 39

[74] R.T. Downs, Topology of the pyroxenes as a function of temperature, pressure, and composition determined from the procrystal electron density, American Mineralogist, 88, 2003, 556. 39

[75] R.M. Thompson, R.T.Downs, Model pyroxenes I: Structural variation as a function of tetrahedral rotation, 89, 2004, 614. 38

[76] J.J.Papike, C.T. Prewitt, S.Sueno, M.Cameron, Pyroxenes: comparisons of real and ideal structural topologies, Z. Kristallogr., 138, 1973, 254. 38, 39

[77] M. Cameron, Structural and chemical variations in pyroxenes, American Mineralogist, 66, 1981, 1. 38, 39

[78] S. Ghose, C. Wan, F. P. Okamura, Crystal structures of $CaNiSi_2O_6$ and $CaCoSi_2O_6$ and some crystal-chemical relation in C2/c clinopyroxenes, American Mineralogist, 72, 1987, 375. 38, 45

[79] H. Ohashi, T. Osawa, K. Tsukimura, Refinement of the structure of manganese sodium dimetasilicate, Acta Cryst., C43, 1987, 605. 38

[80] G.J. Redhammer, G. Roth, W. Paulus, G. Andre, W. Lottermoser, G.Amthauer, W. Treutmann, B. Koppelhuber-Bitschnau, The crystal and magnetic structure of Li-aegirine $LiFeSi_2O_6$: a temperature-dependent study, Phys. Chem. Minerals, 28, 2001, 337. 38, 44

[81] G. J. Redhammer, H. Ohashi, G. Roth, Single-crystal structure refinement of $NaTiSi_2O_6$ clinopyroxene at low temperatures($298<T<100K$), Acta Cryst., B59, 2003, 730. 38

[82] G.J. Redhammer, G. Roth, Structural changes upon the temperature dependent C2/c-P21/c phase trransition in $LiMe^{3+}Si_2O_6$ clinopyroxenes, Me=Cr, Ga, Fe, V, Sc and In, Z. Kristallogr., 219, 2004, 585. 38

[83] G.J. Redhammer, G. Tippelt, Pyroxene-type compounds $NaM^{3+}Ge_2O_6$, with M=Ga, Mn, Sc and In, Acta Cryst., C70, 2014, 852. 38, 44

[84] Jinguang Cheng, Wei Tian, Jianshi Zhou, Vincent M. Lynch, Hugo Steinfink, Arumugam Manthiram, Andrew F. May, et al., Crystal and Magnetic Structures and Physical Properties of a New Pyroxene $NaMnGe_2O_6$ Synthesized under High Pressure, J. Am. Chem. Soc.,135, 2013, 2776. 13, 42, 44

[85] G.J. Redhammer, G. Roth, W. Treutmann, W. Paulis, et al., Magnetic ordering and spin structure in Ca-bearing clinopyroxenes $CaM^{2+}(Si,Ge)_2O_6$, M=Fe, Ni, Co, Mn, J. Solid State Chem., 181, 2008, 3163. 45

[86] G.J. Redhammer, G. Roth, A. Senyshyn, G. Tippelt, C. Pietzonka, Crystal and magnetic spin structure of Germanium-Hedenbergite, $CaFeGe_2O_6$, and a comparison with other magnetic/magnetoelectric/multiferroic pyroxenes, Z.Kristallogr., 228, 2013, 140. 45

[87] G. Durand, S. Vilminot, P. Rabu, A. Derory, J.P. Lamboour, E. Ressouche, Synthesis, structure and magnetic properties of $CaMSi_2O_6$(M=Co, Ni) compounds and their solid solutions, J. Solid State Chem., 124, 1996, 374. 45

[88] S. Jodlauk, P. Becker, J. AMydosh, D. I. Khomskii, T. Lorenz, S.V. Streltsov, D. C. Hezel, L. Bohaty, Pyroxenes: a new class ofmultiferroics, J. Phys.: Condens. Matter, 19, 2007, 432201. 41, 44

[89] S. V. Streltsov and D. I. Khomskii, Electronic structure and magnetic properties of pyroxenes $(Li,Na)TM(Si,Ge)_2O_6$: Low-dimensional magnets with 90° bonds, Phys. Rev. B 77, 2008, 064405 41

[90] A. N. Vasiliev, O. L. Ignatchik, A. N. Sokolov, Z. Hiroi, M. Isobe, and Y. Ueda, Long-range magnetic order in quasi-one-dimensional chromium-based (S=32) pyroxenes $(Li,Na)Cr(Si,Ge)_2O_6$, Phys. Rev. B 72, 2005, 012412. 42, 44

[91] Redhammer, G. J.; Roth, G.; Amthauer. G. (2008) Chromium- based clinoyproxene-type germanates $NaCrGe_2O_6$ and $LiCrGe_2O_6$ at 298 K, Acta Cryst., C64, 2008, i97. 44

[92] Nenert, G.; Kim, I.; Isobe, M.; Ritter, C.; Vasiliev, A. N.; Kim, K. H.; Ueda, Y., Magnetic and magnetoelectric study of the pyroxene $NaCrSi_2O_6$, Phys. Rev. B 81, 2010, 184408. 44

[93] Nenert, G.; Ritter, C.; Isobe, M.; Isnard, O.; Vasiliev, A. N.; Ueda, Y., Magnetic and crystal structures of the one- dimensional ferromagnetic chain pyroxene $NaCrGe_2O_6$, Phys. Rev. B, 80, 2009, 024402. 44

[94] G. Nenert, M. Isobe, C. Ritter, O. Isnard, A. N.Vasiliev, Y.Ueda, Magnetic and crystal structure of the magnetoelectric pyroxene $LiCrSi_2O_6$, Phys. Rev. B, 79, 2009, 064416. 44

[95] G. Nenert, M. Isobe, I. Kim, C. Ritter, C. V.Colin, A. N.Vasiliev, K. H.Kim, Y.Ueda, Interplay between low dimension- ality and magnetic frustration in the magnetoelectric pyroxenes $LiCrX_2O_6$ (X=Ge, Si), Phys. Rev. B, 82, 2010, 024429. 44

[96] Ohashi, H.; Osawa, T.; Sato, A. $NaVSi_2O_6$. Acta Cryst. C50 (1994) 1652–1655. 38

[97] Emirdag, M.; Kolis, J. W.: Hydrothermal synthesis, characterization and magnetic properties of $NaVGe_2O_6$ and $LiVGe_2O_6$. Mat. Res. Bull. 39 (2004) 1557–1567. 41

[98] A. N. Vasiliev, O. L. Ignatchik, M. Isobe, and Y. Ueda, Long range Néel order in the quasi-one-dimensional vanadium-based (S=1) pyroxenes (Li,Na)V(Si,Ge)$_2$O$_6$, Phys. Rev. B 70, 2004, 132415. 44

[99] G. J. Redhammer, G. Roth, W. Treutmann, M. Hoelzel, W. Paulus, G. André, C. Pietzonka, G. Amthauer, The magnetic structure of clinopyroxene-type LiFeGe$_2$O$_6$ and revised data on multiferroic LiFeSi$_2$O$_6$, J. Solid State Chem., 182, 2009, 2374. 44

[100] Y. Sasago, M. Hase, K. Uchinokura, M. Tokunaga, N. Miura, Discovery of a spin-singlet ground state with an energy gap in CaCuGe$_2$O$_6$, Phys. Rev. B, 52, 1995, 3533. 42

[101] Roser Valentí, T. Saha-Dasgupta, and Claudius Gros, Nature of the spin-singlet ground state in CaCuGe$_2$O$_6$, Phys. Rev. B 66, 2002, 054426. 42, 45

[102] M. Isobe, E. Ninomiya, A.N. Vasilev, Y. Ueda, Novel Phase Transition in Spin-1/2 Linear Chain Systems: NaTiSi$_2$O$_6$ and LiTiSi$_2$O$_6$, J. Phys. Soc. Jpn., 71, 2002, 1423. 42, 44

[103] E. Ninomiya, M. Isobe, Y. Ueda, M. Nishi, K. Ohoyama, et al., Observation of lattice dimerization in spin-singlet low temperature phase of NaTiSi$_2$O$_6$, Physica B, 329, 2003, 884. 42

[104] M. J. Konstantinović, J. van den Brink, Z. V. Popović, V. V. Moshchalkov, M. Isobe, and Y. Ueda, Orbital dimerization in NaTiSi$_2$O$_6$: An orbital analogue of the spin-Peierls phase transition, Phys. Rev. B 69, 2004, 020409(R). 13, 42

[105] Zoran S. Popović, Željko V. Šljivančanin, and Filip R. Vukajlović, Sodium Pyroxene NaTiSi$_2$O$_6$: Possible Haldane Spin-1 Chain System, Phys. Rev. Lett. 93, 2004, 036401. 42, 44

[106] J.L. Gavilano, S.Mushkolaj, H.R. Ott, P. Millet, F. Mila, LiVGe$_2$O$_6$, an Anomalous Quasi-1D, S=1 System, as Revealed by NMR, Physs. Rev. Lett., 85, 2000, 409. 42, 44

[107] P. Millet, F. Mila, F.C. Zhang, M. M.ambrini, et al., Biquadratic Interactions and Spin-Peierls Transition in the Spin-1 Chain LiVGe$_2$O$_6$, Phys. Rev. Lett., 83, 1999, 4176. 42, 44

[108] B. Pedrini, S. Wessel, J. L. Gavilano, H. R. Ott, S. M. Kazakov, J. Karpinski, Quenching of the Haldane gap in LiVSi$_2$O$_6$ and related compounds, Eur. Phys.J.B, 55, 2007, 219. 42, 44

[109] M. D. Lumsden, G. E. Granroth, D. Mandrus, S. E. Nagler, J. R. Thompson, J. P. Castellan, and B. D. Gaulin, Long-range antiferromagnetic order in the S=1 chain compound LiVGe$_2$O$_6$, Phys. Rev. B, 62, 2000, R9244. 42

[110] S. V. Streltsov, J. McLeod, A. Moewes, G. J. Redhammer, and E. Z. Kurmaev, Electronic properties of pyroxenes NaCrSi$_2$O$_6$ and NaFeSi$_2$O$_6$, Phys. Rev. B 81, 2010, 045118. 41

[111] F. Nestola, T. B. Ballaran, R.J. Angel, J. Zhao, H. Ohashi, High pressure behavior of Ca/Na clinopyroxenes: The effect of divalent and trivalent 3d-transition elements, Am. Mineral., 95, 2010, 832.

45

Chapter 2

Experimental methods

This chapter gives a brief introduction of the experimental methods used in this dissertation to synthesize and characterize samples. First we will present the basic description of the synthesis methods, more attentions will be paid to the high-pressure and high-temperature method, which is more complex and may be very effective in synthesizing specific compounds. Then, the most common technique in exploring the microscopic structural characteristics of materials, namely diffraction, will be presented in some depth. The last three sections provide a brief survey on the measurement techniques which we used to characterize various physical properties, including magnetic properties, thermal and electric properties.

2.1 Synthesis methods

In this section, we discuss preparative routes and underlying mechanisms for oxide materials in three basic types of reaction used in this thesis. The first one is the conventional solid state reaction, in which the solid-solid interface is the key factor considered. An elevated pressure as well as high temperature, in principle, will accelerate the reaction rate, and more importantly, stabilize the phase with smaller cell volume, and realize some oxidation states or electronic states that are not achievable at ambient condition. As a very efficient and rapid reaction, sol-gel processing, involving the solid-liquid interface, will be described in this section. Furthermore, some key points of the growth of single crystals, including flux method and floating zone method, will also be addressed.

2.1.1 Solid state reaction[1]

We begin with the survey of solid-solid interface. When simply considering the interface formed by two crystalline materials, the general feature of the solid-solid interface is that both phases are tightly packed. The diffusion from one phase to another seems to be impossible without any energy cost. However, analogous to the chemical reaction rate, the diffusion coefficient is temperature dependent due to the related energy barrier. This means that higher temperatures will result in higher diffusion coefficients, and in turn raise the reaction rate in solid state reaction. Another factor which affects the reaction is the particle size of the

chemical reagents. Smaller size of particle as well as long annealing time both improve the completion of reaction.

The starting materials should be identified by x-ray diffraction to ensure their purity. Then, the stoichiometric mixture of starting materials are ground in an agate mortar. The mixed powder is often pressed into a pellet in order to get the particles in close contact and eliminate the air. The solid state reaction is realized by heating the pellet in an open crucible at temperature around 1000°C for several days or weeks. It should be pointed that intermediate regrindings and reheatings may often be necessary in order to obtain the desired compound as a single phase. In the next chapter, we will give many examples beyond this theoretical description to show the detailed process and diverse conditions to successfully synthesize our samples.

2.1.2 High pressure and high temperature

2.1.2.1 Syntheses requiring high pressure

Referring to traditional solid state reaction, an intuitive consideration is that many of them are extremely slow or result in poorly crystallized materials. When combining another thermodynamic variable-high pressure- into the reaction, the reaction times may be reduced remarkably to less than an hour, at the same time, giving improved crystallinity of the sample. This is because high pressure may alter the kinetics of a reaction so as to greatly facilitate synthesis of a phase stable at atmospheric pressure. In addition to this common reason, which can hold for most of the high pressure and high temperature (HPHT) solid state syntheses, HPHT can be more specifically used to prepare otherwise unstable compounds often associated with interesting physical properties related to high-pressure transformation of stoichiometry, site preference or electronic states. In solid state chemistry, the very known examples which exhibit the significance of HPHT are perovskite-related compounds.[2]

In fact, HPHT has become an important part in the field of solid-state synthesis of transition-metal oxides with perovskite-related structures. It has the advantages not only to increase the reaction rate of solid-sate reactions at high temperature, but also to stabilize many metastable phases to atmosphere pressure. Several displacive phase transition were observed experimentally in perovskite oxides due to octahedral-site tilting and distortion. However, high pressure favors the denser phases with smaller volume, giving rise to new materials which are unstable at atmospheric pressure. On the other hand, reactions between several compositions or phases to form a compound require that the new phase has a lower free energy than the sum of the initial compositions. When solid state reaction does not take place at ambient pressure, high pressure may play an essential role in synthesizing new compounds by lowering its free energy. Many examples have been listed in the book by Goodenough, which well identifies this situation.[2] Obviously, by HPHT method, one can expect the appearance of octahedral-site Cr^{4+}ions in oxides, stabilization of a cation in a higher valence state, synthesis of multiferroic-type compounds, control of site-preference of cations, and formation of phases stabilized by metallic bonds. When a cation is large, the formation of a layered compound may

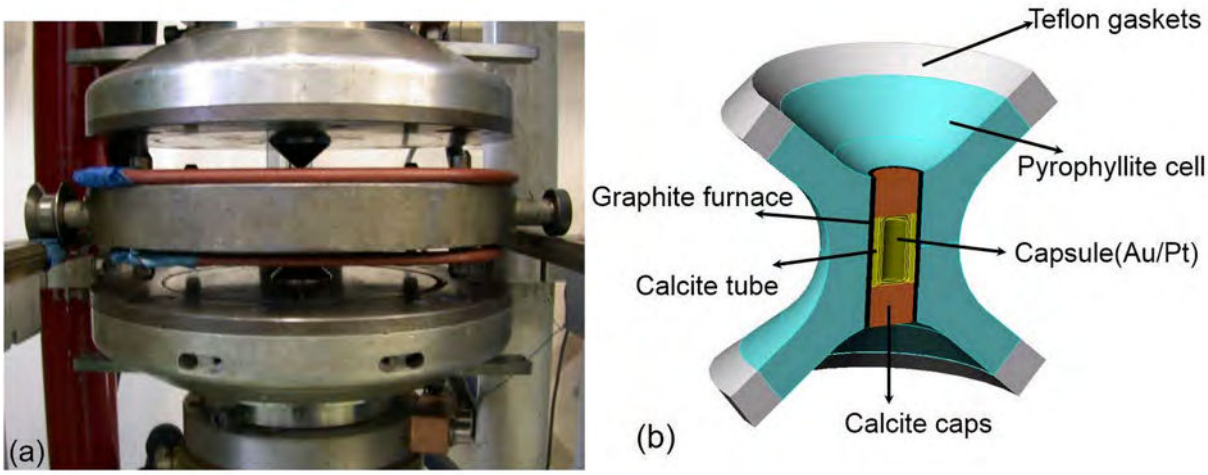

Figure 2.1: (a)High-pressure belt apparatus. The middle section is the toroidal belt of the machine, consisting of the chamber and the cooling system (not visible in this figure). The upper and lower tungsten carbide pistons are clearly shown. (b)Section drawing of the typical sample cell of the BELT type press.

even be favored under high pressure. A variety of different compounds have been prepared by high pressure and high temperature method, often displaying new phenomena and interesting physical properties such as multiferroism and colossal magnetoresistence.

2.1.2.2 HP-HT systems

Belt press

Most of the HPHT synthesis work in this dissertation was carried out using an apparatus with belt-type anvils , as seen in figure 2.1, which is capable of developing pressures to 8 GPa and temperatures to 1500°C. The belt apparatus is similar to that illustrated in Ref. [5], and the principle of operation is the following. Two conical shaped tungsten carbide pistons push into each side of a specially designed tungsten carbide chamber[5]. The pistons and the chamber are held in place and strengthened by hardened steel binding rings, respectively. The binding rings are tapered and are forced into each other, which ensures them to stretch close to their elasticity limit. The name of the device is given because the apparatus with the corresponding binding rings forms a toroidal belt around the sample. A water cooling circuit with chilling system is connected to the toroidal belt. The sample is placed in the center of the chamber in a special assembly, illustrated by figure 2.1(b). The sample cell uses pyrophillite as the pressure-transmitting medium which also provides electric and thermal insulation.[2] High temperature is achieved by an internal heater embedded into the sample cell. A high intensity electric current (hundreds of amperes) from the pistons is imposed on the heater which is usually composed by a graphite sleeve.

The specimen is encapsulated in a nonreactive, malleable material. For oxides, the capsule we used is of noble metal to prevent reaction between capsule and specimen. For temperature above 1000°C, platinum has proven satisfactory. At lower temperature, gold is preferable, as it is easier to handle; less reactive and makes better high-pressure seals. Neither gold nor platinum is sufficiently inert for use in the synthesis of many compounds containing sulfur, selenium or tellurium. In these cases, one has to encapsulate specimen into BN, MgO, or similar other inert materials.[2] The capsule we used is 3 mm in diameter, the small size being necessary to reach high pressure without the need of extremely large forces. However, this is the shortcoming of the system, since the volume of sample that can be encapsulated is relatively small, only 0.04 cm^3. A special device is needed to fill the capsule and slightly compress the specimen in order to make the powder more compact by expelling some of the air trapped inside the powder during the grinding / mixing process. Some starting materials having sensitivities, reactivity, are not stable under ambient atmosphere. In this case, the manipulation of filling capsule should be carried out in inert atmosphere such as in glove box.

Conac system

The other apparatus for HPHT synthesis used in this study is the Conac anvil. Although the principle of operation of the Conac system is quite similar to that of the Belt , the constituents of the Conac anvil and the assembly of sample are totally different. This gives to the Conac anvil system the merit of obtaining larger sample volume and the drawback of reaching lower pressure (maximum of 6 Gpa) when comparing to Belt press.

The Conac system was developed in the 1980s at the Institute for High Pressure of Physics of the Russian Academy of Sciences on the basis of the toroid concept.[3] This high pressure device is composed of two identical facing dies in tungsten carbide, taper fitted into two or three steel rings, as shown in figure 2.2(a). The Conac dies are characterized by a 'cone-shaped hole' and geometrical parameters provide suitable conditions for syntheses of large sample volumes of materials in a high pressure range. More particularly, the 40mm hole Conac assembly (named 'Conac 40') is designed to reach 6GPa and 1500°C for a sample volume of about 0.8 cm^3. In a standard synthesis experiment, the sample is inserted in the assembly as shown in figure 2.2(b). It is composed of a solid transmitting medium in lithographic stone (calcite $CaCO_3$), a resistive heater in graphite, thermal and electrical insulators in limestone or pyrophyllite, and conductive pieces (steel cylinders and molybdenum disks). The pressure calibration of this high pressure device is based on the method of polymorphic transitions of bismuth and barium at room temperature. The estimated precision varies from 6% to 9% between 2 and 5.5 GPa.[4]

2.1.3 Sol-gel processing

A very interesting solution-based synthetic technique for the preparation of both amorphous solids and crystalline ceramics is the sol-gel process, which originated from the pioneering work in the mid-nineteenth century by Jacques Joseph Ebelman and Thomas Graham.[1] In fact,

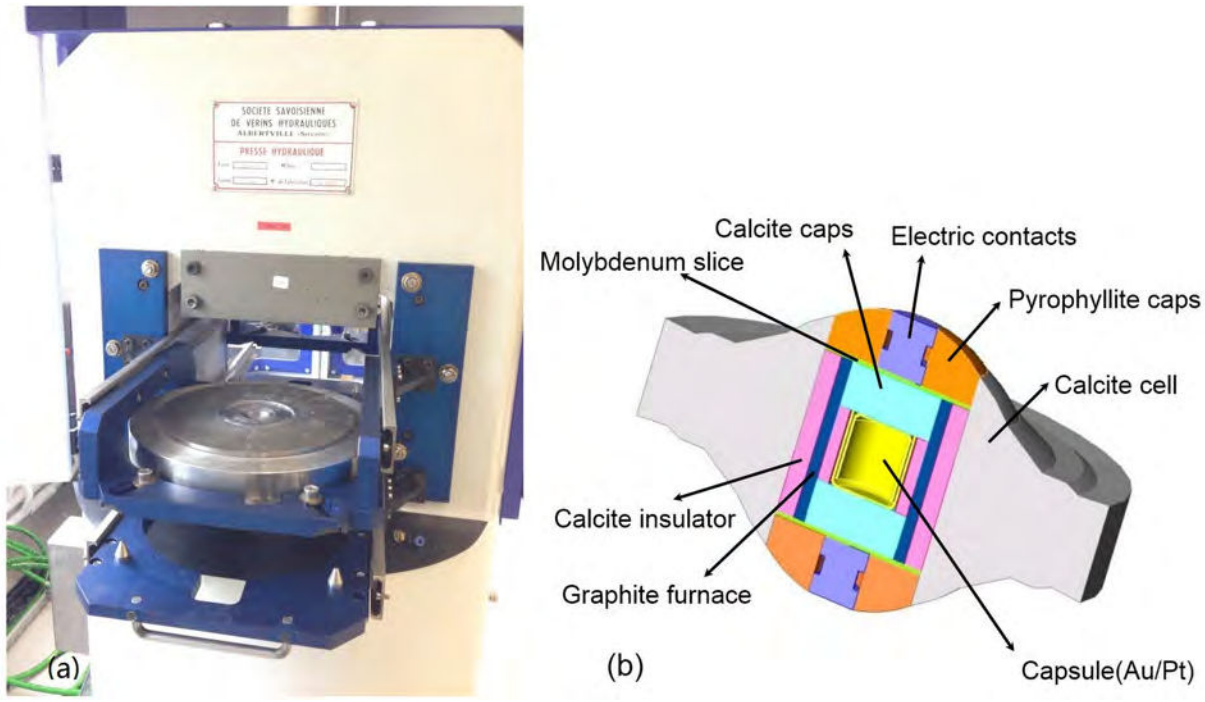

Figure 2.2: (a) The Conac 40 press. (b)Conac 40 assembly used for a standard synthesis experiment.

this is a kind of soft chemistry method (chimie douce), possessing numerous applications in synthetic new materials. There are three major steps concerned: with appropriate precursors, a sol (a colloidal suspension of solid particles in a liquid) can be formed through hydrolysis and polymerization processes; and followed by the appearance of a semi-rigid porous gel; the crystallinity of the ultimate compound, which is obtained after removal of solvent and residuals from the pores by aging, drying, and annealing, is highly dependent on the experimental conditions applied. [1]

The sol-gel method can be used to synthesize powders, films, or monolithic castings. Whereas this processing can result in several different forms of the same starting materials, they are all made in the same way as the monolith. Two approaches are in general used in making sol-gel monoliths: gelation of colloidal powders, or hydrolysis and polymerization of alkoxide precursors. Sol-gel reaction can be realized using metal alkoxides, solvated metal cations, or organometallic precursors. Alkoxides are so far the most common starting materials for sol-gel reaction due to the stable nature and ease of hydrolysis, for which the hydrolysis rate can be controlled by the ratio of ethanol to water. There are generally seven steps to preparing a sol-gel material: mixing, casting, gelating, aging, drying, dehydration or stabilization, and finally, annealing. Mixing is the important step in determining the size and composition uniformity of the grains in the colloidal sol, so a device with condenser is often necessary, such as the one shown in figure2.3. As the sol is allowed to react, the sol becomes more and more connected, giving rise to gelation. Aging of the converted gel is called syneresis, which separates the liquid from the gel to allow further solidification. This step determines the average

Figure 2.3: The device with condenser we used to obtain the precusor by sol-gel method.

pore size and the resultant density of the monolith. Drying of the gel is the last step to remove the solvent and water from the monolith. The dry monolith is still very reactive, owing to the surface silanol bonds in the pores. These bonds are stabilized through thermal treatment. After an appropriate annealing process, heated at high temperature (typically ~1000°C), the objective material can be obtained.

In our case sol-gel processing is used to obtain precursor powders where the local composition is the stoichiometric one, so that the diffusion of species is no longer a limiting parameter as for classical solid state reaction. This improves the purity and stoichiometry of the samples obtained, allows to lower the reaction temperatures and to decrease reaction time.

2.1.4 Single crystal growth

Detailed investigation of the intrinsic physical properties of materials often requires the measurement of single crystal samples. We have performed the growth of single crystal for pyroxene compounds using flux and floating zone methods. This section is intended to provide a brief introduction to appreciate some of the techniques used to grow single crystals from a molten solution. In many respects, crystallization from the molten state is analogous to that from a solvent phase. For example, in both processes slow cooling tends to result in larger crystals, while faster cooling typically gives smaller crystals. A flux method therefore is very suitable to grow single crystal. However, the most essential concepts, for growing single crystals from molten solutions, are congruence and incongruence. For congruently melting compounds, one can cool a stoichimetric melt. Because the entire system nominally freezes simultaneously, this typically results in a densely intergrown polycrystalline ingot. According to the size of the individual crystals, single crystals can sometimes be mechanically separated.[6] Use of a temperature gradient enables directional solidification, and use of a tapered crucible (usually

it is platinum) can favor the nucleation processing. As a result, larger single crystals can be grown under the appropriate conditions. In cases for which the melting temperatures are excessively high or for the incongruently melting compounds, it can be very helpful to use an additional compounds as a flux which is not necessarily incorporated into the resulting crystal and lowers the melting point of the charge (mixture of starting materials and flux). In many cases, the choice of an appropriate flux is considered to be the key in determining the growth of single crystal, and which is really empirical and practical. The floating zone method is a synthesis technique suitable for the synthesis of large single crystals due to the good control of nucleation. The basic idea in float zone crystal growth is to move a liquid zone through the material (actually, a feed rod). If properly seeded, a single crystal can be produced with high purity. This method is restricted to grow single crystal from congruently melting compounds.

2.2 Thermal analysis

Thermal analysis involves the measurement of certain physical and chemical properties, such as enthalpy, mass and heat capacity, as a function of temperature. Thermal analysis can be used to study solid state reactions, thermal decompositions and phase transitions etc. In this thesis, three thermal analysis techniques, TG, DTA and DSC, were employed to study the thermal decompositions and phase transitions.

Thermogravimetry (TG) measures the change in mass of a substance as a function of temperature or time. The sample is usually heated at a constant rate and has a constant mass, until it reacts with the environment or begins to decompose at a specific temperature. The latter can be reflected in the TG curve with weight loss at vicinity of decomposition. The changes of the mass provide useful information on the sample and can be used to calculate the composition changes. TG results depend on variables such as heating rate, nature of the solid and atmosphere used during the measurement.

In differential thermal analysis (DTA),[10] the temperature of a sample is compared with that of an inert reference material during a controlled change of temperature. Therefore, the sample temperatures should be the same as that of the reference until some thermal variations, such as melting, decomposition, or displacive phase transition, take place. In such case the sample temperature becomes either higher, corresponding to an exothermic reaction, or smaller, corresponding to an endothermic reaction, than the reference temperature. The DTA technique is highly sensitive to thermal changes, but this can be at the expense of losing a calorimetric response in which peak areas are only qualitatively related to the magnitude of the enthalpy changes. The complementary technique is differential scanning calorimetry (DSC). Unlike the design of DTA cells, in a DSC cell, the sample and reference are placed at the same environment during heating and the extra heat input to the sample or to the reference required in order to maintain this balance is measured, directly giving rise to the enthalpy changes. For many cases, it is advantageous to use both DTA/DSC and TG together, because the counterpart change of mass in TG will reflect some complementary effects. A very effective way to use thermal analysis is to follow the thermal changes on cooling as well as on

heating. This allows a separation of reversible changes, such as melting or solidification, from irreversible changes, such as most decomposition reactions.

2.3 Morphology and microstructural analysis

A wide variety of microscopic, spectroscopic and other techniques, in addition to diffraction, could be employed to obtain information on the composition, structure and microstructure of materials. In this section, we will discuss why and how some of these techniques (microscopy and spectroscopy techniques) are so useful to analyze, identify and characterize a solid. For microscopy, we first see why electronic microscopy is essential, then by appreciating the interaction of electrons with matter we describe some techniques such as spectroscopy derived from this interaction. We will restrict our discussion to scanning electron microscopy (SEM) and Energy dispersive X-ray spectroscopy (EDX) since they are commonly used in this thesis.

2.3.1 Electron microscopy: Electrons interact with specimen

Electron microscopy is extremely versatile for giving morphological, structural and compositional information of samples over a wide range of magnification. It is also capable of recording diffraction patterns in addition to magnified images, simultaneously. In general, SEM is used in observing the texture, topography and surface features of powders or solid pieces and, because of the depth of focus of SEM, the resultant images have a 3D quality. On the other hand, TEM is more powerful in giving structural and composition information at an atomic scale. Accordingly, electron microscopes operate in either transmission or reflection mode.

Electrons are one type of ionizing radiation, which is the general term given to radiation that is capable of removing one of the tightly bound inner-shell electrons from the attractive field of the nucleus. [11] This ionizing radiation interacts with the specimen to produce a wide range of secondary signals. Some of these are shown in figure 2.4. Many of these signals can be used in analytical electron microscopy, providing us with chemical information and many other features of the sample. It is worth noting that the interactions can be either elastic or inelastic. Signals from elastic interaction will give rise to measurable diffraction, as in XRD. The inelastic scattering can be used to obtain information on the chemistry of samples, such as in the EDX technique.

SEM[24]

Secondary electrons and backscattered, the principal signals used to form images in SEM, are generated within the above mentioned interaction. These signals are capable of giving information about composition, shape, local surface texture and thickness of samples. The process of formation of various types of SEM images is explained in the following.

Secondary electrons (SE) are produced through inelastic scattering that results in the ejection of loosely bound electrons from the specimen. Secondary electrons lie in an energy range of 2~50eV, and they are therefore readily deflected by a low-bias voltage and collected

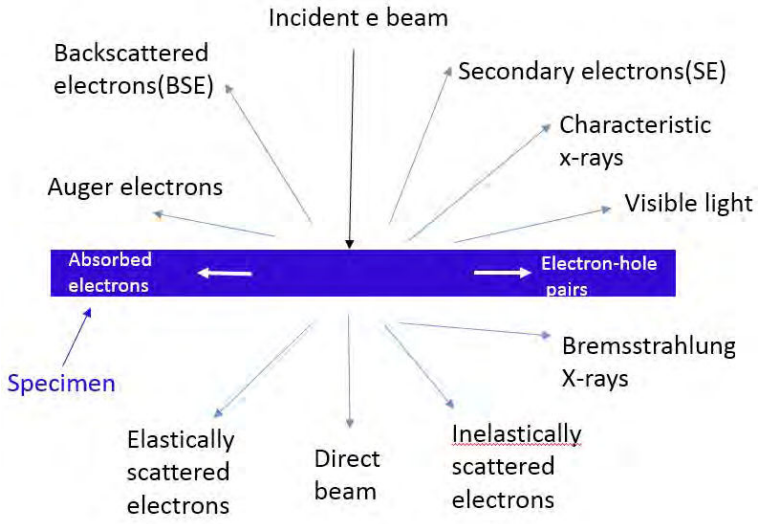

Figure 2.4: Signals generated when a high-energy beam of electrons interacts with a specimen. The directions shown for each signal do not always represent the physical direction of the signal but indicate where the signal is strongest or where it is detected in a relative manner. Inspired by Ref. [11]

with very high efficiency. Given the low energy feature, SE are emitted from a shallow surface of the sample, typically below 10 nm. The most pronounced effect is that of surface topography. This makes the SE image more suitable for studies of rough surfaces at high resolution and in good contrast. In any case, it is necessary to coat the sample with a thin layer of conducting Au or carbon to prevent the build-up of charges on the surface of sample.

Backscattered electrons (BSE) are produced through an elastic scattering interaction with the atoms in the sample that results in the primary electron being re-emitted from the specimen. In the backscattering process, the electron trajectory is changed by a angle greater than 90 degree from the incident beam. The proportion of these BSE will depend on the average atomic numbers of the specimen, but is almost independent of the incident beam energy. Note that in the elastic interactions, the emmitted electrons may also take part in subsequent inelastic scattering events, which will reduce the electron energy. Therefore, the average energy of BSE, is usually less than that of the incident beam, but of the same order of magnitude (in the kV range) . Thus, BSE are able to escape from a relatively thick region of the sample, with the drawback of lower resolution than the image obtained from SE. A very useful feature of BSE in image contrast is that any region of the specimen surface which is tilted towards a BSE detector will provide an enhanced signal, and vice versa. A topographic image of the surface thus can be obtained. On the other hand, the variation of the composition of the sample can be reflected from the BSE signals due to atomic-number contrast which is very useful to distinguish and identify various phases in a sample.

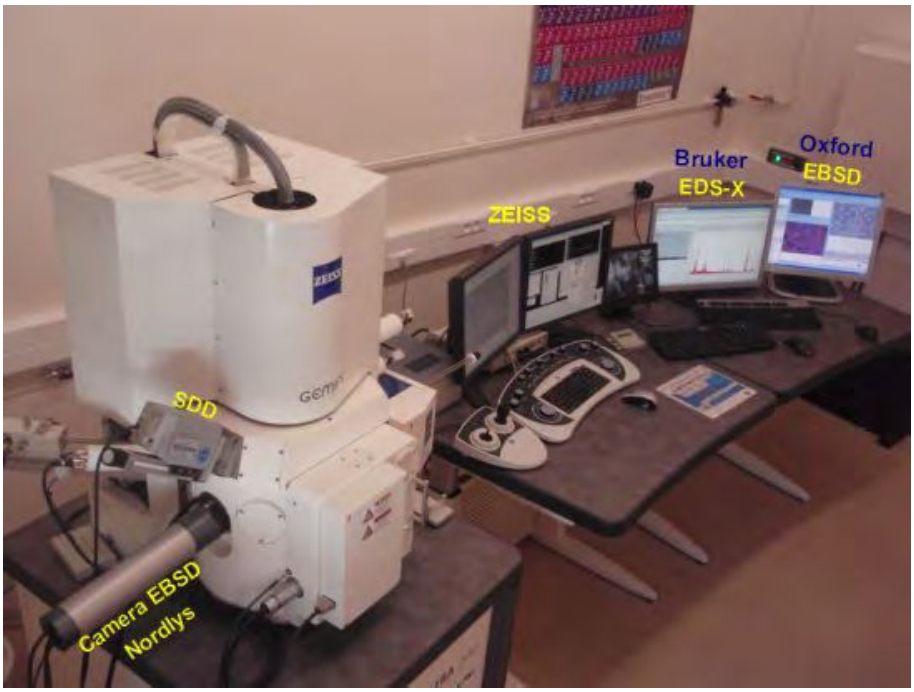

Figure 2.5: FESEM, Zeiss Ultraplus equipped with EDX.

EDX

Energy dispersive x-ray spectroscopy is usually implemented into SEM instruments and utilizes the characteristic x-ray emission spectra when electrons of inner shells of atoms are ionized by high energy bombardment. In EDX, the whole x-ray emission spectrum is collected simultaneously by a specific detector such as Silicon Drift Detector used in this thesis. X-rays are absorbed in a semiconducting material and then generating electron-hole pairs. The corresponding voltage pulse is amplified and displayed on a screen. The voltage pulse is proportional to the energy of the incoming x-rays emmitted by the sample, which are characteristic of the elements it contains. By analyzing the energies, and distribution of energies , of the excited electrons, the x-ray emission spectrum of the sample region in question is obtained. EDX is very useful to get an overview of the elements present in a specimen, although it is less sensitive for light elements (Z>4). Semiquantitative analysis is possible with EDX with an approximate detection limit of 1000-3000 ppm (~10 wt%). [10]

In this thesis, morphology and chemical composition were investigated by field-emission scanning electron microscopy (FESEM,Zeiss Ultaplus) equipped with an energy-dispersive x-ray spectrometer (EDX, Bruker). A photo of FESEM is presented in figure . The sample was gold- or carbon- coated prior to SEM and EDX analysis.

2.4 Structural characterization

Having described several techniques of microstructural analysis and appreciated some of the principles of crystal structures in previous sections, we now have to consider how crystal

structures can be determined. A beam of radiation, for which the wavelength is of the order of magnitude than typical interatomic distances, has to be used in order to perform diffraction experiments. Almost all beams of radiation will be absorbed to some extent or will lead to some damage, but the effects of these processes can be minimized with x-rays, electrons or neutrons. These beams of radiation will interact with atoms, giving rise to scattering processes. Diffraction is the process of coherent elastic scattering from the periodic crystal structure and can provide detailed information about it. X-rays and electrons interact with the atom electron clouds, while the interaction of neutrons with atom is through a nuclear reaction and thus concerns primarily the nucleus. In addition, neutrons with variable energies have magnetic moment that interacts with unpaired electrons in specimen allowing the studies of magnetic order. Thus, this section is devoted to the studies of crystal and magnetic structures.

2.4.1 Comparison of the characteristics of X-ray and neutron beams

In the laboratory, x-rays are produced when an accelerated beam of electrons strikes a metal target. However, high flux neutron beams can not be produced in the laboratory, and currently generated by a nuclear reactor or spallation source. This implies that the conventional x-ray sources have many operational advantage over neutrons. In fact, x-ray and neutron diffraction have complementary merits, depending on the real samples of interest, and there may often be good reasons to choose either x-ray or neutron.

The main difference between the diffraction of x-ray and neutron arises from the fact that the scattering mechanisms are different. X-rays are scattered by electrons, as a result, the scattering power of atom is proportional to the atomic number. This gives the drawback that light atoms have weak diffracted x-ray radiation and distinction between two close elements in the elementary table gets difficult. X-ray scattering power of an atom falls off drastically with increasing scattering angle. Neutrons scatter predominantly from the nuclei of atoms via the strong nuclear interaction, and therefore provide accurate information about the positions of the nuclei in the material. Accordingly, there is no corresponding correlation in the scattering length for neutron scattering from atomic nuclei and the atomic number, and the sign of the scattering length can be either positive or negative. And because of the range of the nuclear scattering potential is of the order 1fm, comparing to x-ray, there is no variation of scattering length with scattering angle. Unlike x-ray, neutron diffraction will be a better technique to distinguish between atoms that have similar numbers of electrons. However, some atoms that have very similar scattering length but have different numbers of electrons, such as Cl and Br, will be better distinguished by x-ray diffraction.[25] Neutrons possess another strength in determining the atomic position of light elements such as hydrogen. However, there are some atoms where the scattering length of neutrons is almost zero, so these atoms such as vanadium can be used as sample container for neutron diffraction. Probably, the most interesting advantage of neutron diffraction is that neutrons can be scattered by the atomic magnetic moments through the interaction with the magnetic moment of neutrons. Since the atomic magnetic moment is carried by the electron cloud, the form factor for magnetic neutron

scattering shows a fall-off effect similar as that of x-rays.

Note that x-ray beams are much more intense than neutron beams. Therefore, it is possible to use smaller samples for x-ray diffraction than for neutron diffraction. For example, with x-ray diffraction, the sample are likely to be much smaller than 1 mm^3, whereas the samples for neutron diffraction are likely to be several cm^3 in volume. For x-ray diffraction, with transmission geometry (see below), even smaller amount of powder is needed to get quite good diffraction patterns.

2.4.2 X-ray instruments and operations

2.4.2.1 X-ray powder diffractometer

The powder diffraction is the most frequently used technique to identify a specimen. Each powder diffraction pattern represents a one-dimensional projection of the three-dimensional reciprocal lattice of a crystal. This accidentally causes peak overlapping effects which result in a reduction of information compared to single crystal diffraction data. However, quantitative analysis of the pattern using modern computers and software provides the wealth of underneath information about the structure of a powder sample. A good illustration of the general information, which can be extracted from a powder diffraction pattern, and the related analysis methods is shown in figure 2.6. What makes the powder diffraction so powerful is that a number of details about a material's structure at various length scales, its phase and chemical composition can be obtained when diffraction data are properly collected and processed.[14]

The quality of the powder diffraction patterns is primarily determined by the nature of the available radiation, and the resolution of the instrument, and the physical and chemical properties of specimen. In addition, proper operation of a conventional diffractometer and careful sample preparation also affect the results of a diffraction experiment. Below we first describe the diffractometers used in this work, and then relevant factors affecting the quality of diffraction data will be discussed.

Three diffractometers, Siemens D5000R, D5000T, Bruker D8 ere mainly used in this work for phase identification, determination of crystal structure and crystal structure refinement. Among them, a D5000R diffractometer with Co Kαradiation selected , was used to identify materials in reflection mode. The diffraction patterns from D5000R are collected by a point detector placed after a graphite (002) diffracted beam monochromator. D5000T and D 8 diffractometers are both equipped by position sensitive detectors and use Cu Kα1 radiation filtered by a Ge (111) primary beam monochromator. They were employed to measure high qualilty diffraction patterns used to obtain the detailed structure information by Rietveld refinement. D5000T with transmission mode has the advantage of measuring small amount of materials. The geometries of D5000R and D5000T are shown in figure 2.7 and figure 2.8, repsectively.

Both preparation of a specimen and choice of instrument parameters will now be considered in turn from a practical perspective. Proper sample preparation is one of the most important requirements in powder diffraction experiment. Preparation influences the quality of a powder

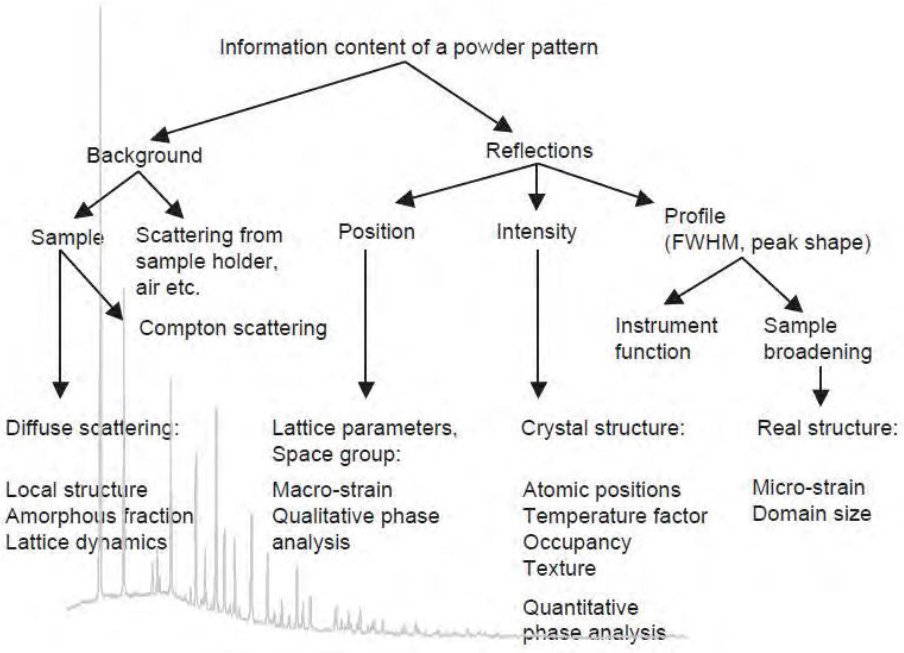

Figure 2.6: General information of a powder diffraction pattern.[13]

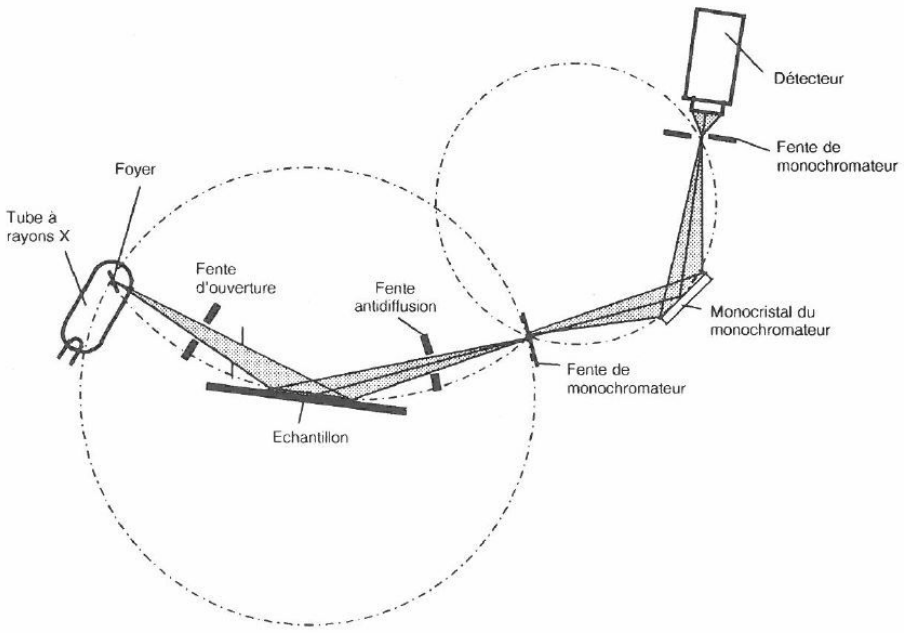

Figure 2.7: The geometry of Siemens D5000R diffractometer.[15]

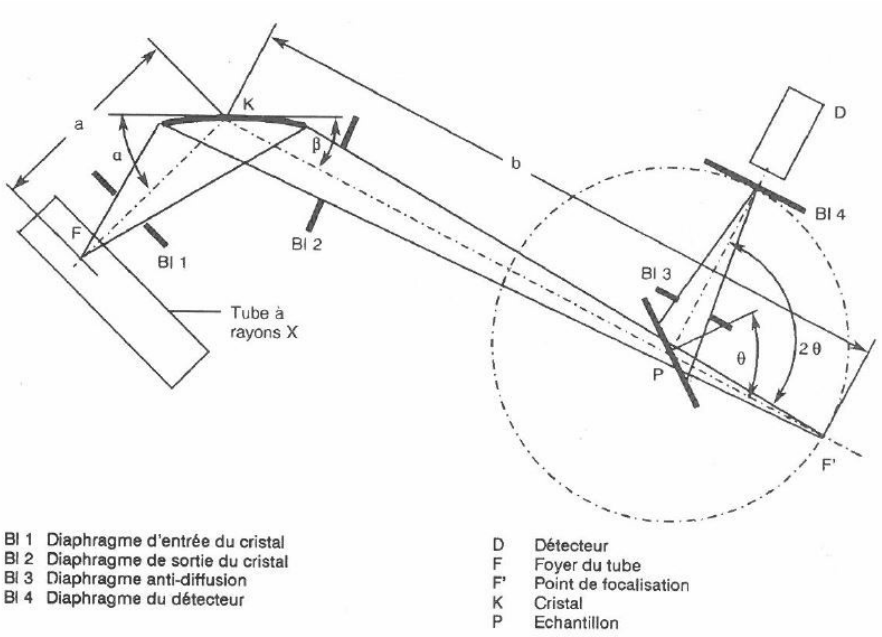

Figure 2.8: The geometry of D5000T with transmission mode. [15]

pattern by either altering intensities or distorting shape of Bragg reflections. The grains in the specimen should be randomly distributed, and this can be achieved by reducing the size of particles (by grinding with agate mortar and pestle) and increasing the number of diffracting particles. To improve the powder statistics, the powder specimen is often rotated during measurement. However, this is not available for all machines. One improper manipulation which has to be avoided during sample preparation is to fill the sample holder too high or too low. Both cause a significant shift of reflection positions which makes the analysis task difficult. When mounting the specimen on sample holder, some special precaution should be taken. When platelet-like or needle-like particles are produced by grinding, the severe preferred orientation or texture will be caused. They will obviously affect diffracted intensities. Take D5000R as an example, first, the sample can be prepared by filling the volume of the cavity of sample holder with powder, then remove the excess powder from the surface of the holder by a single sweep with the edge of a glass slide. Never press the surface of sample holders in order to avoid the strong preferred orientation effect. For the transmission mode, such as D5000T, the sample should be prepared by dusting the powder on an transparent tape with one side glued. Then, one should make the distribution of particles more average on the surface of the tape using a small brush.

When it comes to the instrument related parameters, many variables will influence the quality of diffracted data. Nevertheless, we here only pay attention to the choice of wavelength and scanning parameters one can control, since many important factors related to the instrument are generally optimized and fixed. The first consideration of wavelength comes from the purpose of the diffraction experiment. Long wavelengths such as Fe and Co are preferably used when the accuracy of lattice parameters is of greater interest. Another most

important selection criterium is whether or not the diffracted specimen contains chemical elements with one of their absorption edges located just above the used characteristic wavelength (wavelength of used x-rays). For instance, the K-absorption edge of Co is about 1.74Å. The strongest Kα spectral lines of copper have typical wavelength of 1.54Å, which is the case for D8 and D5000T diffractometers. Therefore, nearly all Kα characteristic Cu radiation is absorbed by Co in the specimen, giving rise to strong fluorescence background, so that this type of radiation becomes unsuitable for x-ray diffraction of Co-bearing materials. Alternatively, diffractometer such as D5000R with Co radiation is a suitable choice for this case. The two most significant parameters of the commonly used step-scan experiment, tuned freely by user, are the size of the step $\triangle 2\theta$ and counting time, t. For using Cu radiation, the step size is typically chosen as 0.02. But it is worth noting that many factors affect step-size for diffraction of different materials, and a rule of thumb for its selection is that at least 8-12 points should be recorded for well-resolved peaks (without obvious overlap) within one full width at half maximum in order to keep the accuracy on measurement of reflection shape.[14] Counting time is a very flexible parameter, for samples with strong absorption of radiation, long counting time may be helpful to improve the diffraction pattern intensity.

2.4.2.2 X-ray single crystal diffractometer

The most frequently used technique for the determination of crystal structures is single crystal analysis. Single crystal x-ray diffraction experiments were performed at room temperature on Kappa CCD diffractometer using Ag Kα1 radiation (0.56087 Å). Unit cell refinement was carried out with the program Dirax (Duisenberg & Schreurs, 1989-2000), then EvalCCD was used for data reduction[18]. Final structure solution was obtained from SIR97[19], followed by structure refinement with SHELXL-97(Sheldrick, 1997).

2.4.3 Determination of crystal structure from powder diffraction

Ab initio indexing is used to determine and refine the unit cell of an unknown phase and give preliminary information about space group. A single-phase powder and diffraction pattern with good quality are prerequisite. Several automatic indexing programs such Treor, Dicvol and ITO have been developed and commonly used to determine the unit cell for an unknown phase. Dicvol is a potentially exhaustive trial-and-error indexing program with variation of parameters by successive dichotomy and partitioning of the unit cell volume.[16] The indexing strategy is based on exploring for a solution from high to low symmetry using partitioning of the unit cell volume in 400Å^3 increments (except for a triclinic case).[14] Dicvol or Treor are implemented into the Fullprof Suite program. We now take Dicvol as an example to deduce the indexing process. The first step is to search for peaks and extract the peak information from diffraction patterns using WinPlotR(2006). When choosing the Dicvol format to save the peaks, all the data are redirected to Dicvol. By running the Dicvol program, the possible unit cell parameters and a PCR file are automatically generated. A Lebail fit should be followed. Based on the extracted integrated intensities, the Checkgroup program suggests a tentative

space group.

To solve the crystal structure from powder diffraction, the FOX (free objects for crystallography) program was used.[17] It uses a global-optimization algorithm to solve the structure by performing trials in direct space. Using simulated annealing, the Monte Carlo approach lead to convergence. But very often, false minima of the parameter space will be attained, accordingly, the algorithm can be trapped in a local minimum instead of the global minimum. To overcome this possible trapping effect, parallel tempering is combined into this optimization process in FOX. Generally, the operation of FOX starts with the indexing step for an unknown phase, using the DICVOL algorithm. The most probable space group is obtained by successive LeBail fits for all space groups of Laue symmetry lower or equal to the Laue class of the unit cell.. Then a random atomic model is provided to the program and the global optimization process is followed to get the positions of all atoms. Then, by performing Rietveld refinement using Fullprof Suite based on the solution provided by FOX, the crystal structure of the unknown phase is obtained.

2.4.4 Neutron scattering and magnetic structure

2.4.4.1 Neutron diffractometer[20]

The most widespread use of neutron diffraction is to determine the magnetic structure of materials. We used the D1B spectrometer at Institut Laue Langevin (ILL) to obtain the neutron diffraction data on powder samples. D1B is a two-axis spectrometer dedicated to diffraction experiments with a high neutron flux. The layout of instrument of D1B is shown in figure 2.9. The instrument is specially designed for the magnetic structures determination with a high spatial resolution at low angle, i.e. the FWHM reaches 0.2° (for a sample with diameter of 8mm) around 2θ=40°. For this purpose, pyrolytic graphite monochromator with (002) Bragg reflection gives neutron flux of 6.5×10^6 n cm^{-2} s^{-1} with wavelength of 2.52Å. The high flux allows to detect weak magnetic reflections and the long wavelength is not a limitation since magnetic scattering is limited to relatively low diffraction angles due to the rapid fall off of the corresponding form factor.

An 1.28Å wavelength corresponding to the (311) Bragg reflection of a germanium monochromator is also available in order to explore a larger portion of the reciprocal space and refine the nuclear structure. With this mode, the incident neutron flux onto the sample is reduced to 0.4×10^6 n cm^{-2} s^{-1}. D1B is equipped with a position sensitive detector composed of a system of multi-electrodes with 1280 cells, which span a 2θ range of 128° covering the angular range of 0.8-128.8°. Several sample environment are available, typical orange cryostat, give access to a temperature range from 1.7K to 300K. Vanadium sample container almost totally spin incoherent, is often used.

2.4.4.2 Magnetic structure determination

The fundamental equations for magnetic structure determination is expressed with the differential magnetic cross section,[23] which is given by:

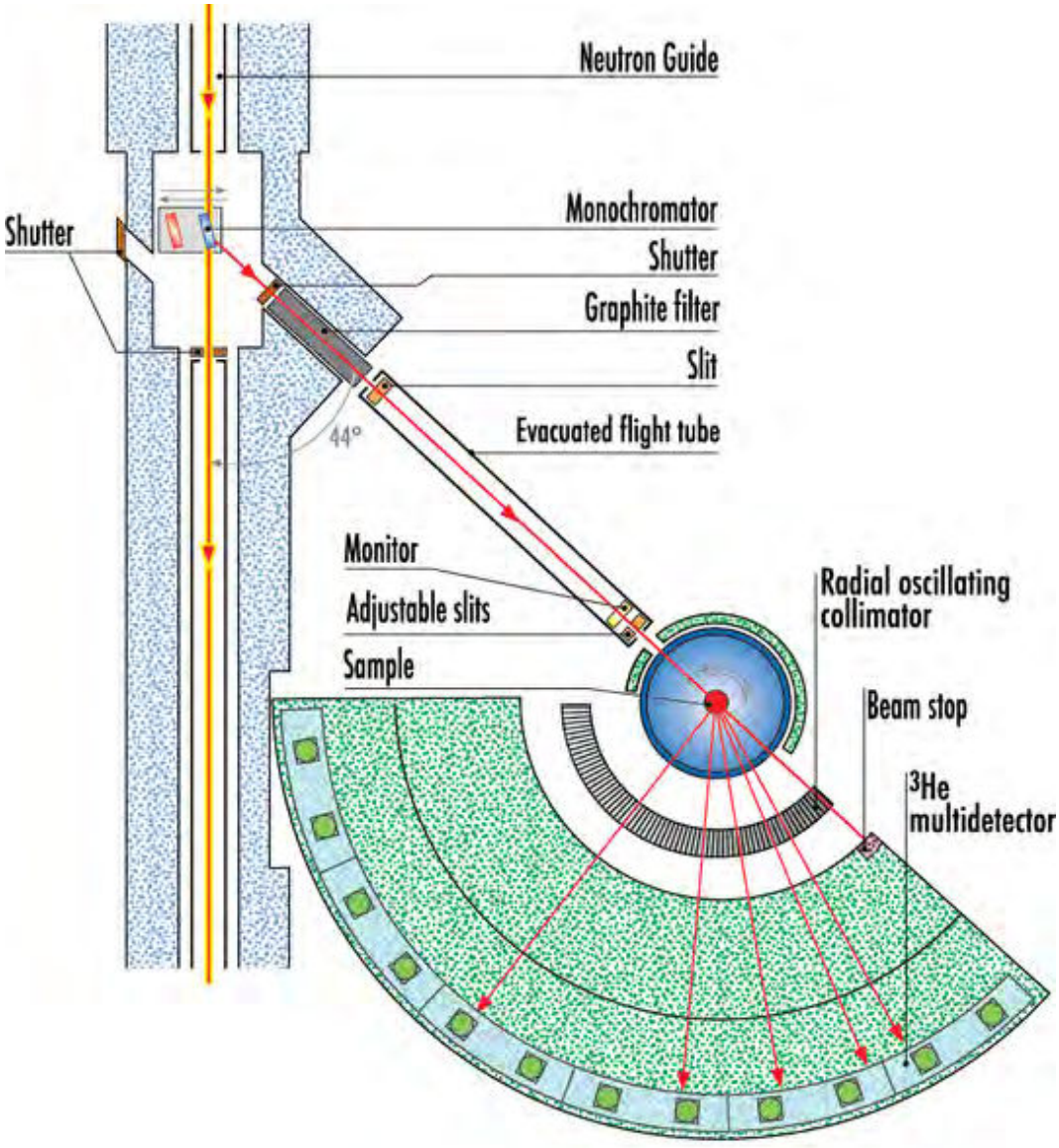

Figure 2.9: Instrument of D1B at ILL, Grenoble.[20]

$$\frac{d\sigma_M}{d\Omega}(\mathbf{Q}) = \frac{(2\pi)^3}{V} N \sum_{\mathbf{H}} \sum_{\mathbf{k}} \mid \mathbf{F}_{M\perp}(\mathbf{Q}) \mid^2 \delta(\mathbf{Q} - \mathbf{H} - \mathbf{k}) \tag{2.1}$$

where the magnetic structure factor is described as:

$$\mathbf{F}_M(\mathbf{Q} = \mathbf{H} + \mathbf{k}) = p \sum_{\nu} f_\nu(\mathbf{Q}) \mathbf{m}_{\nu,\mathbf{k}} \exp(i\mathbf{Q}.\mathbf{r}_\nu) \tag{2.2}$$

In practice, the determination of a magnetic structure follows three steps: (i) the identification of the propagation vectors $\mathbf{k}$ at lowest temperature, (ii) the determination of the coupling between the Fourier components $\mathbf{m}_{\nu,\mathbf{k}}$ and (iii) the determination of the direction and amplitudes of these Fourier components, giving the direction and amplitudes of the true magnetic moments. The first step can be performed with the K-search software implemented into Fullprof Suite. Then, the determination of magnetic structure, corresponding to the two remaining steps, can be done by symmetry analysis, following the representation analysis technique developed by Bertaut.[22] For this purpose, we used the two softwares SARAh-Representatin analysis[21] and BasIreps integrated in Fullprof Suite[23]. The magnetic structure determination process using representation theory, including the decomposition of the magnetic representation into irreducible representations of little groups and basic vectors for atomic moments, are illustrated in the thesis for each compound investigated.

In general, the k vector may be any point of the first Brillouin zone, and will give either a commensurate structure or an incommensurate one. Depending on the dimension of the corresponding irreducible representation, there are two types of incommensurate structures: sin wave modulated structure with one dimensional irreducible representation and helical structure with irreducible representation with two-dimension. The magnetic structure determination for compounds with commensurate magnetic symmetry are given in chapter 5,6, 7 and 8. And incommensurate magnetic structure can be found in chapter 8.

2.5 Magnetization measurement

The magnetization measurements presented in this thesis were taken using a Quantum Design MPMS XL and MPMS SQUID VSM dc magnetometer. Both them exhibit very high sensitivity, and SQUID VSM has the additional merit of speed because it combines the speed of VSM and the sensitivity of a SQUID magnetometer.

2.5.1 MPMS_XL

The Quantum Design MPMS XL is composed of several components: temperature control system, magnet control system, superconducting quantum interference device (SQUID) amplifier system, sample handling system and computer operating system.[7] Among them, the SQUID detector is the heart of the magnetic moment detection system, and provides the sensitivity of MPMS. The maximum sensitivity of the instrument is in the range of 10^{-8} emu. Therefore, it is extremely sensitive for all kinds of AC and DC magnetic measurements. The sample

is placed in an environment with Helium flow cryostat, which can be cooled down to a base temperature of 1.7 K. A magnetic field is applied in the vertial direction by a superconducting magnet, which has an operating magnetic field range of 0-5T. All of the measurements are computer controlled using software which was designed specifically by Quantum Design. Data can be collected between μ_0H = 0 to ± 5T and T = 1.7 K to 400 K. In order to measure the magnetic susceptibility the sample is typically mounted in the center of a plastic straw of diameter ~5mm and length ~19.6cm, in contrast to the sample chamber with diameter of 9 mm, and the diamagnetic moment of which is very small. The weighted powder sample is tightly wrapped up by thin film.

Even if we mentioned above that SQUID is the source of the remarkable sensitivity, it does not measure directly the magnetic flux. In general, SQUID can be regarded as a highly linear current-voltage convertor. In addition to the traditional AC/DC measurement modes, the MPMS features a reciprocating sample operation (RSO). This technique features small amplitude and periodic displacement of a sample inside the MPMS second order gradiometer. The movement of the sample results in an oscillating AC signal that is detected by the SQUID sensor. The principle of measurement of magnetization is shown schematically in figure 2.10. The plastic straw containing the sample moves vertically between three superconducting detection coils, in which a current proportional to the magnetic moment from sample is induced. Because the detection coils, the connecting wires, and the SQUID input coil form a closed superconducting loop, any variation of magnetic flux in the detection coils produces a change in the persistent current in the detection circuit, which is strictly proportional to the change in the magnetic flux. Thus small changes in the sample magnetization are measured as small current. Then, the SQUID electronics produce an output voltage which is strictly proportional to the current flowing in the SQUID input coil. Samples are typically 20 to 40 mg but strongly magnetic materials can be measured with less material.

All the magnetic measurements were carried out with zero-field cooling (ZFC) and field cooling (FC) processes. The measurement of ZFC means that the sample was first cooled down to 2K without any magnetic field, and then by applying a magnetic field (typically 100Oe) the magnetization of sample was measured on warming. The FC process is performed with opposite manner.

In an AC model, an oscillating AC magnetic field is applied to the sample. The change in flux seen by the detection circuitry is caused only by the changing magnetic moment of the sample since it responds to the applied AC field. The AC susceptibility obtained from these measurements is described as having both real and imaginary components, where the imaginary component is proportional to the energy losses in the sample. A standard measurement of the AC susceptibility of a sample is a two-point measurement that positions the sample in two locations (the center of the bottom pickup coil and the center of the two middle coils) within the SQUID pickup coils and, at each location, measures the effect of a nulling waveform on the sample's magnetic moment. By this way, all spurious signals at the AC measurement frequency are nulled, allowing extremely accurate measurement of the AC susceptibility.

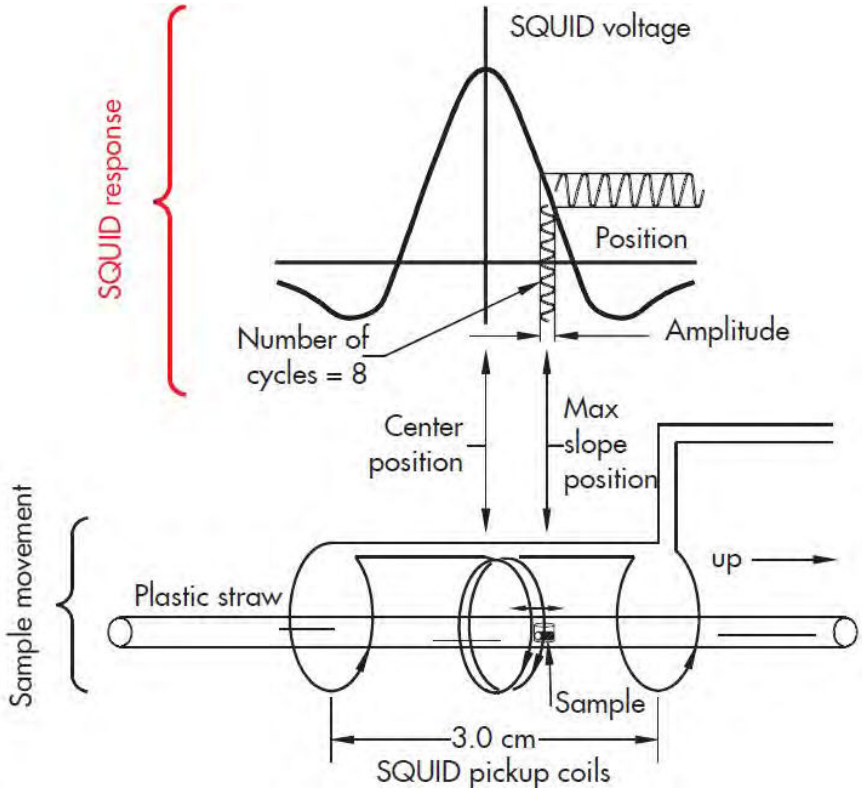

Figure 2.10: RSO measurement with a very small amplitude[7]

2.5.2 SQUID-VSM

With optimized speed and sensitivity, the MPMS SQUID VSM utilized some analytic techniques employed by Vibrating Sample Magnetometers (VSMs).[8] Specifically, the sample is vibrated at a known frequency and phase-sensitive detection is employed for rapid data collection and spurious signal rejection. Unlike traditional (non-superconducting) VSMs, the size of the signal produced by a sample is not dependent on the frequency of vibration, but only on the magnetic moment of the sample, the vibration amplitude, and the design of the SQUID detection circuit. The MPMS SQUID VSM uses a superconducting magnet (a solenoid of superconducting wire) to subject samples to magnetic fields up to 7 Tesla. The SQUID and magnet must both be cooled with liquid helium. Liquid helium is also used to cool the sample chamber, providing temperature control of samples from 400 down to 1.8 K. To help conserve liquid helium, the system is designed to use less costly liquid nitrogen to intercept heat bound for the helium tank. The SQUID VSM will only operate properly with both cryogens in use: liquid helium and liquid nitrogen.

2.6 Heat capacity measurement

The measurements of heat capacity in this thesis were all carried out using a Quantum Design Physical Properties Measurement System (PPMS). The PPMS heat capacity option measures

the heat capacity of sample at constant pressure by controlling the heat added to and removed from a sample while monitoring the resulting change in temperature. During a measurement, a known amount of heat is applied at constant power for a fixed time, and then this heating period is followed by a cooling period of the same duration.[9] A schematic of thermal connections to sample and sample platform, known as the puck, is shown in figure 2.11[9]. The platform heater and platform thermometer are placed to the bottom side of the sample platform, and are connected by small wires which also provide the thermal connection. A good thermal contact between the sample and the platform is ensured by mounting the sample to the platform by using a thin layer of grease.

In the measurement, the basic puck configuration accommodates small samples weighing approximately 1 to 200 mg. By considering the time consumption from large sample and accuracy factor from small sample limited by addenda heat capacity, the appropriate sample mass will be in the range of 3~5mg. The heat capacity option can measure heat capacity up to about 400 K, but the worthwhile note is that at high temperature the relaxation times get relatively long above 100 K.

A simple model associated with relaxation method, which is the most basic analysis of the raw measurement data, makes the assumption that the sample and sample platform are in good thermal contact with each other and are always at the same temperature during the measurement. In this simple model, the temperature of the platform as a function of time is given by:

$$C_{total}\frac{dT}{dt} = -K_w(T - T_b) + P(t) \tag{2.3}$$

where C_{total} is the total heat capacity of the whole system; $K_w$is the thermal conductance of the wires; $T_b$is the temperature of the thermal bath; P(t) is the power applied by the heater. By solving this differential equation the heat capacity is calculated from the exponential decay time constant of the sample temperature. The solution is given by:

$$T(t) \sim e^{-\frac{t}{\tau}}, \tau = \frac{C_{total}}{K_w} \tag{2.4}$$

In order to extract the heat capacity of the sample, the heat capacity contribution from puck and used grease must be subtracted, so an addenda calibration file has to be estimated before any measurement of sample.

2.7 Magneto-electric measurement

A common method of measuring spontaneous or induced polarization is to measure the pyroelectric current. Pyroelectricity is the a first rank tensor property describing a change polarization P to a change in temperature δT. This relation is given by:

$$Ps = p(T)\delta T[C/m^2] \tag{2.5}$$

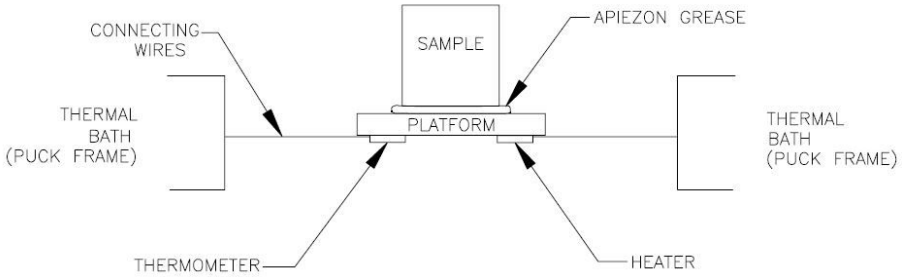

Figure 2.11: Thermal connections to sample and sample platform[12]

This property occurs in certain classes of materials which have polar point-group symmetry. In an ionic crystal with polar symmetry, the displacements between ions take place with changing temperature, generating a net dipole moment and a polarization current in the lattice. An electroded sample is heated in the sample chamber and its change in polarization monitored as current. The current is proportional to the rate of change of temperature:

$$I = p(T)AdT/dt \tag{2.6}$$

where I is the measured current, A represents the surface area of the electroded sample, and p(T) is the pyroelectric coefficient at T. By combining equations 2.5 and 2.6, we have:

$$Ps = \frac{I}{A}dt \tag{2.7}$$

Thus, by integrating the measured pyrocurrent to time, the spontaneous polarization can be obtained. It is worth noting that the so-called poling process is required to align the net dipole moments of randomly oriented domains.

The measurement of pyroelectric current was performed on the set-up shown in figure 2.12. The sample mounted on the sample holder (see figure 2.13) was transmitted into the crysostat with He4 filled (the He gas is used to regulate the temperature) through a long stick. The superconductor magnet was implemented into the set-up which supplies horizontal magnetic field in order to satisfy measurement in different orienations.

Sample preparation: The sample was pressed into pellets as the shape of a capacitor, and then was coated with silver epoxy on both sides to make conducting electrodes. The electroded sample was contacted with copper wires, as shown in figure 2.13. The two points measurements were carried out on a Keithley 6517A electrometer, which combine a voltage source and precise ammeter. The circuit setup consists of a triaxial cable which connects the ammeter probe to one side of sample by Cu wires, and a coaxial cable connects another side of sample to voltage source, intercepted by a box acted as a shield. Precaution have to be taken for the shielding because of the very small signal.

The first step of the measurement is the magnetoelectric annealing. It was perfomed by simultaneously applying an electric fields E of 200V and a magnetic field of 8T in perpendicular directions (for multiferroic properties measurements, only electric fields are applied), at 100K

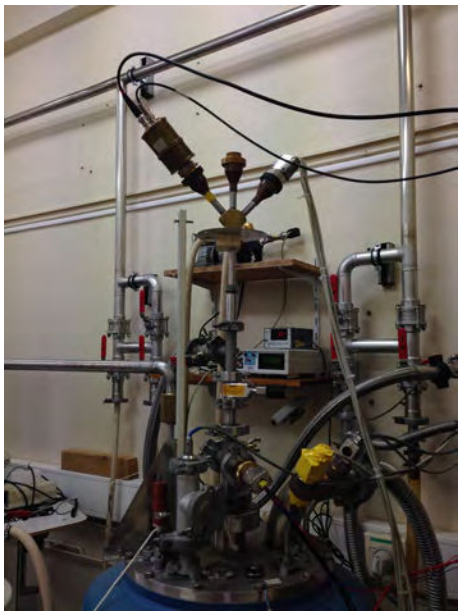

Figure 2.12: The set-up used for pyroelectric current measurement.

Figure 2.13: The sample holder used for pyroelectric current measurement.

and then cooled the sample down to 2K. At 2K, both electric and magnetic fields were removed. After the magnetoelectric poling, the expected pyroelectric current under various magnetic fields, which has the maximum value at around magnetic transition temperature, can be recorded on warming at a rate of 3K/min by multimeter. Consequently, electric polarization is obtained by integration of the measured pyroelectric current over time.

Bibliography

[1] John N. Lalena, David A. Cleary, Everett E. Carpenter, Nancy F. Dean, Inorganic materials synthesis and fabrication, Wiley Interscience, 2008. 2, 57, 60, 61

[2] J. B. Goodenough, J. A. Kafalas, and J. M. Longo, High-Pressure Synthesis, Preparative Methods in Solid State Chemistry (Academic Press, Inc., New York and London), 1972. 58, 59, 60

[3] N.A. Nikolaev and M.D. Shalimov, Device for producing superhigh pressure and temperature, Patent, SU1332598, 1990. 60

[4] C. Goujon, M. Legendre, P. Plaindoux, A. Prat, R. Bruyere, A new differential thermal analysis setup for measuring high pressure phase transitions, High Pressure Research, 31, 2011, 375-387. 60

[5] H. Tracy Hall, Ultra-High-Pressure, High-Temperature Apparatus: the "Belt", The Review of Scientific Instruments, 31, 1960, 125-131. 59

[6] I. R. Fisher, M. C. Shapiro, and J. G. Analytis, Principles of crystal growth of intermetallic and oxide compounds from molten solutions, Philos. Mag. 92, 2012, 2401. 62

[7] Quantum Design Inc., Magnetic Property Measurement System, User's Manual, 2009. 74, 76

[8] Quantum Design Inc., Magnetic Property Measurement System, SQUID VSM User's Manual, 2009. 76

[9] Quantum Design Inc. PPMS Manual, 2008. 77

[10] A. R. West, Solid state chemistry and its applications, Wiley, 2014. 63, 66

[11] D.B.Williams, C.B. Carter, transmission electron microscopy, Basics I, Plenum Press, 1996. 64, 65

[12] Quantum Design Inc., Physical Property Measurement System, Heat Capacity Option User's Manual, 2004. 78

[13] Robert E. Dinnebier, Simon J.L.Billinge, Powder Diffraction Theory and Practice, RSCPublishing, 2008. 69

[14] V.Pecharsky and P. Zavalij, Fundamentals of Powder Diffraction and Structural Characterization of Materials, Second Edition, Springer, 2009. 68, 71

[15] Siemens, Monochromateur primaire de transmission pour le diffractometre D 5000, Instructions, Ref. C79000-B3477-C160-01. monochromateur secondaire pour le diffractometre D 5000, Instructions, Ref. C79000-B3477-C152-01. 69, 70

[16] A. Boultif, D. Louër, Powder pattern indexing with the successive dichotomy method, J. Appl. Cryst. 37, 2004, 724. 71

[17] V. Favre-Nicolin and R. Cerny, FOX, 'free objects for crystallography': a modular approach to ab initio structure determination from powder diffraction. J. Appl. Cryst., 35, 2002, 734-743 72

[18] A.J.M. Duisenberg, L.M.J. Kroon-Batenburg and A.M.M. Schreurs, An intensity evaluation method: EVAL-14, J.Appl.Cryst 36, 2003, 220-229. 71

[19] G. Cascarano A. Altomare, C. Giacovazzo, SIRWARE, Acta Cryst.,1996, A52, C79. 71

[20] http://www.ill.eu/instruments-support/instruments-groups/instruments/d1b. 2, 72, 73

[21] A.S. Wills, A new protocol for the determination of magnetic structures using simulated annealing and representational analysis (SARA h),Physics B, 278, 2000, 680. 74

[22] E.F. Bertaut, Representation analysis of magnetic structures, Acta Crystallogr.Sec. A, 1968, 24, 217. 74

[23] Juan Rodríguez-Carvajal, Recent Advances in Magnetic Structure Determination by Neutron Powder Diffraction, Physica B, 192, 1993, 55-69. 72, 74

[24] J. Goldstein, D. Newbury, et al. Scanning Electron Microscopy and X-ray Microanalysis, Third Edition, Kluwer Academic Plenum Publishers, 2003. 64

[25] M.T. Dove, Structure and Dynamics An atomic view of materials, Oxford University Press, 2003.

67

Chapter 3

Synthesis strategy

This chapter is devoted to sum up the synthetic pyroxenes in this work and underline the story how to obtain a single phase sample in detail. It covers most of all the attempts to get a single phase objective pyroxene compound using solid state reaction, high pressure high temperature method, and soft chemistry method. We have also performed the growth of single crystal for some pyroxenes by flux method and floating zone method, and the relevant results will also be discussed in this chapter. In this chapter, all the synthesis experiments were classified into four parts, each one corresponds to one synthesis method. Within each part, remarks on some interesting synthesis routes for specific samples are given.

3.1 Solid state reaction

The survey, in the opening chapter, of crystal structures, magnetic properties and physical properties has shown that pyroxene compounds can be regarded as a good candidate in exploring new multiferroic materials and studying exotic physical properties. The intriguing physical properties mainly ascribe from their magnetic symmetry which is determined by their unique crystal structure. This monoclinic structure can accommodates a variety of transition metal cations which covers a continuous variation of the d-orbital occupancy. The syntheses of pyroxene systems $CaMGe_2O_6$ with M=$Mn^{2+}(3d^5)$, $Co^{2+}(3d^7)$, $Ni^{2+}(3d^8)$,$Cu^{2+}(3d^9)$ and $Zn^{2+}(3d^{10})$ have been carried out in order to have an extensive investigation on their structure-property relationship. With conventional solid state reaction, compounds $CaMGe_2O_6$ with M=$Mn^{2+}(3d^5)$, $Co^{2+}(3d^7)$, $Ni^{2+}(3d^8)$,$Cu^{2+}(3d^9)$ and $Zn^{2+}(3d^{10})$ can be synthesized, as listed in table3.1. In between them, $CaZnGe_2O_6$ will be used as a lattice standard of phonon contribution to get the magnetic component of specific heat capacity for magnetic pyroxenes in this thesis. In order to study the crystal structure and physical properties of solid solution, the syntheses of solid solutions $CaMn_{1-x}Co_xGe_2O_6$, $CaMn_{1-x}Ni_xGe_2O_6$, $CaCo_{1-x}Ni_xGe_2O_6$ and $CaMn_{1-x}Fe_xGe_2O_6$ have been performed. As shown in table 3.1, solid solution of Mn/Co, Mn/Ni, Co/Ni can be prepared by solid state reaction, while several attempts on solid solution between Mn and Fe did not yield pyroxene phase (see table 3.2). The failure of synthesis of Fe-bearing solid solution may be due to the atmosphere condition, since $CaFeGe_2O_6$ has

Table 3.1: Summary of technique routes for synthesizing pyroxenes using solid state reaction. Bold: new pyroxenes.

Compound	Chapter	Label	Starting materials	Conditions	Results(impurity)	Note
$CaCuGe_2O_6$	-	R	$CaCO_3$,CuO,GeO_2	1000°C,100+100h	$CuGeO_3$(0.87%)	T_{melt}=1100°C
		1	$CaCO_3$,CuO,GeO_2	1100°C,100h	single crystal $CuGeO_3$	Single crystal
$CaMnGe_2O_6$	5	R	$CaCO_3$,MnO_2,GeO_2+Regrinding	1100°C,100+100h	$Ca_3Mn_2Ge_3O_{12}$(0.15%)	Decomposed@1250°C
$CaZnGe_2O_6$	5		$CaCO_3$,ZnO,GeO_2	1100°C,100h	Zn_2GeO_4(2.96%)	
$CaCoGe_2O_6$	7		$CaCO_3$,Co_3O_4,GeO_2	1100°C,100h	Co_2GeO_4	
$CaNiGe_2O_6$	-	R	$CaCO_3$,NiO,GeO_2+Regrinding	1000°C(100h)+1100°C(100h)	Ni_2GeO_4	
$\mathbf{CaMn_{0.25}Co_{0.75}Ge_2O_6}$	7		$CaCO_3$,Co_3O_4,MnO_2,GeO_2	1100°C,100h	$CaGeO_3$(4.73%)	
$\mathbf{CaMn_{0.5}Co_{0.5}Ge_2O_6}$	7		$CaCO_3$,Co_3O_4,MnO_2,GeO_2	1100°C,100h	$CaGeO_3$(5.36%)	
$\mathbf{CaMn_{0.625}Co_{0.375}Ge_2O_6}$	7	1	$CaCO_3$,Co_3O_4,MnO_2,GeO_2	1120°C,100h		
	7	2	$CaCO_3$,Co_3O_4,MnO_2,GeO_2	1120°C,100h	$CaGeO_3$(3.6%)	For Neutron diffraction
$\mathbf{CaMn_{0.75}Co_{0.25}Ge_2O_6}$	7		$CaCO_3$,Co_3O_4,MnO_2,GeO_2	1100°C,100h	$CaGeO_3$(6.81%)	
$\mathbf{CaMn_{0.875}Co_{0.125}Ge_2O_6}$	7	1	$CaCO_3$,Co_3O_4,MnO_2,GeO_2	1120°C,100h	$Ca_3Mn_2Ge_3O_{12}$(0.04%)	
	7	2	$CaCO_3$,Co_3O_4,MnO_2,GeO_2	1120°C,100h	$CaGeO_3$(4.76%)	For Neutron diffraction
$\mathbf{CaMn_{0.25}Ni_{0.75}Ge_2O_6}$	7		$CaCO_3$,NiO,MnO,GeO_2	1200°C,100h	Ni_2GeO_4	
$\mathbf{CaMn_{0.5}Ni_{0.5}Ge_2O_6}$	7	R	$CaCO_3$,NiO,MnO_2,GeO_2+Regrinding	1100°C,100+50h	$Ca_3Mn_2Ge_3O_{12}$	
$\mathbf{CaMn_{0.75}Ni_{0.25}Ge_2O_6}$	7		$CaCO_3$,NiO,MnO,GeO_2	1100°C,100h	$CaGeO_3$	
$\mathbf{CaCo_{0.25}Ni_{0.75}Ge_2O_6}$	-		$CaCO_3$,Co_3O_4,NiO_2,GeO_2	1100°C,100h	Ni_2GeO_4	
$\mathbf{CaCo_{0.5}Ni_{0.5}Ge_2O_6}$	7		$CaCO_3$,Co_3O_4,NiO_2,GeO_2	1100°C,100h	Ni_2GeO_4	
$\mathbf{CaCo_{0.75}Ni_{0.25}Ge_2O_6}$	-		$CaCO_3$,Co_3O_4,NiO_2,GeO_2	1100°C,100h	Ni_2GeO_4	
$\mathbf{SrCoGe_2O_6}$	8	R	$SrCO_3$,Co_3O_4,GeO_2+Regrinding	1100°C,100h+100h	$Sr_3CoGe_5O_{14}$(0.98%)	
$\mathbf{SrMnGe_2O_6}$	9	1	$SrCO_3$,MnO_2,GeO_2	1170°C,100h	Unknown phase(tiny)	T_{melt}=1200°C
		2	$SrCO_3$,MnO_2,GeO_2	1200°C,100h	Unknown phase(tiny)	Single crystal

recently been synthesized in evacuated tube using solid state reaction.[1]

As Cu^{2+}-bearing compounds can exhibit strong quantum effect, we have tried to prepare $CaCuSi_2O_6$, a counterpart of pyroxene $CaCuGe_2O_6$. Neither solid state reaction (see table 3.2)nor soft chemistry (see soft chemistry section, 3.4) can produce compound with pyroxene structure.

However, a new family of Sr-based pyroxene compounds was prepared. As shown in table 3.1, polycrystalline $SrMnGe_2O_6$ was prepared at 1170°C with long duration time, and with suitable conditions (T>1200), single crystal of $SrMnGe_2O_6$ could be synthesized. Single phase of polycrystalline $SrCoGe_2O_6$ was prepared at 1100°C with intermediate grinding. The single crystal determination of $SrMnGe_2O_6$ and ab initio determination from powder diffraction of $SrCoGe_2O_6$ reveal that both of them crystallize into monoclinic unit cell with space group C2/c. This finding enriched the family of pyroxenes, and may bring in new interests on structural chemistry and physical properties, and the respecting work on these compound will be given in chapter 8 and 9, respectively. To have a systematic study of this new family, some efforts have been taken on synthesizing other Sr-based pyroxenes containing transition metal cations such as Fe^{2+},Ni^{2+},Cu^{2+},Zn^{2+}. As shown in table 3.2, no targeted pyroxene compound can be prepared.

In summary, table 3.1 reflects that heating over several days and intermediate grindings are necessary to obtain a single phase sample. The reaction temperatures are in the range of 1000-1200°C. Some important characters of sample, which are useful information on single crystal growth, are listed in the "note" column such as melting point.

Table 3.2: Summary for attempts of synthesizing new compounds using solid state reaction.

Compound	Label	Starting materials	Conditions	Results(impurity)
$CaMn_{0.5}Fe_{0.5}Ge_2O_6$	1	$CaCO_3$,Fe_2O_3,MnO_2,GeO_2	1100°C,100h	$Ca_3Fe_2Ge_3O_{12}$, $Ca_2Ge_7O_{16}$ $Ca_3Mn_2Ge_3O_{12}$
	R1	$CaCO_3$,Fe_2O_3,MnO_2,GeO_2	1200°C,50h	melted
	2	$CaCO_3$,Fe_2O_3,MnO_2,GeO_2	1000°C,20h	$Ca_3Fe_2Ge_3O_{12}$ $Ca_2Ge_7O_{16}$ $Ca_3Mn_2Ge_3O_{12}$ GeO_2,$CaGeO_3$
$CaMn_{0.9}Fe_{0.1}Ge_2O_6$		$CaCO_3$,Fe_2O_3,MnO_2,GeO_2	1100°C,100h	$CaMnGe_2O_6$,$Ca_3Mn/Fe_2Ge_3O_{12}$
$CaCuSi_2O_6$	1	$CaCO_3$,CuO,SiO_2	1000°C, 20h	$CaSiO_3$, SiO_2,CuO
	2	$CaCO_3$,CuO,SiO_2	1000°C, 40h	$CaSiO_3$, SiO_2,CuO
$CuCoSi_2O_6$		CuO,Co_3O_4,SiO_2	1000°C,20h	Co_2SiO_4,SiO_2,
$CuCoGe_2O_6$		CuO,Co_3O_4,GeO_2	1000°C,50h	$CuGeO_3$,$CoGeO_3$
$SrCuGe_2O_6$	1	$SrCO_3$,CuO,GeO_2	1100°C,100h	$CuSr_3Ge_5O_{14}$,metled
	2	$SrCO_3$,CuO,GeO_2	1000°C,50h	$CuSr_3Ge_5O_{14}$,partial metled
	3	$SrCO_3$,CuO,GeO_2	950°C,50h	$CuSr_3Ge_5O_{14}$,$SrGeO_3$, $SrGe_4O_9$,$CuGeO_3$
$SrFeGe_2O_6$		$SrCO_3$,Fe_2O_3,GeO_2	1100°C,100h	$Sr_3Fe_2Ge_4O_{14}$,$SrGe_4O_9$,Fe_2O_3
$SrNiGe_2O_6$	1	$SrCO_3$,NiO,GeO_2	1150°C,100h	$NiSr_3Ge_5O_{14}$,Ni_2GeO_4,$SrGeO_3$
	2	$SrCO_3$,NiO,GeO_2	1250°C,40h	$NiSr_3Ge_5O_{14}$,N_2GeO_4,$SrGeO_3$
	3	$SrCO_3$,NiO,GeO_2	1000°C,40h	$NiSr_3Ge_5O_{14}$,N_2GeO_4,$SrGeO_3$
$SrZnGe_2O_6$	1	$SrCO_3$,ZnO,GeO_2	1150°C,100h	$Sr_3ZnGe_2O_7$,$Sr_3ZnGe_5O_{14}$,Zn_2GeO_4,$SrGe_4O_9$
	2	$SrCO_3$,ZnO,GeO_2	1050°C,50h	$Sr_2ZnGe_2O_7$,$Sr_3ZnGe_5O_{14}$,Zn_2GeO_4,$SrGe_4O_9$

3.2 High pressure high temperature method(HPHT)

We have carried out the high pressure and high temperature synthesis for some of pyroxenes compounds. As a counterpart of $CaMnGe_2O_6$, $CaMnSi_2O_6$ has been found to crystallize into space group C2/c based on theHPHT synthetic sample.[2] But its magnetic properties are still unknown. We thus synthesized this silicate pyroxene by high pressure high temperature method. Take the synthesis of $CaMnSi_2O_6$ as an example, we show the program of HPHT procedure using Conac setup which could produce big volume of powder aiming to neutron diffraction. First , pressure is slowly applied until 5GPa (equivalent to 900T)is reached with a typical increment rate of 7T/min. After reaching the target pressure, the heating process with a rate of 25W/min is automatically followed by the control of program. After heating 3 hours at 1200°C (∼1180W), the system is quenched by turning off the energy power of heating. The process of release pressure should be as slow as possible, especially at high pressure, in order to prevent blowout. For Conac, a decreaing rate of 7t/min was used.

$NaMnGe_2O_6$ has been found to exhibit cooperative Jahn-Teller distortion and spin flip transition.[3] It adopts an up-up-down-down spin configuration which may be the origin of multiferroic properties. Therefore, we carried out the synthesis of $NaMnGe_2O_6$. In addition, the synthesis and crystal structure of analogous compound $NaMnSi_2O_6$ has been investigated[4]. To study its magnetic properties and compare its crystal structure to germanate pyroxene, the synthesis of $NaMnSi_2O_6$ has been performed.

Analogous to $NaMnGe_2O_6$, stoichiometric $LiMnGe_2O_6$ was expected to be a new pyroxene and show interesting physical properties due to the Jahn-Teller active cation Mn^{3+}. By high pressure high temperature synthesis, we did not obtain any new pyroxene compound, instead, new phases were observed within the sample by x-ray diffraction. In system of stoichiometric $LiMnGe_2O_6$, different synthesis conditions can suppress one phase while favor other phase, as listed in table 3.3. By this control, we found a new quasi-monoclinic phase with super unit cell by TEM technique. All the relevant determination work is currently in progress.

The attempts for synthesizing $SrMGe_2O_6$ (M=Fe^{2+},Ni^{2+},Cu^{2+})with high pressure method reveal that neither solid state reaction nor high pressure can produce the pyroxene phase, as listed in table 3.3. However, some unknown phases have been observed in the samples from high pressure synthesis. With the strength of electron diffraction of TEM, some new phases could be identified or solved. This work is a collaboration with Dr. Holger Klein from TEM team at Institut Neel. For example, in the high pressured synthesized sample with stoichiometric $SrCuGe_2O_6$, a rich phase with tentative chemical composition $Sr_5CuGe_8O_x$ (determined by EDX) can be indexed with a super monoclinic unit cell.

3.3 Soft chemistry method

As discussed in chapter 1, copper containing pyroxenes are of great interest due to the spin$\frac{1}{2}$ of Cu^{2+} cations which could lead to strong quantum effects. As a new compound containing Cu^{2+}, $CuMgSi_2O_6$ compound may bring some new physical properties. The most important

Table 3.3: Summary of compounds synthesized using high pressure and high temperature method. Red: failed.

Compound	Label	Starting materials	Conditions	Results	Note
$CaMnSi_2O_6$	hp1	CaO,MnO,SiO_2	1200°C,5GPa,5h	Ca/$MnCO_3$	Belt
	hp2	CaO,MnO,SiO_2	1200°C,5GPa,3h	Ca/$MnCO_3$	Conac
	hp2_1	CaO,MnO,SiO_2	1200°C,5GPa,3h	Ca/$MnCO_3$	Conac
$NaMnGe_2O_6$	hp1	Precursor: $NaCO_3$, GeO_2, MnO_2	800°C,24h 850°C,3GPa,1.5h	$NaMnGe_2O_6$,$Na_2Ge_4O_9$	Belt
	hp2	Precursor	950°C,3GPa,1.5h	$NaMnGe_2O_6$,$Na_2Ge_4O_9$,GeO_2	Belt
	hp3	Precursor	800°C,3GPa,1.5h	$NaMnGe_2O_6$,$Na_2Ge_4O_9$,GeO_2	Belt
$NaMnSi_2O_6$in progress	hp1	Na_2SiO_3+Mn_2O_3+SiO_2	1200°C, 6GPa, 1h	Unknown phases	Belt
$LiMnGe_2O_6$	hp1	Precursor: $LiCO_3$, $GeO2_2$, MnO_2	800°C,24h 850°C,3GPa,1h	GeO_2, Unknown phases:Cubic1(strong)+x	Belt
	hp1_1	Precursor	700°C,3GPa,1h	GeO_2, Mn_2O_3, Unknown phases:Cubic2+x	Belt
	hp1_2	Precursor	950°C,3GPa,1h	Unknown phase	Belt
	hp1_3	Precursor	1000°C,3GPa	GeO_2, Unknown phase(Cubic1)	Belt
$CuMgSi_2O_6$	hp	CuO,MgO,SiO_2	1100°C,4GPa,1h	$Mg(Mg_{0.56}Cu_{0.44})Si_2O_6$, SiO_2,Cu_2O	Belt
$SrFeGe_2O_6$	hp1	SrO,Fe_2O_3,GeO_2	940°C,5GPa,0.5h	$Sr_3Fe_2Ge_4O_{14}$+Unknown phase 1	Glove box
	hp2	SrO,FeO,GeO_2	940°C,5GPa,0.5h	Fe_2GeO_4,$Sr_3FeGe_5O_{14}$,GeO_2+Unknown phase 2	Glove box
	hp2_1	SrO,FeO,GeO_2	800°C,5GPa,0.5h	Fe_2GeO_4,$Sr_3FeGe_5O_{14}$,GeO_2+Unknown phase 2	Glove box
$SrCuGe_2O_6$	hp	SrO,CuO,GeO_2	900°C,4GPa,2h	Unknown phase(strong),CuO,Cu_2GeO4_4	Glove box
$SrNiGe_2O_6$	hp	SrO,NiO,GeO_2	900°C,4GPa,2h	$Sr_3NiGe_5O_{14}$,Ni_2GeO_4.	Glove box

results obtained from soft chemistry method is the successful synthesis of a clinopyroxene compound $CuMgSi_2O_6$, even the high pressure can not favor the formation of this monoclinic phase, as seen in table 3.3. Within chapter 4, we will address the effort in synthesizing $CuMgSi_2O_6$ compound using solid state reaction and sol-gel processing in detail. Table 1 in chapter 4 reflects that the immensely effective way to get $CuMgSi_2O_6$ is soft chemistry, which enables us to realize more Cu composition in $CuMgSi_2O_6$. From the viewpoint of magnetism, we expect the synthesis of derivations from $CuMgSi_2O_6$ by replacing the Mg site with transition metal cations such as Co^{2+} and Ni^{2+}. However, all attempts for this idea were failed(table 3.4 and table 3.2). The attempts of synthesizing other Cu-bearing pyroxene $CaCuSi_2O_6$ with soft chemistry always yield $CaCuSi_4O_{10}$.

Table 3.4: Summary of trials for synthesis of pyroxene compounds by soft chemistry method.

Compound	Label	Starting materials	Conditions	Results
$CoMgSi_2O_6$	cd1	Mg acetate, Co acetate, TEOS	1000°C,10h	CoO, MgO
$CuCoSi_2O_6$	cd1	Cu acetate, Co acetate, TEOS	1000°C,10h	Co_2SiO_4,SiO_2,unknown phase
	cd2	Cu acetate, Co acetate, TEOS	1100°C,20h	Co_2SiO_4,SiO_2,CuO,unknown phase
	cd3	Cu nitrate , Co nitrate, TEOS	1200°C,20h	Co_2SiO_4,SiO_2,CuO
$CuNiSi_2O_6$	cd1	Cu acetate, Ni acetate, TEOS	1000°C,10h	Ni_2SiO_4,SiO_2,CuO, unknown phase
	cd2	Cu acetate, Ni acetate, TEOS	800°C,20h	CuO,SiO_2,NiO
$CaCuSi_2O_6$	cd1	Cu acetate, Ca nitrate, TEOS	1000°C, 10h	$CaCuSi_4O_{10}$,CuO,$CaSiO_3$
	cd2_1	Cu acetate, Ca acetate, TEOS	800°C,30h	$CaCuSi_4O_{10}$, CuO,$SiO2_2$
	cd2_2	Cu acetate, Ca acetate, TEOS	1100°C,30h	$CaCuSi_4O_{10}$, CuO,SiO_2

3.4 Single crystal growth

In previous chapter, we discussed the principles of crystal growth from two kind of molten solutions. One of them is congruent, in fact, $CaCuGe_2O_6$ and $SrMnGe_2O_6$ compounds are belonging to this category. Therefore, we have started the growth of single crystal from their powder samples using floating zone method.

On the other hand, $CaMnGe_2O_6$ decomposed into other compounds at around 1250°C, so flux method should be an appropriate way. We have tried with self flux method in which $CaCl_2$ and Bi_2O_3 was respectively taken as flux. Both these ways give single crystal $Ca_3Mn_2Ge_3O_{12}$(dark brown) and $CaGe_2O_4$(green). The flux method for which MoO_3 was taken as flux yielded $CaGe_2O_4$ single crystal. The experiments are still in progress on single crystal growth. This work is in collaboration with researchers of Pole Cristaux Massifs at Institut Neel.

Bibliography

[1] G.J. Redhammer, G. Roth, A. Senyshyn, G. Tippelt, C. Pietzonka, Crystal and magnetic spin structure of Germanium-Hedenbergite, $CaFeGe_2O_6$, and a comparison with other magnetic/magnetoelectric/multiferroic pyroxenes, Z.Kristallogr., 228, 2013, 140. 85

[2] F. Nestola, T. B. Ballaran, R.J. Angel, J. Zhao, H. Ohashi, High pressure behavior of Ca/Na clinopyroxenes: The effect of divalent and trivalent 3d-transition elements, Am. Mineral., 95, 2010, 832. 86

[3] Jinguang Cheng, Wei Tian, Jianshi Zhou, Vincent M. Lynch, Hugo Steinfink, Arumugam Manthiram, Andrew F. May, et al., Crystal and Magnetic Structures and Physical Properties of a New Pyroxene $NaMnGe_2O_6$ Synthesized under High Pressure, J. Am. Chem. Soc.,135, 2013, 2776. 86

[4] H.Ohashi, T. Osawa, K. Tsukimura, Refinement of the structure of manganese sodium dimetasilicate, Acta Cryst., C43, 1987, 605-607.

86

Chapter 4

A copper-bearing silicate with the low clinopyroxene structure

4.1 Introduction

With respect to chemical structure, the pyroxene containing Jahn-Teller (JT) cations have been subject to particular attention. The difficulty to accommodate the corresponding polyhedral distortions may play a role in the ability of pyroxenes to contain large amounts of JT cations. In addition, pyroxenes containing magnetic cations have recently attracted great interest from a viewpoint of physical properties because of the investigations of multiferroic properties[8, 9], magnetoelectric effect[12][11], and quasi-one-dimensional (Q1D) magnetic behavior[21]. These physical properties ascribe from their unique crystal structure. The competition between inter- and intra-chain magnetic interactions leads to magnetic frustration and the appearance of various exotic magnetic properties such as spin singlet ground state[17] and spin-Peierls transition [7], as we have appreciated in the opening chapter. In that regard, copper containing pyroxenes are of foremost interest due to the spin$\frac{1}{2}$ of Cu^{2+} cations which could lead to enhanced quantum effects. According to previous investigations, the magnetic configuration in pyroxene compounds can be changed via chemical substitution on the M1 and/or M2 site. In the case of $CaCuGe_2O_6$ the behavior of magnetization was interpreted as due to a spin-singlet ground state [17]. Ab initio calculations indicated that this behavior derives from the intra-chain interactions of Cu^{2+} dimers[21]. Since the magnetic properties are strongly influenced by interatomic distances in this family of materials, it is tempting to look for compounds where Ge cations are substituted for smaller Si cations. To our knowledge, $CaCuSi_2O_6$ preparation was never reported and despite many attempts, we were unable to synthesize it. For the larger Ba cation, the $BaCuSi_2O_6$ compound adopts the Han purple crystal structure [6, 18]. Attempts to synthesize $MgCuSi_2O_6$ by original soft chemistry methods lead to the preparation of a compound with composition close to $CuMgSi_2O_6$. The existence of the $CuMgSi_2O_6$ pyroxene was reported by Breuer et al.[3], but only the cell parameters and tentative space group were given. In fact, the only other Cu-bearing pyroxene silicate compound for which a complete structure analysis was reported is the orthopyroxene $(Cu_{0.44}Mg_{1.56})Si_2O_6$ compound[19] with

space group Pbca. It is important to notice that at variance from the $CaCuGe_2O_6$ compound, here the Cu^{2+} cations occupies the M2 site, which may have considerable impact on the physical properties. In this chapter, we report the synthesis based on the preparation of a precursor by a soft chemistry method and detailed structural analysis of the $Cu_{0.8}Mg_{1.2}Si_2O_6$ compound, which can bring valuable insight into the role of the Jahn-Teller effect in the metal site selectivity, structure distortion and chemical composition in pyroxene compounds[4].

4.2 Experimental

4.2.1 Sample preparation and characterization

Copper acetate $Cu(C_2H_3O_2)_2.H_2O$, magnesium acetate $Mg(C_2H_3O_2)_2.4H_2O$, and tetraethoxysilane (TEOS: $C_8H_{20}O_4Si$, 99.9%) were dissolved in ethanol with vigorous stirring at 110°C for 3h. The solution was dried at 60°C for several hours in order to remove the solvents before further thermal treatment. The resulting precursor was calcined at temperature between 800°C and 1000°C with various sintering durations (between 10-50h, with intermediate regrinding) in air. This temperature range was chosen in order to avoid reduction of Cu^{2+} to Cu^{1+}, known to occur at about 1020°C in air. A Thermogravimetric and Differential Scanning Calorimetry (TG-DSC) analysis was carried out by using a Netzsch Thermal Analysis System to investigate the behavior of the precursor with temperature. The TG-DSC curves were recorded on ~20.9 mg of precursor powder placed in an alumina crucible, by warming and cooling at a rate of 10°C/min between RT and 800°C. A mixed atmosphere (Ar 80% and O_2 20%) was used. Morphology and chemical composition were investigated by field-emission scanning electron microscopy (FESEM, Zeiss Ultraplus) equipped with an energy-dispersive x-ray spectrometer (EDX, Bruker). The sample was gold-coated prior to SEM and EDX analysis. The zero field cooling (ZFC) and field cooling (FC) temperature dependence of magnetic susceptibility for $Cu_{0.8}Mg_{1.2}Si_2O_6$ was measured between 5 K and 350 K on a commercial superconducting quantum interference device (SQUID) magnetometer (Quantum Design, MPMS-XL).

4.2.2 X-ray powder diffraction

All samples were characterized using x-ray powder diffraction data collected with a Siemens D5000 diffractometer in transmission geometry, using a focusing Ge(111) monochromator for CuKα1 radiation and a linear PSD. For structure solution and refinement, a diffraction pattern was collected on the best sample obtained in terms of purity and crystallinity (sample No.6, bold in table 4.1). The measurement was carried out at room temperature in the 10°–90° 2ϑ range with a step of 0.032°. The Fox program[5], was used to index the pattern, determine the most probable space group and provide a starting model for structure refinement, which was carried out by the Rietveld method using the Fullprof program[15]. The background was described by linear interpolation of selected points in the pattern. A Thomson-Cox-Hastings model[20] of the reflection profile including anisotropic peak broadening was used. The size broadening effect was described using a uniaxial model with b as unique axis, while a tensorial

Table 4.1: Summary of synthesis conditions and resulting sample composition and pyroxene phase stoichiometry for $CuMgSi_2O_6$.

No.	Starting materials	Calcination Con.	Title (wt%)	SiO_2(wt%)	CuO(wt%)	Cu	Mg
1	Cu acetate,TEOS Mg acetate	1000°C, 10h	95.09(1.95)	1.48(0.19)	3.44(0.13)	0.79(2)	1.21(2)
2	Cu acetate, TEOS Mg acetate	1000°C, 40h	93.91(1.47)	1.84(0.20)	4.25(0.15)	0.80(2)	1.20(2)
3	Cu acetate, TEOS Mg acetate(excess 3 mol%)	1000°C, 10h	91.10(1.35)	1.12(0.19)	7.78(0.15)	0.79(2)	1.21(2)
4	Cu acetate, TEOS Mg acetate(excess 6 mol%)	1000°C, 10h	93.86(0.73)	4.11(0.07)	2.04(0.05)	0.81(1)	1.19(1)
5	Cu acetate, TEOS Mg acetate(excess 6 mol%)	1000°C, 50h regrinding	95.94(0.61)	3.72(0.08)	0.34(0.04)	0.81(1)	1.19(1)
6	**Cu acetate, TEOS Mg acetate(excess 6 mol%)**	**1000°C, 10h**	**98.89(0.06)**	**<0.5 (excluded)**	**1.11(0.06)**	**0.79(1)**	**1.21(1)**
7	Cu acetate, TEOS Mg acetate(excess 10 mol%)	1000°C, 10h	94.81(1.41)	2.91(0.21)	2.28(0.12)	0.86(2)	1.14(2)
8	Cu acetate, TEOS Mg acetate(excess 20 mol%)	1000°C, 10h	79.81(1.00)	9.06(0.36)	11.12(0.14)	0.77(1)	1.23(1)

description was applied for strain. Low angle peak asymmetry was taken into account using the Bérar-Baldinozzi model[2]. In order to reduce the number of structural parameters, atoms of the same element were given equal isotropic displacement parameters. For the two metal sites, the composition was refined assuming possible substitution between Cu and Mg with full total site occupancies. The global Cu/Mg stoichiometry was left unconstrained. A small amount of CuO and probably SiO_2 were detected as impurities; only CuO was introduced in the pattern description and its cell parameters and scale factor were refined. The final refinement yielded a weight fraction of 1.11(6)% for this phase. A single weak reflection tentatively attributed to SiO_2 at 21.9° was excluded from the pattern.

4.3 Results and discussion

4.3.1 Synthesis and characterization

Pyroxene compounds are classically prepared using solid state reaction techniques at elevated temperatures, and sometimes high pressure conditions. Single crystals may also be obtained using flux growth methods, as for example reported By [19] for Cu-bearing orthopyroxene $Cu_{0.44}Mg_{1.56}Si_2O_6$. In this case, the amount of copper introduced in the pyroxene framework remained rather limited. In our work, many efforts to synthesize the $CuMgSi_2O_6$ compound have been made via a traditional solid state reaction with intermediate grindings according to Breuer et al. [3], however, they systematically resulted in mixtures of CuO, MgO, SiO_2, Mg_2SiO_4, and clinopyroxene phases. The amount of impurity phases precluded an accurate physical and structural analysis of the samples. Therefore, we decided to investigate a soft

chemistry route for the preparation of precursor. The best results were obtained with the method described above in the Experimental section. Typical yields depending on preparation conditions are summarized in table 4.1. All samples were submitted to Rietveld refinement of x-ray powder diffraction data to determine the proportion of impurity phases as well as the pyroxene phase stoichiometry. The obtained samples contained the clinopyroxene compound as major phase, plus impurities (SiO_2, CuO) mainly depending on the starting composition of the solution. It is worth noting that the amounts of impurity phases are systematically much less than in the case of standard solid state reaction. In order to obtain an almost single phase clinopyroxene sample, it was necessary to use a 6 molar percent excess of magnesium acetate. An annealing time of 10h at 1000°C was generally used. Longer annealing times, including intermediate regrinding, lead to a small decrease of the proportion of impurity phases but did not modify the pyroxene phase Cu/Mg content (compare for example samples 4 and 5 in table 4.1). In fact, this composition was essentially independent from the synthesis conditions. Moreover, no significant improvement in sample crystallinity as seen from Bragg peak widths and shapes could be detected for longer annealing times. This seems to indicate that a stoichiometric $CuMgSi_2O_6$ compound cannot be prepared under these synthesis conditions. The sample No. 6 in table 4.1 was selected for the detailed structural analysis reported below.

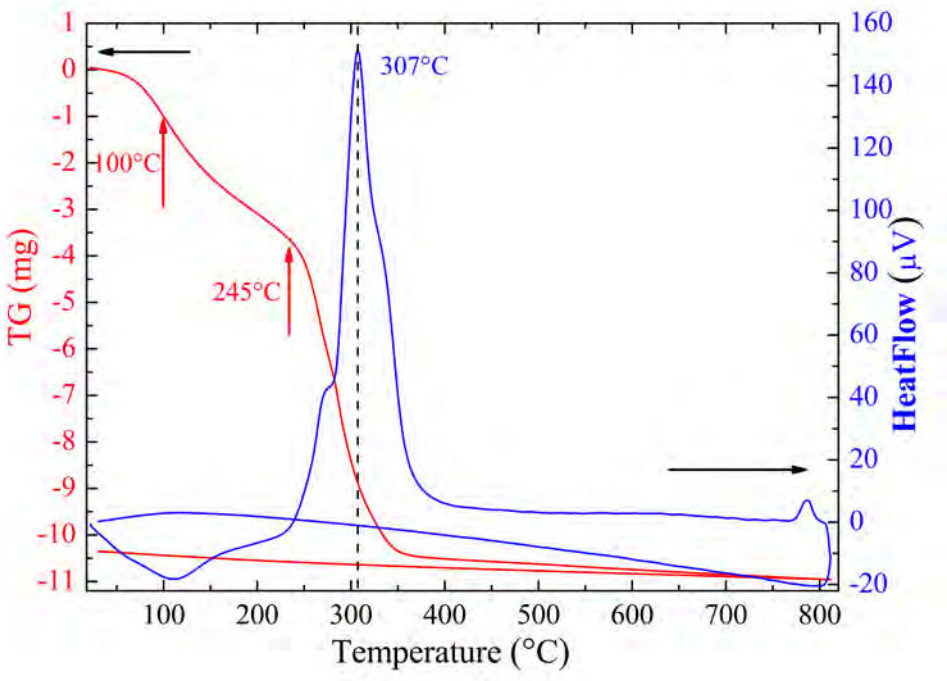

Figure 4.1: TG-DSC curves for the $CuMgSi_2O_6$ precursor.

As shown in figure 4.1, a weak endothermal peak is observed in the DSC curve around 100°C which probably corresponds to the evaporation of water and other remaining solvents. A corresponding small mass decrease upon heating is also detected in the TG curve at a similar temperature. Moreover, a strong exothermal peak is observed at 307°C in the DSC curve, which can be attributed to the decomposition of organic species from the precursor. This is

confirmed by the strong decrease of mass in the TG curve observed in the same temperature range. No marked mass change is then observed up to 800°C, indicating the full decomposition of these species. A small exothermal peak is observed on the DSC curve just below 800°C. Since no other feature is observed, it can be attributed to the formation reaction of the pyroxene phase.

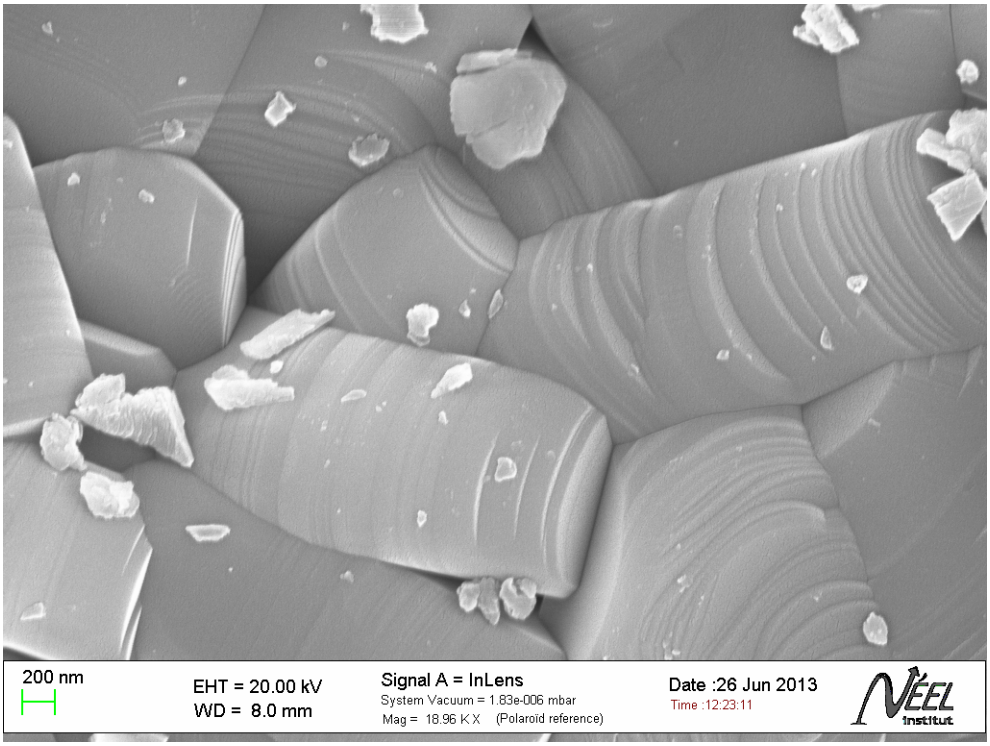

Figure 4.2: SEM image for the $Cu_{0.8}Mg_{1.2}Si_2O_6$ compound.

The SEM observations show that the sample is composed of crystalline grains with a roughly cylindrical shape of diameter up to ~1µm, as shown in figure 4.2. Prominent circular stripes are observed on the surface of each grain at higher magnification, suggesting that the cylinder axis is the preferred growth direction. The Cu/Mg ratio obtained using EDX by averaging the compositions from 12 different points was 0.8(1).

4.3.2 Structural study

The refinement results, main interatomic distances and bond valence sums calculated using the BonStr program[16] are presented in tables 4.2 and 4.3. The final Rietveld refinement plot is shown in figure 4.3. Some information about the structure of $CuMgSi_2O_6$ has been previously reported by Breuer et al.[3], although a full structural analysis was not performed. The authors proposed that $CuMgSi_2O_6$ crystallizes with monoclinic $P2_1/c$ symmetry and unit cell parameters a=9.731Å, b=8.918Å, c=5.224Å, β=110.52°. The results of our ab initio structure determination and Rietveld refinement are in good agreement with the unit cell and symmetry previously proposed, with a=9.7352(1)Å, b=8.90198(8)Å, c=5.22676(6)Å and

β=110.721(1)°, V=423.662(7) Å^3 , with space group P2$_1$/c. The structure is shown in figure 4.4.

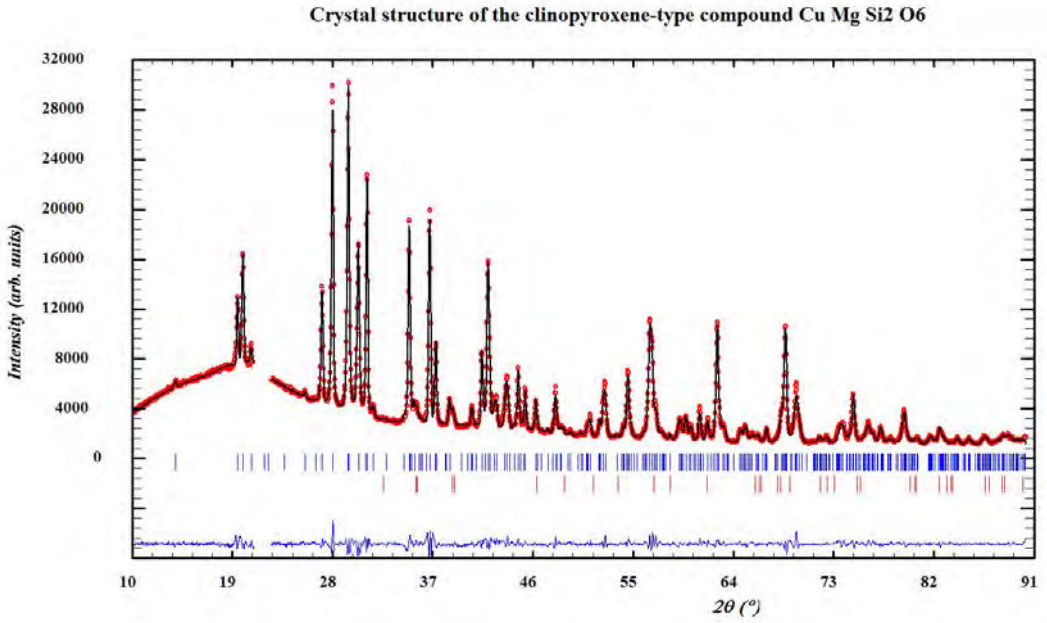

Figure 4.3: Rietveld plot for the refinement of $Cu_{0.8}Mg_{1.2}Si_2O_6$ from PXRD data.

Table 4.2: Agreement factors and refined structural parameters for $Cu_{0.8}Mg_{1.2}Si_2O_6$.

Name	pos.	x	y	z	B (Å2)	occupancy
SiA	4e	0.0496(7)	0.3388(8)	0.2926(11)	1.63(8)	1.0
SiB	4e	0.5497(7)	0.8368(8)	0.2571(11)	1.63(8)	1.0
M1 Mg/Cu	4e	0.2504(10)	0.6506(5)	0.2266(14)	0.95(14)	0.930/0.070 (7)
M2 Cu/Mg	4e	0.2545(5)	0.0054(2)	0.2286(7)	1.26(8)	0.72/0.28 (1)
O1A	4e	0.8768(14)	0.3376(14)	0.176(2)	0.95(10)	1.0
O2A	4e	0.1256(11)	0.5040(12)	0.3416(18)	0.95(10)	1.0
O3A	4e	0.1062(10)	0.2740(9)	0.617(2)	0.95(10)	1.0
O1B	4e	0.3683(13)	0.8385(14)	0.1353(18)	0.95(10)	1.0
O2B	4e	0.6422(12)	0.9825(12)	0.4087(18)	0.95(10)	1.0
O3B	4e	0.6019(10)	0.7033(10)	0.496(2)	0.95(10)	1.0
Space Group: P2$_1$/c						
a=9.7352(1)Å, b=8.90197(8) Å, c=5.22676(6) Å, α=90°, β=110.721(1)°, γ=90°						
Rp: 2.92, Rwp: 4.07, Rexp: 1.60, Chi2: 6.46, RBragg: 3.02						

This compound belongs to the well-known family of low clinopyroxenes with space group P2$_1$/c for which all atoms are located in 4e general positions. This structure is characterized by the alternate stacking perpendicular to the a-axis of layers made of SiO_4 tetrahedra and layers made of MO_6 octahedra (M=Cu, Mg). Each tetrahedron in a layer shares two corners with two adjacent tetrahedra to form zigzag chains running along the c-axis direction (figure 4.5). The bases of the tetrahedra are roughly parallel to the (100) plane and all tetrahedra in a given chain point toward the same direction along the a-axis. Two consecutive chains

Table 4.3: Principal cation-anion distances (Å) for $Cu_{0.8}Mg_{1.2}Si_2O_6$.

SiA-O	Distance(Å)	SiB-O	Distance(Å)
SiA-O1A	1.57(1)	SiB-O1B	1.65(1)
SiA-O2A	1.63(1)	SiB-O3B	1.67(1)
SiA-O3A	1.69(1)	SiB-O3B	1.65(1)
SiA-O3A	1.58(1)	SiB-O2B	1.62(1)
Ave. Dist.	1.62	Ave. Dist.	1.65
BVS	4.10(7)	BVS	3.75(6)
M1-O	Distance(Å)	M2-O	Distance(Å)
M1-O1A	2.24(1)	M2-O1A	2.14(1)
M1-O1A	2.03(1)	M2-O2A	1.963(9)
M1-O2A	2.01(1)	M2-O3A	2.384(9)
M1-O1B	2.17(1)	M2-O1B	2.01(1)
M1-O1B	2.04(1)	M2-O2B	1.808(9)
M1-O2B	2.09(1)	M2-O3B	2.76(1)
Ave. Dist.	2.10	Ave. Dist.	2.18
BVS	Mg^{2+}: 2.06(3)/ Cu^{2+}: 1.98(3)	BVS	Cu^{2+}: 2.06(3)/ Mg^{2+}: 2.14(3)

along the b-axis have their tetrahedra pointing in opposite directions. All Si cations in a given layer are equivalent by symmetry; SiA and SiB layers alternate along the a-axis. The SiA tetrahedra are more distorted with a smaller average Si-O bond length of 1.62(1) Å (BVS=4.10(7)), while the SiB tetrahedra are more regular with a larger average bond length of 1.65(1) Å, resulting in a slight underbonding (BVS=3.75(6)). It is also worth noting that the degrees of extension of the tetrahedra chains, as characterized by the angle between three consecutive tetrahedra-linking oxygen anions along a chain, are quite different for the SiA (O3A-O3A-O3A=161.4(5)°) and the SiB chain (O3B-O3B-O3B=144.7(5)°). In the octahedral layer (figure 4.6), the so-called pyroxene M1 sites are almost entirely (93.0(7) %) occupied by Mg^{2+} cations. The $M1O_6$ octahedra share their O1A-O1B edges to form zigzag chains along the c-axis. They are only moderately distorted with distances ranging from 2.01(1) to 2.24(1) Å and an average bond length of 2.10(1) Å in good agreement with the Mg^{2+} ionic radius (0.72 Å)[1]. This distance is close to the one reported for mineral enstatite $MgSiO_3$ (2.084 (2) Å). The pyroxene M2 site is occupied mainly by Cu^{2+} cations (72(1) %) but also by Mg^{2+} cations (28(1) %). The overall stoichiometry as found by XRPD is then $Cu_{0.8}Mg_{1.2}Si_2O_6$ and the Cu/Mg stoichiometric ratio (0.65) is reasonably close to that found by EDX. Each M2 cation octahedron is connected by edge sharing to three consecutive M1 cation octahedra along one M1 zigzag chain. The M2 octahedra are not connected to each other, and the shortest M2-M2 distances are 5.245(4) Å across a M1 chain, 5.227(6) Å on the same side of a M1 chain and 5.079(4) Å for two M2 octahedra attached to two neighboring M1 chains. In contrast to the M1 site, the M2 octahedral site is strongly distorted with M2-O distances ranging between 1.808(9) and 2.76(1) Å. The four shorter bonds (1.808(9) to 2.14(1) Å) correspond to the O1A, O2A, O1B, and O2B anions shared with M1 octahedra. The remaining O3A and O3B

anions are shared between the M2 octahedra and the Si tetrahedra of the chains above (O3A to SiA, M2A-O3A=2.384(9) Å) and below (O3B to SiB, M2A-O3B=2.76(1) Å) the octahedra layer. This latter M2A-O3B distance corresponds only to negligible bond strength of 0.06 valence unit (v.u.), therefore the M2 cation can be considered as coordinated rather by a distorted square pyramid than by an octahedron of oxygen anions. Both tetrahedra chains connect the M2 octahedra of two consecutive M1-M2 octahedral chains. The SiA tetrahedra share one O2A-O3A edge with the M2 octahedra, while all other connections are made via corner-sharing. The SiB tetrahedra are only connected by corner-sharing, resulting in a less distorted geometry.

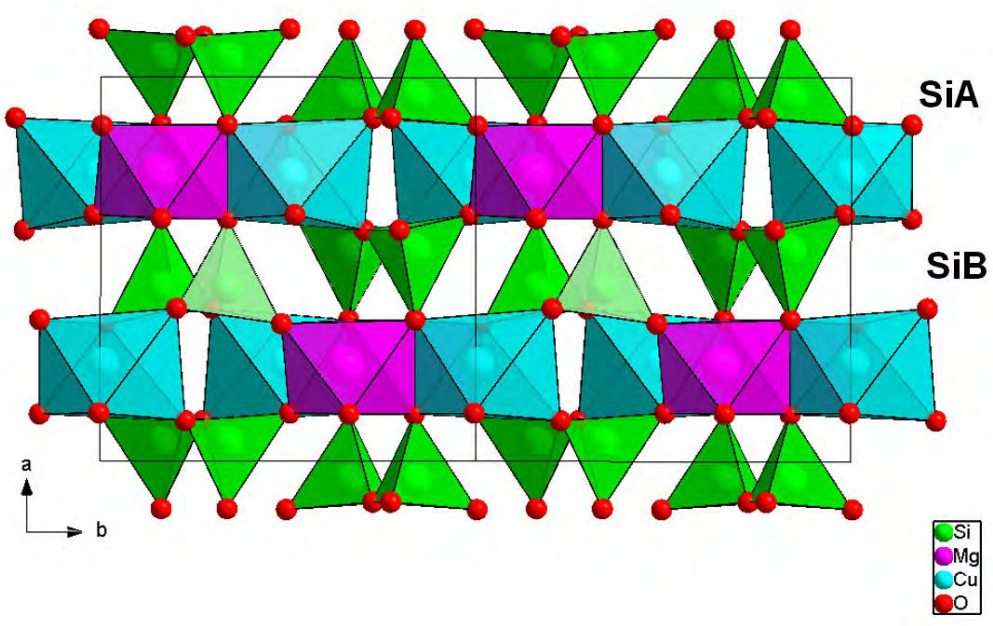

Figure 4.4: Projection of the $Cu_{0.8}Mg_{1.2}Si_2O_6$ structure along the **c**-axis.

4.3.3 Magnetic Properties

As shown in figure 4.7, the compound exhibits a paramagnetic behavior in the whole measured temperature range. No difference can be observed between the field-cooled and zero-field-cooled magnetization curves. The solid line in figure 4.7 represents the Curie fit using $\chi(T)=C/T+\chi_0$ in the temperature range 15-350 K, where C is the Curie constant and χ_0 a diamagnetic contribution. The fit yields C=0.413(2) and $\chi_0=2(3).10^{-5}$ emu/mol, giving an effective moment μ_{eff} =1.82 μ_B/Cu^{2+} which is very close to the expected spin-only value, $1.73\mu_B$. This is in strong contrast with the magnetic behavior observed for $CaCuGe_2O_6$ for which antiferromagnetic interactions and a spin-singlet ground state with a finite energy gap have been reported. However in the latter case, the Cu^{2+} cations occupy the M1 site of the pyroxene structure and are strongly interacting with first neighbor Cu-Cu distances of 3.072 Å [14], to be compared to distances above 5Å for Cu^{2+} cations on the M2 site for

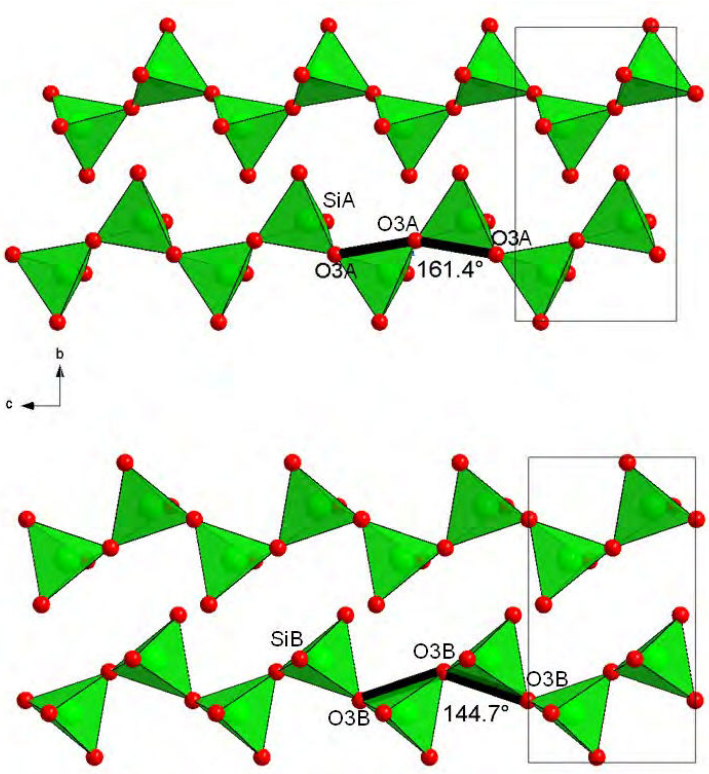

Figure 4.5: Projection of the SiA (top) and SiB (bottom) tetrahedra layers along the a-axis.

$Cu_{0.8}Mg_{1.2}Si_2O_6$. The absence of magnetic ordering observed for $Cu_{0.8}Mg_{1.2}Si_2O_6$ is thus directly related to the weakness of the magnetic interactions due to the structural arrangement.

4.4 Discussion

Although the pyroxene arrangement is known to accommodate a vast diversity of cations, the copper-bearing pyroxenes are quite rare. Indeed, $CaCuGe_2O_6$ is the only known stoichiometric compound with the pyroxene structure , Breuer et al.[3] also reported the study of the $(MgMg)Si_2O_6$ - $(CuCu)Si_2O_6$ system with a solid solution limit attributed to $CuMgSi_2O_6$. However, only cell parameters and a tentative $P2_1/c$ space group were provided. Later on, the preparation and structural study of the $Cu_{0.44}Mg_{1.56}Si_2O_6$ compound with the orthopyroxene structure (space group Pbca) were described [19]. Here we report the study of the low clinopyroxene compound (space group $P2_1/c$) with chemical composition $Cu_{0.8}Mg_{1.2}Si_2O_6$. It is worth noting that the samples obtained by Breuer et al. were prepared by reaction in air at 1000°C of an oxide mixture over very long reaction times (up to several weeks) and the orthopyroxene compound was obtained as a flux-grown single crystal at 850°C. Here, quasi single phase powder samples were obtained through the preparation of a precursor by a soft chemistry route followed by a 10h calcination step at 1000°C. This original process appears as very effective for the preparation of pyroxene-type oxides. Since Mg^{2+} and Cu^{2+} have almost the same ionic radius, the scarcity of Cu-bearing pyroxenes and the difficulty to substitute Mg

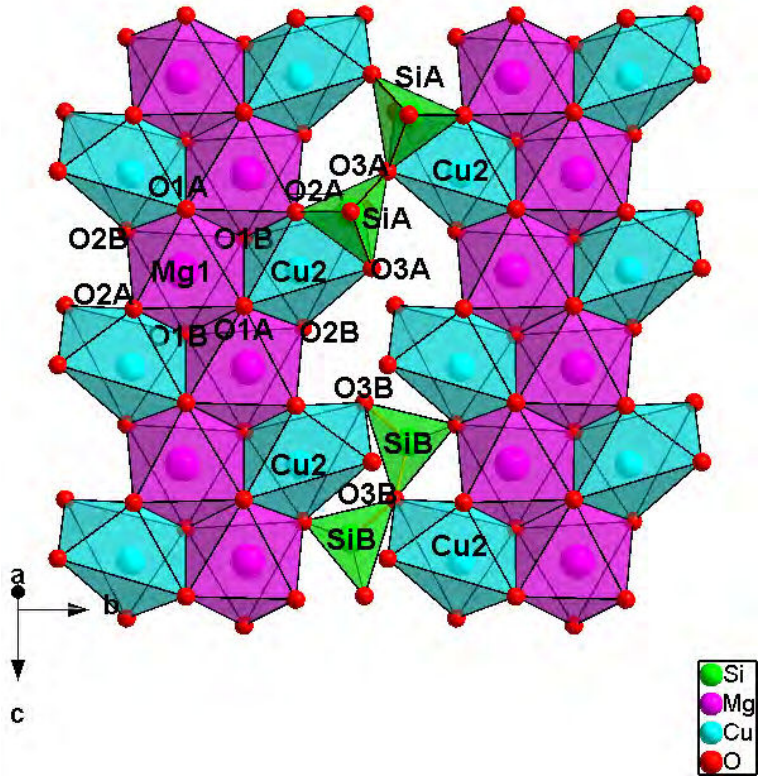

Figure 4.6: Structural arrangement of the M1, M2 octahedra layer of $Cu_{0.8}Mg_{1.2}Si_2O_6$. Some of the linking $SiAO_4$ and $SiBO_4$ tetrahedra have been represented also.

for Cu in enstatite $MgSiO_3$ cannot be attributed to steric effects only. The JT distortion of Cu^{2+} coordination polyhedra has to be invoked. The present compound therefore provides a unique opportunity to better understand the role of the JT effect in the crystallo-chemistry of pyroxenes by comparison with the structures of Cu-bearing orthopyroxene (Cu-OP)[19] and enstatites where Mg is partly replaced by other JT cations such as Cr^{2+} (Cr-CP) [1]. Enstatite being one of the most abundant minerals in the earth crust and upper mantle, such an insightful comparison can be of interest for geochemists to understand the mineral formation and composition from the earth magma in the presence of JT cations.

A first striking observation is the marked preference of JT cations for the M2 site in the case of pyroxene-type silicates. In the present work (Cu-CP), 7% of the M1 site were occupied by Cu^{2+}, 5.4% by Cr^{2+} in Cr-CP and full Mg occupancy was reported in Cu-OP. This strong site selectivity is very probably related to the topology of the pyroxene structure. The configuration of the M1 chains formed by edge-sharing octahedra is unfavorable for strongly distorted polyhedra. This well-known effect can already be observed in pyroxene without JT cations such as enstatite for which the M2 site is markedly distorted with Mg-O distances ranging between 1.985(1) to 2.414(1) Å compared to 2.006(2) to 2.179(1) Å for the M1 site

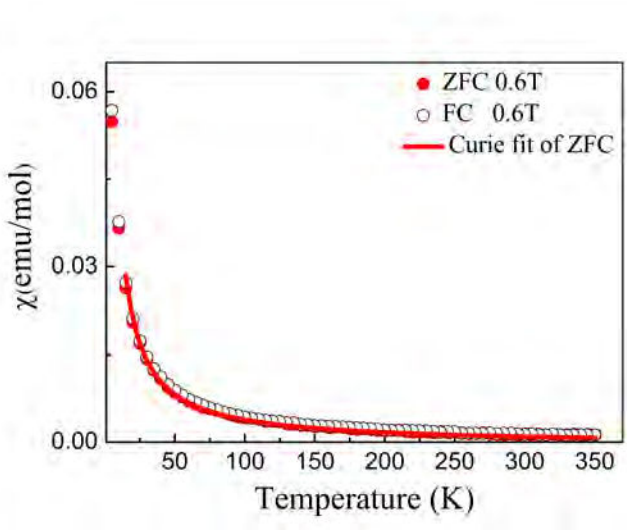

Figure 4.7: Temperature dependence of ZFC and FC magnetic susceptibility for $Cu_{0.8}Mg_{1.2}Si_2O_6$ under a 0.6 T magnetic field. The solid line represents the Curie-type fit to the data between 15 K and 350 K.

[13]. In this case the distortion is a consequence of the steric mismatch between the octahedra and tetrahedra chains which constitute the pyroxene structure. This preexisting distortion is very probably a major cause for the site preference of JT cations for site M2. Moreover, as pointed out by Tachi et al.[19], the presence of JT cations leads to an increase of the M2 site distortion. In order to quantify this effect, polyhedral distortion calculated by using the volume distortion parameter $\nu(\%)$ proposed by Makovicky and Balic-Zunic [10] and computed using the BondStr program have been reported on table 4.4 for the M2 site polyhedra of Cu-OP, Cu-CP, and Cr-CP and clinoenstatite (Mg-CP) [13], together with the M2-O bond lengths and their relative changes with respect to the Mg-CP average M2-O bond length. Both Cu-bearing pyroxenes show very similar average M2-O bond lengths, somewhat larger than that of Mg-CP which may be due to the slightly larger ionic radius of Cu^{2+} (0.73 Å) vs Mg^{2+}(0.72 Å). The distortion scheme of Mg-CP is clearly respected in Cu-OP and Cu-CP, in that the same bonds are elongated or shortened with respect to the average M2-O bond length in Mg-CP. The gradual replacement of Mg^{2+} by Cu^{2+} leads to a strong increase of the distortion from 50.10^{-4} to 158.10^{-4} to 206.10^{-4} while keeping the same scheme: short bonds become shorter and long bonds become longer. Moreover, the M2-O3A, -O2B and -O3B bonds which differ the most from the average are those which undergo the largest changes: from 2.279(1) to 2.384(9) Å for M2-O3A, 1.985(1) to 1.808(9) Å for M2-O2B and 2.414(1) to 2.76(1) Å for M2-O3B. Depending on the bonds, this effect may be quite non-linear with Cu content of the M2 site. For example, the longest distance M2-O3B changes very strongly from Mg-CP to Cu-OP, but only little from Cu-OP to Cu-CP (2.414(1) to 2.732(2) to 2.76(1) Å with a Cu content of 0 to 0.44 to 0.80). The first change indicates that O3B has to be considered as part of the M2 coordination for small Cu contents, since it is highly sensitive to the M2 site composition change. However, for larger Cu contents, the M2-O3B bond valence becomes

only about 0.05 v.u. so that O3B can hardly be considered as part of M2 coordination, as stated above. In that sense, the M2 coordination polyhedron of both Cu-bearing pyroxenes can rather be described as a distorted square pyramid and the O3B cation is probably little affected by further increase of the Cu content.

It must be noticed that this reasoning does not apply to the $CaCuGe_2O_6$ compound since Cu occupies the M1 site [14]. The M2 site occupied by larger 7-coordinated Ca^{2+} cations (ionic radius: 1.06 Å) now displays a quite small distortion (10. 10^{-4}) and a larger average distance of 2.474(1) Å. Clearly, due to its large ionic radius, Ca^{2+} can only be accommodated in the M2 site and Cu^{2+} has to go to M1. The M1-O average bond length is 2.116(1) Å and the octahedral distortion is 81.10^{-4}. The latter value is much larger than those observed for the M1 sites occupied by Mg^{2+} in Cu-bearing clinopyroxenes (15.10^{-4}) or clinoenstatite (8.10^{-4}). This additional distortion could result from the JT effect induced by the Cu^{2+} cations. Following our analysis of clinopyroxene silicates, it would tempting to propose that the driving force for the symmetry lowering between Cu-OP and Cu-CP can be the larger distortion brought about by the highest content of JT Cu^{2+} cation on the M2 site. At a first glance, this is supported by the fact that the Cr-CP compound containing 0.61 Cr^{2+} JT cations on the M2 site adopts the low clinopyroxene structure with $P2_1/c$ space group of. However, one can see in table 4.4 that the M2 site distortion for Cr-CP is much smaller than for Cu-OP (97.10^{-4} vs 158.10^{-4}), which could be related to the different d-orbital population of the Cr^{2+} and Cu^{2+} cations. The increasing distortion of the M2 site due to higher Cu^{2+} content may well be at the origin of the symmetry lowering in Cu-bearing pyroxene.

4.5 Conclusions

The structural investigation of the new $Cu_{0.8}Mg_{1.2}Si_2O_6$ clinopyroxene compound allows a comparative study of the effect of JT cation insertion in pyroxene compounds. It indicates that the marked preference of JT cations for the pyroxene M2 site is most probably related to its pre-existing distortion. The additional distortion brought about by the JT effect respects the pyroxene topology and enhances the M2 site distortion. It is tempting to extend this assumption to other chain silicates and further investigations are required to check whether it can be turned into a general rule. For physicists, the tendency of divalent JT cations to occupy the M2 sites with very weak magnetic interactions make such systems unsuitable for displaying striking magnetic properties. Our observations indicate that increasing the JT cation content leads to (and probably is the driving force for) symmetry lowering from ortho- to clinopyroxene. The extent to which such a strong site distortion can be accommodated by the pyroxene arrangement probably puts the limit to the maximum JT cation content even in the low symmetry phase.

Table 4.4: Comparison of M2-O distances (Å) for clinoenstatite, $Mg_{1.56}Cu_{0.44}Si_2O_6$ orthopyroxene, $Mg_{1.2}Cu_{0.8}Si_2O_6$ (this work), and $Mg_{1.425}Cr_{0.611}Si_{1.946}O_6$. The relative change (%) with respect to the enstatite average bond length is shown in the 3rd column. The average distance, polyhedral distortion and bond valence sum are also given.

$MgSiO_3$ $P2_1/c$ (Ohashi et al.)			$Mg_{1.56}$ $Cu_{0.44}Si_2O_6$ Pbca (Cu-OP) (Tachi et al.)			$Mg_{1.2}Cu_{0.8}Si_2O_6$ $P2_1/c$ (Cu-CP) (this work)			$Mg_{1.425}Cr_{0.611}Si_{1.946}O_6$ $P2_1/c$(Cr-CP) (Angel et al.)		
at1-at2	dist.	Change	at1-at2	dist.	Change	at1-at2	dist.	Change	at1-at2	dist.	Change
Mg2-O1A	2.090(1)	-2.43	Cu2-O1A	2.115(2)	-1.26	Cu2-O1A	2.14(1)	-0.09	Cr2-O1A	2.180(7)	1.77
Mg2-O2A	2.032(1)	-5.14	Cu2-O2A	1.970(2)	-8.03	Cu2-O2A	1.969(9)	-8.08	Cr2-O2A	2.035(5)	-5.00
Mg2-O3A	2.279(1)	6.40	Cu2-O3A	2.340(2)	9.24	Cu2-O3A	2.384(9)	11.30	Cr2-O3A	2.281(5)	6.49
Mg2-O1B	2.053(1)	-4.15	Cu2-O1B	2.048(2)	-4.39	Cu2-O1B	2.01(1)	-6.16	Cr2-O1B	2.092(6)	-2.33
Mg2-O2B	1.985(1)	-7.33	Cu2-O2B	1.934(2)	-9.71	Cu2-O2B	1.808(9)	-15.59	Cr2-O2B	2.008(5)	-6.26
Mg2-O3B	2.414(1)	12.70	Cu2-O3B	2.732(2)	27.54	Cu2-O3B	2.76(1)	28.85	Cr2-O3B	2.648(5)	23.62
Average distance: 2.1420(6)			Average distance: 2.190(1)			Average distance: 2.178(5)			Average distance: 2.207(2)		
Distortion: 50.815 xE-04			Distortion: 158.283 xE-04			Distortion: 206.013 xE-04			Distortion: 96.873 xE-04		
Valence Sum: 1.922(3)			Valence Sum: 1.859(5)			Valence Sum: 2.06(3)			Valence Sum: 2.00(1)		

Bibliography

[1] R.J. Angel, T. Gasparik, L. W. Finger, Crystal structure of a Cr^{2+}-bearing pyroxene, Am. Mineral., 74, 1989, 599-603. 97, 100

[2] J.F. Bérar and G. Baldinozzi, Modeling of line-shape asymmetry in powder diffraction, J. Appl. Cryst., 26, 1993, 128-129. 93

[3] K. H. Breuer, W. Eysel, M. Behruzi, Copper(II) silicates and germinates with chain structures, Z. Kristallogr., 176, 1986, 219-232. 91, 93, 95, 99

[4] 1. Lei Ding, Celine Darie, Claire Colin, Pierre Bordet, $Cu_{0.8}Mg_{1.2}Si_2O_6$-a copper-bearing silicate with the low clinopyroxene structure, Mineralogical Magazine, 2015 (In press). 92

[5] V. Favre-Nicolin and R. Cerny, FOX, 'free objects for crystallography': a modular approach to ab initio structure determination from powder diffraction, J. Appl. Cryst., 35, 2002, 734-743. 92

[6] L.W. Finger, R.M. Hazen, R.J. Hemley, $BaCuSi_2O_6$: a new cyclosilicate with four-membered tetrahedral rings, Am. Mineral., 74, 1989, 952-955. 91

[7] M. Isobe, E. Ninomiya, A.N. Vasilev, Y. Ueda, Novel phase transition in Spin-1/2 linear chain systems: $NaTiSi_2O_6$ and $LiTiSi_2O_6$, J. Phys. Soc. Jpn, 71, 2002, 1423-1426. 91

[8] S. Jodlauk, P. Becker, J.A. Mydosh, D.I. Khomskii, T. Lorenz, S.V. Streltsov, D.C. Hezel, L. Bohaty, Pyroxenes: a new class of multiferroics, J. Phys.: Condens. Matter, 19, 2007, 432201-9. 91

[9] I. Kim, G.G. Jeon, D. Patil, S. Patil, G. Nenert,K. H. Kin, Observation of multiferroic properties in pyroxene, J. Phys.: Condens. Matter, 24, 2012, 306001-7. 91

[10] E. Makovicky and T. Balic-Zunic, New Measure of Distortion for Coordination Polyhedra, Acta Cryst. B, B54, 1998, 766-773. 101

[11] G. Nenert, M. Isobe, I. Kim, C. Ritter, C.V. Colin, A.N. Vasiliev, K.H. Kim, Y. Ueda, Interplay between low dimensionality and magnetic frustration in the magnetoelectric pyroxenes $LiCrX_2O_6$ (X=Ge, Si). Phys. Rev. B, 82, 2010, 024429. 91

[12] G. Nenert, I. Kim, M. Isobe, C. Ritter, A.N. Vasiliev, K.H. Kim, Y. Ueda, Magnetic and magnetoelectric study of the pyroxene $NaCrSi_2O_6$, Phys. Rev. B, 81, 2010, 184408. 91

[13] Y. Ohashi and L.W. Finger, The effect of Ca substitution on the structure of clinoenstatite, Carnegie Institution of Washington: Yearbook, 75, 1976, 743-746. 101

[14] G.J. Redhammer, G. Tippelt, M. Merz, G. Roth, W. Treutmann, G. Amthauer, Structure of the clinopyroxene-type compound $CaCuGe_2O_6$ between 15 and 800 K, Acta Cryst. B, 61, 2005, 367-380. 98, 102

[15] J. Rodriguez-Carvajal, Recent Advances in Magnetic Structure Determination by Neutron Powder Diffraction. Physica B, 192, 1993, 55-69. 92

[16] J. Rodrıguez-Carvajal, BondStr, 2010, www.ill.eu/sites/fullprof/ 95

[17] Y. Sasago, M. Hase, K. Uchinokura, Discovery of a spin-singlet ground state with an energy gap in $CaCuGe_2O_6$. Phys. Rev. B, 52, 1995, 3533-3539. 91

[18] K.M. Sparta and G. Roth, Reinvestigation of the structure of $BaCuSi_2O_6$-evidence for a phase transition at high temperature. Acta Cryst. Sec. B Structural Science, B60, 2004, 491-495. 91

[19] T. Tachi, H. Horiuchi, H. Nagasawa, Structure of Cu-bearing orthopyroxene, $Mg(Cu_{0.56},Mg_{0.44})Si_2O_6$, and behavior of Cu^{2+} in the orthopyroxene structure, Phys. Chem. Minerals, 24, 1997, 463-476. 91, 93, 99, 100, 101

[20] P. Thompson, D.E. Cox, J.B. Hastings, Rietveld refinement of Debye-Scherrer synchrotron X-ray data from Al_2O_3, J. Appl. Cryst., 20, 1987, 79-83. 92

[21] R. Valenti, D.T. Saha, C. Gros, Nature of the spin-singlet ground state in $CaCuGe_2O_6$. Phys. Rev. B, 66, 2002, 054426.

91

Chapter 5

$CaMnGe_2O_6$: magnetoelectricity and one-dimensional short range magnetic correlations

5.1 Introduction

Multiferroics, which present simultaneous magnetic and electric long range order, have been attracting considerable research activity for their fundamental scientific interest and potential applications in technology such as four-state logic memory[1] and magnetoelectric random access memory (MERAM)[2]. In solids, the electric and magnetic ordering are often considered incompatible. The strong coupling of these degrees of freedom can be ascertained in magnetoelectric materials, that is, the cross coupling of magnetization and polarization, to their conjugate fields, E and H, which is known as magnetoelectric (ME) effect[3]. The cross coupling between the vectors is mediated by a second rank tensor. The linear ME effect was first experimentally verified on the antiferromagnetic Cr_2O_3 [4] after the theoretical prediction by Landau and Lifshitz[7]. They found that specific symmetry elements, spatial-reversal and time-inversion, must be broken for the tensor to be non-zero. Thus, by taking account of magnetic symmetry and the thermodynamic potential in one system, much information about ME effect can be given. Combining with the Neumann's principle, one may establish the relationship between themagnetic space group and magnetoelectric properties. In this respect, the linear ME effect could be predicted by symmetry consideration in a specific material. Unlike the electric polarization yielded in typical type I multiferroics, linear ME materials are characterized by weak polarization values. However, this does not impede their possible applications on random access memory since the small linear ME effect has recently been shown to control spintronic devices very efficiently in a magnetoelectric exchange bias system[2]. Nevertheless, the underlying mechanism leading to a linear ME coupling is still unclarified, but apparently, it is strongly material-dependent. Neutron diffraction, employed to determine the magnetic symmetry, will be essential for the study of linear ME effect as well as exploring new materials exhibiting linear ME effect.

A fourth ferroic order, the ferrotoroidic order has been recently reported. It is represented by a time-odd polar vector, which changes sign under both space inversion and time reversal, and is generally associated with a circular or ring-like arrangement of spins.[5] Materials in which the toroidal moments are spontaneously aligned are so-called ferrotoroidics. Ferrotoroidicity is related to the antisymmetric part of the linear magnetoelectric tensor, thus present only when the tensor of linear ME effect is nondiagonal.[6] From macroscopic symmetry considerations, the ferrotoroidic order parameter gives rise to antisymmetric contributions to the ME effect, indicating that the indirect evidence for the presence of a spontaneous toroidal moment in a system can be obtained by measuring the linear ME effect.

Recently, clinopyroxenes containing magnetic cations have attracted revitalized interest because some of them were found to present rich magnetic properties. Multiferroic properties was found in $NaFe(Si/Ge)_2O_6$ [8, 9], magnetoelectric effect in $LiCr(Si/Ge)_2O_6$[10], $NaCrSi_2O_6$ [11] and $LiFeSi_2O_6$ [8] and the expected ferrotoroidal order in $LiFe(Si/Ge)_2O_6$ [12]. These intriguing physical properties are attributed to their respective magnetic structure (incommensurate or commensurate) which are determined by their specific crystal structure. In the reported multiferroics, $NaFeSi_2O_6$ shows a spiral spin structure while $NaFeGe_2O_6$ adopts a helical spin configuration. In contrast, the pyroxenes exhibiting magnetoelectric effect usually have a commensurate magnetic structure.

In addition, the competition between inter- and intra-chain magnetic interactions in pyroxenes may lead to magnetic frustration and the appearance of various exotic magnetic properties such as orbit-ordering [13], spin singlet ground state [14], spin-Peierls transition [16] and quasi-one-dimensional (Q1D) magnetic behavior [17]. Furthermore possible presence of short range spin correlation in chain have been reported in $NaMnGe_2O_6$[13], $LiFeSi_2O_6$ and $NaFeSi_2O_6$[15]. The main contribution to the magnetic entropy is associated with the buildup of magnetic correlations in the quasi-one-dimensional Fe^{3+} chains. Pyroxene family compounds thus are regarded as an appropriate candidate to study the coupling of spin, orbit and charge and consequent diverse physical properties.

The vast majority of compounds mentioned previously are monovalent metal bearing pyroxenes, however, no investigation has been paid to the magnetoelectric property of Ca^{2+}-bearing pyroxene. Most of these divalent compounds crystallize into monoclinic C2/c symmetry. Divalent magnetic clinopyroxenes Ca(Mn, Fe, Co, Ni)Ge_2O_6 [19, 20] order all in commensurate collinear antiferromagnetic structures. As mentioned in earlier chapter, the magnetic symmetry of a compound is associated to the symmetry of its physical properties. A linear magnetoelectric effect can only be non-zero in materials when they are neither time-reversal nor space-inversion symmetric. Among the reported Ca^{2+}-bearing pyroxenes, only $CaMnGe_2O_6$ can satisfy this symmetry requirement when considering its magnetic symmetry.

Accordingly, we present here the investigation of the magnetic properties of $CaMnGe_2O_6$ by means of neutron diffraction, heat capacity and magnetic measurements. All these techniques coincidentally reveal the presence of 1D intrachain short range spin correlations appearing above the long range antiferromagnetic order at 15 K. Then, by combining magnetic interactions within and between chains and building one-dimensional magnetic correlation model, the

physical picture underlying short-range spin correlations is drawn. Moreover, the linear magnetoelectric effect of $CaMnGe_2O_6$ is experimentally confirmed with respect to the long range spin ordering below 15 K. We also propose that $CaMnGe_2O_6$ should be a pure ferrotoroidic compound by considering the antisymmetric tensor of linear ME effect and the responding electric polarization under magnetic field. The toroidization of $CaMnGe_2O_6$ is also evaluated by considering the crystal and magnetic structure parameters.

5.2 Experimental details

5.2.1 Sample preparation

Polycrystalline $CaMnGe_2O_6$ was synthesized by solid-state reaction. The stoichiometric mixture of reagent-grade $CaCO_3$, MnO_2 and GeO_2 was ground in an agate mortar and pestle and then pelletized. The pellets were placed in a platinum boat and heated in air to 1373 K at 2K/min, then held at 1373 K for 100 h and cooled down to room temperature. Intermediate regrinding and reheating were required in order to obtain a single phase $CaMnGe_2O_6$ sample(impurity $Ca_3Mn_2Ge_3O_{12}$less than 0.2 weight%).

5.2.2 X-ray and neutron powder diffraction

The sample was characterized by x-ray powder diffraction (XRPD) using a Bruker D8 diffractometer with Cu Kα1 radiation (1.5406 Å) selected by a Ge (111) primary beam monochromator in the range 10˜90° with a 0.02° step size. To investigate the nuclear and magnetic structures, a neutron powder diffraction (NPD) experiment was carried out on the two-axis diffractometer D1B at Institut Laue Langevin (ILL), between 1.7 K and room temperature. For nuclear structure refinement, NPD patterns were recorded at 100 K and 300 K with the 1.28 Å wavelength corresponding to the (311) Bragg reflection of a germanium monochromator. The 2.52 Å wavelength corresponding to the (002) Bragg reflection of a pyrolytic graphite monochromator was used for magnetic structure investigation, with longer data collections at 2, 20 and 50 K as well as a temperature ramp between 2 K and 300 K on heating process. The XRPD and NPD data were analyzed by the Rietveld method using the Fullprof suite programs[18].

5.2.3 Magnetic susceptibility measurement

The temperature-dependent magnetic susceptibility was measured on a Quantum Design Magnetic Property Measurement System (MPMS). The dc magnetic susceptibility was measured from 2 K to 350 K in zero field cooled (ZFC) and field cooled (FC) procedures under magnetic fields of 0.1, 1 and 5 T. Magnetic hysteresis loops between -5T and 5 T were recorded at 4, 20, 40 and 60 K. In addition, field-dependent magnetization was measured between 2 K and 350 K with a field sweep from 0 to 5 T. Moreover, alternating current (ac) susceptibility was measured at frequencies of 1, 250, 500, and 1000Hz over the temperature range of 4K$\leq T \leq$ 100K. At 250Hz, ac susceptibility was recorded under selected magnetic fields of 50, 100,

150 and 200Oe through the temperature range of 4K$\leq T \leq$ 100K. For all ac susceptibility measurements, a drive amplitude of 2 Oe was applied.

5.2.4 Specific heat measurement

The specific heat measurement was carried out using a relaxation technique with a Quantum Design Physical Property Measurement System(PPMS) in the temperature range of 2-100K. The pelletized sample was mounted on sample platform with Apiezon N-grease for better thermal contact.

5.2.5 Electrical properties

To study the magnetoelectric properties of $CaMnGe_2O_6$ the temperature dependence of electric polarization was measured under various magnetic fields (0, 2, 4, 6 and 8 T). The sample was sintered to improve grain connectivity by heat treatment of a pressed pellet (thickness 0.29 mm and surface 19 mm^2) at 1073 K for 10 hours. Then, the pellet was coated with silver epoxy on both sides to make conducting electrodes. Electrical polarization was then determined by using the pyroelectric current measurement technique, as described in chapter 2. The magnetoelectric annealing was performed by simultaneously applying an electric field E of $\pm$690 KV/m and a magnetic field μ_0H of $\pm$8 T in perpendicular directions, at 100 K and then cooled the sample down to 2 K. Then, the pyroelectric current curves under various magnetic fields were recorded using a Keithley 6514A electrometer while increasing the temperature at a rate of 3 K/min. Electric polarization was obtained by integration of the time dependence of the pyroelectric current.

5.3 Results and discussion

5.3.1 Crystal structure

The crystal structure of $CaMnGe_2O_6$ has been previously reported[19]. It crystallizes with monoclinic C2/c symmetry corresponding to the high clinopyroxene structure type. In most pyroxene compounds, the long range magnetic ordering stems from the competition of intrachain and interchain interactions. The precise description of crystal structure, especially the atomic position, is thus of great importance to explain the magnetic properties. The final Rietveld plot for room temperature NPD pattern of $CaMnGe_2O_6$ is shown in figure 5.1. The background was described by linear interpolation of selected points in the pattern. A Thomson-Cox-Hastings model of the reflection profile was used[21]. Low angle peak asymmetry was taken into account using the Berar-Baldinozzi model[22]. $Ca_3Mn_2Ge_3O_{12}$ was the only phase detected as impurity; it was introduced in the pattern description and its cell parameters and scale factor were refined. The final refinement yielded a weight fraction of 0.15(1) % for this phase. The refinement results and main interatomic distances and bond valence sums calculated using the BondStr program[23] are presented in table 5.1 and 5.2. They are in good agreement with previously reported values[19].

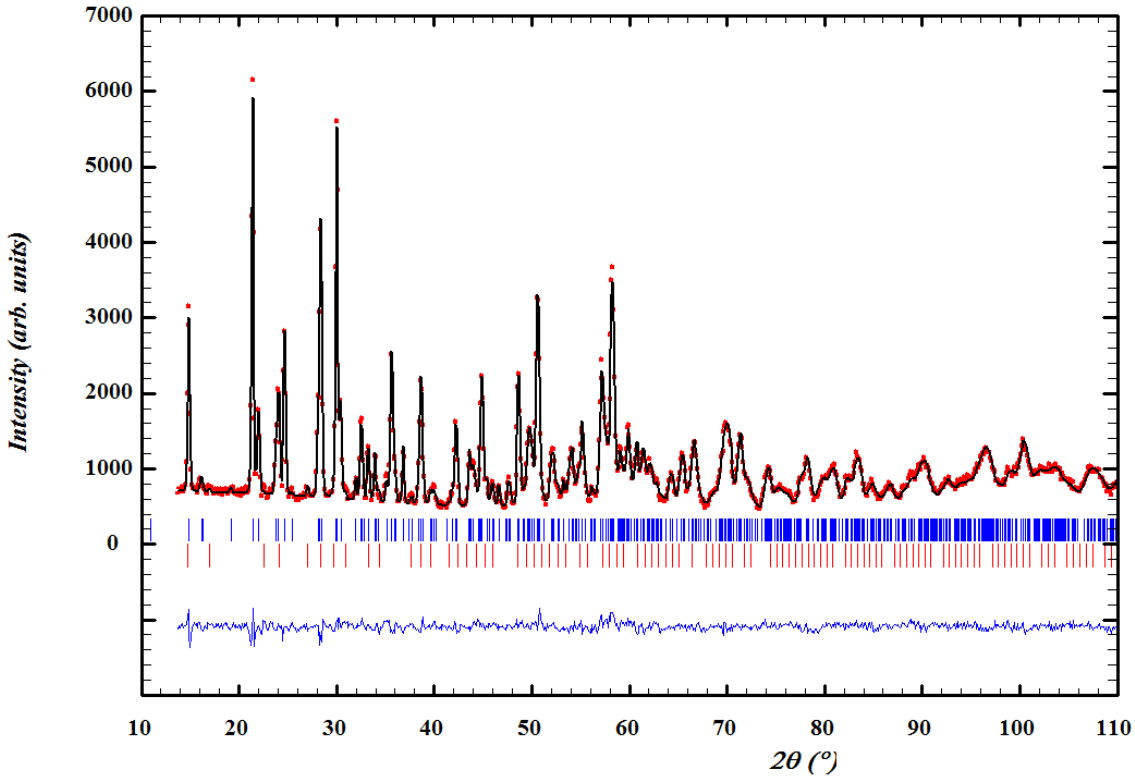

Figure 5.1: Rietveld refinement of $CaMnGe_2O_6$ from NPD data taken at room temperature. Observed (red), calculated (black), and difference (blue) plots are shown. Bragg reflections are denoted by blue tick marks. The lower set of Bragg reflections (red marks) belong to a $Ca_3Mn_2Ge_3O_{12}$ impurity phase.

Table 5.1: Agreement factors and refined structural parameters for $CaMnGe_2O_6$.

Name	position	x	y	z	B(Å^2)
Ca	4e	0.00000	0.3075(8)	0.25000	0.9(1)
Mn	4e	0.00000	0.905(1)	0.25000	1.4 (2)
Ge	8f	0.2860(3)	0.0958(3)	0.2319(4)	0.20(4)
O1	8f	0.1133(3)	0.0949(5)	0.14443(1)	0.17(6)
O2	8f	0.3668(4)	0.2532(4)	0.3545(8)	0.55(6)
O3	8f	0.3565(4)	0.0324(5)	0.9802(8)	0.51(6)
R_p=8.06, R_{wp}=9.33, R_{exp}=1.90, Chi^2=23.99, R_{bragg}=3.65					
a=10.2794(3) Å, b=9.1756(3) Å, c=5.4714(2) Å, α=90°, β=104.244(2)°, γ=90°					

Table 5.2: Principal cation-anion distances (Å) and angles for $CaMnGe_2O_6$.

Ca-O1	2.417(7)	Ge-O1	1.716(4)
Ca-O2	2.326(4)	Ge-O2	1.718(5)
Ca-O3	2.746(7)	Ge-O3	1.803(5)
Ca-O3	2.614(6)	Ge-O3	1.808 (5)
Ave.Dist.	2.526(2)	Ave.Dist.	1.761(2)
BVS	1.94(1)	BVS	3.89(3)
Mn-O1	2.255(9)	Mn-Mn (intra)	3.249(8)
Mn-O1	2.187(9)	Mn-Mn (inter1)	5.918(7)
Mn-O2	2.125(8)	Mn–Mn(inter2)	6.889(1)
Ave.Dist.	2.189(3)	Mn-O1-Mn	94.0(4)°
BVS	2.06(2)	Mn-O1-O2	126.1(2)°
		O1-O2-Mn	141.3(4)°
		O2-O1-Mn	138.1(4)°

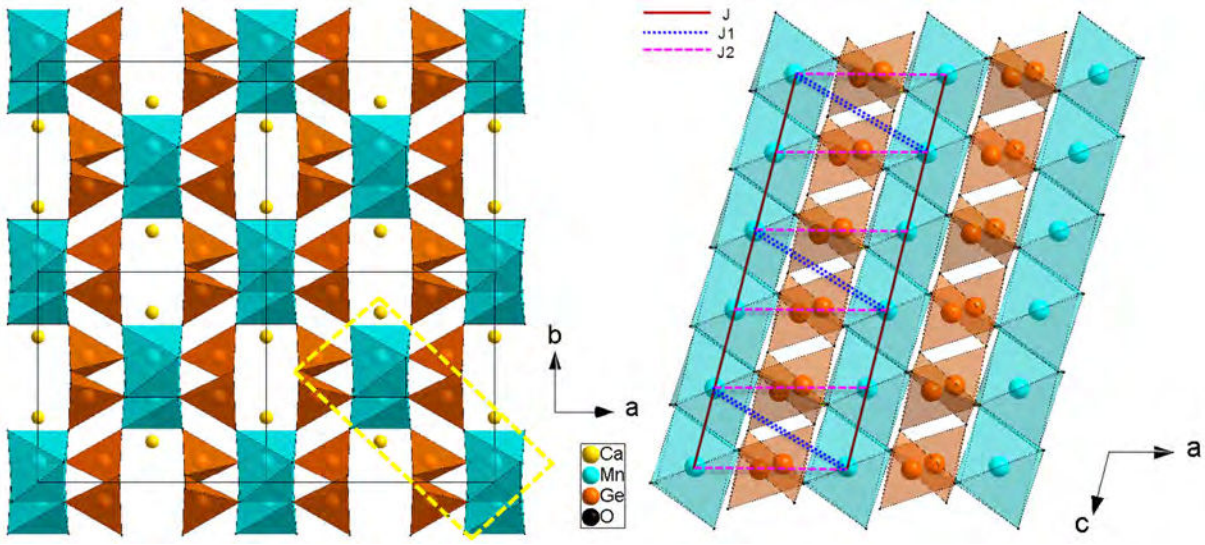

Figure 5.2: (Left) Projection of the $CaMnGe_2O_6$ structure along the c-axis. Note that the dashed rectangle marks the nearest-neighbor octahedra chains which are responsible for the magnetic interaction. (Right) The MnO_6 zigzag chains separated by GeO_4 tetrahedra via corner sharing, derived from NPD at room temperature. Magnetic interaction pathways being triangular geometry in $CaMnGe_2O_6$. J represents the interaction along the zigzag chain and connects NN Mn^{2+}sites; J1 denotes the possible exchange between adjacent octahedra chains but via two tetrahedra; J2 shows the possible exchange between octahedra chains through one tetrahedron.

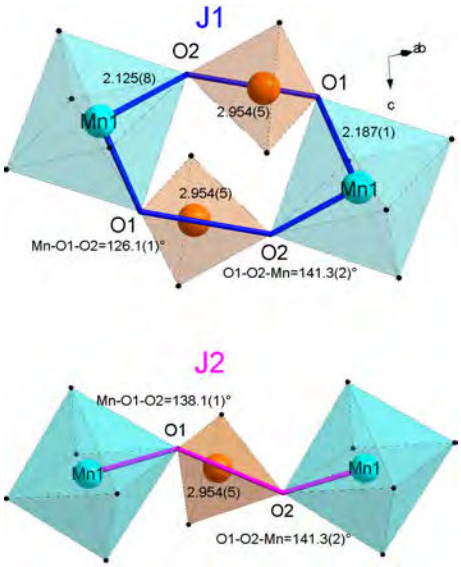

Figure 5.3: The polyhedral drawing shows the two interchain exchange pathways J1 and J2 for $CaMnGe_2O_6$.

The crystal structure of $CaMnGe_2O_6$ is shown in figure 5.2. It is characterized by the alternate stacking perpendicular to the a-axis of layers made of MnO_6 octahedra and layers of GeO_4 tetrahedra. In the octahedral layer, MnO_6 octahedra share their O1-O1 edges to form zigzag infinite chains along the c-axis. They are slightly distorted with three distinct Mn-O bond lengths ranging from 2.125 Å to 2.255 Å and an average bond length of 2.189 Å in good agreement with the ionic radius for Mn^{2+} ($3d^5$) in the high spin state (0.83Å). Within the octahedra chains, the shortest (intrachain) Mn-Mn distance is 3.249 Å. According to the band structure calculations of exchange interactions for pyroxenes[24], the edge-sharing character of MO_6 with M-O-M angle close to 90° results in the competition between direct and superexchange magnetic interactions. In $CaMnGe_2O_6$, the Mn-O1-Mn angle was obtained as 94° from the NPD data, substantially deviating from the ideal 90 ° value. As marked with yellow rectangle in figure 5.2(left), the MnO_6 octahedra chains are linked by corner-sharing GeO_4 chains along the a-axis. From the viewpoint of magnetism, the structural arrangement leads to two possible magnetic super-super exchange pathways between Mn^{2+} cations belonging to adjacent octahedra chains through a GeO_4 tetrahedron edge. They were marked with blue and purple lines in figure 5.2(right), an equivalent schematic drawing of considered exchange interactions is also shown in figure 5.10. As shown in figure 5.3, the J1 interaction is mediated through two different paths (Mn-O1-O2-Mn and Mn-O2-O1-Mn) while for J2 only a single path exists.

5.3.2 Magnetic properties

The temperature dependence of magnetization of $CaMnGe_2O_6$ was measured with ZFC and FC processes under different magnetic fields μ_0H=0.1, 1 and 5 T. As shown in figure 5.4(a) and in the enlarged view of the low temperature part in figure 5.4 (b) , we observed a large

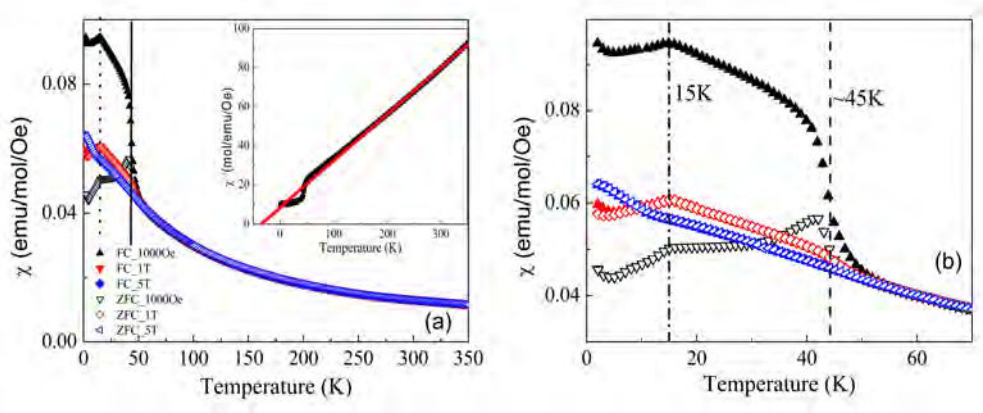

Figure 5.4: (a) Temperature dependence of the magnetic susceptibility of $CaMnGe_2O_6$ under different magnetic fields. The inset shows the Curie-Weiss fit for inverse magnetic susceptibility (red line). (b) Enlarged view of the low temperature part.

difference between the ZFC and FC curves below 45 K under 0.1 T as well as a sharp transition at 15 K. No such difference can be observed under higher magnetic fields of 1 and 5 T. All measurements exhibit a cusp at T_N=15 K, indicating a long-range AFM ordering transition. In the previous report [19] the susceptibility curve measured at 0.5 T was shown up to 50 K only and did not display any feature around 45 K; only one transition at 12 K was observed. As shown in the inset of figure 5.4 (a), the inverse magnetic susceptibility at 0.1 T was fitted with the Curie-Weiss law between 175 K and 350 K. This yields an effective moment μ_{eff} = 5.79 (1) μ_B, consistent to the expected spin-only value of 5.92 μ_B for Mn^{2+} cations in the high spin state, in agreement with the previous report. The negative Weiss temperature of -35(1) K indicates that antiferromagnetic interactions are predominant in this system. An empirical measure of frustration can be given by the frustration index f defined as f=$\frac{-\theta_{CW}}{T_N}$ [32]. For $CaMnGe_2O_6$, f=2.33.

The characterization of the magnetic transition via the measurement of the heat capacity was carried out. Figure 5.5 (a) shows the temperature dependence of the specific heat for $CaMnGe_2O_6$. The presence of a cusp in C_p around 15K indicates the magnetic ordering transition. This temperature is consistent with the Neel temperature observed in magnetic susceptibility and the appearance of the magnetic reflection peaks in neutron diffraction (see below). The magnetic component of the specific heat capacity of $CaMnGe_2O_6$, C_{mag}, as shown in figure 5.5(b) was obtained by subtracting the phonon contribution with a nonmagnetic analogue $CaZnGe_2O_6$. The plotted C_{mag} vs T clearly shows that only the transition observed at around 15 K in the magnetic susceptibility can also be seen in the specific heat data, evidencing the nature of long-range order at~15 K. The experimental magnetic entropy with S_m=13.5J/mol/K at 75 K, derived from the C_{mag}-T curve, is about 91% of the theoretical value of 14.9 J/mol/K for the spin S=5/2 Mn^{2+} ions given by Rln(2S+1), as seen in figure 5.5 (b). The magnetic entropy first drops down slowly on cooling over a broad temperature range between 60K and Neel temperature T_N=15K, then below ~15K, a rapid decrease is observed.

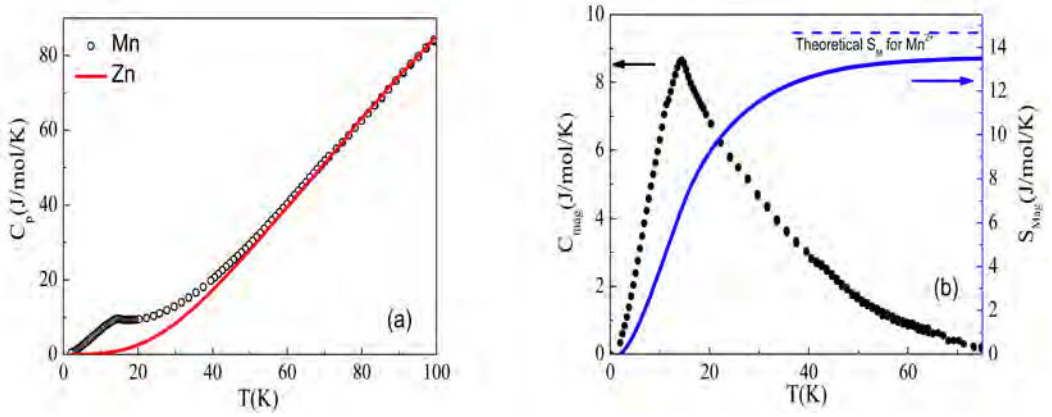

Figure 5.5: (a)Specific heat capacity of $CaMnGe_2O_6$ and $CaZnGe_2O_6$ which is used as a lattice standard. (b)(black)The magnetic component of the specific heat capacity of $CaMnGe_2O_6$; (blue)The entropy released through magnetic ordering. Blue dash line represents the theoretical maximum.

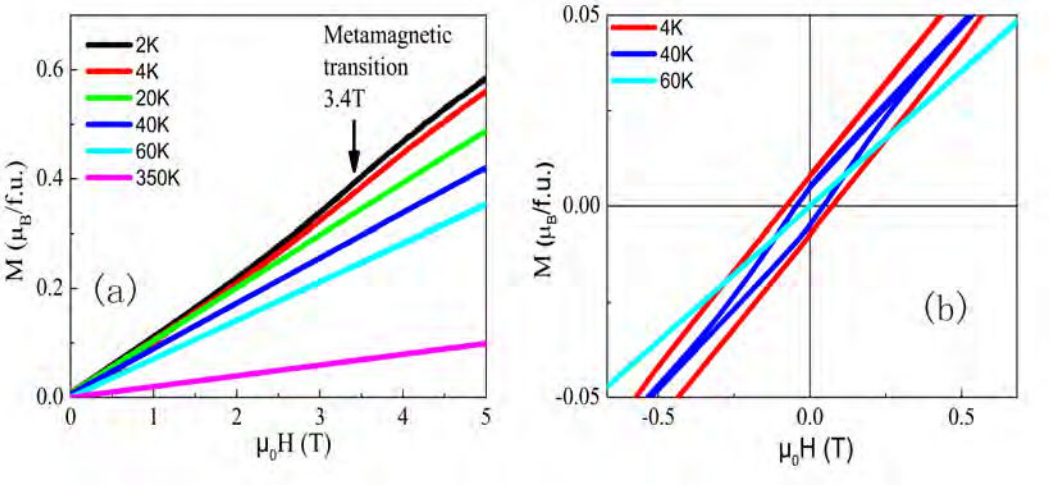

Figure 5.6: (a) Isothermal magnetization curves of $CaMnGe_2O_6$ collected at T=2, 4, 20, 40, 60 and 350 K. (b) The magnetic hysteresis loops for $CaMnGe_2O_6$ at various temperature 4, 40 and 60 K.

The former phenomenon corresponds to a considerable entropy release, indeed, about half of the magnetic entropy (51%) is released above T_N. This characteristic probably arises from short-range spin correlation, as discussed below. A similar phenomenon occurs in $NaMnGe_2O_6$, $LiFeSi_2O_6$ and $NaFeSi_2O_6$[15]showing up the formation of strong short-range magnetic correlations within the quasi-1D spin chains far above the long-range ordering temperature[13]. In fact, for $NaMnGe_2O_6$ it has been found that a majority of the magnetic entropy (68%) under zero magnetic field[13] is released above the long range ordering temperature, while $LiFeSi_2O_6$ has around 80% of the magnetic entropy and $LiFeSi_2O_6$ has around 65% well above their long range ordering temperatures[15].

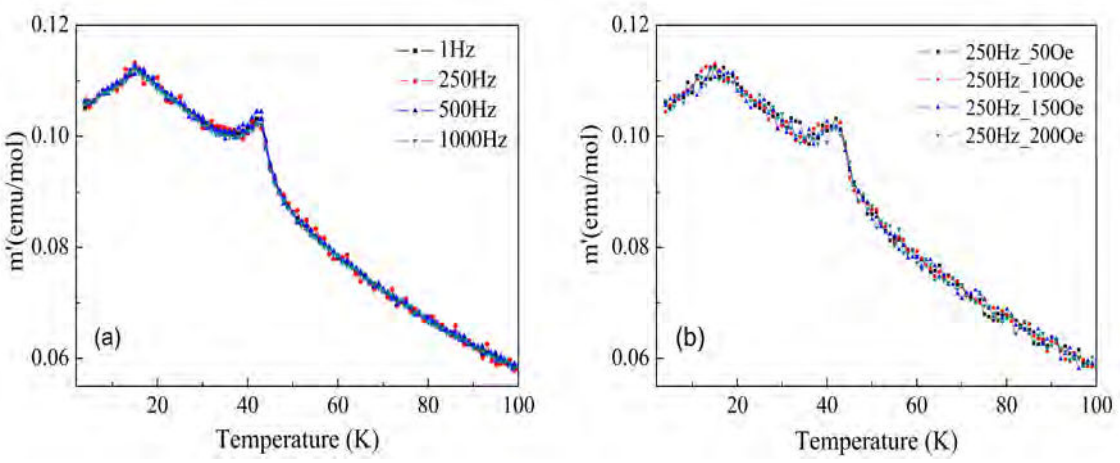

Figure 5.7: (a)Temperature and frequency dependence of the real parts of the ac susceptibility of $CaMnGe_2O_6$.(b)Temperature dependence of ac susceptibility of $CaMnGe_2O_6$ at 250Hz under different dc magnetic fields.

Table 5.3: Basis vectors for Mn^{2+} at 4e site (indicate position of Mn1(0, 0.905, 0.25), Mn2(0.5, 0.405, 0.25), Mn3 (0, 0.095, 0.75), Mn4(0.5, 0.595, 0.75). Notations: F=S1+S2+S3+S4, C= S1+S2-S3-S4.

IR	Basis vector	Space group
Γ1	(0,Fy,0)	C2/c
Γ2	(0,Cy,0)	C2/c'
Γ3	(Fx, 0, Fz)	C2'/c'
Γ4	(Cx,0,Cz)	C2'/c

Field-dependent magnetization isotherms M(H) were measured between 2 K and 350 K and are presented in figure 5.6(a). The field-induced magnetization is linear up to applied fields of 5T above T_N. However, on the curves at 2 K and 4 K, a change of slope can be seen at $\mu_0 H \tilde{}$3.4 T determined by the maximum of derivative of dM/dH, as denoted by arrow. This is indicative of a field induced metamagnetic transition. No saturation can be achieved with the maximum field applied ($M<0.6\mu_B/Mn^{2+}$ at 5T). Isothermal magnetic hysteresis loops were measured at various temperatures. As shown in figure 5.6(b), no magnetic hysteresis can be detected at 60 K, whereas a magnetic hysteresis signal is clearly observed below 40 K which increases with decreasing temperature. This indicates the existence of a small ferromagnetic component : the values at 40K, 20K and 4K are respectively 4.8×10^{-3} μ_B/Mn^{2+}, 7.2×10^{-3} μ_B/Mn^{2+} and 7.8×10^{-3} μ_B/Mn^{2+}. The coercive fields at 40K, 20K, 4K derived from the hysteresis loops are 0.045T, 0.070T and 0.073T, respectively. The rise of both ferromagnetic component and coercive field from 40K to 20K are more substantial than that of from 20K to 4K.

The temperature and frequency dependence of the ac magnetic susceptibility of $CaMnGe_2O_6$ is shown in figure 5.7. It is apparent, from figure 5.7(a), that the real part of ac susceptibility is frequency independent. Similar to the results of dc magnetic susceptibility measurement,

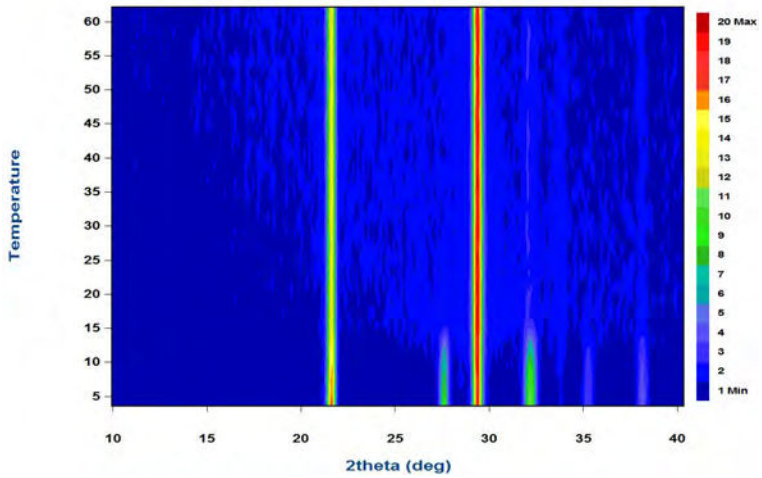

Figure 5.8: Plot of neutron powder diffraction scans showing up the magnetic transition at 15K using a wavelength of 2.52Å.

two magnetic transitions can be observed in the ac susceptibility curves, characterized by two cusps. They appear at around 15 K and 43 K, respectively, determined as the maximum of peak. The measured ac susceptibility at a fixed frequency of 250Hz under various dc magnetic fields is presented in figure 5.7 (b). Again, the ac susceptibility is almost unchanged with various magnetic fields. Both these ac susceptibilities show the presence of two magnetic phase transitions independent of the applied magnetic field and frequency, which discards the existence of a spin-glass-like behavior in this temperature range.

5.3.3 Magnetic structure

Figure 5.8 shows temperature dependent NPD patterns below 60 K for $CaMnGe_2O_6$. One can easily observe the appearance of magnetic reflections below 15 K. It is worth noting that there is no magnetic reflection above 15 K, indicating that the magnetic transition observed at 45 K in our low field susceptibility measurements cannot be attributed to long range magnetic ordering. At low temperature all magnetic reflections can be indexed with a commensurate magnetic propagation vector k=(0,0,0). The determination of the magnetic structure was done by symmetry analysis, following the representation analysis technique described by Bertaut[25]. Calculations were carried out using version 2 K of the program SARAh-Representation analysis[26] and BasIreps integrated in Fullprof Suite [27]. For the Mn^{2+} cations on the 4e Wyckoff position of space group C2/c, the decomposition of magnetic representation is $\Gamma=1\Gamma_1^1+1\Gamma_2^1+2\Gamma_3^1+2\Gamma_4^1$. The different basis vectors calculated using the projection operator technique associated with each IR are presented in table 5.3. There are 4 magnetic ions in the cell but only two possible magnetic couplings. Indeed, because of the C centering which is preserved by the k vector, the magnetic moment carried by the two Mn^{2+} cations symmetrically related by the C translation are automatically identical. Consequently the two magnetic coupling possibilities are a ferromagnetic one F=(S1+S2)+(S3+S4) and an antiferromagnetic one C= (S1+S2)-(S3+S4). According to the magnetization measurements,

the possible antiferromagnetic structure models determined from the symmetry analysis (Γ_2 and Γ_4) were tested by Rietveld refinement. The best fit was achieved with the model described by the IR Γ_4 with the magnetic space group C2'/c. The final refinement for the 2 K NPD pattern is shown in figure 5.9(a).

A representation of the magnetic structure is shown in figure 5.10. The Mn^{2+} magnetic moment is constrained by symmetry in the (a,c) plane, aligned mainly along the a-axis with a small angle of 14.13°, with m_a=4.30(1)μ_B, m_c=1.14(3)μ_B. Note that this result differs from the magnetic structure reported previously[19] with a magnetic moment component along the b-axis of 0.78(9)μ_B which is not allowed by symmetry. The total ordered magnetic moment refined at 2 K is 4.17(5)μ_B which is smaller than the theoretical spin-only value for Mn^{2+}. The temperature dependence of the magnetic moment is shown in figure 5.9 (b) and confirms the T_N=15 K value for the magnetic ordering temperature, in agreement with our dc and ac magnetic susceptibility measurements. The magnetic ordering corresponds to antiferromagnetic coupling between the Mn^{2+} cations within the MnO_6 octahedra zigzag chains, while the spin couplings between neighboring chains (as marked with yellow dashed rectangle in figure 5.2) are competing due to the two super-super exchange paths J1 (double) and J2. If both J1 and J2 interactions are considered as antiferromagnetic in nature, then the magnetic order observed leads to the J2 interaction to be unsatisfied and the system to be frustrated.

5.3.4 Short range spin correlations

Evidence for short range ordering can be obtained when one checks carefully the background intensity of NPD as a function of temperature. For $CaMnGe_2O_6$, Figure 5.12(a) shows the comparison of NPD data between 20 K and 50 K. The NPD difference pattern between them (the inset of figure 5.12(a)) displays clearly a maximum in the magnetic diffuse scattering at about d=5.4(1) Å with asymmetric shape, signifying the existence of short range magnetic correlations. This broad asymmetric peak featured by the sharp rise at low Q (high d value) and a gradual decrease toward high Q (low d value), is characteristic of low-dimensional short-range order. Few numerical models have previously been developped to describe these kind of feature. In particular the Warren function, describing the scattering from random layer stacking systems (2D) , has been used to describe the diffuse magnetic scattering from a layered magnet in which there are long-range correlations within a plane, but no correlation between them[33, 34, 35]. The comparison of the diffraction theory between randomly oriented line gratings, which are defined as a periodic linear structure, and the three-dimensional crystals and two-dimensional arrays shows that the long tails at high Q side in the patterns are characteristic of both randomly oriented two-dimensional arrays and randomly oriented line gratings[36]. In the case of the two-dimensional arrays, the intensity in the tail varies as a function of Q^{-2}, whereas with the line gratings the intensity in the tail varies as Q^{-1}. Inspection of this asymmetric peak reveals the slow decay at high Q side, thus, suggesting the one-dimensional nature of diffuse magnetic scattering in $CaMnGe_2O_6$. Compared to the next-nearest Mn^{2+} intrachain distance of 5.4 Å, this scattering can be attributed to the presence

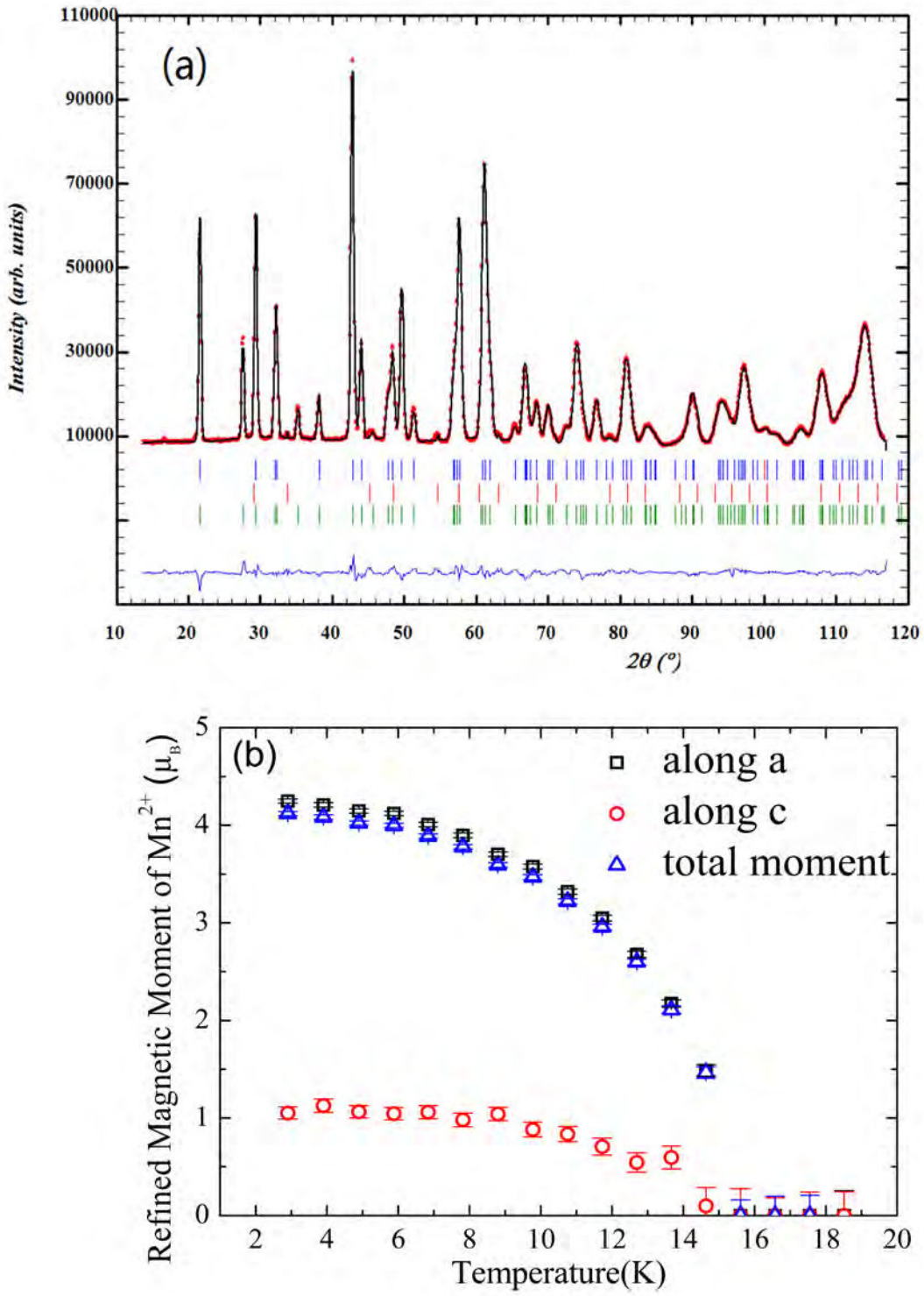

Figure 5.9: (a) Observed (symbols) and calculated (line) powder neutron diffraction patterns for $CaMnGe_2O_6$ at 2 K. The green tick marks shows the magnetic reflections. The nuclear reflections are denoted by blue tick marks. The reflections marked in red belong to a $Ca_3Mn_2Ge_3O_{12}$ impurity phase. The blue line shows the difference between the observed and calculated diffraction patterns. (b) Evolution of the refined Mn^{2+} magnetic moment components with temperature.

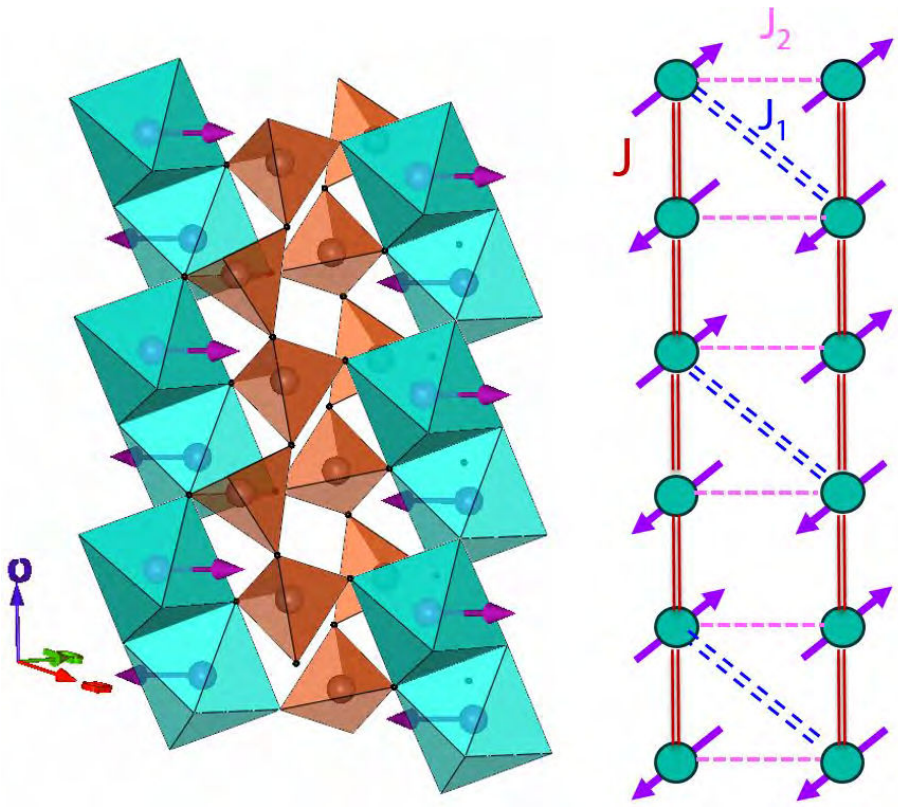

Figure 5.10: (Left) Representation of the magnetic structure of $CaMnGe_2O_6$; (Right) the schematic drawing of exchange interactions, and here magnetic moments were added arbitrarily in order better to exhibit the triangular exchange interaction.

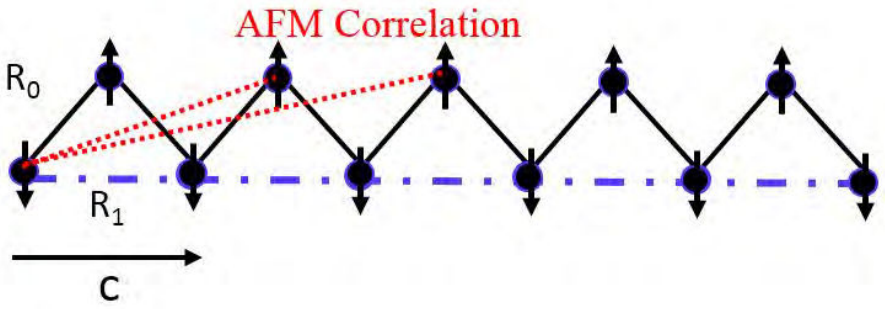

Figure 5.11: A model constructed for one dimensional correlation in a zigzag chain system. R_0(3.24Å) represents the distance between the first neighbor of Mn^{2+}cation which are aligned antiferromagnetically. R_1 (=unit cell c parameter) denotes the distance between second neighbor which are ferromagnetic.

of short range magnetic correlations between Mn^{2+} cations along the octahedra chains with vanishing interchain interaction. An analytical model describing the diffuse scattering in the presence of 1D magnetic correlations for our system has been developed in collaboration with Julien Robert (Néel Institut).

According to the zigzag characteristic of the MnO_6 octahedra chains in $CaMnGe_2O_6$, along with the determined magnetic structure, a quasi-one-dimensional magnetic correlation model can be constructed. As shown in figure 5.11, all magnetic moments at Mn sites running exactly along c direction are aligned ferromagnetically whereas the nearest-neighbors are coupled with AFM configuration.

As a result, the AFM order is likely to correlate along the phenomenologically expressed 1D chain. The exponentially decaying AFM correlations can be modeled by :

$$< S_0 S_i >= (-1)^i S^2 \exp(-\frac{d_i}{\xi}) \tag{5.1}$$

where S is the spin, and d_i designates the distance between spins, and ξ is the correlation length in angstroms. Further, the function for describing the correlated signal at low temperature (20K) is given by:

$$S(Q) = f(Q)^2 \sum_i < S_0 S_i > \frac{Sin(QR_i)}{QR_i} \tag{5.2}$$

where the f(Q) is the magnetic form factor with analytical approximations, in which all the coefficients were taken from International tables for crystallography[37], R_i represents the distance between the sites in 1D chain. Since the diffuse scattering data were obtained by subtracting the high temperature scattering data (at 50K) from the low temperature data, the fit of experimental data can be performed according to the following expression:

$$I_{experimental} = I_l S(Q) - I_h f(Q)^2 \tag{5.3}$$

where the variables are the correlation length ξ, the intensity of the correlated signal I_l, and

the intensity of the high temperature signal I_h.

The best fit is given in figure 5.12(b). The fitted intensities for the correlated signal I_l and the high temperature signal I_h are 4162.71 and 4313.92, respectively. The fit gives a correlation length ξ= 10±1 Å for the magnetic correlations along the c-axis, evidencing the short-range characteristic. In opposition to the numerical Warren analysis, we have an analytical form of S(Q), so that it is possible to make really physical sense by fitting the data and determining an error bar for each refined parameter.

The signature of this 1D short range spin correlations can also be observed in the temperature dependence of the lattice parameters for $CaMnGe_2O_6$ extrated from Rietveld refinement of NPD data collected in the 2-300K temperature range. They are shown in figure 5.13. The a- and b- parameters as well as the monoclinic beta angle follow a standard evolution in the whole temperature range. No anomaly can be detected at either of the magnetic transition temperatures observed from magnetic measurements. On the contrary, the c-parameter exhibits a strong anomaly below 40-50 K, with a sharp decrease down to the lowest temperature. This can be attributed to a magnetostrictive effect related to the short range magnetic correlations above 15 K. This anomaly being detected only along the c-axis supports the fitting results of diffuse neutron scattering that this short range spin correlations is due to 1D intrachain antiferromagnetic correlations between the Mn^{2+} cations.

5.3.5 Linear magnetoelectric effect

The magnetic structure determined from neutron diffraction with space group C2'/c allows linear magnetoelectric effect, and this can be verified by symmetry consideration below. As discussed in chapter 1, the linear magnetoelectric effect can be established in the form:

$$P_i = \alpha_{ij} H_j \tag{5.4}$$

We have seen that antiferromagnetic $CaMnGe_2O_6$ has magnetic point group $2'/m$ below 15 K. Accordingly the generating symmetry elements are twofold rotation accompanied by time reversal ($2'$) parallel to the b-axis, and a mirror plane perpendicular to the b-axis. Applying Neumann's principle, first for $2' \parallel b$:

$$\begin{pmatrix} \alpha'_{11} & \alpha'_{12} & \alpha'_{13} \\ \alpha'_{21} & \alpha'_{22} & \alpha'_{23} \\ \alpha'_{31} & \alpha'_{32} & \alpha'_{33} \end{pmatrix} = (-1)(+1) \begin{pmatrix} -1 & 0 & 0 \\ 0 & 1 & 0 \\ 0 & 0 & -1 \end{pmatrix} \begin{pmatrix} \alpha_{11} & \alpha_{12} & \alpha_{13} \\ \alpha_{21} & \alpha_{22} & \alpha_{23} \\ \alpha_{31} & \alpha_{32} & \alpha_{33} \end{pmatrix} \begin{pmatrix} -1 & 0 & 0 \\ 0 & 1 & 0 \\ 0 & 0 & -1 \end{pmatrix} \tag{5.5}$$

$$= \begin{pmatrix} -\alpha_{11} & \alpha_{12} & -\alpha_{13} \\ \alpha_{21} & -\alpha_{22} & \alpha_{23} \\ -\alpha_{31} & \alpha_{32} & -\alpha_{33} \end{pmatrix}$$

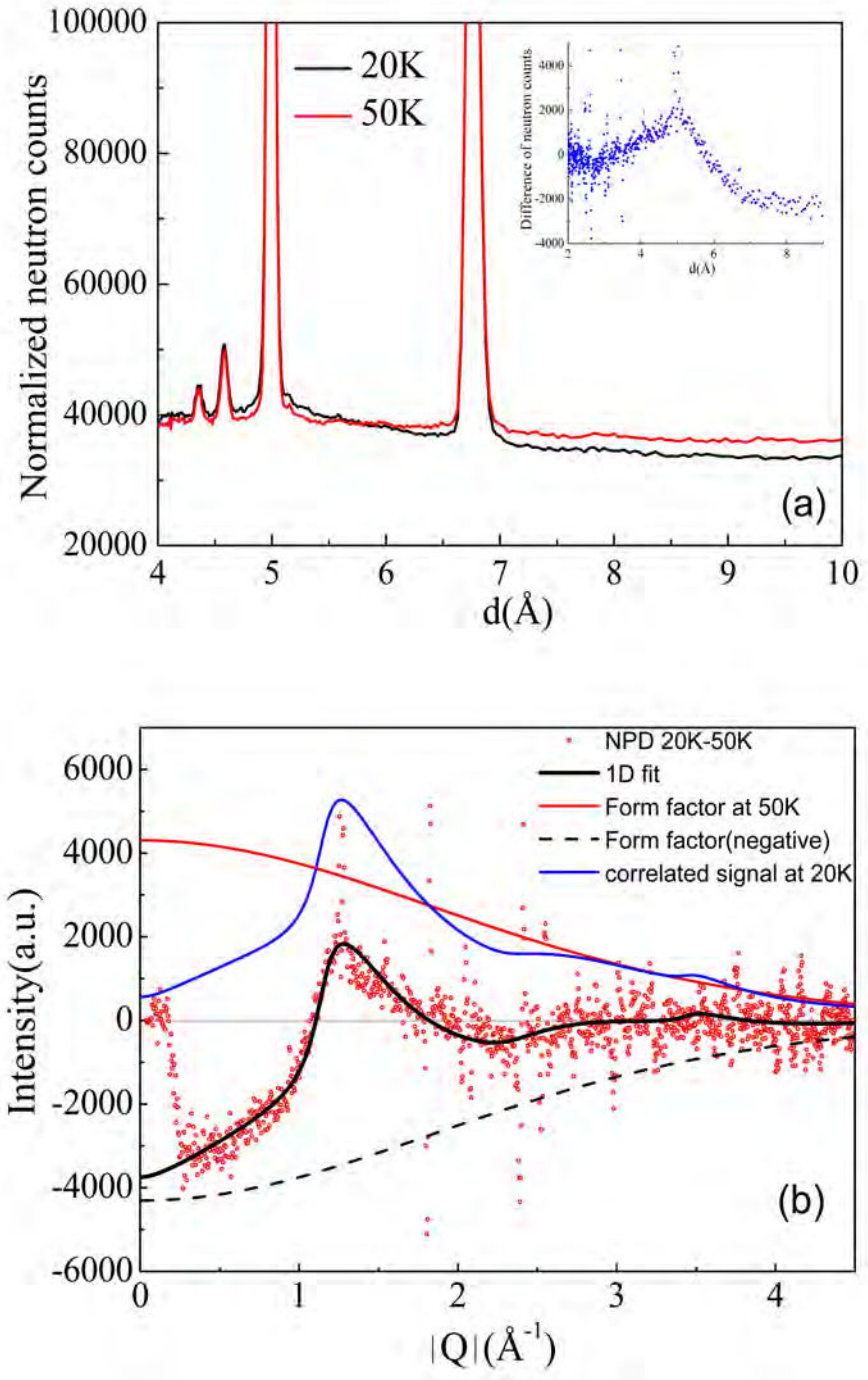

Figure 5.12: (a) Comparison between NPD data collected at 20 K and 50 K in $CaMnGe_2O_6$. Inset shows the NPD difference pattern between 20K and 50K. (b) Diffuse neutron scattering by subtracting the NPD pattern at 50 K from pattern at 20 K. The peak was well fitted by a model of 1D scattering.

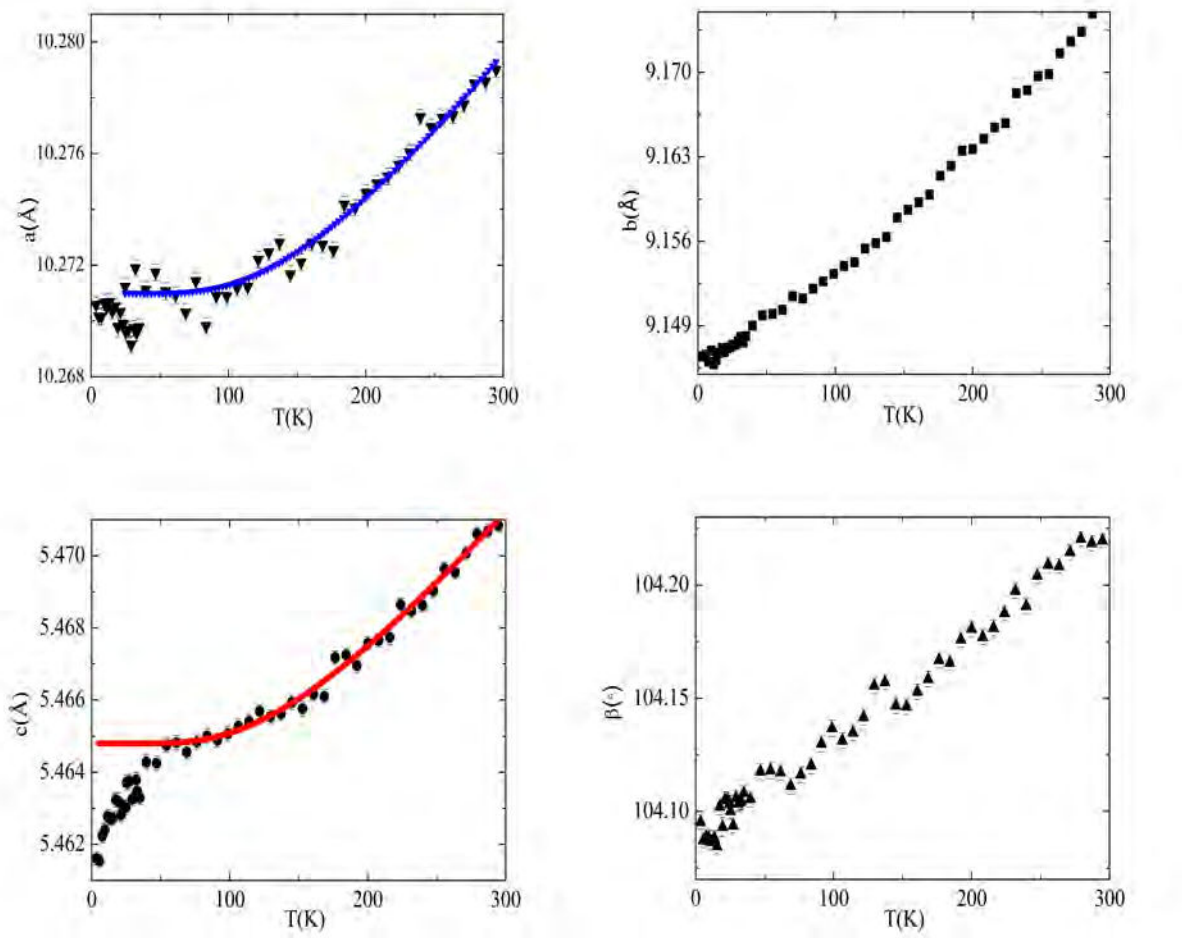

Figure 5.13: Lattice parameters of $CaMnGe_2O_6$ as a function of temperature from refinement of NPD.

This equality can be satisfied if α_{11}=α_{13}=α_{22}=α_{31}=$\alpha_{33} = 0$. Then the matrix is transformed under $m \perp b$:

$$\begin{pmatrix} \alpha'_{11} & \alpha'_{12} & \alpha'_{13} \\ \alpha'_{21} & \alpha'_{22} & \alpha'_{23} \\ \alpha'_{31} & \alpha'_{32} & \alpha'_{33} \end{pmatrix} = (+1)(-1) \begin{pmatrix} 1 & 0 & 0 \\ 0 & -1 & 0 \\ 0 & 0 & 1 \end{pmatrix} \begin{pmatrix} 0 & \alpha_{12} & 0 \\ \alpha_{21} & 0 & \alpha_{23} \\ 0 & \alpha_{32} & 0 \end{pmatrix} \begin{pmatrix} 1 & 0 & 0 \\ 0 & -1 & 0 \\ 0 & 0 & 1 \end{pmatrix} \quad (5.6)$$

$$= \begin{pmatrix} 0 & \alpha_{12} & 0 \\ \alpha_{21} & 0 & \alpha_{23} \\ 0 & \alpha_{32} & 0 \end{pmatrix}$$

This transformation does not affect the matrix. Therefore, the matrix representation of the tensor characterizing the linear magnetoelectric effect is expressed as:

$$\alpha_{ij} = \begin{pmatrix} 0 & \alpha_{12} & 0 \\ \alpha_{21} & 0 & \alpha_{23} \\ 0 & \alpha_{32} & 0 \end{pmatrix} \quad (5.7)$$

The off-diagonal character indicates that the perpendicular configuration between H and E for ME annealing must be used in order to observe the effect.

The evolution of electric polarization vs magnetic field was followed by measuring the pyroelectric current. It can be clearly seen from figure 5.14(a) that no polarization current is observed in the absence of external magnetic field. However, the induced current appears under magnetic field just below the AFM transition, and the current becomes stronger with the increase of magnetic field. By reversing the annealing electric field, we were able to change the sign of induced current. The temperature dependence of electric polarization was obtained by integrating the pyroelectric current with respect to time. As shown in figure 5.14(c), no polarization is observed with zero magnetic field while a magnetically induced polarization monotonically increases with increasing magnetic field. The induced electric polarization increases linearly with the increase of magnetic field at a rate of ~0.05(1) $\mu C/m^2/T$ (see figure 5.15). The observed maximum polarization value ($0.42\mu C/m^2$ under 8T) is smaller in magnitude as compared to the typical magnetoelectric material such as the first reported ME effect in Cr_2O_3[4]. However, it is comparable to the ME polarization value observed in $LiCrSi_2O_6$ (single crystal) and $LiCrGe_2O_6$ (polycrystalline) which was measured under simultaneously applied magnetic and electric field[10].

The temperature dependence of induced current was also recorded under negative magnetic fields. This measurement was performed after ME annealing with perpendicular configuration of (±)E and (-)H. As shown in figure 5.14(b) and (d), the temperature dependence of pyroelectric current and electric polarization becomes stronger with increasing magnetic field. And again, the sign of the pyroelectric current and polarization switches simultaneously with the polarity of ME annealing electric field.

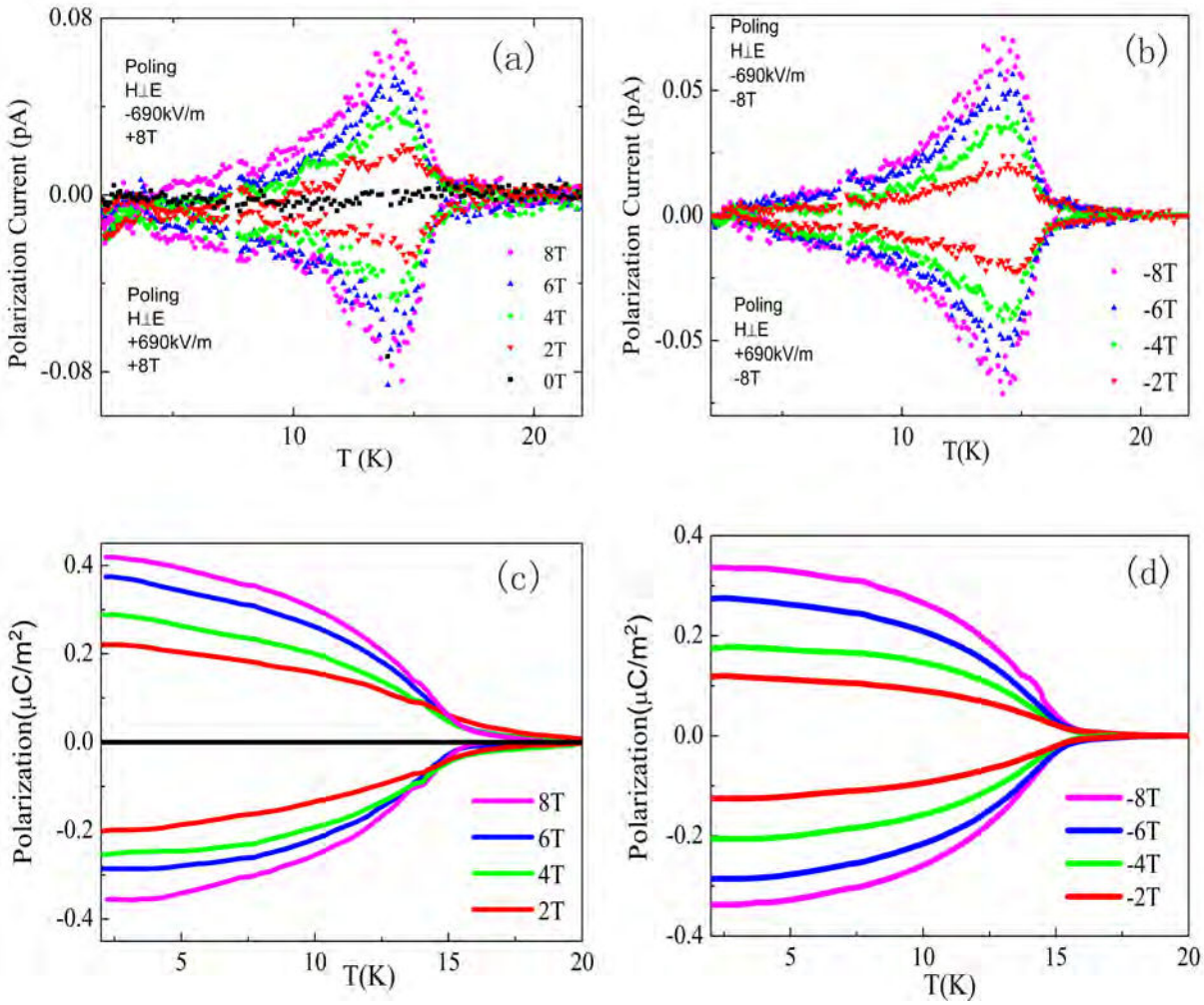

Figure 5.14: Temperature dependence of the pyroelectric current (a) and polarization (c) under various (positive) magnetic fields; temperature dependence of the pyroelectric current (b) and polarization (d) under various (positive) magnetic fields.

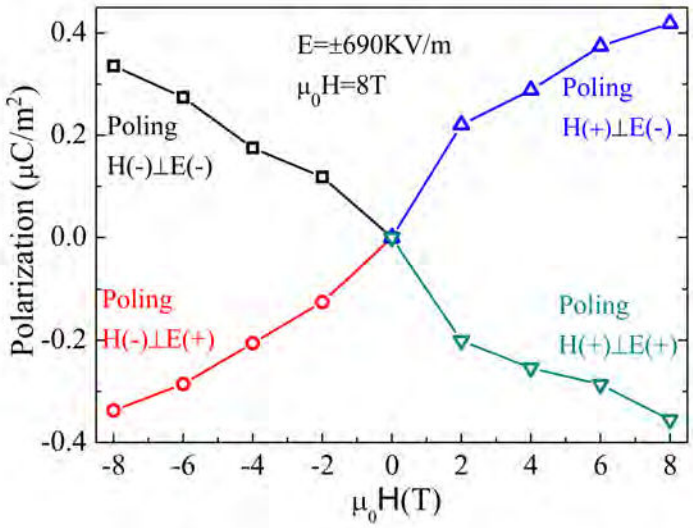

Figure 5.15: The induced electric polarization as a function of applied magnetic field with different ME annealing manners.

It is interesting to note that the polarization reversal is only achieved by varying the polarity of ME annealing electric field but not the magnetic field, as represented in figure 5.15. The same phenomenon has also been found in $NdCrTiO_5$,[31] although there the pyroelectric current was recorded under both magnetic and electric fields after ME annealing. The invariance of polarization under positive and negative magnetic fields may ascribe to the polycrystalline nature of $CaMnGe_2O_6$. Note that this phenomenon is not present in $LiCrSi_2O_6$, $LiCrGe_2O_6$ and $NaCrSi_2O_6$[10][11], where they measured the ME effect under both magnetic and electric fields.

5.3.6 Ferrotoroidicity

In addition, it is worth noting that this non-diagonal ME tensor has, in principle, an antisymmetric part that results in a toroidic moment and provides a pure ferrotoroidic compound, i.e., the alignment of toroidic moments. This has been observed recently in the $MnPS_3$ compound with the same magnetic point group 2'/m[28]. It has been found that in $MnPS_3$ AFM domains can be simply manipulated by cooling the sample under crossed magnetic and electrical fields evidenced by neutron polarimetry.

According to $\alpha_{ij} \propto \sum_k \epsilon_{ijk} T_k$, derived from the free energy expansion by considering the couplings between toroidization, magnetization, and polarization[30], a toroidic moment can always be represented by the antisymmetric part of the linear magnetoelectric effect tensor. The measurement of linear ME effect has been proposed as an indirect approach to observe the spontaneous toroidal moment [29]. By taking into account the pure ferrotoroidicity in $CaMnGe_2O_6$, the observed linear magnetoelectric effect supports the presence of a spontaneous toroidal moment. However, we could not reproduce a similar measurement for our compound,

Table 5.4: Position r_i and magnetic moment direction M_i of the Mn^{2+} cations in $CaMnGe_2O_6$. $\delta = 0.095$, is internal structural parameter.

Site	r_x	r_y	r_z	M_x	M_y	M_z
Mn	0	-δ	0.25	4.3	0	1.14
Mn	0	δ	0.75	-4.3	0	-1.14
Mn	0.5	0.5-δ	0.25	4.3	0	1.14
Mn	0.5	0.5+δ	0.75	-4.3	0	-1.14

mainly because we do not have the large size single crystal required.

A significant volumetric toroidic moment could be estimated in the monoclinic unit cell based on the definition of spontaneous toroidization which has been described as the toroidic moment per unit cell volume. A toroidic moment t is given by:

$$t = \frac{1}{2}\sum_{\alpha} r_\alpha \times M_\alpha \tag{5.8}$$

where r_α is the vector position of site α of a system, and M_α is the corresponding magnetic moment. By following the definition of toroidization in Ref. [30], we have the toroidization for periodic bulk material in unit cell:

$$T = \frac{t}{V} = \frac{1}{2V}\sum_{i} r_i \times M_i \tag{5.9}$$

where r_i represent the positions of the magnetic moments in unit cell, and M_i is relative to the same site within each unit cell, and the sum runs over all moments in the unit cell of volume V. In an infinite periodic solid, the choice of the basis is actually ambiguous with respect to the primitive unit cell of the crystal. Any spin of the basis can be translated by a lattice vector R_n, leaving the crystal structure invariant, but such a translation of magnetic moment m_i by R_n yields a change in the toroidization, given by:

$$\triangle T_{ni} = \frac{1}{2V} R_n \times M_i \tag{5.10}$$

This means that periodic boundary conditions lead to a multivaluedness of the toroidization (with respect to lattice translations), which suggests that only the differences of the toroidization between a ferrotoroidic state and its nontoroidic reference state are physically observable quantities[30].

In a system, the centrosymmetric set of toroidization values, can be regarded as a nontoroidal state of the corresponding system. In $CaMnGe_2O_6$, as presented in table 5.4, the nontrivial macroscopic toroidization can be obtained only when δ is nonzero because if δ is equal to zero, the system will be centrosymmetric and thus nontoroidal. According to equations 5.9 and 5.10, the "toroidization lattice" of the $CaMnGe_2O_6$ is given by:

$$T_{nml} = T + \triangle T_{ni} = \frac{1}{2V} \begin{pmatrix} -4 \cdot \delta \cdot b \cdot Mz + m \cdot b \cdot Mz \\ -c \cdot Mx + l \cdot c \cdot Mx - m \cdot a \cdot Mz \\ 4 \cdot \delta \cdot b \cdot Mx - m \cdot b \cdot Mx \end{pmatrix} \tag{5.11}$$

Thus the spontaneous toroidization is given by:

$$2T_s = T(\delta) - T(-\delta) = \frac{1}{2V} \begin{pmatrix} -8 \cdot \delta \cdot b \cdot Mz \\ 0 \\ 8 \cdot \delta \cdot b \cdot Mx \end{pmatrix} \tag{5.12}$$

For $CaMnGe_2O_6$, with the experimental parameters listed in table 5.4, the corresponding value is calculated by:

$$T_s = \frac{1}{4V} \begin{pmatrix} -8 \cdot \delta \cdot b \cdot Mz \\ 0 \\ 8 \cdot \delta \cdot b \cdot Mx \end{pmatrix} = (-0.004, 0, 0.015)\mu_B/\mathring{A}^2 \tag{5.13}$$

Actually, this result is very similar in magnitude to the toroidization in $MnPS_3$. Note that both compounds share the same magnetic point group.

The availability of large single crystals would be highly invaluable to measure the individual terms of the ME tensor and perform neutron polarimetry experiments that could allow a direct observation of the ferrotoroidic order.

5.4 Discussion

The neutron diffraction experiments confirm the nature of long range antiferromagnetic order at 15 K. The magnetic structure of $CaMnGe_2O_6$ can be described with a commensurate vector k=(0,0,0). The determined magnetic space group, C2'/c, allows for linear ME effect, in good agreement with the one we observe. The magnetic structure can be described as AFM chains that are coupled ferromagnetically.

Let's first examine the AFM intra-chain exchange J. The edge-sharing octahedra make Mn-O-Mn angles close 94^o, which leads to the competition between direct and super-exchange (SE) interactions within the chain. To determine which interaction is dominant, the Mn^{2+} orbital occupancy has to be taken into account. The Mn^{2+} cations have the simple configuration $d^5(t_{2g}{}^3e_g{}^2)$ without any orbital degeneracy, thus the exchange is uniform along the chain. The direct exchange originates from the overlap integral between singly occupied t_{2g} and e_g orbitals, and this exchange is relatively weak ferromagnetic. For what concerns super-exchange, either half-filled t_{2g} and e_g or half-filled t_{2g} and t_{2g} orbital overlaps via the same oxygen 2p orbital will give rise to strong AFM exchange. The dominant coupling within the chains should be then AFM, which is in accordance with our magnetic measurements and neutron diffraction results. Note that this is contrary to the results obtained for $CaMGe_2O_6$ compounds were M=Fe, Co, Ni [19, 20], for which ferromagnetic ordering of the chains is observed. This may be attributed to the different orbital occupancies and also marginally to different distances and

angles within the chains. It makes the case of this Mn^{2+} containing pyroxene quite unique.

Now, we will consider interchain couplings. In $CaMnGe_2O_6$, the MnO_6 octahedra chains are well bridged by the chains of GeO_4 tetrahedra. The two leading inter-chain exchanges are super-super-exchange (SSE) via double bridges of GeO_4 tetrahedra for J1 and a single bridge for J2, as presented in figure 5.3. As a result, the general topology of the three J, J1 and J2 exchanges turns out to be triangular-like, as shown in figure 5.10. According to the topology of the spin lattice determined by neutron diffraction, the coupling through exchange integrals J and J1 are AFM whereas J2 links two Mn^{2+} cations that are coupled ferromagnetically. If the exchange interaction J2 is antiferromagnetic, then it is not satisfied and a magnetic frustration is accordingly produced. It is worth noticing that DFT and quantum Monte-Carlo calculations for the $LiCrGe_2O_6$ pyroxene compound[38] show that the two inter-chain exchange integrals are antiferromagnetic with the same order of magnitude as the intra-chain one. Further work to determine the strengths of the various exchange integrals in $CaMnGe_2O_6$ will be very helpful to gain insight into the origin and role of frustration in that particular compound. As for now, the observed magnetic structure indicates a J>J1>J2 hierarchy of the magnetic exchange couplings. Note also that this reasoning about frustration does not apply to compounds such as $CaFeGe_2O_6$, $CaCoGe_2O_6$ and $CaNiGe_2O_6$, since their magnetic structures are described by antiferromagnetically arranged ferromagnetic chains, which satisfy all the magnetic exchanges.

Several of our experimental results indicate that strong 1D short-range spin correlations exist at temperatures far above the long-range magnetic ordering. No peak can be detected above the Néel temperature in the heat capacity measurements, but a large release of magnetic entropy is observed between 15 K and 60 K. No magnetic reflection can be seen by neutron diffraction above the T_N=15 K, however, diffuse magnetic scattering is observed up to about 50 K and can be characterized as one-dimensional by considering its line shape. Furthermore, an abnormal variation of the c lattice parameter as a function of temperature is observed about 50 K which can be attributed to magnetostriction caused by the onset of magnetic correlations along the octahedra chains. To account for these observations, we constructed a phenomenological 1D magnetic correlation model based on exponentially decaying AFM correlations with the analytical form of S(Q) in this system, which produced a satisfactory fit to the diffuse neutron scattering data, yielding a quite small correlation length ξ=10±1 Å at 20 K. Here again, such intrachain 1D spin correlations are not observed for pyroxenes of other 3d divalent cations, for which the intrachain interactions are ferromagnetic. In the case of $CaMnGe_2O_6$ the competition between interchain antiferromagnetic interactions might prevent the system to reach a three-dimensional magnetic order above 15 K, despite the onset of strong intrachain AFM correlations at about 50 K.

The origin of the magnetic transition observed around 45 K and detected by ac and dc magnetic susceptibility measurements remains unclear. Field-dependent magnetization and the opening between the FC-ZFC curves demonstrate that this magnetic transition is associated to a very weak ferromagnetic component. This cannot be explained solely by the presence of these intrachain AFM correlations. The question is then to know the origin of

this ferromagnetic component. The presence of impurity phases was carefully checked by x-ray and neutron diffraction and EDX analysis. The only impurity detected in the sample is the antiferromagnetic garnet $Ca_3Mn_2Ge_3O_{12}$ with a Néel temperature of 13.85 K[40]. We checked in the literature the ordering temperature for known magnetic compounds containing Mn and/or Ca, Ge and O. The first one could be involved is the olivine-type Mn_2GeO_4 which is a weak ferromagnet below 47 K (around $8.10\times10^{-3}\mu_B$/f.u.) [41]. Since it was not observed and therefore must remain below the detection limit for our x-ray and neutron diffraction experiment (around 1%), the presence of this impurity phase could by far not explain the size of the signal observed in our magnetization measurements. Another possible impurity phase is Mn_3O_4 which undergoes a ferrimagnetic phase transition at 42 K[42]. It has a net saturation magnetization Ms=2. From the magnetization of our sample it would correspond to a contamination of 0.7 mol% of Mn_3O_4 . Furthermore, all strong Bragg reflections from Mn_3O_4 have very close positions to $Ca_3Mn_2Ge_3O_{12}$, therefore, this impurity phase cannot be ruled out in our sample. It is then likely that the magnetic transition observed at around 45K is due to the Mn_3O_4 impurity phase.

5.5 Conclusion

In summary, the magnetic and magnetoelectric properties of $CaMnGe_2O_6$ were specifically investigated by combining powder neutron diffraction, magnetic susceptibility (dc and ac), heat capacity and electrical polarization measurements. Far above the Néel ordering atT_N=15 K, we observed the appearance of 1D short-range AFM correlations with a correlation length at 10 Å at 20 K. A 1D AFM correlation model was developed to fit the diffuse magnetic scattering. Magnetic frustration present in $CaMnGe_2O_6$ could be the main mechanism governing the present observations. The electrical polarization measurement performed on polycrystalline $CaMnGe_2O_6$ evidences the linear magnetoelectric effect below T_N which was allowed by considering the magnetic space group symmetry (C2'/c). The experimental results reveal that no spontaneous polarization arises below T_N until an external magnetic field is applied. The behavior of polarization shows a linear ME effect. Furthermore, the linear magnetoelectric effect has antisymmetric part which could result in a toroidic moment and makes the $CaMnGe_2O_6$ being a pure ferrotoroidic compound.

Bibliography

[1] M. Gajek, M. Bibes, S. Fusil, K. Bouzehouane, J. Fontcuberta, A. Barthelemy, A. Fert, Tunnel junctions with multiferroic barriers, Nature Mater. 6, 2007, 296. 107

[2] Xi Chen, Andreas Hochstrat, Pavel Borisov, and Wolfgang Kleemann, Magnetoelectric exchange bias systems in spintronics, Appl. Phys. Lett., 89, 2006, 202508. 107

[3] Hans Schmid, Multiferroic magnetoelectrics, Ferroelectrics, 162, 1994, 317. 107

[4] D.N. Astrov, Magnetoelectric effect in chromium oxide, Soviet Phys. -JETP, 13, 1961, 729. 107, 125

[5] V.M. Dubovik, V.V. Tugushev, Toroid moments in electrodynamics and solid-state physics, Physics Reports, 187, 1990, 145. 108

[6] Gorbatsevich A. A., Kopaev, Y.V., Toroidal order in crystals, Ferroelectrics, 161, 1994, 321. 108

[7] L.D. Landau, E. M. Lifshitz, Electrodynamics of continuous media. First Edition: Volume 8, 1960, 119. 107

[8] S. Jodlauk, P. Becker, J. AMydosh, D. I. Khomskii, T. Lorenz, S.V. Streltsov, D. C. Hezel, L. Bohaty, Pyroxenes: a new class ofmultiferroics, J. Phys.: Condens. Matter, 19, 2007, 432201. 108

[9] I. Kim, B. G. Jeon, D. Patil, S. Patil, et al., Observation of multiferroic properties in pyroxene $NaFeGe_2O_6$, J. Phys.: Condens. Matter 24, 2012, 306001. 108

[10] G. Nenert, M. Isobe, I. Kim, C. Ritter, C. V.Colin, A. N.Vasiliev, K. H.Kim, Y.Ueda, Interplay between low dimension- ality and magnetic frustration in the magnetoelectric pyroxenes $LiCrX_2O_6$ (X=Ge, Si), Phys. Rev. B, 82, 2010, 024429. 108, 125, 127

[11] Nenert, G.; Kim, I.; Isobe, M.; Ritter, C.; Vasiliev, A. N.; Kim, K. H.; Ueda, Y., Magnetic and magnetoelectric study of the pyroxene $NaCrSi_2O_6$, Phys. Rev. B 81, 2010, 184408. 108, 127

[12] C. Lee, J. Kang, J. Hong, J. H. Shim, M. H. Whangbo, Analysis of the Difference between the Pyroxenes $LiFeSi_2O_6$ and $LiFeGe_2O_6$ in Their Spin Order, Spin Orientation, and Ferrotoroidal Order, Chem. Mater. 26, 2014, 1745-1750. 108

[13] Jinguang Cheng, Wei Tian, Jianshi Zhou, Vincent M. Lynch, Hugo Steinfink, Arumugam Manthiram, Andrew F. May, et al., Crystal and Magnetic Structures and Physical Properties of a New Pyroxene $NaMnGe_2O_6$ Synthesized under High Pressure, J. Am. Chem. Soc.,135, 2013, 2776. 108, 115

[14] Y. Sasago, M. Hase, K. Uchinokura, M. Tokunaga, N. Miura, Discovery of a spin-singlet ground state with an energy gap in $CaCuGe_2O_6$, Phys. Rev. B, 52, 1995, 3533. 108

[15] P.J. Baker, H.J. Lewtas, S.J.Blundell, T. Lancaster, I.Franke, et al., Muon-spin relaxation and heat capacity measurements on the magnetoelectric and multiferroic pyroxenes $LiFeSi_2O_6$ and $NaFeSi_2O_6$, Phys. Rev. B, 81, 2010, 214403. 108, 115

[16] M. Isobe, E. Ninomiya, A.N. Vasilev, Y. Ueda, Novel Phase Transition in Spin-1/2 Linear Chain Systems: $NaTiSi_2O_6$ and $LiTiSi_2O_6$, J. Phys. Soc. Jpn., 71, 2002, 1423. 108

[17] Roser Valentí, T. Saha-Dasgupta, and Claudius Gros, Nature of the spin-singlet ground state in $CaCuGe_2O_6$, Phys. Rev. B 66, 2002, 054426. 108

[18] J. Rodriguez-Carvajal, Recent Advances in Magnetic Structure Determination by Neutron Powder Diffraction. Physica B, 192, 1993, 55-69. 109

[19] G.J. Redhammer, G. Roth, W. Treutmann, W. Paulis, et al., Magnetic ordering and spin structure in Ca-bearing clinopyroxenes $CaM^{2+}(Si,Ge)_2O_6$, M=Fe, Ni, Co, Mn, J. Solid State Chem., 181, 2008, 3163. 108, 110, 114, 118, 129

[20] G.J. Redhammer, G. Roth, A. Senyshyn, G. Tippelt, C. Pietzonka, Crystal and magnetic spin structure of Germanium-Hedenbergite, $CaFeGe_2O_6$, and a comparison with other magnetic/magnetoelectric/multiferroic pyroxenes, Z.Kristallogr., 228, 2013, 140. 108, 129

[21] P. Thompson, D.E. Cox, J.B. Hastings, Rietveld refinement of Debye-Scherrer synchrotron X-ray data from Al_2O_3, J. Appl. Cryst., 20, 1987, 79-83. 110

[22] J.F. Bérar and G. Baldinozzi, Modeling of line-shape asymmetry in powder diffraction, J. Appl. Cryst., 26, 1993, 128-129. 110

[23] J. Rodrıguez-Carvajal, BondStr, 2010, www.ill.eu/sites/fullprof/ 110

[24] S. V. Streltsov and D. I. Khomskii, Electronic structure and magnetic properties of pyroxenes (Li,Na)TM(Si,Ge)$_2$O$_6$: Low-dimensional magnets with 90° bonds, Phys. Rev. B 77, 2008, 064405. 113

[25] E.F. Bertaut, Representation analysis of magnetic structures, Acta Crystallogr. Sec. A 24, 1968, 217. 117

[26] A. S. Wills, A new protocol for the determination of magnetic structures using simulated annealing and representational analysis (SARAh), Physica B 278, 2000, 680. 117

[27] J. Rodriguez-Carvajal, BasIreps: a program for calculating irreducible representations of space groups and basis functions for axial and polar vector properties (see FullProf site: http://www.ill.eu/sites/fullprof). 117

[28] E. Ressouche, M. Loire, V. Simonet, R. Ballou, A. Stunault, and A. Wildes, Magnetoelectric $MnPS_3$ as a candidate for ferrotoroidicity, Phys. Rev. B, 82, 2010, 100408(R). 127

[29] N.A Spaldin, M. Fiebig, M. Mostovoy, The toroidal moment in condensed-matter physics and its relation to the magnetoelectric effect, J.Phys.:Condens. Matter, 20, 2008, 434203. 127

[30] C.Ederer, N.A. Spaldin, Towards a microscopic theory of toroidal moments in bulk periodic crystals, Phys.Rev. B, 76, 2007, 214404. 127, 128

[31] J.Hwang, E.S.Choi, H.D. Zhou, J.Lu, P. Schlottmann, Magnetoelectric effect in $NdCrTiO_5$, Phys.Rev.B, 85, 2012, 024415. 127

[32] A.P.Ramirez, Strongly geometrically frustrated magnets, Annu.Rev.Mater. Sci., 24, 1994, 453. 114

[33] B.E.Warren, X-ray diffraction in random layer lattices, Phys. Rev., 59, 1941, 693. 118

[34] A.S.Wills, N.P.Raju, C. Morin, J.E.Greedan, Two-dimensional short-range magnetic order in the tetragonal spinel $Li_2Mn_2O_4$, Chem. Mater., 11, 1999, 1936. 118

[35] J.E.Greedan, N.P.Raju, Long range and short range magnetic order in orthorhombic LiMnO2, J. Solid State Chem., 128, 1997, 209. 118

[36] R.Clark Jones, X-ray diffraction by randomly oriented line gratings, Acta Cryst., 2, 1949, 252. 118

[37] P. J. Brown, Magnetic form factors, chapter 4.4.5, International tables for crystallography vol. C (A. J. C. Wilson, ed.), pp. 391-399. 121

[38] O.Janson, G.Nenert, M.Isobe, Y. Skourski, Y. Ueda, H.Rosner, A.A. Tsirlin, Magnetic pyroxenes LiCrGeO and LiCrSiO: Dimensionality crossover in a nonfrustrated $S=\frac{3}{2}$ Heisenberg model, Phys. Rev. B, 90, 2014, 214424. 130

[39] D.A. Tennant, T.G. Perring, R.A. Cowley, S.E. Nagler, Unbound spinons in the S=1/2 antiferromagnetic chain $KCuF_3$, Phys. Rev. Lett., 70, 1993, 4003.

[40] R. Plumier, M. Sougi, and M. Lecomte, J. Appl. Phys. 61, 1987, 3280. 131

[41] N.V. Volkov, N.V. Mikhashenok, K.A. Sablina, O. A. Bayukov, M.V. Gorev, A. D. Balaev, A. I. Pankrats, V. I. Tugarinov, D. A. Velikanov, M. S. Molokeev, S. I. Popkov, J. Phys. Condens, Matter 25, 2013, 136003. 131

[42] R. Tackett and G. Lawes, B.C. Melot, M.Grossman, E.S. Toberer, R. Seshadri, Phys. Rev. B 76, 2007, 024409.

131

Chapter 6

Short-range magnetic correlations and magnetoelectric properties in high-pressure synthesized $CaMnSi_2O_6$

6.1 Introduction

Many physical systems in condensed matter are at least partly frustrated, caused by either lattice geometry (such as triangular) or the effects of further-neighbor interactions, in which several competing interactions exist, each favoring a different type of ordered state[1]. Such a competition can usually be revealed by varying a parameter of the system, such as temperature or magnetic field, which can energetically favor a particular interaction and drive the system into a specific ordered state. Magnetic moments on a lattice will often exhibit periodic order at low temperature. It is known, however, that long-range order could not occur in one-dimensional systems. The observation of 1D magnetic order in a 3D lattice is indeed rarely observed. A suitable system would contain paramagnetic ions, dominant super-exchange interactions in one-dimensional chains, as well as large separation between chains to weaken the interchain interaction but to retain the competition.

Pyroxenes family matches well with these characteristics. In fact, compounds belonging to this family exhibit diverse physical properties. Although they are characterized by a seemingly one dimensional structural topology, recent theoretical and experimental works have shown that some magnetic pyroxenes behave as three dimensional, while others have been found to display two-dimensional behavior[3, 4]. Spin 1/2 pyroxenes have been reported to show one-dimensional character, such as $LiTiSi_2O_6$ and $NaTiSi_2O_6$,[7] and $CaCuGe_2O_6$,[6, 8] and they all present exotic and strong quantum effects related to their specific orbital occupancies. In the pyroxenes with 3D magnetic ordering, the underlying magnetic couplings are quite complex. As we introduced, strong competing interactions are involved in which the magnetic moments couple strongly within chains while slightly weaker exchange interactions exist between chains composed of several interaction pathways. Magnetic frustration arising from these competing interactions and the 3D interactions may lead to the appearance of short-range magnetic

correlations along the chains at low temperature, such as the case of $CaMnGe_2O_6$.

In this chapter, we will demonstrate the existence of such 1D spin correlations in $CaMnSi_2O_6$, whose crystal structure has been determined recently by Nestola et al.[5]. This compound crystallizes with the C2/c space group, similar with the structure of $CaMnGe_2O_6$ but with a reduced unit cell volume. The magnetic properties of $CaMnSi_2O_6$ have not yet been reported, so we will investigate the magnetic properties and magneto-electric properties in $CaMnSi_2O_6$. The comparison of the $CaMnGe_2O_6$ and $CaMnSi_2O_6$ structures will also be addressed.

6.2 Experimental details

6.2.1 Sample preparation

Polycrystalline $CaMnSi_2O_6$ was prepared under high-pressure and high-temperature (HPHT) conditions in Belt-type and Conac anvil systems. The latter was used in order to synthesize one sample with large volume ($\sim$0.8cm^3) for neutron diffraction. The setups of Belt- and Conac-type have been described in chapter 2. Note that in this chapter, all the characterizations and measurements were performed on the sample synthesized using the Conac system. The stoichiometric mixture of reagent-grade CaO, MnO and SiO_2 was ground in an agate mortar. Then, the mixed powder was filled into a platinum capsule. The capsule was put into a special assembly as illustrated in chapter 2. Then the HPHT synthesis experiment was carried out under 5GPa, 1200°C for 3 hours. The detailed description of HPHT experimental process can be found in chapter 3.

6.2.2 X-ray and neutron powder diffraction

The sample was characterized by x-ray powder diffraction (XRPD) using a Bruker D8 diffractometer with Cu Kα1 radiation (1.5406 Å) selected by a Ge (111) primary beam monochromator in the range 10$\sim$90° with a 0.02° step size. To investigate the nuclear and magnetic structures, a neutron powder diffraction (NPD) experiment was carried out on the two-axis diffractometer D1B at Institut Laue Langevin (ILL), between 1.7 K and room temperature. For nuclear structure refinement, NPD patterns were recorded at 300 K with the 1.28 Å wavelength corresponding to the (311) Bragg reflection of a germanium monochromator. The 2.52 Å wavelength corresponding to the (002) Bragg reflection of a pyrolytic graphite monochromator was used for magnetic structure investigation, with longer data collections at 2, 15, 30, 100 and 300 K as well as a temperature ramp between 2 K and 300 K on heating process. The XRPD and NPD data were analyzed by the Rietveld method using the Fullprof suite programs[9].

6.2.3 Magnetic susceptibility measurement

The temperature-dependent magnetic susceptibility was measured on a Quantum Design Magnetic Property Measurement System (MPMS). The dc magnetic susceptibility was measured from 2 K to 350 K in zero field cooled (ZFC) and field cooled (FC) procedures under magnetic

field of 0.1T. Field-dependent magnetization was measured between 2 K and 350 K with a field sweep from 0 to 5 T.

6.2.4 Specific heat measurement

The specific heat measurement was carried out using a relaxation technique with a Quantum Design Physical Property Measurement System (PPMS) in the temperature range of 2-100K. The pelletized sample was mounted on sample platform with Apiezon N-grease for better thermal contact.

6.2.5 Electrical properties

To study the magnetoelectric properties of $CaMnSi_2O_6$ the temperature dependence of electric polarization was measured under various magnetic fields (0, 2, 4, 6 and 8 T). The sample was sintered to improve grain connectivity by heat treatment of a pressed pellet at 623 K for 20 hours. Then, the pellet was coated with silver epoxy on both sides to make conducting electrodes. Electrical polarization was then estimated by using the pyroelectric current measurement technique, as described in chapter 2. The magnetoelectric annealing was performed by simultaneously applying an electric field E of ±435 KV/m and a magnetic field μ_0H of 8 T in perpendicular directions, at 100 K and then cooled the sample down to 2 K. Then, the pyroelectric current curves under various magnetic fields were recorded using a Keithley 6514A electrometer while increasing the temperature at a rate of 3 K/min. Electric polarization was obtained by integration of the time dependence of the pyroelectric current.

6.3 Results and discussion

6.3.1 Crystal structure

The crystal structure of $CaMnSi_2O_6$ under various pressures has been previously reported a part as an investigation of its crystal structure under pressure[5]. It crystallizes with monoclinic C2/c symmetry corresponding to the high clinopyroxene structure type. Here the crystal structure was first examined by XRPD at room temperature. As shown in figure 6.1, $CaMnSi_2O_6$ crystallizing with C2/c space group was prepared as a majority phase, with $CaCO_3$ (R-3c) as only impurity phase. The Rietveld refinement of XRPD was in good agreement with the published data, and was used as a starting structure model for following NPD refinements. Figure 6.2 shows the morphology of $CaMnSi_2O_6$ grains. The figure on the right presents a grain with typical shape and crystal faces. In order to extract the precise atomic positions aiming to compare $CaMnSi_2O_6$ to the isostructural $CaMnGe_2O_6$, the NPD patterns of $CaMnSi_2O_6$ at room temperature, measured at a wavelengths of 1.28Å and 2.52Å, were refined, and the final Rietveld plot is shown in figure 6.3 . For the 2.52Å data, the background was described by linear interpolation of selected points in the pattern; for the 1.28Å data, a polynomial function with 12 parameters was adopted to describe the upward tendency of background at low angles. A Thomson-Cox-Hastings model of the reflection profile was used[10].

Low angle peak asymmetry was taken into account using the Berar-Baldinozzi model[11]. Two $CaCO_3$ phases with R-3c and Pmcn space groups were detected as impurity phases; they were introduced in the pattern description and their cell parameters and scale factor were refined. The final refinement yielded 3.11 (15)% for $CaCO_3$ (R-3c) and 3.45(50)% for $CaCO_3$ (Pmcn) in weight fraction. The refinement results and main interatomic distances, bond valence sums and polyhedra distortion calculated using the BonStr program[12] are presented in table 6.1 and 6.2.

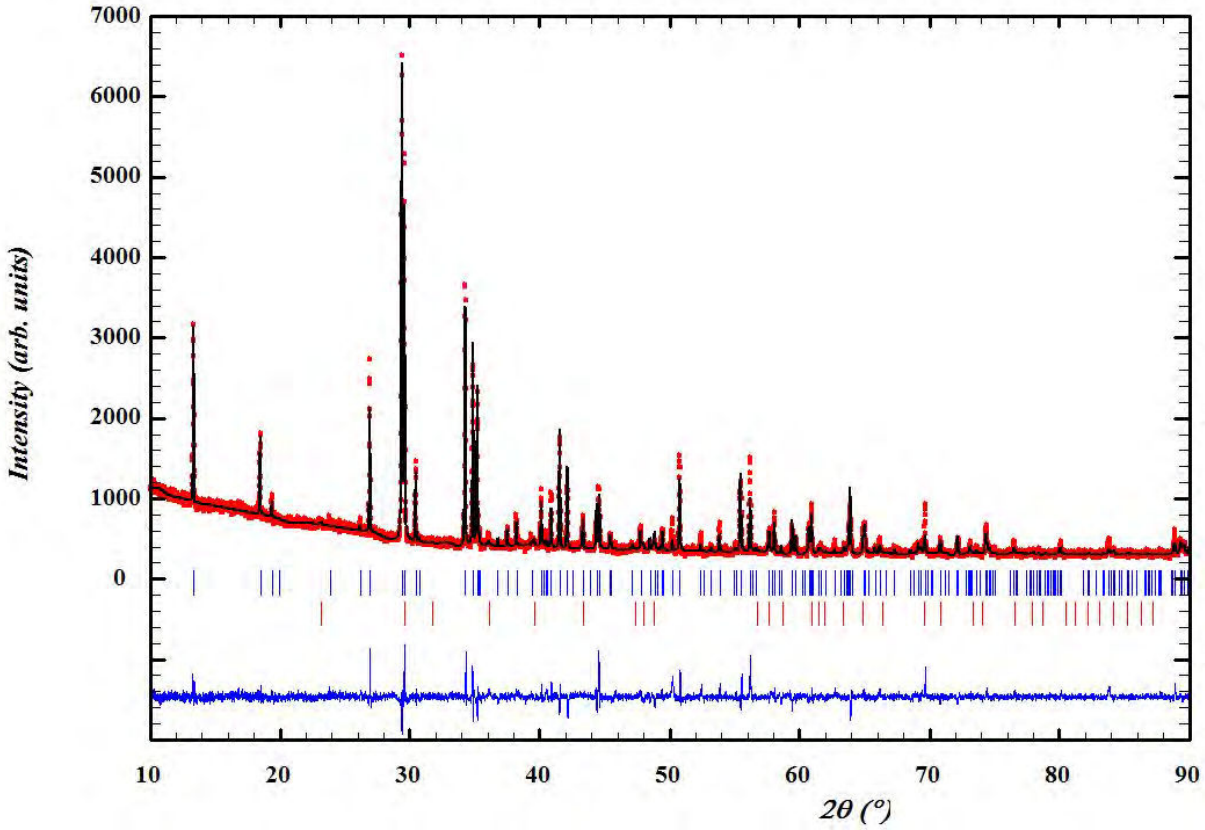

Figure 6.1: Rietveld refinement of $CaMnSi_2O_6$ from XRPD data taken at room temperature. Observed (red), calculated (black), and difference (blue) plots are shown. Bragg reflections of $CaMnSi_2O_6$ are denoted by blue tick marks. The lower set of Bragg reflections belong to a $CaCO_3$(R-3c) impurity phase.

The crystal structure of $CaMnSi_2O_6$ is shown in figure 6.4. Similar to the structure of $CaMnGe_2O_6$, $CaMnSi_2O_6$ is formed by the alternate stacking of layers made of MnO_6 octahedra and layers of GeO_4 tetrahedra along the a-axis. In the octahedral layer, MnO_6 octahedra share their O1-O1 edges to form zigzag infinite chains along the c-axis. As shown in figure 6.4, the MnO_6 octahedral chains are linked by corner-sharing SiO_4 chains along the a-axis via the O1-O2 edge. This structural stacking gives rise to two possible magnetic super-super exchange pathways between Mn^{2+} cations belonging to adjacent octahedral chains (see the marked shade in figure 6.4) through the O1-O2 edge of SiO_4 tetrahedron.

The structure parameters extracted from Rietveld refinement of NPD are in good agree-

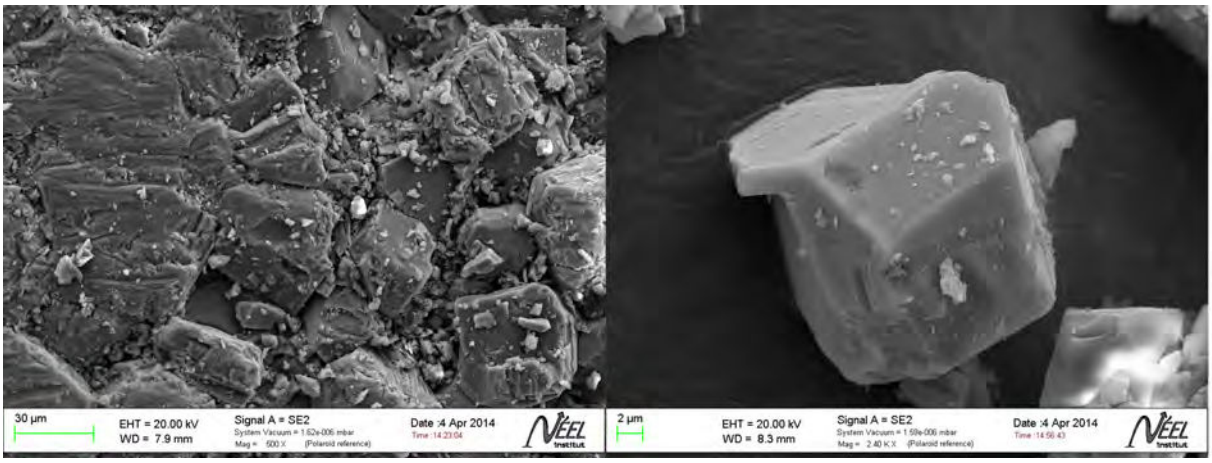

Figure 6.2: SEM images show the morphology of NPD pattern of $CaMnSi_2O_6$.

ment with the reported results from single crystal sample[5]. From both structural chemistry and magnetism viewpoints, it is tempting to compare the principal structural parameters for $CaMnGe_2O_6$ and $CaMnSi_2O_6$. Table 6.3 summarized the main structural parameters. The substitution of Ge by Si decreases the unit cell volume by 7.7%, which is mainly the consequence of the decrease of the a and c unit cell parameters (the b unit cell parameter seems not to be affected with smaller decrease of 0.4%, comparing to the reduction of 3.5% and 3.6% for a and c parameters respectively). However, the beta angle slightly increases from $CaMnGe_2O_6$ to $CaMnSi_2O_6$. Intuitively, the difference on structure parameters between $CaMnGe_2O_6$ and $CaMnSi_2O_6$ is associated with the Si/Ge site. The average distance <Si/Ge-O> decreases by 7.2% from $CaMnGe_2O_6$ to $CaMnSi_2O_6$ because of the bigger ionic radius of Ge^{4+} (0.39Å) when comparing to Si^{4+} (0.26Å). This increment also leads to the considerable increase of O3-O3-O3 angle of kinking tetrahedra chains from 155.48° ($CaMnGe_2O_6$) to 163.52° ($CaMnSi_2O_6$), as presented in figure 6.5. Referring to the ideal topology of pyroxene, as discussed in chapter 1, the pyroxenes with ideal O-rotation have O3-O3-O3 angle equal to 120°, while the so-called extended structures (E-chain) are characterized by a 180° O3-O3-O3 angle. In this respect, the tetrahedra chains of $CaMnSi_2O_6$ are closer to the E-chain model. As the c-axis corresponds to two corner-sharing tetrahedra, the increase of the O3-O3-O3 angle accordingly results in an extension along the c-axis. Because of the accompanied reduction of volume of tetrahedra, this effect indeed does not increase the c unit cell parameter.

The previously reported rigid-group thermal-vibration analysis reveals that in pyroxene structure, the Si/GeO_4 tetrahedron is the most rigid whereas the O3-O3 edge within the tetrahedron is quite flexible[17]. And according to the steric effect of stereochemical relations in pyroxenes, the tetrahedra chains will inevitably interact with adjacent octahedra chains by the O1-O2 edge of tetrahedron. In the MnO_6 octahedron, the alternation of Mn-O2 distance is vanishing, and can be neglected, however, the two Mn-O1 distances are comparably reduced from $CaMnGe_2O_6$ to $CaMnSi_2O_6$. This reduction matches well with the variation of tetrahedra chains. Consequently, the distortion of octahedron in $CaMnSi_2O_6$ is smaller than that of in

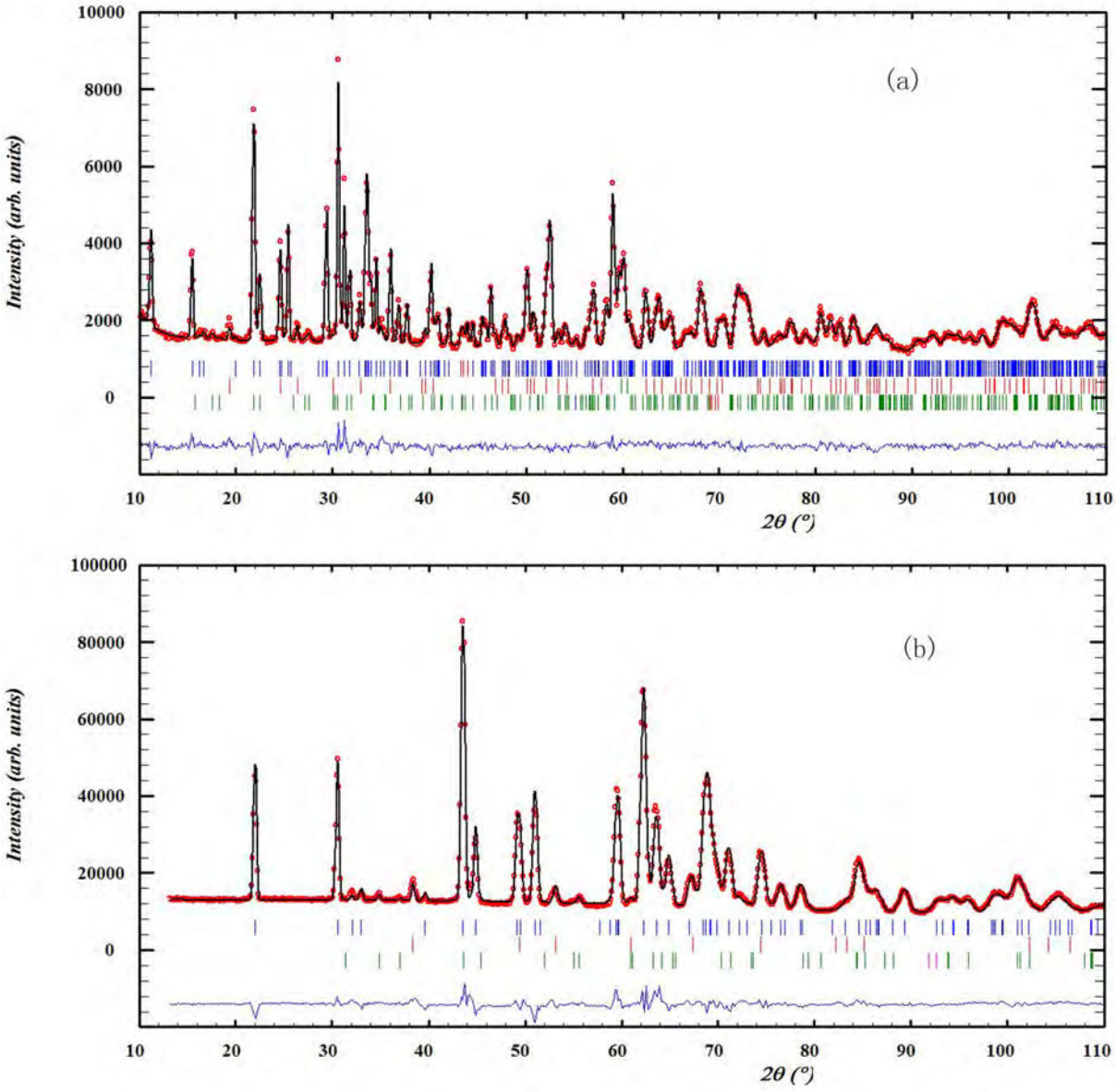

Figure 6.3: Rietveld refinement of $CaMnSi_2O_6$ of NPD data taken at room temperature with neutron wavelengths of 1.28Å (a) and 2.52Å(b). Observed (red), calculated (black), and difference (blue) plots are shown. Bragg reflections of $CaMnSi_2O_6$ are denoted by blue tick marks. The middle set of Bragg reflections belong to a $CaCO_3$(R-3c) impurity phase, and the lowest set of tick marks denote another impurity phase $CaCO_3$ (Pmcn).

$CaMnGe_2O_6$, and the bonding Mn-O is more covalent in $CaMnSi_2O_6$. The distance of nearest-neighbors (NN) Mn-Mn within the octahedra chain decreases by 3.4%, and the Mn-O1-Mn angle between NN Mn^{2+} cations, which is responsible for the possible super-exchange magnetic interactions, decreases by 2.23°.

Table 6.1: Agreement factors and refined structural parameters for $CaMnSi_2O_6$at 300K.

Name	position	x	y	z	B(Å^2)
Ca	4e	0.00000	0.3029(8)	0.25000	1.71(15)
Mn	4e	0.00000	0.9068(10)	0.25000	0.47 (13)
Si	8f	0.2896(5)	0.0908(6)	0.2383(9)	0.57(9)
O1	8f	0.1216(4)	0.0920(4)	0.1551(7)	0.43(7)
O2	8f	0.3645(4)	0.2424(4)	0.3303(7)	0.58(7)
O3	8f	0.3485(3)	0.0209(4)	0.9966(7)	0.30(6)
R_p=2.89, R_{wp}=3.67, R_{exp}=0.95, Chi^2=14.9, R_{bragg}=4.84					
a=9.9209(2) Å, b=9.1370(2) Å, c=5.2747(1) Å, α=90°, β=105.128(3)°, γ=90°					

Table 6.2: Principal cation-anion distances (Å) and angles for $CaMnSi_2O_6$ and $CaMnGe_2O_6$ at 300K (NPD using λ =1.28Å).

	$CaMnSi_2O_6$	$CaMnGe_2O_6$		$CaMnSi_2O_6$	$CaMnGe_2O_6$
Ca-O1	2.395(7)	2.417(7)	Si/Ge-O1	1.609(6)	1.716(4)
Ca-O2	2.308(4)	2.326(4)	Si/Ge-O2	1.587(6)	1.718(5)
Ca-O3	2.639(6)	2.746(7)	Si/Ge-O3	1.662(7)	1.803(5)
Ca-O3	2.750(6)	2.614(6)	Si/Ge-O3	1.680(6)	1.808(5)
Ave.Dist.	2.523(2)	2.526(2)	Ave.Dist.	1.635(3)	1.761(2)
BVS	1.99(1)	1.94(1)	BVS	3.91(3)	3.89(3)
Distortion	50.213×E-04	42.456×E-04	Distortion	5.432×E-04	6.340×E-04
Mn-O1	2.210(8)	2.255(9)	Mn-Mn (intra)	3.140(7)	3.249(8)
Mn-O1	2.162(3)	2.187(9)	Mn-Mn (inter1)	5.740(7)	5.918(7)
Mn-O2	2.131(8)	2.125(8)	Mn–Mn(inter2)	6.744(9)	6.889(1)
Ave.Dist.	2.168(3)	2.189(3)	Mn-O1-Mn	91.77(12)°	94.0(4)°
BVS	2.17(2)	2.06(2)	O3-O3-O3 (SiO_4)	163.52(19)°	155.48(21)°
Distortion	2.266×E-04	5.947×E-04			

Table 6.3: Comparison of principal structural parameters(distance in Å) for $CaMnGe_2O_6$ and $CaMnSi_2O_6$.

Parameter	$CaMnGe_2O_6$	$CaMnSi_2O_6$	△	%
a	10.2794(3)	9.9209(2)	0.3585	3.5
b	9.1756(3)	9.1370(2)	0.0386	0.4
c	5.4714(2)	5.2747(1)	0.1967	3.6
beta	104.244(2)°	105.128(3)°	-0.884°	-0.9
V(Å^3)	500.20(3)	461.57(2)	38.63	7.7
<Ge/Si-O>	1.761(2)	1.635(3)	0.126	7.2
Mn-Mn(intra)	3.249(8)	3.140(7)	0.109	3.4
Mn-O1-Mn	94.0(4)°	91.77(12)°	2.23°	2.4
O3-O3-O3(Ge/SiO_4 chain)	155.48(21)°	163.52(19)°	-8.04°	-5.2

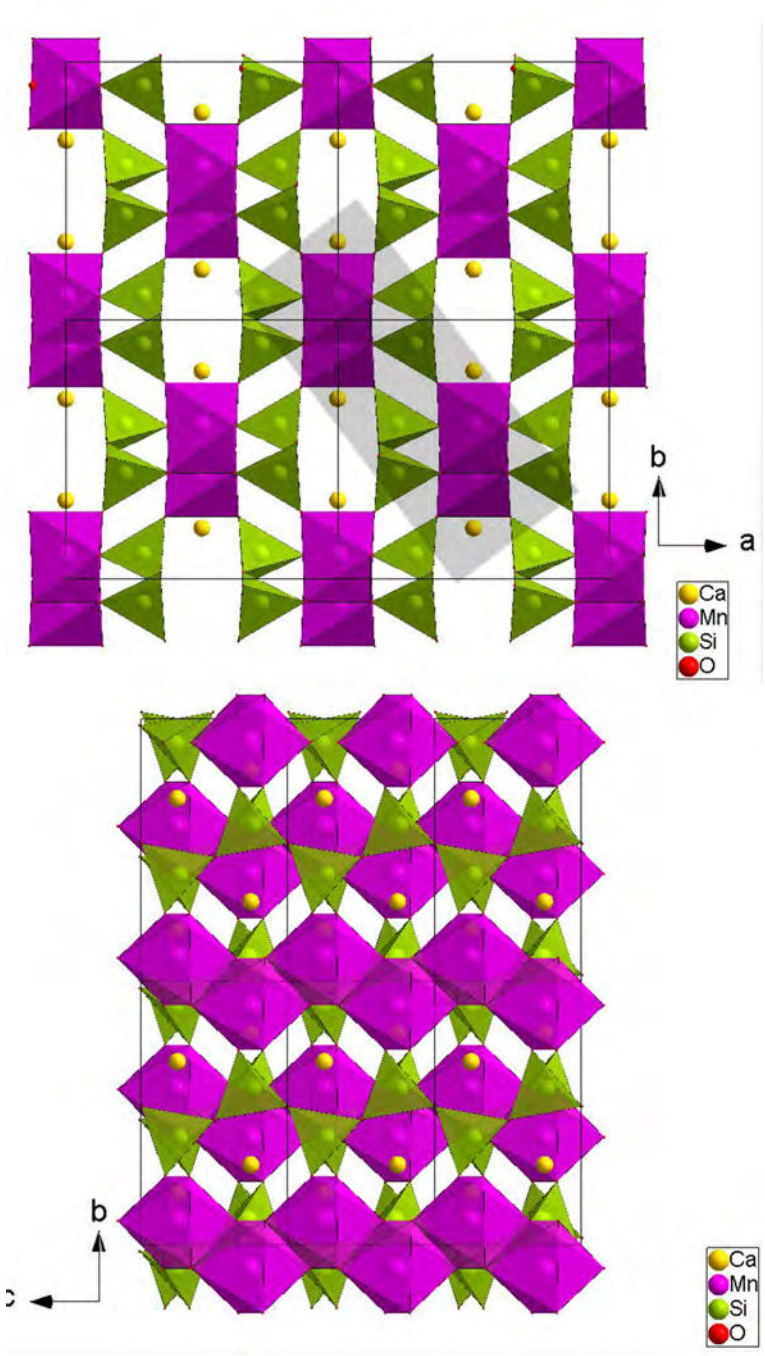

Figure 6.4: (upper) Projection of the $CaMnSi_2O_6$ structure along the c-axis. (Lower) The edge-sharing MnO_6 zigzag chains and the SiO_4 tetrahedra via corner sharing, derived from NPD at room temperature.

6.3.2 Magnetic properties

Figure 6.6 shows the temperature dependence of magnetic susceptibility for $CaMnSi_2O_6$. A cusp in the susceptibility at T_N=12K signals a transition to an AFM state, and the data collected under ZFC and FC conditions slightly bifurcate at lower temperature (see the inset

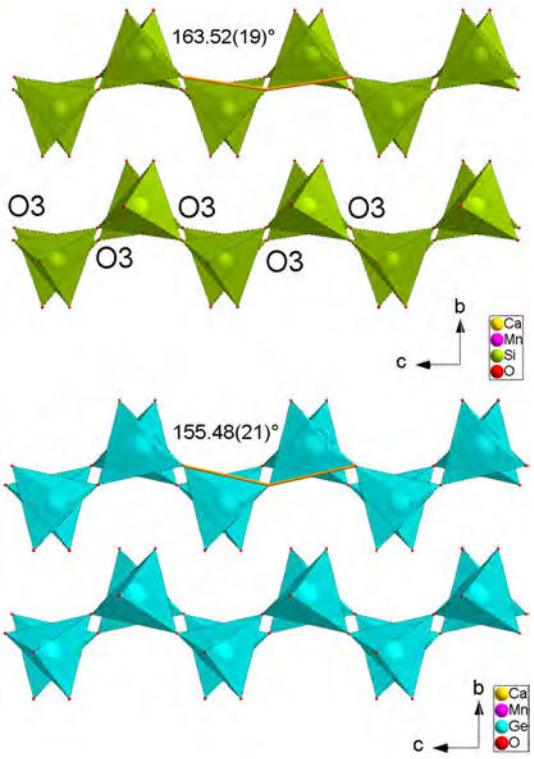

Figure 6.5: (upper) Projection of the Si tetrahedra layers along the a-axis; (lower) projection of the Ge tetrahedra layers. The O3-O3-O3 angles are marked.

of figure6.6). Inspection of the M-T curve collected under 0.01T reveals that there is a small opening bifurcation of ZFC and FC curves below 100K. The origin of this magnetic anomaly , which is attributed to short-range magnetic correlation, is discussed in the neutron diffraction section. The Curie-Weiss law (χ=C/(T-θ)) was used to fit the paramagnetic portion of the inverse magnetic susceptibility at 0.1 T between 200 K and 350 K. This yields an effective moment μ_{eff} = 5.76 (1) μ_B/Mn^{2+}, which is close to the spin-only value of 5.92 μ_B for Mn^{2+} cations in the high spin state. The negative Weiss temperature of -39(1) K indicates that antiferromagnetic interactions are predominant in this system. The empirical frustration index f for $CaMnSi_2O_6$ is determined as 3.56 which is a slightly larger than that of $CaMnGe_2O_6$ (2.33). The reinforcement of magnetic frustration is likely to be the result of coincidentally decreased crystal structure parameters.

Field-dependent magnetization isotherms M(H) were measured between 2 K and 350 K and are presented in figure 6.6(b). The field-induced magnetization is almost linear up to applied fields of 5T above T_N. However, the derivative of M-H curve at 2K, as shown in the inset of figure 6.6 (b), exhibits an apparent variation of the slope of M-H at μ_0H$\sim$2.28T (the maximum of dM/dH), indicative of a field induced metamagnetic transition. No saturation can be reached with the maximum field applied (M$\sim$0.5μ_B/Mn^{2+} at 5T).

To further clarify the magnetic anomaly, the measurement of the heat capacity on $CaMnSi_2O_6$ was carried out. Figure 6.7 (a) shows the temperature dependence of the specific heat for $CaMnSi_2O_6$. A maximum in C_p-T curve around 12K supports the AFM ordering transition

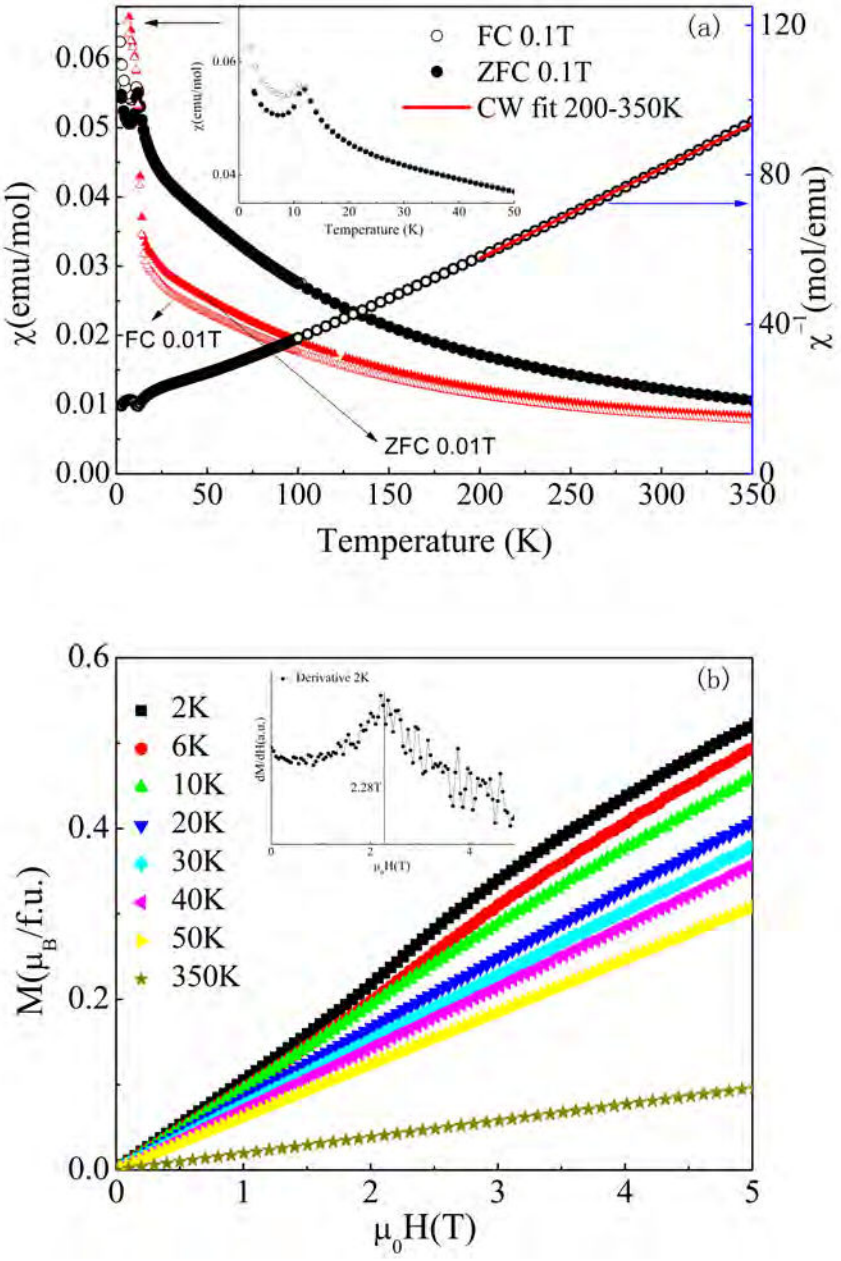

Figure 6.6: (a) Temperature dependence of the magnetic susceptibility of $CaMnSi_2O_6$ under magnetic fields of 0.1 and 0.01T. The Curie-Weiss fit for inverse magnetic susceptibility was presented with red solid line. Inset shows the low temperature regime. (b) Isothermal magnetization curves of $CaMnSi_2O_6$ between 2K and 350 K. Inset presents the dM/dH curve at 2 K, showing the magnetic field induced metamagnetic transition under magnetic field of 2.28T.

as measured by magnetic susceptibility. This temperature coincides with the appearance of the magnetic reflection peaks in neutron diffraction (see below). In order to properly extract the magnetic component of the specific heat capacity of $CaMnSi_2O_6$, the heat capacity of

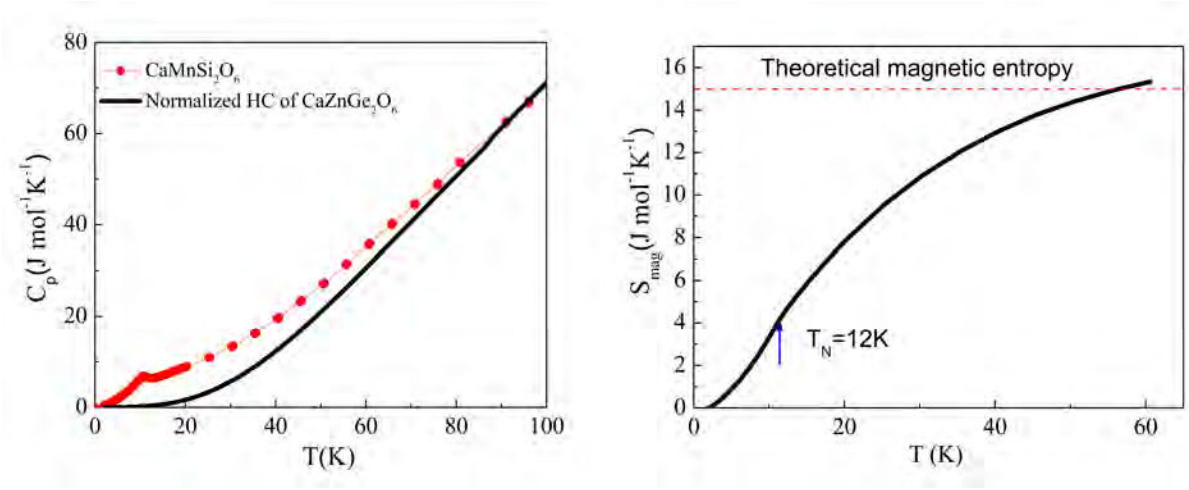

Figure 6.7: (a)Specific heat capacity of $CaMnSi_2O_6$ and $CaZnGe_2O_6$ which is used as a lattice standard after normalizing the scale at 100K. (b)(black)The magnetic component of the specific heat capacity of $CaMnSi_2O_6$; (blue)The entropy released through magnetic ordering.

a diamagnetic isostructural compound $CaZnGe_2O_6$ was measured to account for the lattice component of $CaMnSi_2O_6$. The Cp vs T curves of $CaZnGe_2O_6$ and $CaMnSi_2O_6$ display distinct behavior, although the compounds are isostructural. These two Cp curves cross over at around 50 K, and above, the heat capacity value of $CaZnGe_2O_6$ is bigger than that of $CaMnSi_2O_6$ over the measured temperature range. This discrepancy may arise from their different molar masses and volumes. We may estimate the lattice contribution of $CaMnSi_2O_6$ by normalizing the temperature of the Cp(T) of $CaZnGe_2O_6$. The magnetic component of heat capacity of $CaMnSi_2O_6$, C_{mag}, as shown in figure 6.7(b) was obtained by subtracting the normalized phonon contribution from $CaZnGe_2O_6$. The experimental magnetic entropy with S_m=15.2J/mol/K at 100 K, derived from the C_{mag}-T curve by integrating C_{mag}/T dT, is close to the theoretical value of 14.9 J/mol/K for the spin S=5/2 Mn^{2+} ions given by Rln(2S+1), as seen in figure 6.7 (b). The magnetic entropy first drops down slowly on cooling over a broad temperature range between 100K and Neel temperature T_N=12K, then below ~12K, a sharp decrease follows. The former phenomenon is consistent with a considerable entropy release, indeed, a majority of the magnetic entropy (73.7%) is released above T_N. This feature, very similar to that of $CaMnGe_2O_6$, will also be attributed to 1D short-range magnetic correlations, as explained in the following section.

6.3.3 Magnetic structure

Figure 6.8 shows temperature dependent NPD patterns below 15 K for $CaMnSi_2O_6$. The magnetic reflections below 12K can be clearly observed. Figure 6.9 presents the observed, calculated and difference NPD patterns below 100K for $CaMnSi_2O_6$. The patterns collected at 100, 30 and 15K can be refined well by a structural model with C2/c space group used at room temperature. Even though no structural phase transition is observed between 15K and 100K, the diffuse scattering, which is characteristic of a broad diffracted intensity, is found

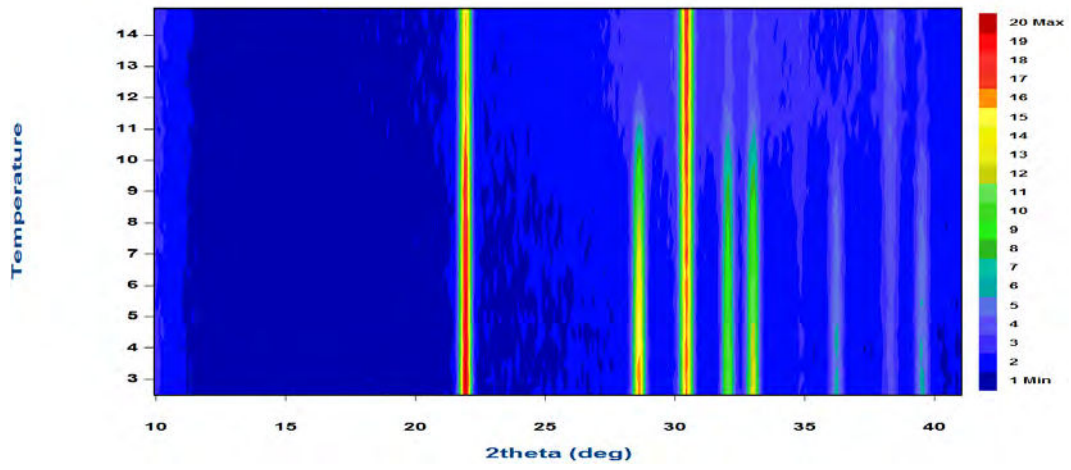

Figure 6.8: Plot of neutron powder diffraction scans showing up the magnetic transition at 12K using a wavelength of 2.52Å.

centered around 2θ=28.9° for patterns at 15K and 30K. This diffuse scattering clearly reflects the presence of short-range magnetic ordering at those temperatures. It is worth noting that the appearance of diffuse scattering below 100K is consistent with the change of slope of M-T curve. The physical picture and mechanism of observed short-range ordering will be discussed in the next section.

At low temperature all magnetic reflections can be indexed with a commensurate magnetic propagation vector k=(0,0,0). The magnetic structure was determined by symmetry analysis, following the representation analysis technique invented by Bertaut[13]. Calculations were carried out using version 2 K of the program SARAh-Representation analysis[14] and BasIreps integrated in Fullprof Suite [15]. For the Mn^{2+} cations on the 4e Wyckoff position of space group C2/c, the decomposition of magnetic representation is Γ=1Γ_1^1+1Γ_2^1+2Γ_3^1+2Γ_4^1. The different basis vectors calculated using the projection operator technique associated with each IR are presented in table 6.4. Four magnetic ions are confined in the unit cell but there are only two possible magnetic couplings. Since the C centering is preserved by the k vector, the magnetic moments carried by the two Mn^{2+} cations related by the C translation are symmetrically identical. Consequently the two magnetic coupling possibilities are : a ferromagnetic one represented by F=(S1+S2)+(S3+S4) and an antiferromagnetic one represented by C=(S1+S2)-(S3+S4). According to the magnetization measurements, the possible antiferromagnetic structure models determined from the symmetry analysis are Γ_2 and Γ_4. They were tested by Rietveld refinement with NPD at 2 K. The best fit was achieved with the model described by the IR Γ_4 with the magnetic space group C2'/c. However, in FC and ZFC M(T) curves, it is clear that there is a ferromagnetic component below 12K. The model used to refine the neutron data (Γ_4) is purely AFM therefore incompatible with the ferromagnetic component detected in magnetization measurements. The final refinement for the 2 K NPD pattern is shown in figure 6.9. The presence of systematic discrepancies in the difference plot reveals that the refinement used as Γ_4 is not perfect, suggesting that the ferromagnetic model IR has

to be taken into account. In fact, we have considered other models by combining Γ_4 and Γ_1 (a pure ferromagnetic model). However, all attempts give a vanishing moment for ferromagnetic component. As a result, we adopted the Γ_4 IR to describe the magnetic structure for the title compound.

Table 6.4: Basis vectors for Mn^{2+} at 4e site (indicate position of Mn1(0, 0.9068, 0.25), Mn2(0.5, 0.4068, 0.25), Mn3 (0, 0.0932, 0.75), Mn4(0.5, 0.5932, 0.75). Notations: F=S1+S2+S3+S4, C= S1+S2-S3-S4.

IR	Basis vector	Space group
Γ1	(0,Fy,0)	C2/c
Γ2	(0,Cy,0)	C2/c'
Γ3	(Fx, 0, Fz)	C2'/c'
Γ4	(Cx,0,Cz)	C2'/c

The magnetic structure of $CaMnSi_2O_6$ at 2K is shown in figure 6.10. The Mn^{2+} spins are confined by symmetry in the (a,c) plane, arranged mainly along the a-axis with a small angle of 12.87° and 91.92° to the c-axis, with magnetic moment of m_a=4.300(2)μ_B, m_c=0.958(4)μ_B. The total ordered magnetic moment refined at 2 K is 4.16(1)μ_B/Mn^{2+} which is smaller than the theoretical spin-only ordered value gS=5μ_B for Mn^{2+}cation. The magnetic order is represented by antiferromagnetic coupling (J) between the Mn^{2+} cations within the MnO_6 octahedra zigzag chains, while the spin couplings between neighboring chains are complex due to the two super-super exchanges, J1 and J2. If both interactions are considered as antiferromagnetic, then the magnetic order observed leads to one of them (J2) to be unsatisfied. The temperature dependence of the magnetic moment is shown in figure 6.11 and confirms the T_N=12 K value for the magnetic ordering temperature, in agreement with our magnetic susceptibility and heat capacity measurements.

6.3.4 One dimensional short range spin correlations

To clarify the nature of short-range ordering below 100K, we compare the NPD patterns taken at 15, 30 and 100K for $CaMnSi_2O_6$. Figure 6.12(a) shows the comparison of NPD data between 15 , 30 and 100 K. The intensity of diffuse scattering around 2θ=29° clearly increases with the decrease of temperature featuring the gradual establishing of short range spin correlations. The NPD difference patterns between 15 and 100K, and between 30 and 100K (figure 6.13(b)) both clearly display a maximum in the magnetic diffuse scattering at about Q=1.25 $Å^{-1}$(corresponding to d=4.97Å) with an asymmetric shape, signaling the presence of short range magnetic correlations. This broad asymmetric peak featured by the sharp rise at low Q (high d value) and a gradual decrease toward high Q (low d value), similar to that of $CaMnGe_2O_6$, is characteristic of one-dimensional short-range order. Compared to the next-nearest Mn^{2+} intrachain distance of 5.27 Å, this scattering can be attributed to the presence of short range magnetic correlations between Mn^{2+} cations along the octahedra chains with vanishing interchain interaction.

On account of the zigzag characteristic of the MnO_6 octahedra chains in $CaMnSi_2O_6$,

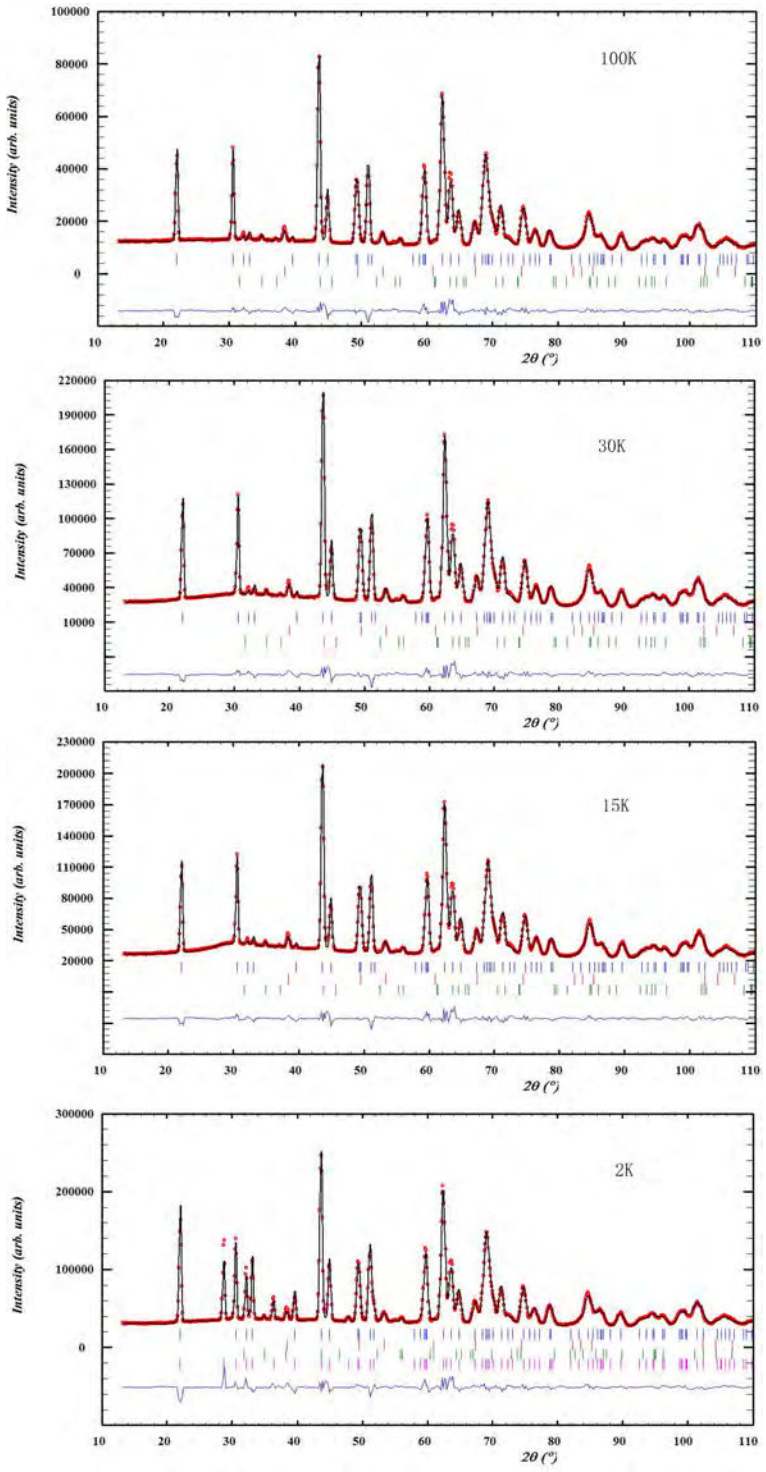

Figure 6.9: (a) Observed (symbols) and calculated (line) powder neutron diffraction patterns for $CaMnSi_2O_6$ taken at 2, 15, 30, 100 K. The lowest tick marks shows the magnetic reflections. The nuclear reflections are denoted by blue tick marks. The reflections marked in red and green belong to $CaCO_3$ impurity phases. The blue line shows the difference between the observed and calculated diffraction patterns.

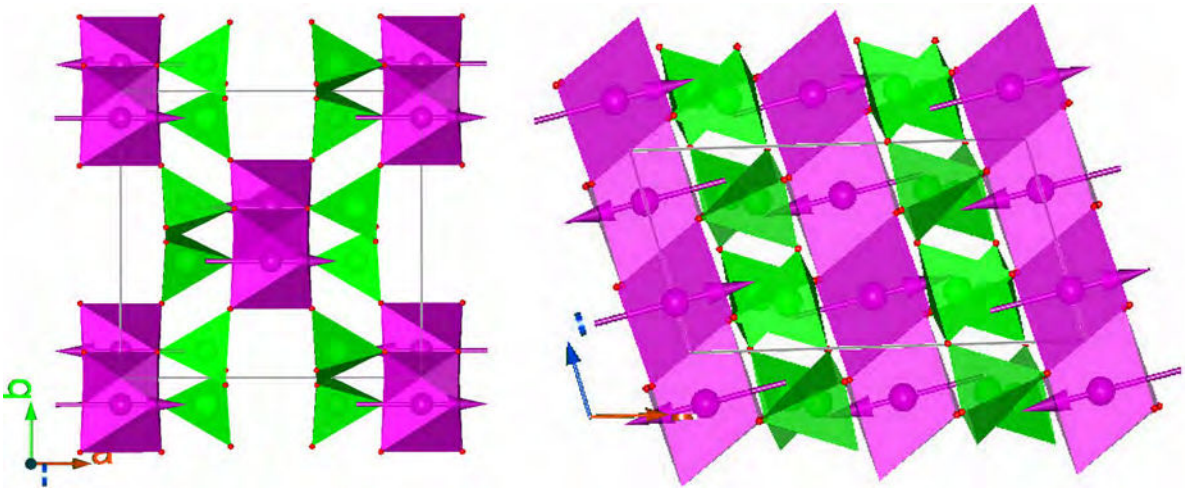

Figure 6.10: Representation of the magnetic structure of $CaMnSi_2O_6$.

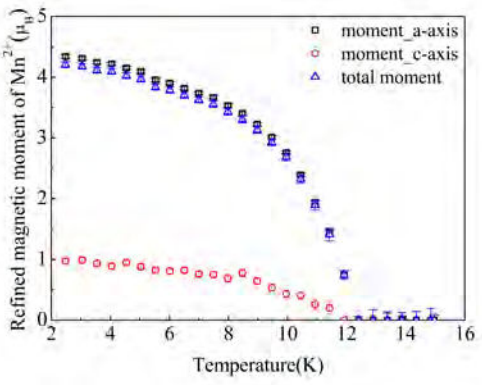

Figure 6.11: Evolution of the refined Mn^{2+} magnetic moment components as a function of temperature.

along with the determined magnetic structure, a one-dimensional magnetic correlation model, which has been described in the previous chapter, can be used to describe the diffuse scattering data. The 1D model describes that magnetic moments at Mn sites running exactly along c direction are aligned ferromagnetically whereas the nearest-neighbors are coupled with AFM configuration.

By applying this model and using the analytical structure factor S(Q) for magnetic correlation, the experimental data can be properly fitted by:

$$I_{exp} = I_l S(Q) - I_h f(Q)^2 \tag{6.1}$$

where the variables are the correlation length ξ, the intensity of the correlated signal I_l, and the intensity of the high temperature signal I_h; f(Q) is the form factor at 100K. The best fits are given in figure 6.13. For the data obtained by subtracting NPD pattern at 100K from that at 30K, the fit gives a correlation length ξ= 7.45±1 Å for the magnetic correlations along the

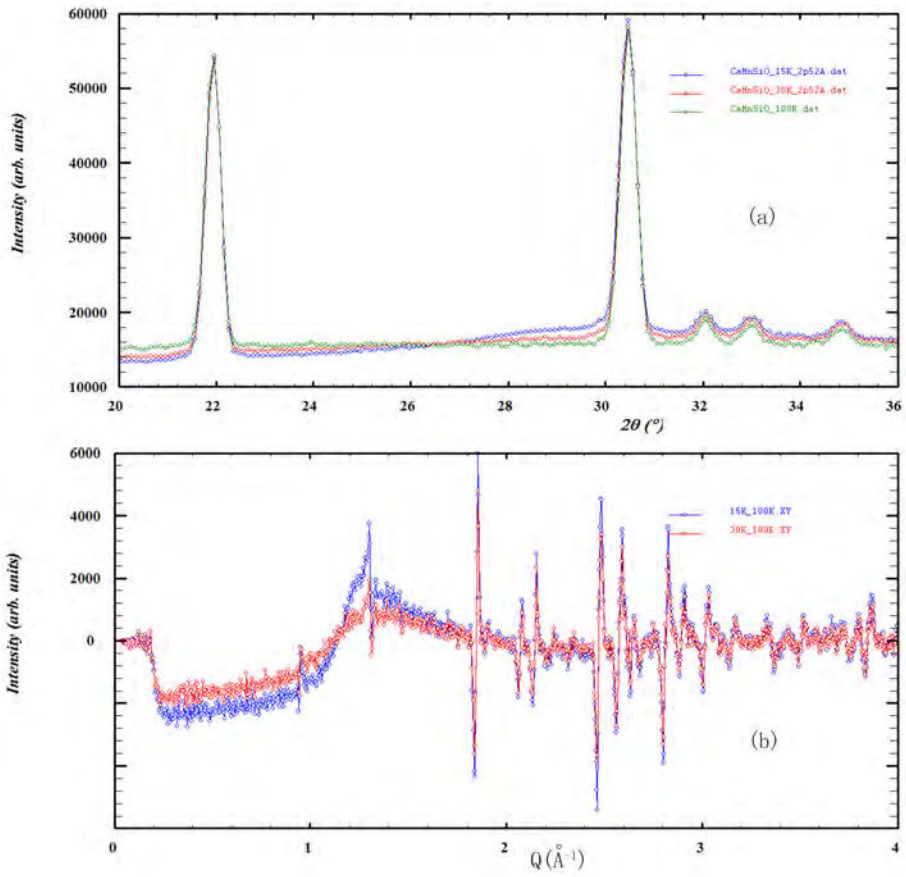

Figure 6.12: (a) Comparison between NPD data collected at 15, 30 K and 100 K in $CaMnSi_2O_6$. (b) The difference between NPD patterns from $CaMnSi_2O_6$ at T=15K and 100K (blue), and at T=30K and 100K(red).

c-axis, confirming the short-range characteristic. Interestingly, for the NPD pattern difference between 15K and 100K, a correlation length ξ= 17.29±2.45 Å is found, which is two times bigger that the former one. It is worth noting that the increase of correlation length from 30K to 15K clearly elucidates the evolution of one-dimensional short-range spin correlations along the c-axis. To summarize we have seen that the system first undergoes an evolution from the paramagnetic regime to 1D AFM state , with a correlation length increasing with the lowering of temperature , until at 12K, where a 3D AFM order sets in.

The temperature dependence of the lattice parameters for $CaMnSi_2O_6$ derived from Rietveld refinement of NPD data collected in the temperature range of 2-300K are shown in figure 6.14. The a- and b- parameters follow a standard evolution over the entire measured temperature range. No structure anomaly can be detected in the vicinity of the magnetic transition temperature. However, the c-parameter as well as the monoclinic beta angle exhibit a consistent anomaly below 100K, with a sharp decrease down to the lowest temperature. This may be attributed to a magnetostrictive effect associated with the short range magnetic correlations present below 100K. This anomaly being detected only along the c-axis and the beta angle supports that these short range magnetic correlations arise from antiferromagnetic

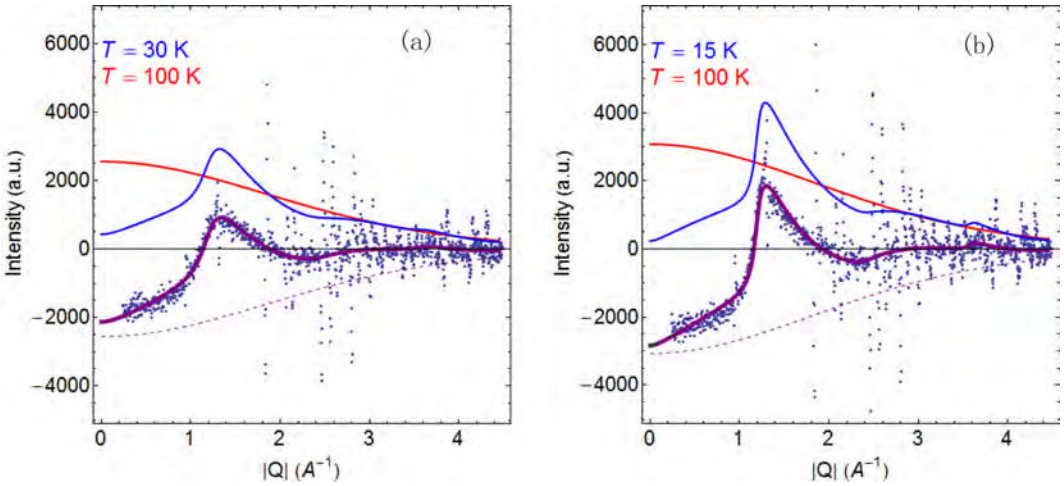

Figure 6.13: Diffuse neutron scattering by subtracting the NPD pattern at 100 K from patterns at 30 K (a) and 15K (b). The peak was well fitted by a model of 1D scattering. Red line shows the structure factor at paramagnetic regime (100K), blue line represents the simulated signal at 30K and 15K, the purple line shows the fit result to the experimental data (scatter points).

correlations between the Mn^{2+} cations of isolated 1D chains.

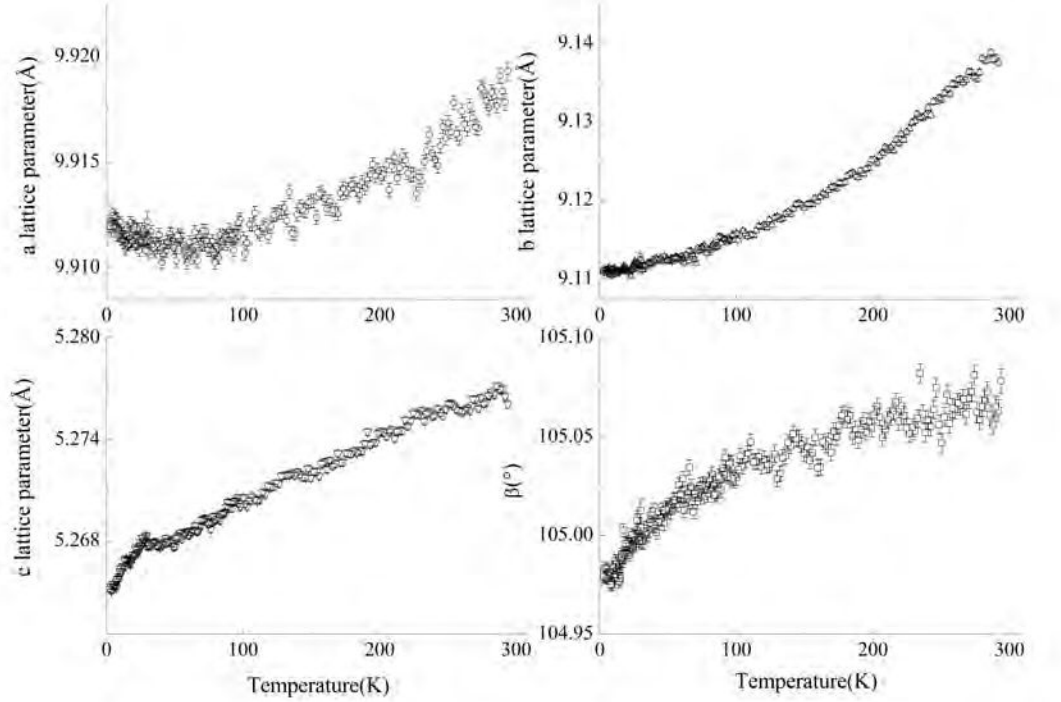

Figure 6.14: Lattice parameters of $CaMnSi_2O_6$ as a function of temperature from refinement of NPD.

6.3.5 Linear magnetoelectric effect of $CaMnSi_2O_6$

The magnetic symmetry with space group C2'/c derived from neutron diffraction at low temperature allows for linear magnetoelectric effect, and this can be appreciated by symmetry consideration as performed in previous chapter. The linear magnetoelectric effect can be established in the form:

$$P_i = \alpha_{ij} H_j \tag{6.2}$$

According to the symmetry consideration, the second-rank tensor is given by:

$$\alpha_{ij} = \begin{pmatrix} 0 & \alpha_{12} & 0 \\ \alpha_{21} & 0 & \alpha_{23} \\ 0 & \alpha_{32} & 0 \end{pmatrix} \tag{6.3}$$

Analogous to the linear ME in $CaMnGe_2O_6$, the off-diagonal character reflects that the perpendicular configuration between H and E fields for ME annealing must be used in order to measure the linear ME effect. Figure 6.15 shows the pyroelectric current as a function of magnetic field. No pyroelectric current can be observed in the absence of external magnetic field. The current appears with the presence of magnetic field just below the AFM transition temperature of 12K, and it becomes stronger with the increase of magnetic field. By reversing the annealing electric field, we were able to change the sign of induced current. The temperature dependence of electric polarization was then obtained by integrating the pyroelectric current with respect to time. As shown in figure 6.16, no polarization is observed with zero magnetic field while a magnetically induced polarization monotonically increases with increasing magnetic field. The induced electric polarization increases linearly with the increase of magnetic field at a rate of ~0.017(1) $\mu C/m^2/T$ (see the inset in figure 6.16). The observed maximum polarization value ($0.14\mu C/m^2$ under 8T) of $CaMnSi_2O_6$ is smaller in magnitude as compared to that of $CaMnGe_2O_6$. Similar to $CaMnGe_2O_6$, the nondiagonal ME tensor of $CaMnSi_2O_6$ has an antisymmetric part that results in a toroidic moment and makes $CaMnSi_2O_6$ a pure ferrotoroidic compound. In this work, the linear ME effect was observed indicating the presence of a spontaneous toroidal moment[16]. According to the spontaneous toroidic moment equation as shown in chapter 5, we could estimate the volumic toroidic moment in the monoclinic unit cell T=(-0.0042, 0, 0.0159) $\mu_B/Å^2$.

6.4 Discussion

The comparison of crystal structures of $CaMnSi_2O_6$ and $CaMnGe_2O_6$ reveals that the substitution of Ge by Si does not vary the structure symmetry and arrangement even though the volume of unit cell is reduced as seen from the decreased a and c cell parameters. The magnetic properties of $CaMnSi_2O_6$ are very similar to that of $CaMnGe_2O_6$, only the long range ordering temperature is lowered for Si case. The magnetoelectric effect as well as ferrotoroidic properties are also conserved. This is in contrast to other pyroxenes where the replacement of

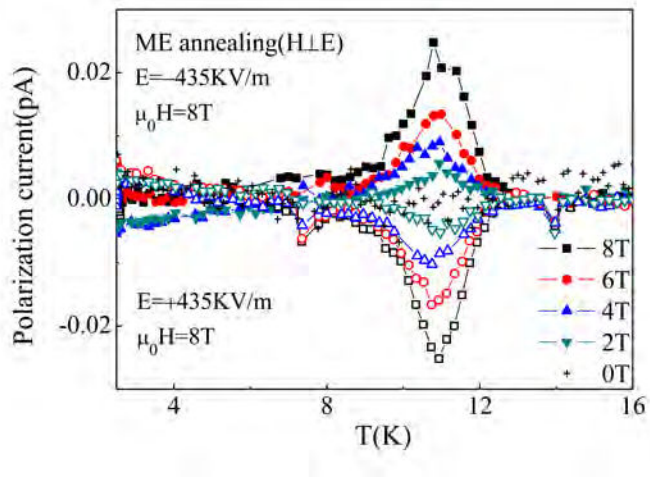

Figure 6.15: Temperature dependence of pyroelectric current under various magnetic fields.

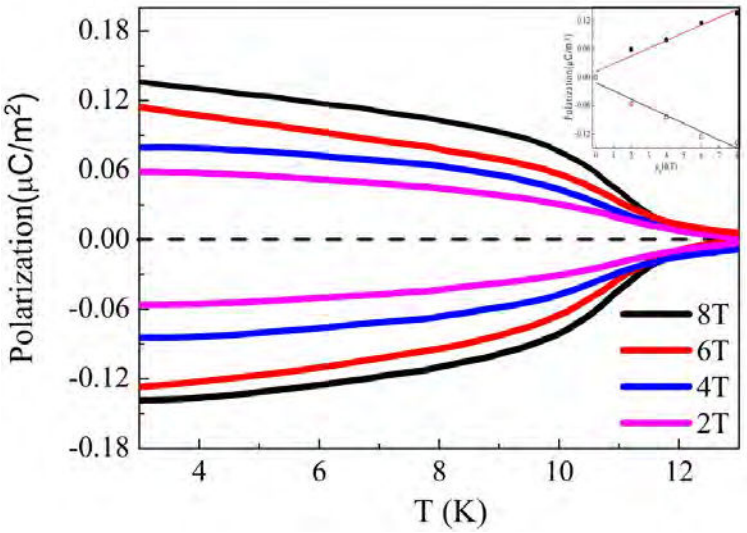

Figure 6.16: Temperature dependence of the polarization in $CaMnSi_2O_6$ under various magnetic fields; the inset shows the induced electric polarization as a function of applied magnetic field with different ME annealing manners.

Ge by Si greatly modifies the magnetic behavior and magnetoelectric properties. For example, ferromagnetic $NaCrGe_2O_6$ will be modified to be antiferromagnetic by the substitution of Ge by Si; $LiFeSi_2O_6$ exhibits linear magnetoelectric effect while $LiFeGe_2O_6$ does not[2, 4]. Therefore, the structural modifications brought by the Ge/Si replacement only marginally vary the magnetic interaction scheme in this $CaMnT_2O_6$ system.

Since $CaMnSi_2O_6$ and $CaMnGe_2O_6$ possess same magnetic structure, the magnetic frustration is also present in $CaMnSi_2O_6$. Since the intrachain exchange integral J is dominant, and if the J1 and J2 are in the same order, a triangular-like topology can be formed giving rise to magnetic frustration.

Several observations reveal that the presence of short-range spin correlations well above T_N in $CaMnSi_2O_6$. This was first supported by the measurement of heat capacity, and the large entropy release above T_N. Then the fit of diffuse scattering data with a phenomenological 1D magnetic correlation model yields correlation lengths $\xi = 7.45 \pm 1$Å (30K) and 17.29±2.45Å(15K), and both reflect the short range AFM correlation in this system. Moreover, the increase of correlation length reveals that the spin order in 1D grows with decreasing temperature.

Rather than showing the broad maximum at low temperature as a typical characteristic for low dimensional magnets, the magnetic susceptibility vs T of $CaMnSi_2O_6$ manifests a 3D nature of the magnetic exchanges. This is similar to the behavior observed in $CaMnGe_2O_6$. And the proposed scenario for $CaMnGe_2O_6$ is still appliable in $CaMnSi_2O_6$: This short range AFM correlation is assumed to be the consequence of magnetic frustration which favors the short-range spin order along the c-axis in a system with 3D exchange interactions.

6.5 Conclusion

In summary, silicate pyroxene $CaMnSi_2O_6$, characterized by zigzag MnO_6 octahedra chains and SiO_6 tetrahedra chains, was synthesized by high-pressure and high-temperature method and characterized by magnetic susceptibility, heat capacity, electric polarization and neutron diffraction measurements. The magnetic measurement reveals that $CaMnSi_2O_6$ undergoes long-range AFM transition at 12K. The short-range spin correlations below 100K was confirmed by combining heat capacity results and fitted diffuse magnetic neutron scattering data, and was complemented by the variation of lattice parameters as a function of temperature. By fitting the diffuse scattering at 15K and 30K to the 1D magnetic correlation model, we have drawn the physical picture of short-range AFM correlations developed below 100K. Magnetic frustration present in $CaMnSi_2O_6$ could be the main mechanism governing the present observations. The measurements of ME properties reveal that no spontaneous polarization arises below T_N until an external magnetic field is applied. The behavior of polarization shows a linear ME effect. Furthermore, the tensor of linear magnetoelectric effect has antisymmetric part which could result in a toroidal moment and makes the $CaMnSi_2O_6$ a pure ferrotoroidic compound.

Bibliography

[1] M.L.Plumer, A.Caille, A.Mailhot, Chapter 1, Critical properties of frustrated vector spin systems, Magnetic system with competing interaction, World Scientific Publishing Co.,1994. 137

[2] I. Kim, B. G. Jeon, D. Patil, S. Patil, et al., Observation of multiferroic properties in pyroxene $NaFeGe_2O_6$, J. Phys.: Condens. Matter 24, 2012, 306001. 155

[3] O.Janson, G.Nenert, M.Isobe, Y.Skourski, Y.Ueda, H.Rosner, A.A.Tsirlin, Magnetic pyroxenes $LiCrGe_2O_6$ and $LiCrSi_2O_6$: Dimensionality crossover in a nonfrustrated s=3/2 Heisenberg model, Phys. Rev. B, 90, 2014, 214424. 137

[4] C. Lee, J. Kang, J. Hong, J. H. Shim, M. H. Whangbo, Analysis of the Difference between the Pyroxenes $LiFeSi_2O_6$ and $LiFeGe_2O_6$ in Their Spin Order, Spin Orientation, and Ferrotoroidal Order, Chem. Mater. 26, 2014, 1745-1750. 137, 155

[5] Fabrizio Nestola, Tiziana Boffa Ballaran, Ross J. Angel, Jing Zhao, Haruo Ohashi, High-pressure behavior of Ca/Na clinopyroxenes: The effect of divalent and trivalent 3d-transition elements, American Mineralogist, 95, 2010, 832. 138, 139, 141

[6] Y. Sasago, M. Hase, K. Uchinokura, M. Tokunaga, N. Miura, Discovery of a spin-singlet ground state with an energy gap in $CaCuGe_2O_6$, Phys. Rev. B, 52, 1995, 3533. 137

[7] M. Isobe, E. Ninomiya, A.N. Vasilev, Y. Ueda, Novel Phase Transition in Spin-1/2 Linear Chain Systems: $NaTiSi_2O_6$ and $LiTiSi_2O_6$, J. Phys. Soc. Jpn., 71, 2002, 1423. 137

[8] Roser Valentí, T. Saha-Dasgupta, and Claudius Gros, Nature of the spin-singlet ground state in $CaCuGe_2O_6$, Phys. Rev. B 66, 2002, 054426. 137

[9] J. Rodriguez-Carvajal, Recent Advances in Magnetic Structure Determination by Neutron Powder Diffraction. Physica B, 192, 1993, 55-69. 138

[10] P. Thompson, D.E. Cox, J.B. Hastings, Rietveld refinement of Debye-Scherrer synchrotron X-ray data from Al_2O_3, J. Appl. Cryst., 20, 1987, 79-83. 139

[11] J.F. Bérar and G. Baldinozzi, Modeling of line-shape asymmetry in powder diffraction, J. Appl. Cryst., 26, 1993, 128-129. 140

[12] J. Rodrıguez-Carvajal, BondStr, 2010, www.ill.eu/sites/fullprof/ 140

[13] E.F. Bertaut, Representation analysis of magnetic structures, Acta Crystallogr. Sec. A 24, 1968, 217. 148

[14] A. S. Wills, A new protocol for the determination of magnetic structures using simulated annealing and representational analysis (SARAh), Physica B 278, 2000, 680. 148

[15] J. Rodriguez-Carvajal, BasIreps: a program for calculating irreducible representations of space groups and basis functions for axial and polar vector properties (see FullProf site: http://www.ill.eu/sites/fullprof). 148

[16] N.A Spaldin, M. Fiebig, M. Mostovoy, The toroidal moment in condensed-matter physics and its relation to the magnetoelectric effect, J.Phys.:Condens. Matter, 20, 2008, 434203. 154

[17] Subrata Ghose, Cheng Wan, Fujio P.Okamura, Crystal structures of $CaNiSi_2O_6$ and $CaCoSi_2O_6$ and some crystal-chemical relations in C2/c clinopyroxenes, American, Mineralogist, 72, 1987, 375-381. 141

[18] Elizabeth M.Seibel, J.H. Roudebush, Hui Wu, Qingzhen Huang, Mazhar N. Ali, Huiwen Ji, R.J. Cava, Structure and magnetic properties of the α-$NaFeO_2$-type honeycomb compound $Na_3Ni_2BiO_6$, Inorganic Chemistry, 52, 2013, 13605.

Chapter 7

Structure and magnetic properties in $CaCo_{1-x}Mn_xGe_2O_6$

7.1 Introduction

An attractive feature of pyroxene structure is the isolated MO_6 chains which can lead to low dimensional magnetic properties. The competing interactions within chains and between chains form a triangular-like geometry and may generate frustration in specific compounds such as $CaMnGe_2O_6$ discussed in chapter 5. The dominant exchange interactions in pyroxenes are often intra-chain interactions which determine the global magnetic configuration. The magnetic coupling in pyroxenes $CaMGe_2O_6$ can then be tuned by the d-orbital occupancy via substituting different transition-metal ions at the M^{2+} site. This makes the magnetic properties extremely rich in this family.

We have previously reported the detailed investigation of the structure, magnetic and physical properties of $CaMnGe_2O_6$, which presents a strong antiferromagnetic (AFM) coupling within the MnO_6 chains (see chapter 5). In contrast to this compound, the isostructural $CaCoGe_2O_6$ has been reported with a totally different magnetic structure, namely, a dominant ferromagnetic (FM) interaction in chains along the c-axis[3]. A compound involving extremely different spin configurations would be expected to exhibit interactions giving rise to different and potentially interesting physical properties. Alterations of the magnetic behavior can then be anticipated.

To reveal these possible phenomena, the solid solution between $CaMnGe_2O_6$ and $CaCoGe_2O_6$ was prepared and studied by means of magnetization and heat capacity measurement, and complementary x-ray and neutron diffraction. In this chapter, we present how the magnetic behavior of $CaCo_{1-x}Mn_xGe_2O_6$ evolves upon substitution of Mn for Co. Indeed, the introduction of Mn gives rise to enhanced magnetic frustration and spin disorder. A compound with complex magnetic structure is also obtained when the doping level of Mn is up to around 0.75. Since $CaNiGe_2O_6$ has similar magnetic structure[3] with $CaCoGe_2O_6$, a solid solution between them and between $CaMnGe_2O_6$ and $CaNiGe_2O_6$ may be helpful in understanding the physical properties. We also report experimental results concerning this substitution.

In addition, the magnetic point group of $CaCoGe_2O_6$ allows for the bilinear magnetic effect, and we will discuss this effect based on symmetry consideration.

7.2 Experimental detail

7.2.1 Sample preparation

Polycrystalline samples of the $CaCo_{1-x}Mn_xGe_2O_6$ solid solution (x=0, 0.25, 0.50, 0.625, 0.75, 0.875 and 1.0) were synthesized by solid-state reaction. The stoichiometric mixtures of reagent-grade $CaCO_3$, Co_3O_4, MnO_2 and GeO_2 were ground in an agate mortar and pressed into pellets. The pellets were placed in a platinum boat and heated in air to 1373 K at 2K/min, then held at 1373 K for 100 h and cooled down to room temperature. Intermediate regrinding and reheating were required in order to obtain essentially single phase samples. By the similar synthesis route, solid solution $CaNi_{1-x}Co_xGe_2O_6$(x=0.25, 0.5, 0.75) and $CaMn_{1-x}Ni_xGe_2O_6$ (x=0.25, 0.5, 0.75, x=1) have also been synthesized.

7.2.2 X-ray and neutron powder diffraction

The samples were characterized by x-ray powder diffraction (XRPD) using a Bruker D8 diffractometer with Cu Kα1 radiation (1.5406 Å) selected by a Ge (111) primary beam monochromator in the range 10˜100° with a 0.02° step size.

To investigate the nuclear and magnetic structures of $CaCo_{1-x}Mn_xGe_2O_6$ series, a neutron powder diffraction (NPD) experiment was carried out on the two-axis diffractometer D1B at Institut Laue Langevin (ILL), between 1.7 K and room temperature. For magnetic structure investigation, NPD patterns were recorded at 2, 40 and 100 K with the 2.52 Å wavelength selected by (002) Bragg reflection of a pyrolytic graphite monochromator as well as a temperature ramp between 2 K and 100 K on heating. The XRPD and NPD data were analyzed by the Rietveld method using the Fullprof suite programs[1].

7.2.3 Magnetic susceptibility measurement

The temperature-dependent magnetic susceptibility was measured on a Quantum Design Magnetic Property Measurement System (MPMS). The magnetization measurement for all three series was carried out from 2 K to 350 K in zero field cooled (ZFC) and field cooled (FC) procedures under magnetic field of 0.01 and 0.1 T.

Moreover, frequency-dependent susceptibility of $CaCo_{1-x}Mn_xGe_2O_6$ samples with x=0.25, 0.5, and 0.75 was recorded from 4 K to 100 K under various frequencies: 1, 100, 500, and 1KHz. At 500Hz, ac susceptibility was also measured under the magnetic field range of 0 Oe$\leqq$H$\leqq$150 Oe through the temperature range of 4-100K. For all ac susceptibility measurements, a drive amplitude of 2 Oe was applied. All the ac susceptibility related measurements were performed on heating and cooling.

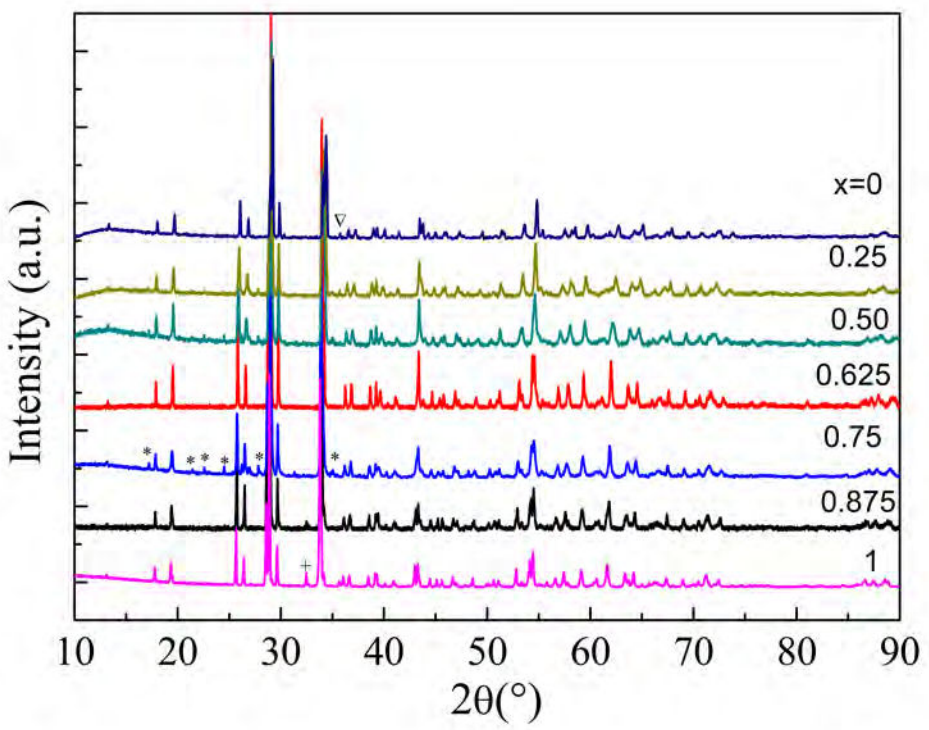

Figure 7.1: X-ray diffraction patterns of $CaCo_{1-x}Mn_xGe_2O_6$. The impurity phases Co_2GeO_4(nabla), $CaGeO_3$ (asterisks) and $Ca_3Mn_2Ge_3O_{12}$ (cross) were marked.

7.2.4 Specific heat measurement

The specific heat measurement was carried out using a relaxation technique with a Quantum Design Physical Property Measurement System (PPMS) in the temperature range of 2-100K. Only the samples $CaCo_{1-x}Mn_xGe_2O_6$ with x=0, 0.5, 0.75, 1 were measured. The pelletized sample was mounted on sample platform with Apiezon N-grease for better thermal contact.

7.3 Results and discussion

7.3.1 Crystal structure of $CaCo_{1-x}Mn_xGe_2O_6$

The crystal structure of $CaCoGe_2O_6$ has been previously investigated. It crystallizes with monoclinic C2/c symmetry corresponding to the high clinopyroxene structure type. Figure 7.1 shows the evolution of powder x-ray diffraction patterns as a function of manganese content for the synthesized solid solution. It is clear that all samples have the same crystal symmetry with the parent $CaCoGe_2O_6$ compound. A slight amount of impurities are marked with nabla (Co_2GeO_4), asterisks ($CaGeO_3$) and cross ($Ca_3Mn_2Ge_3O_{12}$). To investigate the crystal structure information in detail, Rietveld refinement was performed for each sample using the Fullprof program. The background was described by linear interpolation of selected points in the

pattern. A Thomson-Cox-Hastings model of the reflection profile including anisotropic broadening was employed[5]. The size broadening effect was described using a uniaxial model with b as unique axis, while a tensorial description was applied for strain. Low angle peak asymmetry, usually below $2\theta = 40^o$, was taken into account using the Berar-Baldinozzi model[6]. For the M1 site, the composition was fixed with full site occupancies. The ratio of Co/Mn was constrained according to the stoichiometric value. For sample with x=0, Co_2GeO_4 was introduced in the pattern description and its cell parameters and scale factor were refined. For sample with x=0.25, both Co_2GeO_4 and $CaGeO_3$ were introduced in the pattern description and their cell parameters and scale factors were refined. For sample with x=0.5 and 0.75, $CaGeO_3$ was introduced in the pattern description and its cell parameters and scale factor were refined. When it comes to samples with x=0.875 and 1, only $Ca_3Mn_2Ge_3O_{12}$ was introduced in the pattern description and its cell parameters and scale factor were refined. The refined XRD patterns of this series are shown in figure 7.2, 7.3, 7.4 and 7.5. The refinement results, main interatomic distances and bond valence sums calculated using the BondStr program[7] are presented in table 7.1 and 7.2.

The slight shifts observed in individual peak positions can be illustrated in figure 7.7, which presents the refined cell parameters and nearest M-M distance in chain (corresponding to J) and between chains (corresponding to J1) as a function of manganese concentration x. The substitution of Co by Mn leads to a small increase in a, b, c cell parameters and both M-M distances while the beta angle slightly decreases. This linear variation between cell parameters and the concentration of Mn follows the Vegard's law as expected for a solid solution. As a representative of this series, the crystal structure of $CaCoGe_2O_6$ is shown in figure 7.6. This structure is isomorphous with other pyroxenes such as $CaMnGe_2O_6$ discussed in Chapter 5. As shown in the figure 7.6, CoO_6 octahedra are connected with each other via edge-sharing, forming one-dimensional infinite zigzag chains running along the crystallographic c-axis. These octahedra chains are bridged by GeO_4 tetrahedra, which are connected by corner-sharing to form one-dimensional chains parallel to c-axis. As a result, alternating octahedra layers and tetrahedra layers stacked along a-axis are formed.

In $CaCoGe_2O_6$, the $Co^{2+}(3d^7)$ cations have the high spin configuration $t_{2g}{}^5eg^2$, that can result in a weak Jahn-Teller effect. As shown in table 7.2, CoO_6 octahedra are only slightly distorted with distances ranging from 2.072(5) to 2.160(6) Å. Actually the local octahedral-site distortion of CoO_6 have a comparable amplitude as the one observed in MnO_6 and the expected JT effect seems to be not predominant. On the basis of the observed average bond length <Co-O> (2.116(2)Å) in $CaCoGe_2O_6$, we can calculate the effective ionic radius of Co^{2+} cation, assuming the oxygen ionic radius to be 1.40Å. The effective ionic radius is determined as 0.716Å, which is very close to the Co ionic radius (0.745 Å) reported by Shannon[16].

All the principal M-O distances for the solid solution are summarized in table 7.2. It is clearly seen that the average M-O distance is almost monotonously increased with the increment of Mn content, ranging between 2.12 Å (x=0) and 2.19 Å (x=0.75). This is due to the bigger ionic radius of Mn^{2+} (0.83 Å) compared to that of Co^{2+} (0.745 Å). In addition, each CaO_6 octahedron in $CaMGe_2O_6$ is connected by edge-sharing to three consecutive MO_6

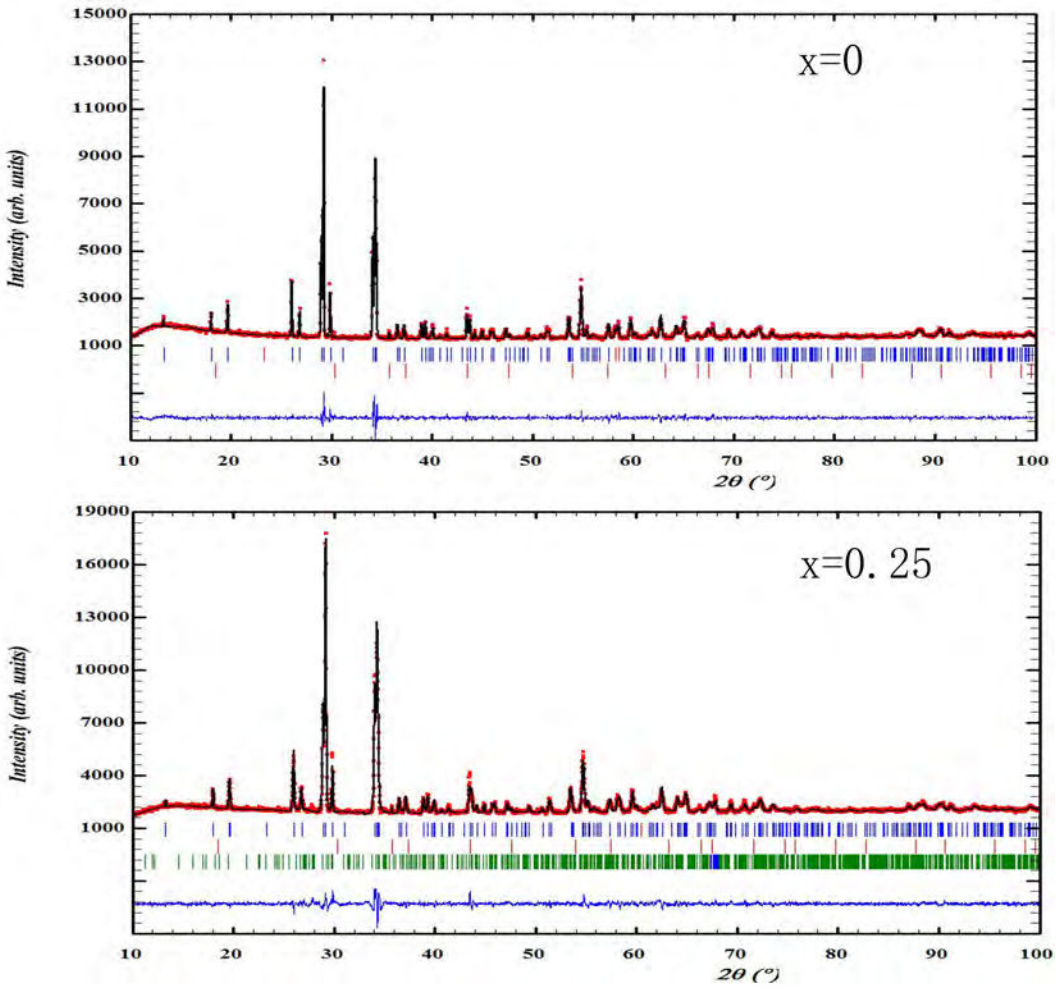

Figure 7.2: Rietveld refinement of samples with x=0 and 0.25 from XRD data taken at room temperature. Observed (red), calculated (black), and difference (blue) plots are shown. Bragg reflections are denoted by blue tick marks. The red tick marks present the Bragg reflections belong to a Co_2GeO_4 impurity phase. For sample with x=0.25, the accommodated impurity phase $CaGeO_3$ during refinement is marked with green tick marks.

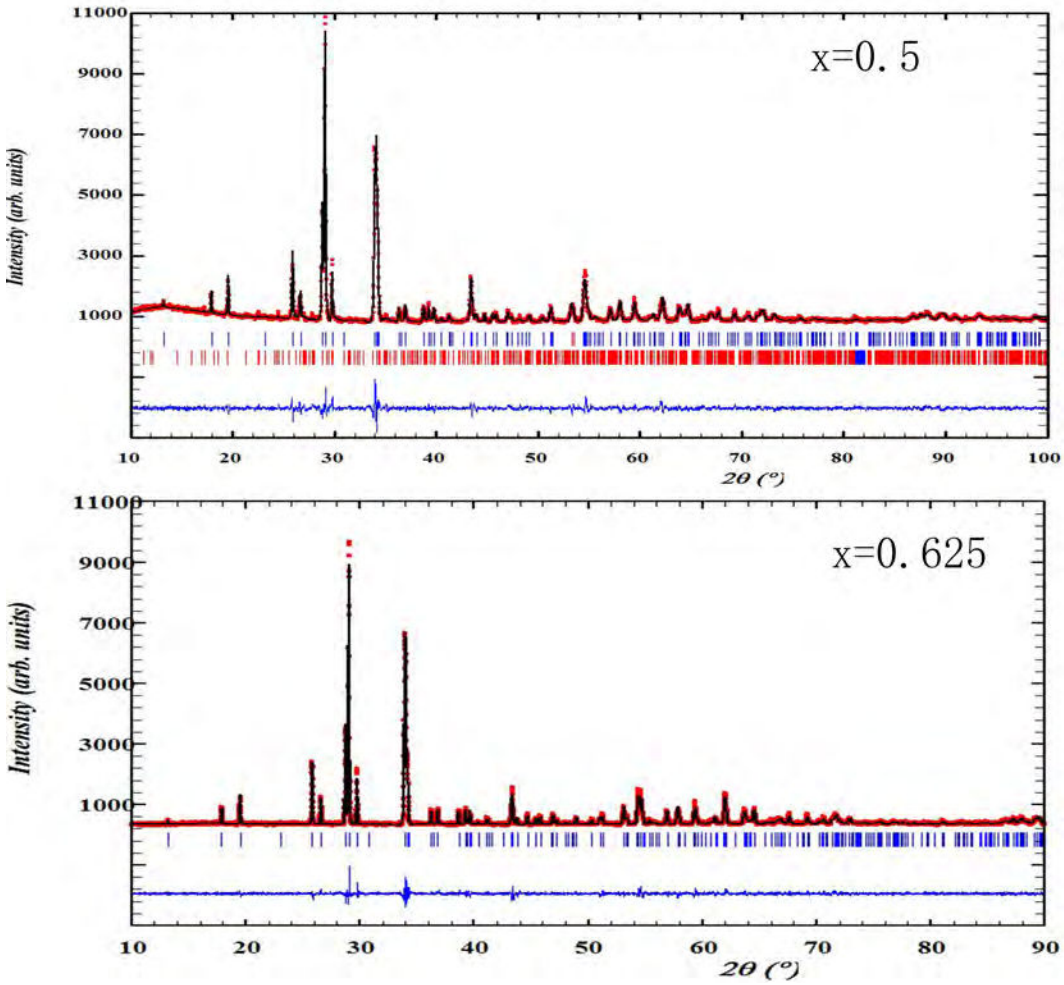

Figure 7.3: Rietveld refinement of samples with x=0.5 and 0.625 from XRD data taken at room temperature. Observed (red), calculated (black), and difference (blue) plots are shown. Bragg reflections are denoted by blue tick marks. In the upper figure, the red tick marks present the Bragg reflections belong to a $CaGeO_3$ impurity phase.

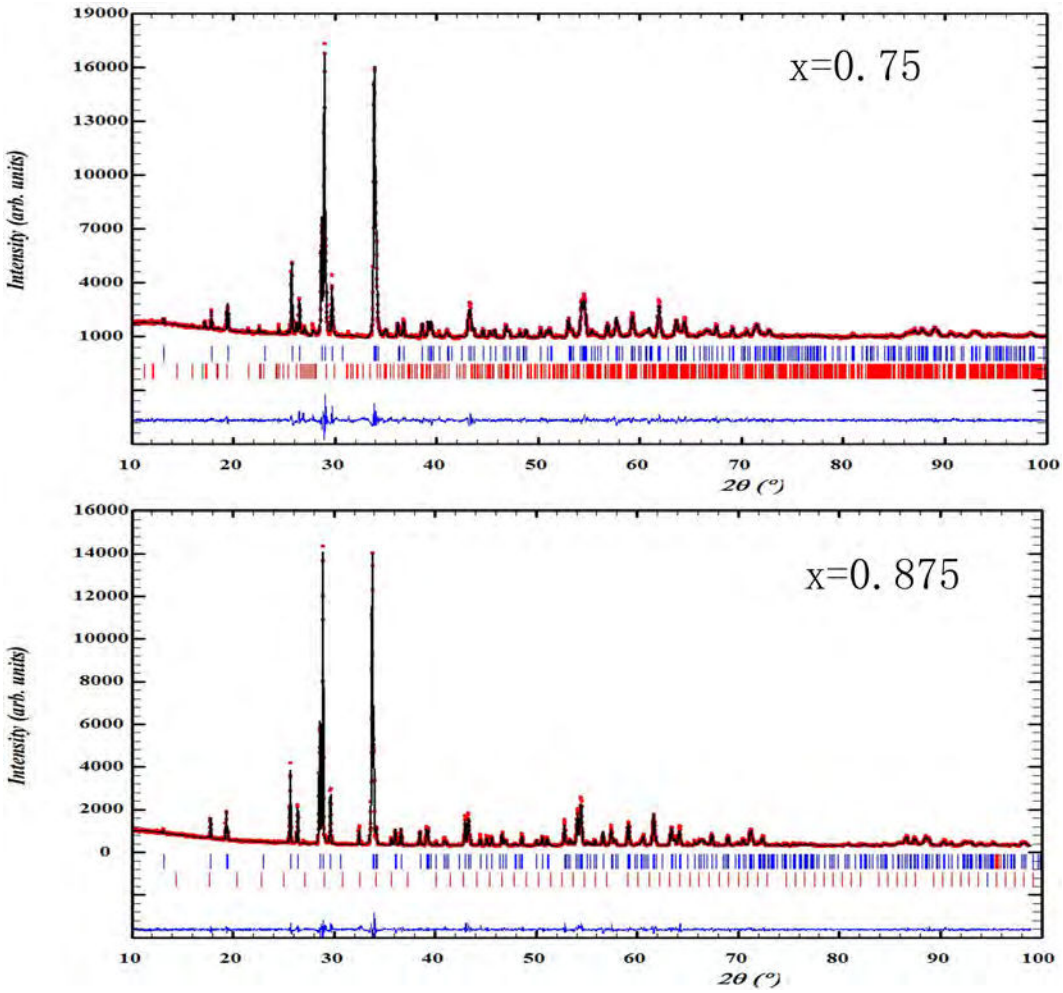

Figure 7.4: Rietveld refinement of samples with x=0.75 and 0.875 from XRD data taken at room temperature. Observed (red), calculated (black), and difference (blue) plots are shown. Bragg reflections are denoted by blue tick marks. In the upper figure, the red tick marks present the Bragg reflections belong to a $CaGeO_3$ impurity phase. For sample with x=0.875, the red tick marks designate a $Ca_3Mn_2Ge_3O_{12}$ impurity phase.

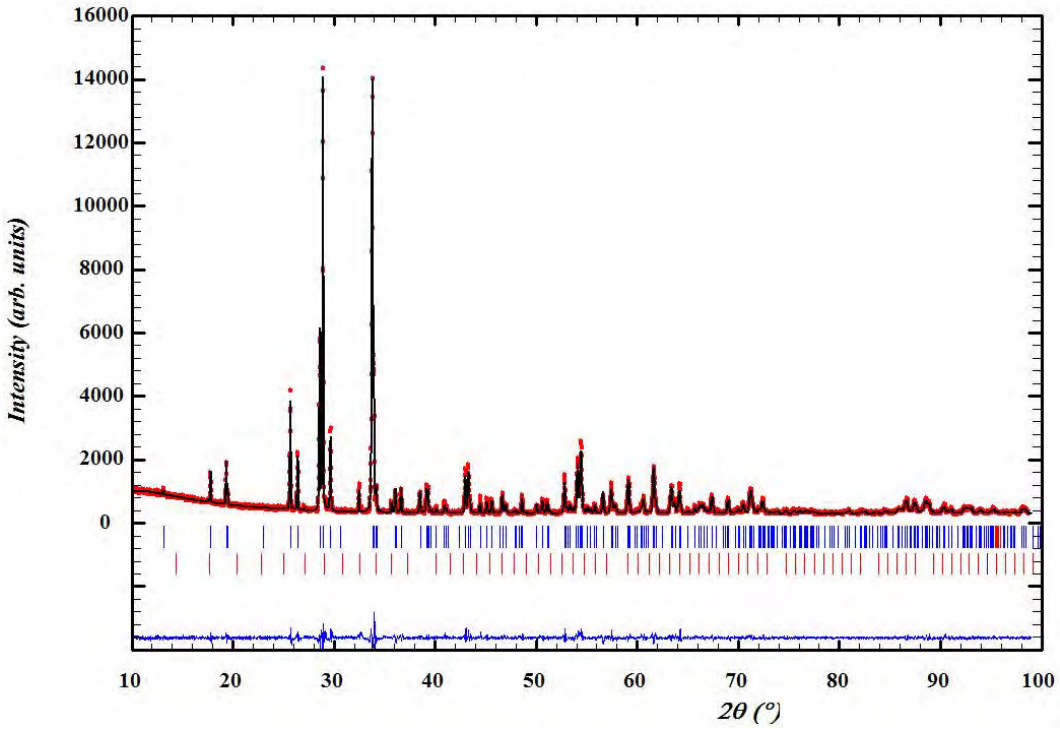

Figure 7.5: Rietveld refinement of $CaMnGe_2O_6$ from XRD data taken at room temperature. Observed (red), calculated (black), and difference (blue) plots are shown. Bragg reflections are denoted by blue tick marks. The lower set of Bragg reflections belong to a $Ca_3Mn_2Ge_3O_{12}$ impurity phase.

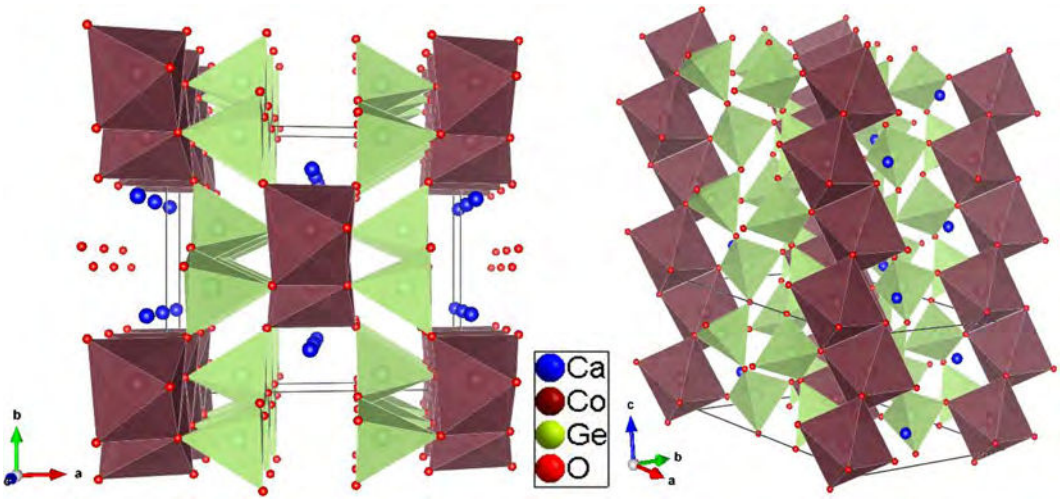

Figure 7.6: (Left) Projection of the $CaCoGe_2O_6$ structure along the c-axis. (Right) The CoO_6 zigzag chains separated by GeO_4 tetrahedra via corner sharing, derived from NPD at room temperature.

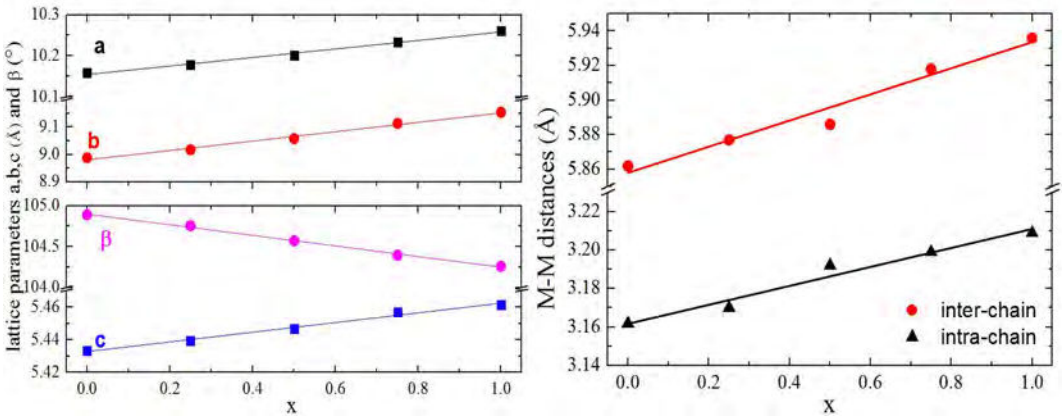

Figure 7.7: Evolution of lattice parameters (left) and M-M distances (right) with manganese content x in the $CaCo_{1-x}Mn_xGe_2O_6$ series.

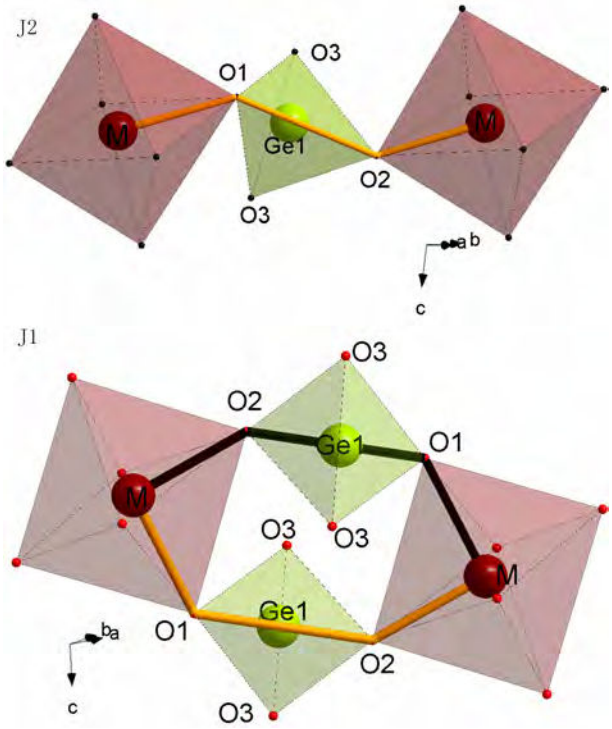

Figure 7.8: The fragments of crystal structure of $CaMGe_2O_6$, highlighting the octahedral and tetrahedral coordinations.

octahedra along one MO_6 zigzag chain. However, the CaO_6 octahedra are not connected to each other even though they are straightly aligned along the c-axis. In contrast to the M site, the CaO_6 octahedra are more distorted, with Ca-O distances ranging between 2.370(4) Å and 2.692(3) Å. This can be indicated by the polyhedral distortion values, calculated by using the volume distortion parameter $\nu(\%)$ proposed by Makovicky and Balic-Zunic[2], as calculated by the BondStr program and shown in table 7.2. The average distance of Ca-O for all samples is nearly identical, and they are in the vicinity of 2.51Å except for sample x=1.

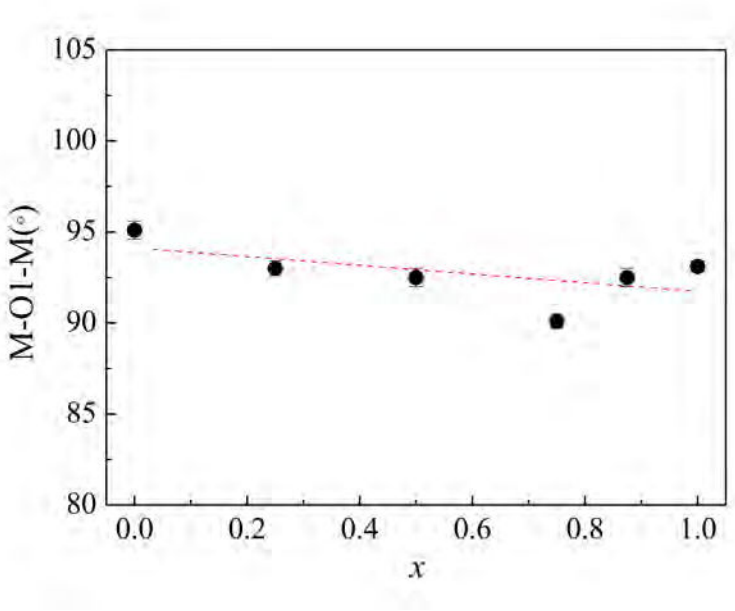

Figure 7.9: M-O1-M angle as a function of Mn concentration in $CaCo_{1-x}Mn_xGe_2O_6$.

We turn now to the Ge coordination. As presented in figure 7.8, the Ge tetrahedra share the O1-O2 edge with the MO_6 octahedra, leading to J1 and J2 pathways for exchange interactions, while the rest O^{2-} anions (O3) on the vertex of tetrahedra form the zigzag GeO_4 tetrahedra chains by connecting the neighboring tetrahedra. The extracted data, in table 7.2, show that the average Ge-O distance for samples with x=0.25, 0.5, 0.625, 0.75 and 0.875 is dependent on the Mn content, i.e. the average Ge-O distance in these samples increases with the increase of Mn concentration. It is worth noting that the Ge-O1 and Ge-O2 bond lengths related to the O1-O2 bridge in both structures are the shortest and are nearly identical to each other.

Recent band structure calculations of exchange interactions for pyroxenes have shown that the edge-sharing character of MO_6 within the octahedra chains with M-O1-M angle close to 90 results in the competition between direct and superexchange magnetic interactions, which gives normally the dominant exchange interaction J as schematically shown in figure 7.16[12]. This angle is shown in table 7.2. The relation between the M-O1-M angle and Mn content x is plotted in figure 7.9, the angle approximately decreases with the increase of Mn concentration.

7.3.2 Magnetic properties of $CaCo_{1-x}Mn_xGe_2O_6$

The magnetic properties of the parent phase $CaCoGe_2O_6$ compound have been previously reported [3]. It was shown to undergo an AFM phase transition around 20 K. In chapter 5, we have demonstrated low dimensional magnetism in the other end member $CaMnGe_2O_6$, which shows 1D-short-range magnetic correlations arising from magnetic frustration, observed in magnetic susceptibility and diffuse scattering from NPD, as well as a long range ordering AFM transition at 15 K. As a result, the solid solution end members exhibit essentially distinct magnetic behaviors, as shown in figure 7.10(a). In Mn compound two magnetic transitions

Table 7.1: Agreement factors and refined structural parameters for $CaCo_{1-x}Mn_xGe_2O_6$ series.

Atom	positions	x=0(XRD)	0.25	0.5	0.625	0.75	0.875	1
Ca(4e)	y	0.298(1)	0.3001(7)	0.3016(8)	0.3033(5)	0.3008(6)	0.3010(7)	0.3028(5)
	B/Å^2	0.3(3)	-0.1(2)	-0.2(2)	0.2(1)	0.1(1)	0.6(2)	0.5(1)
Mn/Co(4e)	y	0.909(1)	0.9094(6)	0.9098(7)	0.9089(4)	0.9088(5)	0.9060(6)	0.9075(4)
	B/Å^2	1.0(2)	-0.04(15)	0.2(2)	0.3(1)	0.8(1)	0.3(1)	0.26(9)
Ge(8f)	x	0.2849(4)	0.2857(3)	0.2859(3)	0.2870(2)	0.2869(2)	0.2873(3)	0.2869(2)
	y	0.0980(4)	0.0992(3)	0.0988(3)	0.0995(2)	0.0981(2)	0.0975(3)	0.095(1)
	z	0.2271(7)	0.2279(5)	0.2307(5)	0.2301(4)	0.2324(4)	0.2318(5)	0.2328(3)
	B/Å^2	0.6(1)	0.72(9)	0.82(9)	0.66(6)	0.74(6)	0.59(6)	0.34(5)
O1(8f)	x	0.113(1)	0.116(1)	0.115(1)	0.1186(7)	0.1181(8)	0.1151(1)	0.1147(6)
	y	0.094(2)	0.094(2)	0.097(2)	0.097(1)	0.102(1)	0.100(2)	0.095(1)
	z	0.130(2)	0.145(2)	0.147(2)	0.151(1)	0.158(2)	0.144(2)	0.1469(13)
	B/Å^2	0.3(3)	0.8(2)	0.9(2)	0.5(1)	0.1(1)	0.8(1)	0.3(1)
O2(8f)	x	0.363(1)	0.3597(9)	0.361(1)	0.3686(7)	0.3691(8)	0.371(1)	0.3667(7)
	y	0.265(2)	0.262(1)	0.258(1)	0.2586(9)	0.261(1)	0.255(1)	0.2542(8)
	z	0.343(3)	0.333(2)	0.334(3)	0.344(2)	0.349(2)	0.359(2)	0.353(2)
	B/Å^2	0.3(3)	0.8(2)	0.9(2)	0.5(1)	0.1(1)	0.8(1)	0.3(1)
O3(8f)	x	0.363(1)	0.363(1)	0.362(1)	0.3596(7)	0.3589(8)	0.360(1)	0.3557(7)
	y	0.022(2)	0.015(1)	0.017(1)	0.0256(8)	0.0316(9)	0.029(1)	0.0295(8)
	z	0.974(3)	0.980(3)	0.990(2)	0.977(2)	0.980(2)	0.986(2)	0.987(2)
	B/Å^2	0.3(3)	0.8(2)	0.9(2)	0.5(1)	0.1(1)	0.80(1)	0.3(1)
R_{Bragg}		5.56	4.53	4.41	4.15	3.34	5.62	3.47
χ^2		1.89	2.71	2.29	1.98	3.06	1.92	2.75

Table 7.2: Principal cation-anion distances (Å) and angles for $CaCo_{1-x}Mn_xGe_2O_6$.

Dis/Angle	x=0	0.25	0.5	0.625	0.75	0.875	1
Ca-O1	2.370(4)	2.35(1)	2.34(2)	2.37(1)	2.30(1)	2.33(1)	2.379(9)
Ca-O2	2.363(2)	2.42(1)	2.42(1)	2.356(7)	2.333(9)	2.28(1)	2.320(7)
Ca-O3	2.692(3)	2.61(1)	2.61(1)	2.701(8)	2.761(9)	2.73(1)	2.742(8)
Ca-O3	2.614(3)	2.68(1)	2.71(1)	2.626(9)	2.63(1)	2.66(1)	2.676(9)
Ave.Dist.	2.510(1)	2.515(4)	2.516(5)	2.514(3)	2.506(4)	2.497(4)	2.530(3)
BVS	1.99(1)	1.95(2)	1.96(3)	1.98(2)	2.12(2)	2.19(3)	1.97(2)
Distortion	33.728E-04	29.359E-04	33.844E-04	36.776E-04	60.153E-04	63.245E-04	52.056E-04
Co/Mn-O1	2.160(6)	2.20(1)	2.21(2)	2.235(9)	2.26(1)	2.28(1)	2.228(9)
Co/Mn-O1	2.116(2)	2.174(9)	2.19(1)	2.221(6)	2.255(7)	2.18(1)	2.197(6)
Co/Mn-O2	2.072(5)	2.08(1)	2.11(1)	2.067(9)	2.06(1)	2.10(1)	2.130(8)
Ave.Dist.	2.116(2)	2.152(5)	2.168(5)	2.175(3)	2.193(4)	2.188(5)	2.185(3)
BVS	1.92(1)	1.75(2)/2.28(3)	1.67(2)/2.18(3)	1.67(2)/2.17(2)	1.60(2)/2.09(2)	1.60(2)/2.09(3)	2.08(2)
Distortion	2.869E-04	5.465E-04	4.02E-04	12.263E-04	17.599E-04	11.276E-04	3.49E-04
Ge-O1	1.722(3)	1.67(1)	1.69(1)	1.668(7)	1.674(8)	1.72(1)	1.713(6)
Ge-O2	1.709(2)	1.68(1)	1.66(1)	1.707(8)	1.750(9)	1.73(1)	1.704(7)
Ge-O3	1.786(3)	1.88(2)	1.84(2)	1.849(9)	1.82(1)	1.80(1)	1.777(9)
Ge-O3	1.804(2)	1.74(1)	1.77(1)	1.777(8)	1.809(9)	1.82(1)	1.812(8)
Ave.Dist.	1.756(1)	1.743(6)	1.741(7)	1.750(4)	1.763(5)	1.765(6)	1.752(4)
Kink. Ang.(°)	157.5(1)	168.3(8)	167.1(8)	160.6(4)	156.2(5)	158.2(5)	157.6(4)
M-O1-M(°)	95.1(5)	93.0(4)	92.5(5)	91.4(3)	90.1(4)	92.5(5)	93.1(3)

Table 7.3: Summary of principal magnetic properties for $CaCo_{1-x}Mn_xGe_2O_6$. Néel temperature, ordered magnetic moment at 2K, propagation vector and magnetic space group were obtained by neutron diffraction refinement. Weiss temperature and effective moment come from the Curie-Weiss fit of magnetic susceptibility. High temperature magnetic transition $T_m$was determined from ac susceptibility.

Mn	x=0	x=0.25	x=0.50	x=0.625	x=0.75	x=0.875	x=1
T_N (K)	21	20	17	16.2	15	14.6	14.5
T_m (K)	-	65	54	55	53	51	45
Weiss temperature (K)	12(7.39)	-5(9.5)	-17(6.88)	-12.9(6.47)	-30(2.33)	-29.8(7.81)	-34.6(6.35)
Effective moment (μ_B)	5.10(6)	5.20(5)	5.50(5)	5.59(6)	5.60(4)	5.65(7)	5.79(6)
Mag.Moment (μ_B)	4.05(4)	2.67(5)	2.00(5)	1.60(7)	-	2.49(7)	4.17(5)
Propagation vector	(100)	(100)	(100)	(100)	(100) and (000)	(000)	(000)
SG	$Pc\ 2_1/c$	$Pc\ 2_1/c$	$Pc\ 2_1/c$	$Pc\ 2_1/c$	-	C2'/c	C2'/c

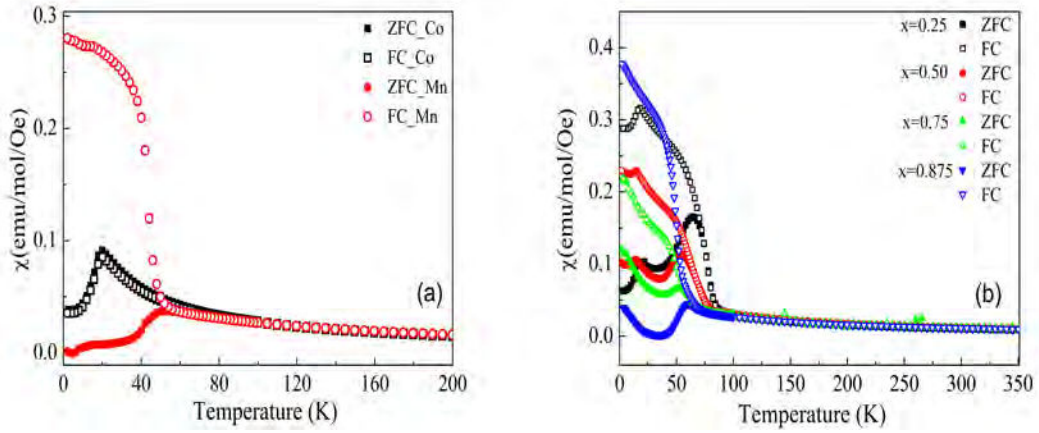

Figure 7.10: (a)Temperature dependence of the magnetic susceptibility (ZFC and FC) of $CaCoGe_2O_6$ and $CaMnGe_2O_6$ under external magnetic field with 100 Oe. (b) Temperature-dependent magnetic susceptibilities of $CaCo_{1-x}Mn_xGe_2O_6$ (x=0.25, 0.5, 0.75, 0.875) series measured at 100 Oe.

can be clearly seen with a divergence between the low-field ZFC and FC curves below 45K, whereas in Co compound, one transition only is detected without noticeable difference between FC and ZFC curves. The temperature dependence of magnetization of all samples under magnetic field of 0.01 T are shown in figure 7.10(b). For all Mn containing samples, a difference can be observed between FC and ZFC curves above the AFM transition temperatures T_N (determined by neutron diffraction). The magnetic behavior of sample with x=0.875 is very similar to that of $CaMnGe_2O_6$. As summarized in table 7.3, the substitution of Co by Mn leads to the monotonous decrease of T_N from 21 K (x=0) to 14.6 K (x=0.875). Concerning the magnetic transition at higher temperature, we will discuss their origin by means of ac magnetic susceptibility measurements and neutron diffraction. The temperatures of appearance of these magnetic transitions also decrease with increasing Mn concentration.

By fitting the high-temperature part of the inverse magnetic susceptibility at 0.1 T to the Curie-Weiss law, we obtained the Weiss temperature and effective moment for all samples,

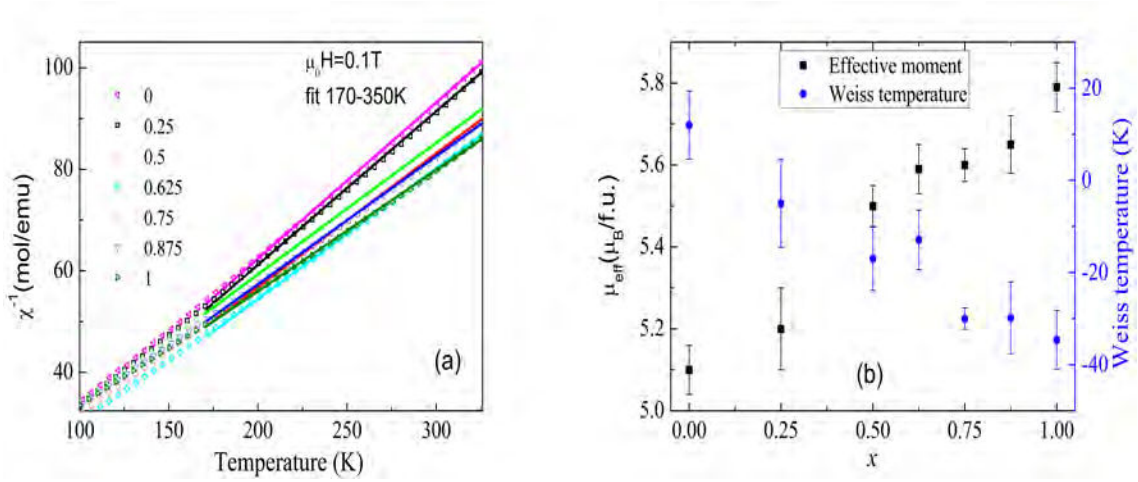

Figure 7.11: (a)Evolution of the inverse magnetic susceptibility as a function of temperature in the $CaCo_{1-x}Mn_xGe_2O_6$. The data were collected under magnetic filed of 0.1T. The solid line represents the Curie-Weiss fit. (b) The fitted effective moment and Weiss temperature as a function of Mn concentration.

as shown in figure 7.11. Note that the fitting with different temperature range gives slightly different effective moments and Weiss temperatures for each sample. In order to properly estimate the variance of fitted results, we have chosen two temperature ranges, 170-350K (employed) and 250-350K. The difference of fitted results for two regimes are adopted as the error bars. The error bars are quite large, that illustrate the sensitivity of the Curie-Weiss fit to the fitting range. Although the large errors, the linear dependence of Weiss and effective moment is clearly visible. The Weiss temperatures exhibit a change of sign from positive to negative with the increase of x, indicating a modification of the predominant character of the magnetic interactions from ferromagnetic to antiferromagnetic. In addition, the effective moment increases with x as theoretically expected. The effective moment for Mn^{2+} ($5.79(6)\mu_B$) is close to the spin-only value for S=3/2 (5.92 μ_B) whereas the effective moment determined for Co^{2+} ($5.10(6)\mu_B$) is much bigger than the spin-only value ($3.87\mu_B$) and is characteristic of a partial unquenched orbital moment.

The temperature dependence of heat capacity was measured for the samples with x=0, 0.50, 0.75 and 1. It is known that phase transitions associated with long-range magnetic ordering are specified by a pronounced λ-shape in heat capacity at the transition temperature. As shown in figure 7.12(a), this character can be observed in specific heat as a function of temperature with apparent cusps close to their magnetic ordering temperatures T_N. In any case, no obvious phase transition above 20 K can be seen. The magnetic component of the specific heat capacity of samples with x=0.5, 0.75, 1, C_{mag}, was obtained by subtracting the phonon contribution with a nonmagnetic analogue $CaZnGe_2O_6$. It is worth noting that as shown in figure 7.12(a), the match in specific heat between $CaCo_{1-x}Mn_xGe_2O_6$ and $CaZnGe_2O_6$ are not very good at high temperature range, particularly, in the case of sample with x=0. To estimate the phonon contribution for $CaCo_{1-x}Mn_xGe_2O_6$(x=0.5, 0.75), the temperature of the specific heat of $CaZnGe_2O_6$ were normalized. The magnetic entropy was estimated by integrating

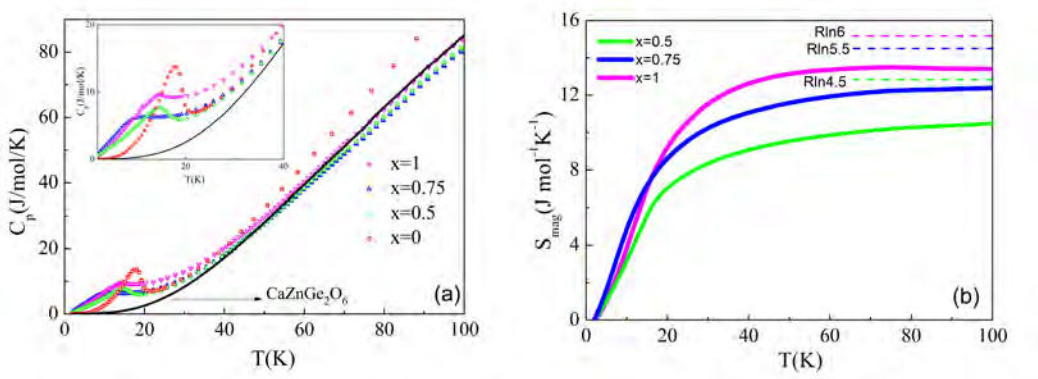

Figure 7.12: (a) Specific heat capacity of $CaCo_{1-x}Mn_xGe_2O_6$ and $CaZnGe_2O_6$(solid line) which is used as a lattice standard. (b) The magnetic component of the specific heat capacity of $CaCo_{1-x}Mn_xGe_2O_6$(x=0.5, 0.75 and 1).

C_{mag}/T dT. The experimental magnetic entropy S_m at 70 K, derived from the C_{mag}-T curve, is 9.4J/mol/K for x=0.5, 11.5J/mol/K for x=0.75, and 13.5J/mol/K for x=1. Obviously, the experimental magnetic entropy increases with the increase of Mn content. Except for the host sample x=0, for which the magnetic entropy was not estimated, the magnetic entropy as a function of temperature for other samples shows similar characteristics: the magnetic entropy first drops down slowly on cooling over a broad temperature range between 70K and Néel temperature T_N, then below T_N, a rapid decrease is observed. The former phenomenon corresponds to a considerable entropy release above T_N. This characteristic probably arises from short-range order, as discussed below. A similar phenomenon occurs in $CaMnGe_2O_6$, as discussed in chapter 5, showing up the formation of strong short-range magnetic correlations within the quasi-1D spin chains far above the long-ranged ordering temperature. In fact, for $CaMnGe_2O_6$ we found that a majority of the magnetic entropy (51%) under zero magnetic field is released above the long range ordering temperature. However, for samples with x=0.5 and 0.75, only around 30% magnetic entropy is released above T_N.

The measurement of ac susceptibility of $CaCo_{1-x}Mn_xGe_2O_6$(x=0.25, 0.5, 0.75,1) was thus performed so as to investigate the dynamic behavior of the magnetic transitions. As an example for x=0.5, we observe in figure 7.13(left), one of the signature of freezing spin transition : a cusp close to T_m in the real part of the ac susceptibility. Moreover, the positions of the peak are frequent-dependent, i.e. with the increase of driven frequency, there is a slight shift of the cusp to higher temperature with a readily reduced amplitude of magnetic susceptibility, whereas the long-range ordering at T_N does not vary with various frequencies. Figure 7.13 (right) represents the temperature dependence of ac magnetic susceptibility of sample with x=0.25 under various dc magnetic fields with fixed frequency f=500 Hz. It is worth noting that just a small magnetic field can decrease the transition temperature T_m, and simultaneously suppress the magnetic susceptibility. In the high temperature regime, χ'decreases monotonically as the strength of the applied field increases. However, neither the various frequencies nor the dc magnetic field can affect the magnetic ordering at T_N, confirming its nature of long-range

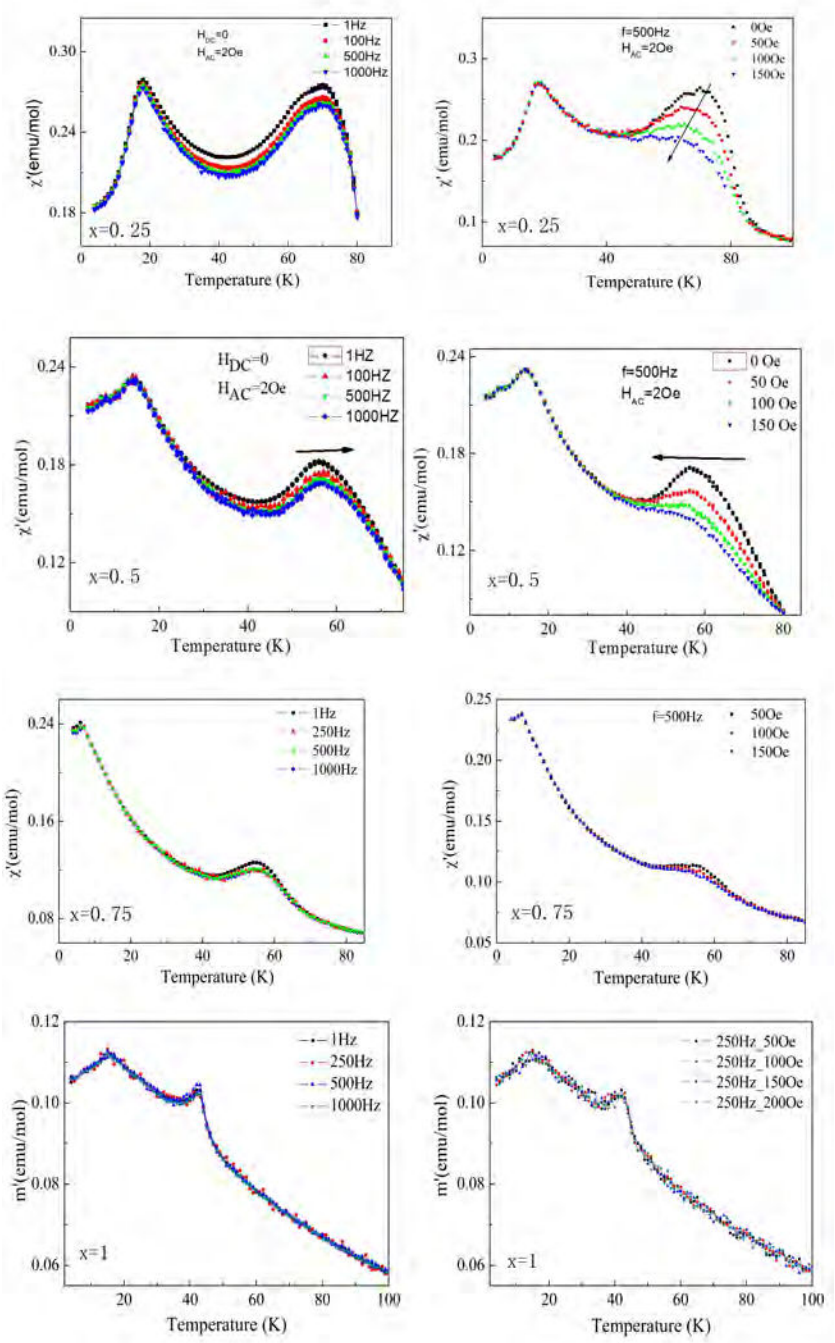

Figure 7.13: (left)Temperature and frequency dependence of the real part of the ac susceptibility of $CaCo_{1-x}Mn_xGe_2O_6$(x=0.25, 0.5, 0.75, 1). (right) Temperature dependence of ac susceptibility of $CaCo_{1-x}Mn_xGe_2O_6$(x=0.25, 0.5, 0.75, 1) at 500Hz under different dc magnetic fields.

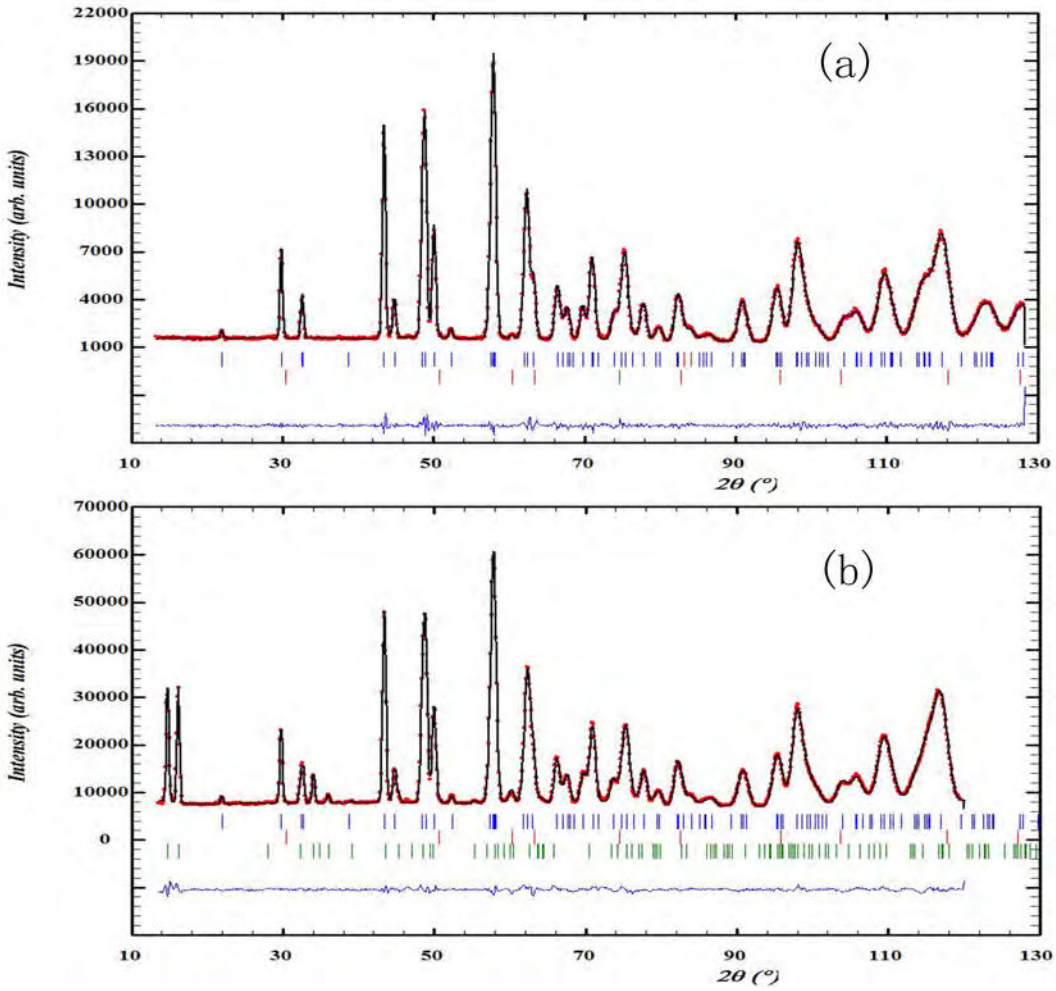

Figure 7.14: (a) Observed (symbols) and calculated (line) powder neutron diffraction patterns for $CaCoGe_2O_6$ at 300 K. (b) Observed (symbols) and calculated (line) powder neutron diffraction patterns for $CaCoGe_2O_6$ at 2 K. The green tick mark shows the magnetic reflections. The nuclear reflections are denoted by blue tick marks. The reflections marked in red belong to a Co_2GeO_4 impurity phase. The blue line shows the difference between the observed and calculated diffraction patterns.

magnetic order. The ac susceptibility measurements for x=0.25, x=0.5 and x=0.75 reveal the similar results, see figure 7.13 and 7.13. It is worth noticing that the amplitude of suppressed magnetic susceptibility under external magnetic fields observed in x=0.75 is obviously smaller than those of in x=0.25 and x=0.5 and can't be observed for x=1.

7.3.3 Magnetic structure of $CaCo_{1-x}Mn_xGe_2O_6$

As the host of solid solution, $CaCoGe_2O_6$ exhibits strong FM interactions within the M chains which dominate the AFM coupling between the chains. This is consistent with the positive Weiss temperature and previous neutron diffraction study[3]. In contrary, the magnetic structure of $CaMnGe_2O_6$ is described by AFM chains coupled ferromagnetically (see chapter 5). We have already specifically investigated the magnetic properties of $CaMnGe_2O_6$ which shows

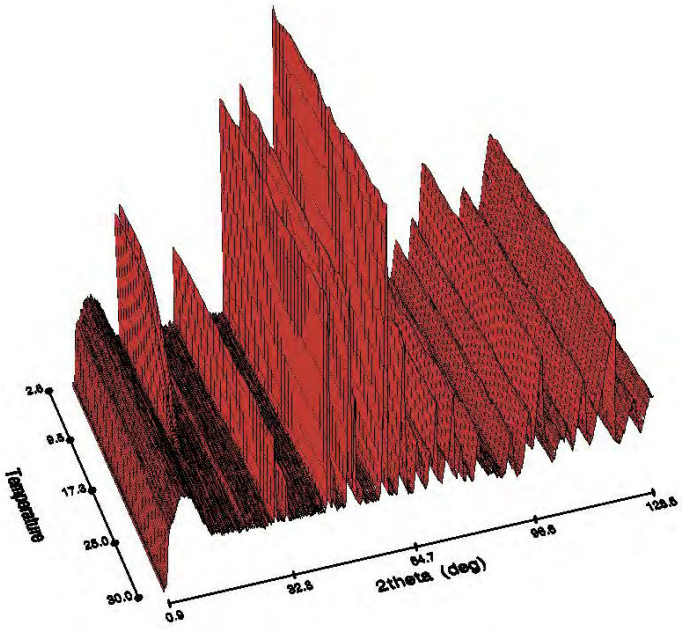

Figure 7.15: 3D plot of neutron powder diffraction scans for $CaCoGe_2O_6$ showing the magnetic transition at 21K using a wavelength of 2.52Å.

a linear magnetoelectric effect and one dimensional short range magnetic correlation. Here we first introduce the magnetic structure of $CaCoGe_2O_6$ and then information about the magnetic structure of $CaMnGe_2O_6$ will be recalled in order to compare these two spin configurations.

The neutron diffraction data collected at room temperature are shown in figure 7.14(a), the refined structural parameters are summarized in table 7.1. This provides a structural model for further Rietveld refinement of patterns at low temperature. Figure 7.15 shows temperature dependent NPD patterns below 30K for $CaCoGe_2O_6$. It is obvious that the magnetic reflections appear below 21K, consistent with our magnetic susceptibility and heat capacity measurements. At low temperature all magnetic reflections of $CaCoGe_2O_6$ can be indexed with a commensurate magnetic propagation vector k1=(1,0,0). To determine all the possible magnetic structures compatible with the crystal symmetry (C2/c), the representation analysis, which is described by Bertaut, was performed[8]. Calculations were carried out using version 2 K of the programs SARAh-Representation analysis[9] and BasIreps integrated in Fullprof Suite[1, 10]. For the Co^{2+} cations on the 4e Wyckoff position of space group C2/c, the decomposition of magnetic representation is

$$\Gamma = 1\Gamma_1^1 + 1\Gamma_2^1 + 21\Gamma_3^1 + 2\Gamma_4^1. \tag{7.1}$$

The different basis vectors calculated using the projection operator technique associated with each IR are presented in table 7.4. There are four magnetic ions in the unit cell but only two possible magnetic couplings. Because of the C center symmetry broken by the k1 vector, the magnetic moments associated with the two Co^{2+} cations related by C centering are intrinsically antiparallel. All possible models determined from the symmetry analysis were

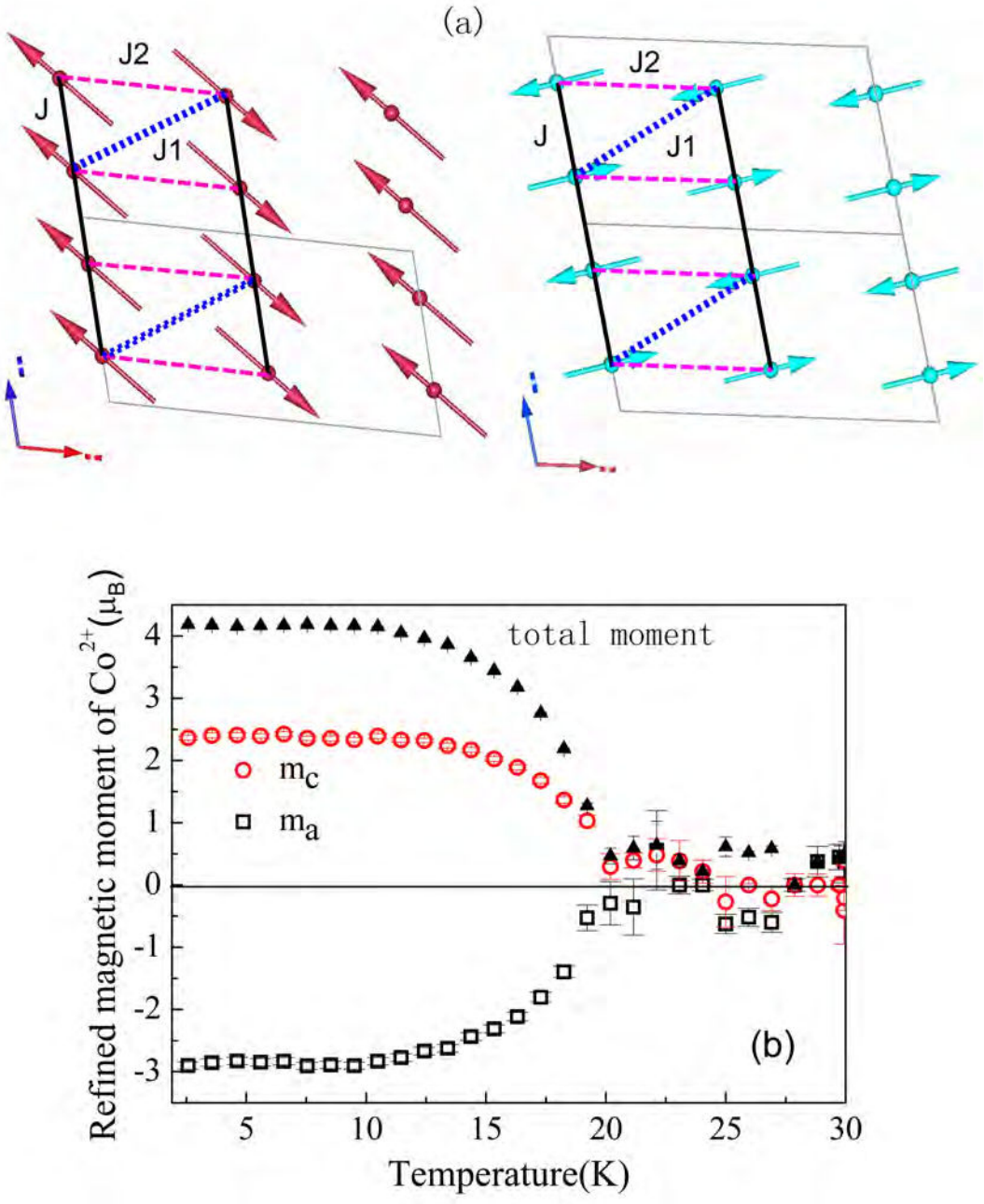

Figure 7.16: (a) Representation of the magnetic structures of $CaCoGe_2O_6$ (left) and $CaMnGe_2O_6$ (right); (b) Evolution of the refined Co^{2+} magnetic moment components with temperature.

Table 7.4: Basis vectors for Co^{2+} at 4e site (Co1 (0, 0.9092, 0.25), Co2 (0, 0.0908, 0.75)). C2/c with propagation vector k1=(1,0,0). Notations: F=S1+S2, C= S1-S2.

IR	Basis vector
Γ1	(0,Fy,0)
Γ2	(0,Cy,0)
Γ3	(Fx, 0, Fz)
Γ4	(Cx,0,Cz)

tested by Rietveld refinement. The best fit was achieved with the model described by the IR Γ3 corresponding to the space group P_c2_1/c. In fact, this space group is not the same as the one previously reported: C2'/c'. It is obvious that the breaking of C-centering is incompatible with the C2'/c' symmetry. We used the mCIF file output from Fullprof and the program FINDSYM[17] in order to properly determine the true symmetry of the magnetic structure refering to k=(1,0,0). It turns out that the magnetic space group of $CaCoGe_2O_6$ is P_c2_1/c in BNS notation and the primitive magnetic cell is obtained from the transformation: (-a, -b, a+c; 1/2, 0, 0).

The final refinement for the 2 K pattern is shown in figure 7.14 (b). The Co^{2+} magnetic moment is constrained by symmetry in the (a,c) plane, with an angle of 145.82° with respect to the a-axis , with ma=-2.72(4)μ_B, mc=2.38(1)μ_B. Note that this result yields a considerably better refinement than the values reported previously[3] with ma=1.92μ_B, mc=2.75μ_B, Mtot=3.28μ_B. In our case, the total ordered magnetic moment refined at 2 K is Mtot=4.05(4) μ_B. This value represents the magnetic moment per Co^{2+} ion in the ordered state and is bigger than the expected spin-only contribution gS=3μ_B/atom due to the considerable spin-orbit coupling in this compound. The magnetic ordering corresponds to FM coupling between the Co^{2+} cations within the CoO_6 octahedra zigzag chains, while the spin couplings between neighboring chains are AFM, consisting of two possible interchain superexchange. A sketch of the magnetic structure of $CaCoGe_2O_6$ is shown in figure 7.16 (a) (red). It is worth noting that the triangular topology of magnetic coupling does not allow any magnetic frustration in that case since all the exchange interactions are satisfied. Let us recall that $CaMnGe_2O_6$ has an opposite spin configuration with FM ordered AFM chains, as represented in figure 7.16 (a)(right), with a magnetic propagation vector k2=0. In opposition to the Co case, this magnetic configuration is actually frustrated. The temperature dependence of the magnetic moment is shown in figure 7.16 (b), the figure shows that the ordered magnetic moment starts to deviate from zero just below 21K, evidencing the magnetic ordering temperature, and in agreement with the magnetic susceptibility measurements.

Figure 7.17 shows the magnetic reflections from NPD pattern differences between 2K and 40 K for all samples. Interestingly, the magnetic reflections of the samples with x=0.25, 0.50, and 0.625 can be well indexed by k1 and the magnetic reflections of $CaCo_{0.125}Mn_{0.875}Ge_2O_6$ can be indexed by k2, while the index of magnetic reflections of the sample with x=0.75 requires these two vectors. There is one small magnetic reflection at around 2θ =27° in the solid solution (marked in figure 7.17 with stars) which cannot be described neither by k1 nor

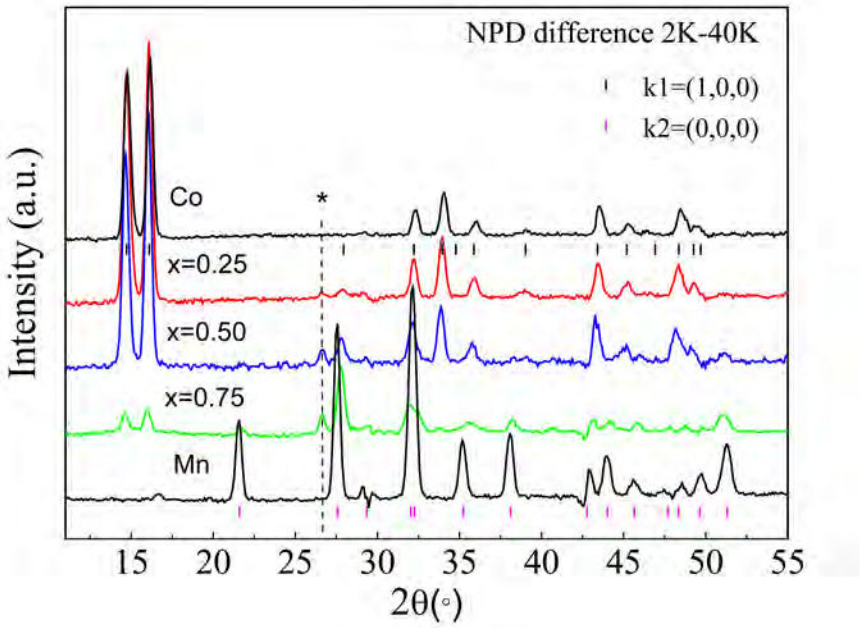

Figure 7.17: Comparison of magnetic reflections from NPD pattern differences between 2K and 40 K for $CaCo_{1-x}Mn_xGe_2O_6$.

by k2 vector. Some attempts have been made to search for other possible propagation vectors, but, no k vector was found which could index all magnetic reflections in the series. This single reflection seems to be attributed to an impurity phase and was not included in the following refinements It is worth noting that for all samples, no magnetic reflection can be observed above T_N, indicating that the magnetic transition observed at higher temperature cannot be attributed to long range magnetic ordering. We performed the representation analysis to all samples except for sample with x=0.75. It turns out that the samples corresponding to vector k1 adopt the analogous spin configurations with $CaCoGe_2O_6$, whilst the samples corresponding to the magnetic propagation vector k2 share the similar magnetic structure with $CaMnGe_2O_6$. Using the same basis vector with respect to each magnetic structure, we refined the magnetic structures of NPD at 2 K for all samples. The final refined NPD patterns at 2K are shown in figure 7.18 and 7.19, and the summarized results are listed in table 7.3. We obtained the magnetic moments of 4.05 μ_B, 2.67 μ_B, 2.0 μ_B, and 1.60 μ_B for samples with x=0.0, 0.25, 0.50, and 0.625, respectively. It is interesting to notice that the ordered magnetic moments for samples with x$\leq$0.625 monotonically decrease with the increase of Mn content, which is quite unexpected since the Mn^{2+} moment is much larger than that of Co^{2+}. In contrast to this tendency, the ordered moments for samples with x>0.75 increase with the increasing Mn content. To better illustrate this behavior, we plotted the effective moment, theoretical spin-only ordered moment and refined ordered moment of M^{2+} as a function of composition of x, as shown in figure 7.20. A possible explanation of this anomalous behavior is that the

substitution of Mn in $CaCoGe_2O_6$ makes the system more frustrated. This could be due to the strong competition between different magnetic interactions in this disordered system and will be addressed further in the discussion section.

For sample with x=0.75, the intensities of (000) and (-110) magnetic reflections corresponding to k1 are shown in figure 7.21 (a), it reveals that the intensity of magnetic reflections become intense below 12K. In contrast, the (001) and (-111) magnetic reflections associated with k2 vs temperature are stronger below 15K, as shown in figure 7.21 (b). The refined NPD pattern at 2K by combining the two kinds of magnetic structures is shown in figure 7.19. The fit quality is equivalent if we use as a model (i) a 2-k magnetic structure or (ii) two single-k magnetic phases. The figure 7.22 show the refined 2-k magnetic structure. The total magnetic moment on each M site has a different amplitude: 3.1 and 7.9μ_B. The reasonable magnetic structure should be the superposition of these two magnetic structures distributed as small domains with slightly different Mn/Co composition (see left part of the figure 7.22), as we argued in the discussion part.

7.3.3.1 Diffuse scattering of $CaCo_{1-x}Mn_xGe_2O_6$

We have constructed an analytical magnetic correlation model to illustrate the physical picture for 1D AFM spin correlations in $CaMnGe_2O_6$ in chapter 5. Thediffuse scattering was fitted successfully with this 1D model. For comparison the diffuse scattering data extracted by making the difference between NPD patterns (at 40 and 100K) for samples with x=0.5, 0.75, 0.875 and 1 are presented in figure 7.23. It is noticeable that apparent diffuse scattering, arising from short range ordering spins, is present in sample with x=0.875, signaling by broad peak at around 2θ=30°. This character is very close to that of $CaMnGe_2O_6$. For sample x=0.75, this feature is really reduced and for samples with Mn content with x$\leq$0.625, it is not observable anymore. (in the figure, the diffuse scattering for x=0.5 is shown as an example).

7.3.4 Bilinear magnetoelectric effect

The commensurate magnetic structure in $CaCoGe_2O_6$ has been shown in the previous report that it adopts magnetic space group C2'/c' that allows bilinear magnetoelectric effect. However, we have determined the true space group P_c2_1/c which actually does not allow bilinear magnetoelectric effect, then we will measure the assumed bilinear ME effect to confirm our determination. In chapter 1, we have discussed the linear magnetoelectric effect (ME) and appreciated the thermodynamic potential of a system. By the definition of linear ME we know that a two-rank tensor can be used to describe the interaction between electric and magnetic terms. More important, we have measured this linear ME effect in $CaMnGe_2O_6$ and $CaMnSi_2O_6$ as addressed in chapter 5 and 6. Actually the bilinear effects arise if the thermodynamic potential contains terms of the form EHH or HEE. We will see what they mean by the expression of thermodynamic potential.

A concise form of thermodynamic potential F can be given by:[13]

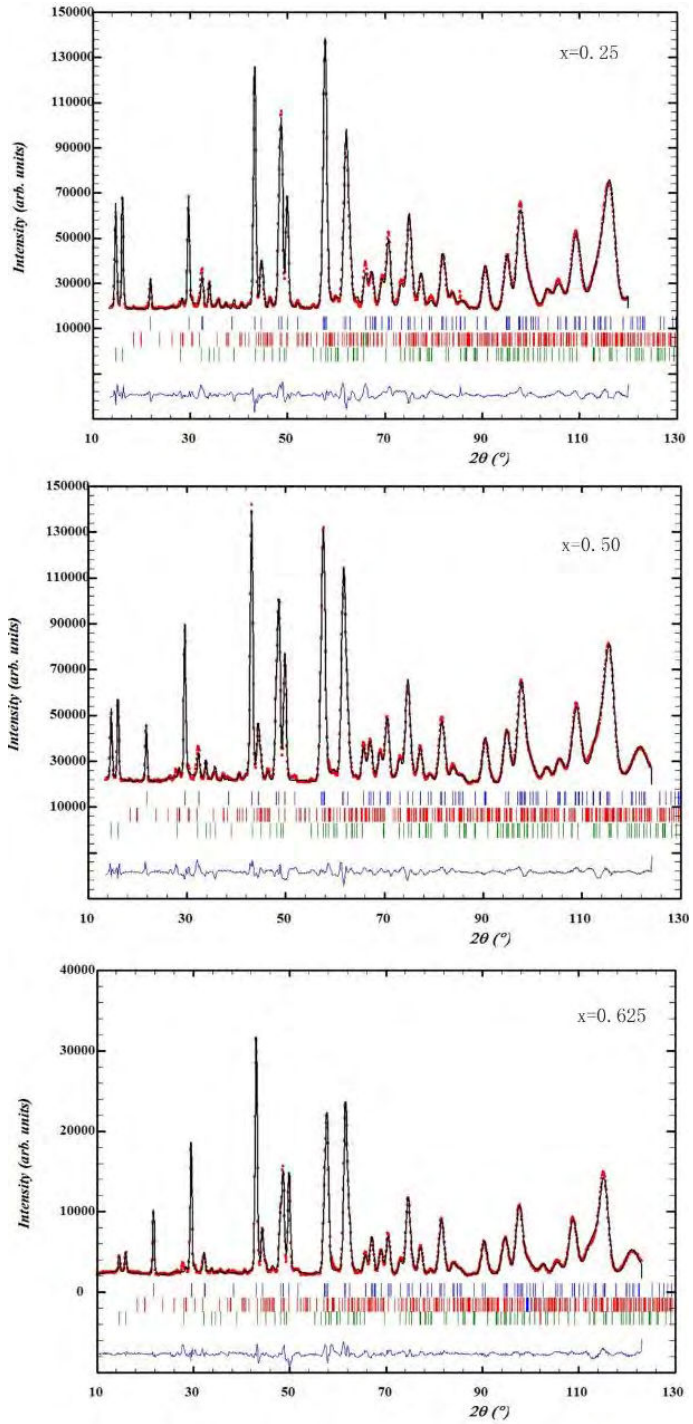

Figure 7.18: Observed (symbols) and calculated (line) powder neutron diffraction patterns for $CaCo_{1-x}Mn_xGe_2O_6$(x=0.25, 0.5, 0.625) at 2 K. The green tick marks show the magnetic reflections. The nuclear reflections are denoted by blue tick marks. The reflections marked in red belong to a $CaGeO_3$ impurity phase. The blue line shows the difference between the observed and calculated diffraction patterns.

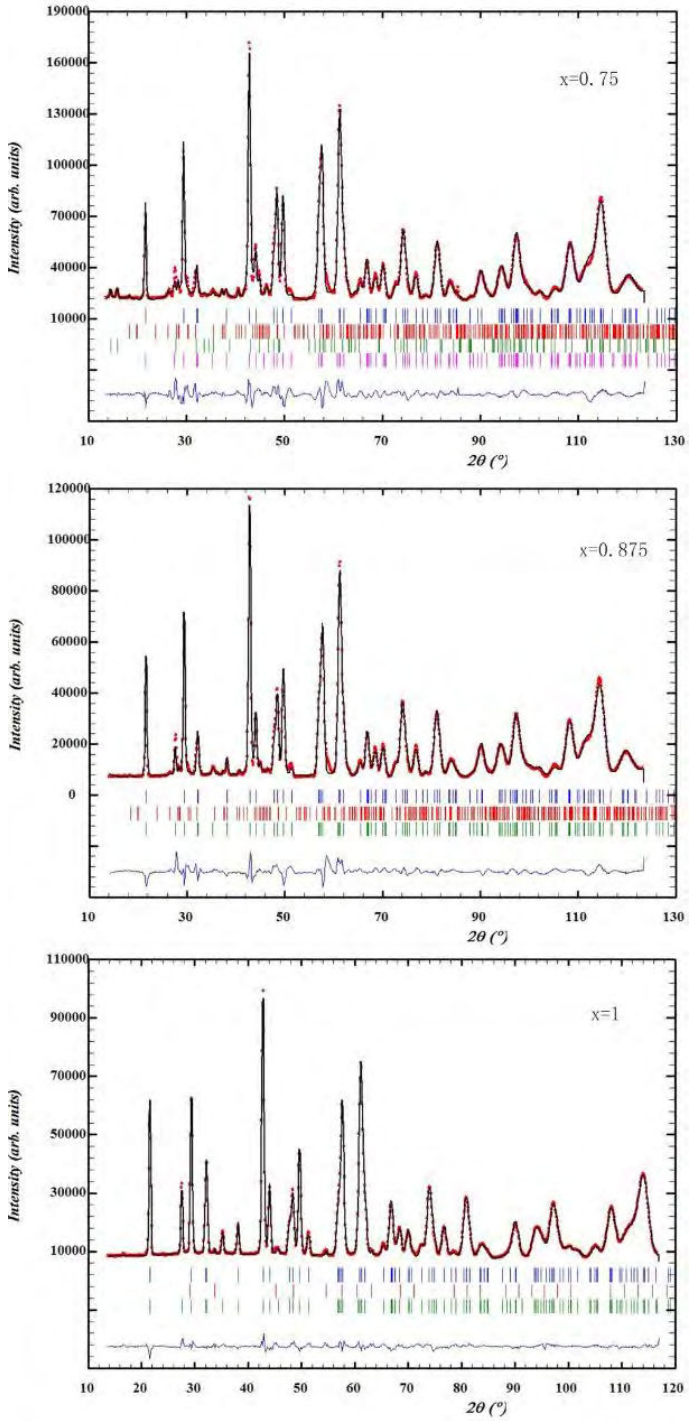

Figure 7.19: Observed (symbols) and calculated (line) powder neutron diffraction patterns for $CaCo_{1-x}Mn_xGe_2O_6$(x=0.75, 0.875, 1) at 2 K. The green and purple tick marks show the magnetic reflections. The nuclear reflections are denoted by blue tick marks. The reflections marked in red belong to a $CaGeO_3$ impurity phase. The blue line shows the difference between the observed and calculated diffraction patterns.

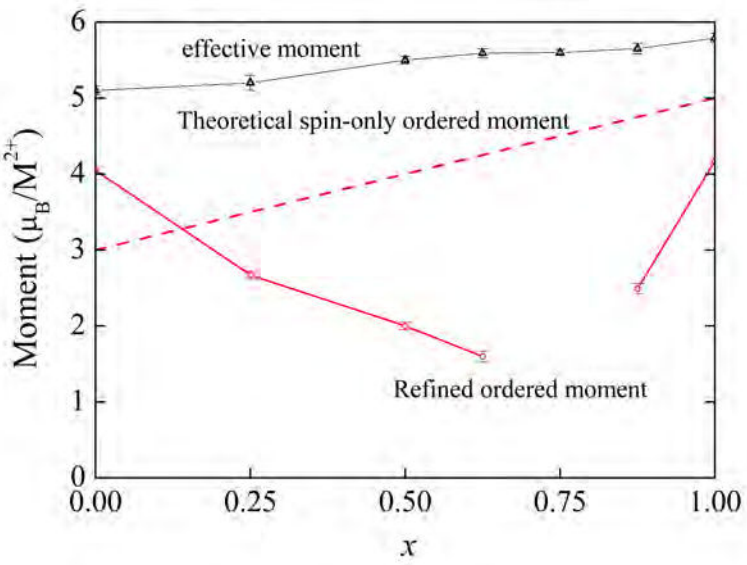

Figure 7.20: Effective moment, theoretical spin-only ordered magnetic moment and refined ordered magnetic moment vs x.

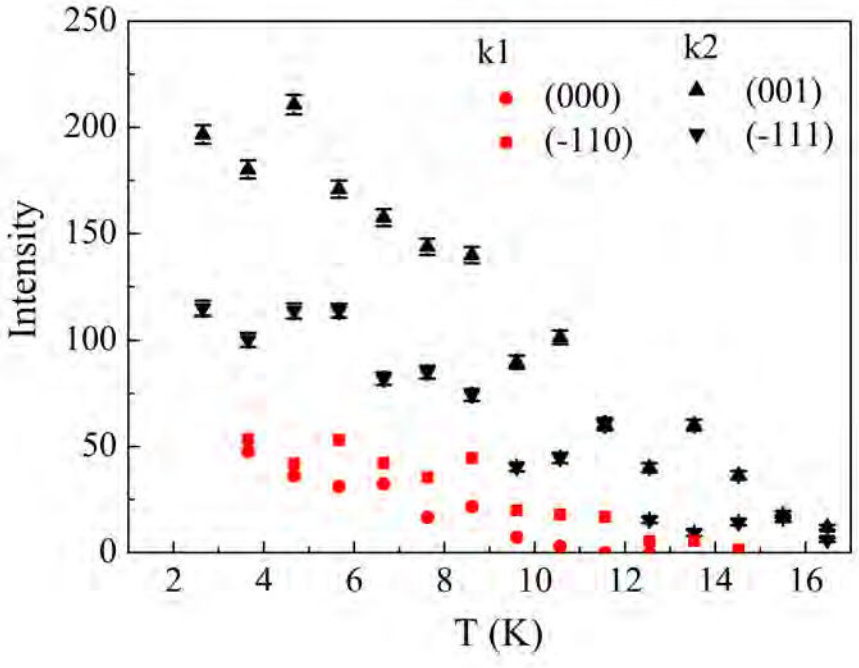

Figure 7.21: (a) Intensities of (000) and (-110) magnetic reflections corresponding to k1, and (b) (001) and (-111) magnetic reflections corresponding to k2 observed by NPD, as a function of temperature in sample with x=0.75.

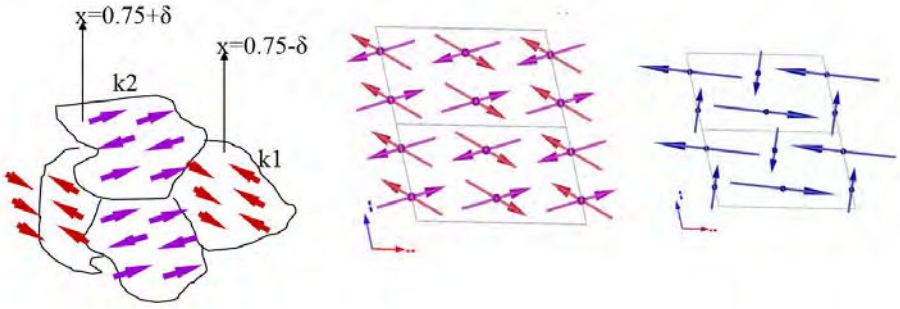

Figure 7.22: 2-k vector magnetic structure for sample with x=0.75. (left) Two types of domains with different k vectors ;(middle) Magnetic moments for k1 and k2 vectors; (right) The modulated magnetic structure.

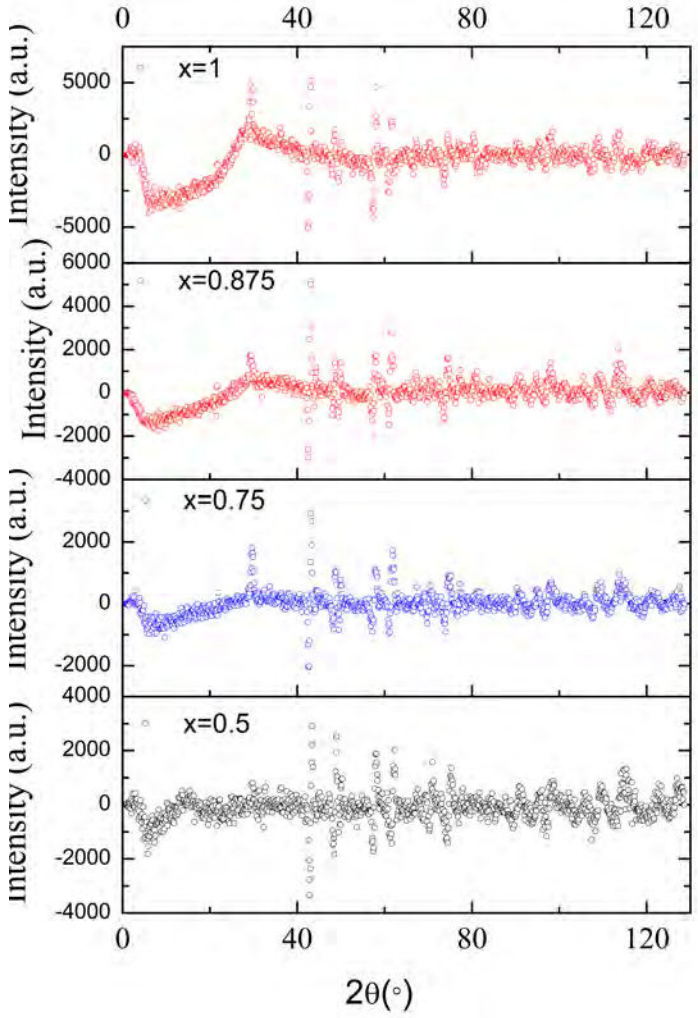

Figure 7.23: Diffuse scattering derived from NPD data for $CaCo_{1-x}Mn_xGe_2O_6$ (x=0.5, 0.75, 0.875, 1).

$$F = F_0 - \alpha_{ik}E_iH_k - \frac{1}{2}\beta_{ijk}E_iH_jH_k - \frac{1}{2}\gamma_{ijk}H_iE_jE_k. \tag{7.2}$$

From this expression, the electric polarization P_i and the magnetization M_i can be obtained:

$$P_i = \alpha_{ik}H_k + \frac{1}{2}\beta_{ijk}H_jH_k + \gamma_{jik}H_jE_k \tag{7.3}$$

$$M_i = \alpha_{ki}E_k + \beta_{jik}E_jH_k + \frac{1}{2}\gamma_{ijk}E_jE_k \tag{7.4}$$

The third term in 7.3 represents the magnetic field dependence of the dielectric susceptibility because $\chi^e_{ik}=\frac{P_i}{E_k}$. The tensors β_{ijk} and γ_{ijk} are symmetric in their last two indices. Indeed, the tensor β_{ijk} has similar form as the piezoelectric tensor while tensor γ_{ijk} has the similar expression as the piezomagnetic tensor. All the magnetic point groups that allow the terms EHH and HEE in the expansion of thermodynamic potential are summarized in table 1.5.8.3 in Ref. [13], By looking up the magnetic point group 2'/m, we see that this group allows only the magnetoelectric effect HEE. It means that materials with these point group possess only one tensor of magnetoelectric susceptibility, i.e. the tensor γ_{ijk} of the bilinear ME effect. The matrix form of γ_{ijk} tensor is given by:

$$\gamma_{ijk} = \begin{pmatrix} \gamma_{11} & \gamma_{12} & \gamma_{13} & 0 & \gamma_{15} & 0 \\ 0 & 0 & 0 & \gamma_{24} & 0 & \gamma_{26} \\ \gamma_{31} & \gamma_{32} & \gamma_{33} & 0 & \gamma_{35} & 0 \end{pmatrix} \tag{7.5}$$

The bilinear ME effect corresponding to HEE has been experimentally observed in YFe_5O_{12}(with magnetic point group -3m') by means of a pulsed magnetic field[14]. The experiment based on dependence of the dielectric permittivity on the magnetic field has also been used to investigate this ME effect on YFe_5O_{12}.[15] It is worth noting that both these experiments were performed on a platelet single crystal, unfortunately, we donot have. All attempts of measuring bilinear magnetoelectric effect have been carried out on $CaCoGe_2O_6$ by measuring the induced current under either magnetic field or electric field and both of them with perpendicular and parallel H and E fields configuration,supporting our determined magnetic symmetry.

7.3.5 Magnetic properties of $CaMn_{0.5}Ni_{0.5}Ge_2O_6$ and $CaCo_{0.5}Ni_{0.5}Ge_2O_6$

In order to have a comparison in magnetic properties with $CaCo_{1-x}Mn_xGe_2O_6$, the dc magnetic susceptibilities of $CaMn_{0.5}Ni_{0.5}Ge_2O_6$ and $CaCo_{0.5}Ni_{0.5}Ge_2O_6$ have been measured with ZFC and FC procedures. Figure 7.24 (a) shows the temperature dependent magnetic susceptibility for $CaMn_{0.5}Ni_{0.5}Ge_2O_6$, a large difference between ZFC and FC curves below 50K as well as a cusp at 12K can be clearly seen. The former transition is very similar to the anomalous magnetic transition observed in $CaMn_xCo_{1-x}Ge_2O_6$(x=0.25,0.5, 0.625, 0.75, 0.875, 1). And the cusp at 12K reflects the AFM magnetic transition in $CaMn_{0.5}Ni_{0.5}Ge_2O_6$. However, $CaCo_{0.5}Ni_{0.5}Ge_2O_6$ undergoes a typical AFM phase transition at around 20K, characteristic of very sharp peak, as shown in figure 7.24 (b). No obvious bifurcation can be observed for

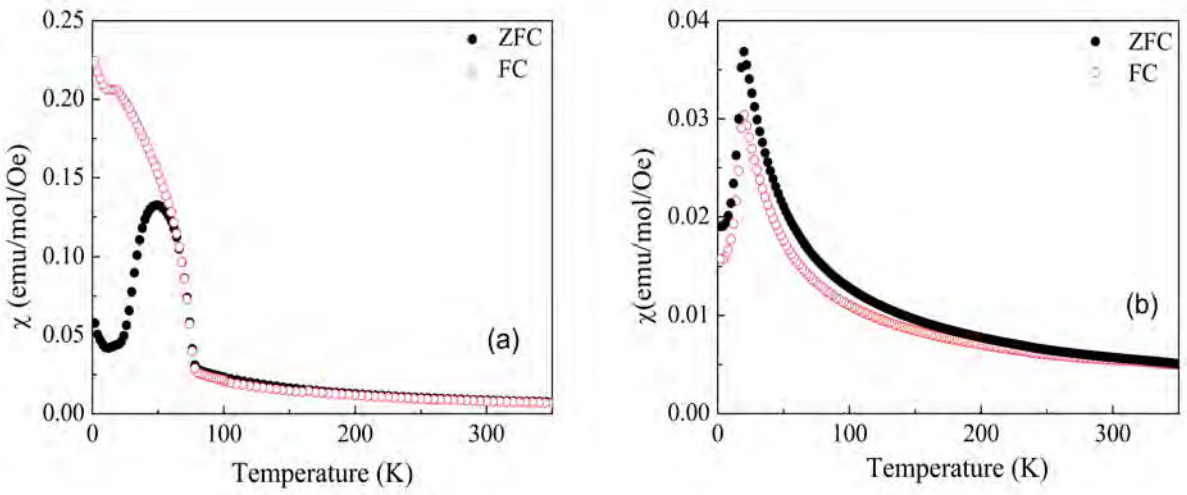

Figure 7.24: Temperature dependence of the magnetic susceptibility (ZFC and FC) of $CaMn_{0.5}Ni_{0.5}Ge_2O_6$ under external magnetic field with 0.01T. (b) Temperature-dependent magnetic susceptibilities of $CaCo_{0.5}Ni_{0.5}Ge_2O_6$ series measured at 0.01T.

ZFC and FC curves.

7.4 Discussion

The crystal structure of $CaCo_{1-x}Mn_xGe_2O_6$ solid solution is not modified, and all structural parameters coincidentally change with increasing Mn content. Let us consider some features of the series of $CaMGe_2O_6$ pyroxenes where M=Mn^{2+}, Fe^{2+}, Co^{2+}, Ni^{2+}, Cu^{2+}, Zn^{2+}. Among them, as we have seen that only $CaCuGe_2O_6$ crystallizes into $P2_1/c$ symmetry. Nevertheless, we expect some common features in this series. Based on the observed <M-O> distances in $CaMGe_2O_6$ pyroxenes, we can calculate the effective ionic radius of the M cation, assuming the oxygen ionic radius to be 1.4Å. The crystal structure of $CaFeGe_2O_6$ is taken from Ref. [4]. These radii are shown in table 7.5 along with those of Shannon[16]. It is apparent that the M cation radii in clinopyroxenes are systematically smaller than the Shannon radii, which were derived from oxides and fluorides. Similar discrepancies are also found in many silicate pyroxenes[11]. This fact reflects that the M-O bonding in pyroxenes is more covalent than that in some corresponding oxides. The plot of the ratio of <M-O>/<Ca-O> vs the effective ionic radii in $CaMGe_2O_6$ pyroxenes where M=Mn^{2+}, Fe^{2+}, Co^{2+}, Ni^{2+}, Cu^{2+}, Zn^{2+} yields nearly linear relationship, as shown in figure 7.25. Thus, this effective radius may be more useful in exploring structural effects of cation substitution in pyroxenes.

The magnetic phase diagram for solid solution $CaCo_{1-x}Mn_xGe_2O_6$ is shown in figure 7.26 which is very rich and complex. All samples containing Mn undergo two magnetic phase transitions, the low temperature one at T_N corresponds to long range AFM transition, the high temperature phase transition at Tm may be due to the existence of tiny amount of impurity phase $(Mn,Co)_3O_4$ which is difficult to be seen by XRD or NPD. We have seen that

Table 7.5: Effective ionic radius of the M cations.

M^{2+}	Eff. Radii(Å)	Shannon(Å)	△
Mn^{2+}	0.785	0.83	0.045
Fe^{2+}	0.739	0.78	0.041
Zn^{2+}	0.727	0.74	0.013
Co^{2+}	0.716	0.745	0.029
Ni^{2+}	0.689	0.69	0.001
Cu^{2+}	0.659	0.65	-0.009

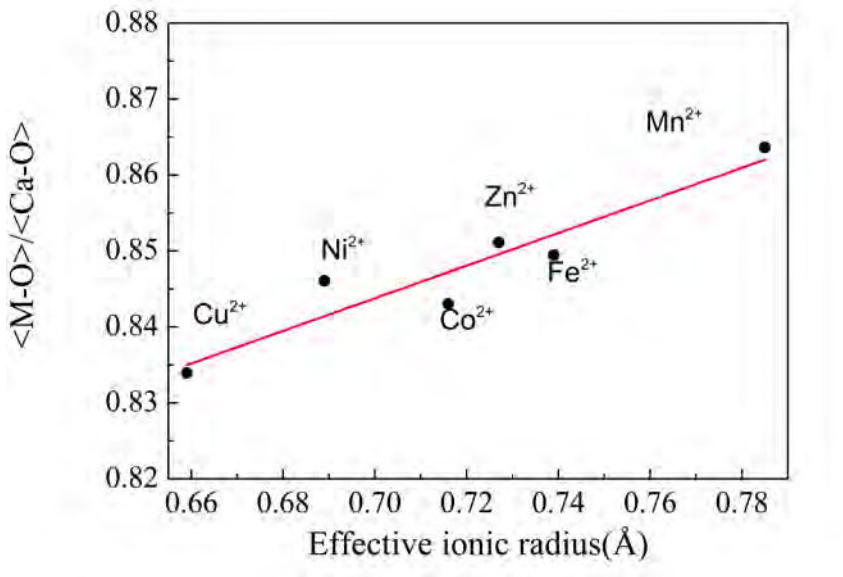

Figure 7.25: The radio of <M-O>/<Ca-O> as a function of effective ionic radius of $CaMGe_2O_6$ pyroxenes where M=Mn^{2+}, Fe^{2+}, Co^{2+}, Ni^{2+}, Cu^{2+}, Zn^{2+}.

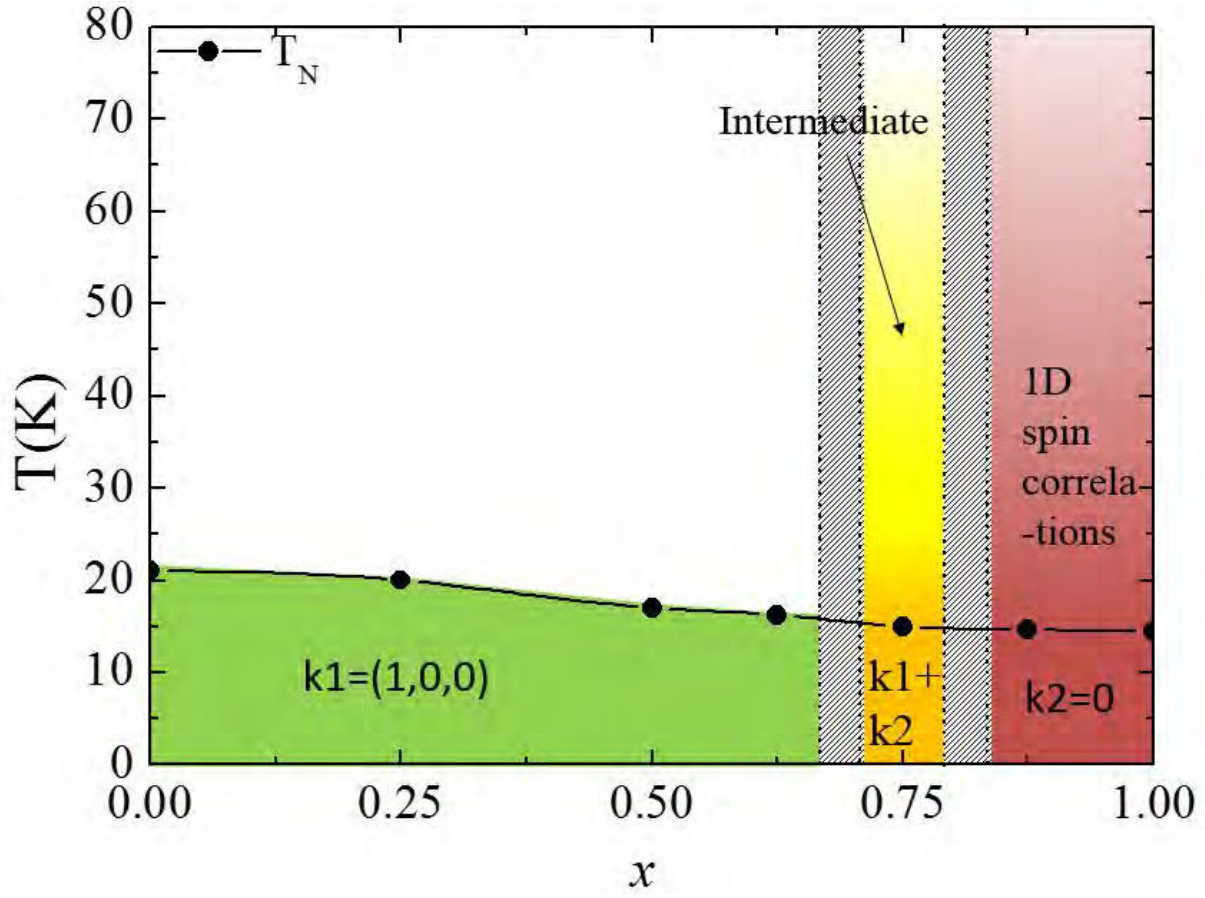

Figure 7.26: Magnetic phase diagram for solid solution $CaCo_{1-x}Mn_xGe_2O_6$(x=0, 0.25, 0.5, 0.625, 0.75, 0.875, 1).

the decrease of Tm with increasing Mn content in $CaCo_{1-x}Mn_xGe_2O_6$, similarly, this behavior has also been observed in the previous investigation about solid solution $(Mn,Co)_3O_4$. [18]

At Co rich side with $0<x\leq 0.625$, below T_N samples have similar magnetic structure with the host compound, and magnetic structure can be described by k1=(1,0,0). The reduced magnetic moment as the increase of Mn content can be explained as a consequence of chemical-substitution-induced spin disorder, in particular, along the chains where the nearest neighboring interactions vary between +J and -J due to spins of Co-Co order in FM and the spins of Mn-Mn are AFM.

We turn to Mn rich side with $x\geq 0.875$ diffuse magnetic scattering observed just above T_N evidences the nature of 1D short-range magnetic correlations, which can be fitted with the model constructed in chapter 5 as done in $CaMnGe_2O_6$. Accordingly, this 1D short range order is attributed to the presence of magnetic frustration in 3D spin ordered system. The magnetic structures of samples are determined to be ferromagnetically arranged antiferromagnetic chains, which is similar with $CaMnGe_2O_6$.

Finally, we found that within a very narrow range of Mn content, samples such as x=0.75 have intermediate state. A striking result is that the magnetic structure of sample with

x=0.75 has to be described by vectors k1 and k2. Two hypotheses related to the magnetic structure emerge here: (i) a double-k homogeneous structure in the whole sample, or (ii) the superposition of two types of magnetic structures present in different domains with slightly different Mn/Co composition. The former one will be ruled out because it is not physical: if it holds, the total moment will have a modulated amplitude, as we addressed above. Concerning the second assumption, the magnetic reflection peaks are not broad, indicating the large domain size. In addition, two magnetic phases indicate two magnetic transition, this shoud be reflected by the different onsets of magnetic ordering temperature. Since for sample with x=0.625 and x=0.875 have very close ordering temperatures, for sample with x=0.75, the transition temperatures for both magnetic structures are so close that it is difficult to discern this difference, as seen from figure 7.21. As a result, the domain hypothesis is more reasonable.

7.5 Conclusion

The solid solution $CaCo_{1-x}Mn_xGe_2O_6$ has been synthesized using solid state reaction, and their crystal and magnetic structures have been extensively studied by means of x-ray diffraction, magnetic susceptibility measurements, heat capacity measurements and neutron diffraction. The diffraction data show all samples crystallized into C2/c space group. The in-situ neutron diffraction reveals that all samples retain the same crystal structure even cooled down to 2K. The steric effect of crystal chemistry was verified in this solid solution.

The magnetic diagram of $CaCo_{1-x}Mn_xGe_2O_6$ is rich and complex. The magnetic transition observed typically below 20K is confirmed as long-range AFM transition, the magnetic structure, can be described as antiferromagnetic arrangement of ferromagnetic chains for Co rich compounds and ferromagnetically ordered antiferromagnetic chains for Mn rich compounds. The magnetic structure for sample with x=0.75 is proposed as the superposition of two magnetic structures present in different domains with slightly different Mn/Co composition.. Transition at high temperature regime probably arises from impurity phase $(Mn,Co)_3O_4$. In Mn-rich side where k=(0,0,0), we observed 1D AFM correlations above T_N. This short-range spin correlations are attributed to the magnetic frustration within triangular-like spin configuration.

Bibliography

[1] J. Rodriguez-Carvajal, Recent Advances in Magnetic Structure Determination by Neutron Powder Diffraction. Physica B, 192, 1993, 55-69. 160, 176

[2] E. Makovicky and T. Balic-Zunic, New Measure of Distortion for Coordination Polyhedra, Acta Cryst. B, B54, 1998, 766-773. 167

[3] G.J. Redhammer, G. Roth, W. Treutmann, et al., Magnetic ordering and spin structure in Ca-bearing clinopyroxenes CaM^{2+}(Si, Ge)2O6, M=Fe, Ni, Co, Mn, J. Solid State Chem. 181, 2008, 3163-3176. 159, 168, 175, 178

[4] G.J. Redhammer, G. Roth, Anatoliy Senyshyn, Crystal and magnetic spin structure of Germanium-Hedenbergite, $CaFeGe_2O_6$, and a comparison with other magnetic/magnetoelectric/multiferroic pyroxenes, Z. Kristallogr., 228, 140-150 (2013). 186

[5] P. Thompson, D.E. Cox, J.B. Hastings, Rietveld refinement of Debye-Scherrer synchrotron X-ray data from Al_2O_3, J. Appl. Cryst., 20, 1987, 79-83. 162

[6] J.F. Bérar and G. Baldinozzi, Modeling of line-shape asymmetry in powder diffraction, J. Appl. Cryst., 26, 1993, 128-129. 162

[7] J. Rodrıguez-Carvajal, BondStr, 2010, www.ill.eu/sites/fullprof/ 162

[8] E.F. Bertaut, Representation analysis of magnetic structures, Acta Crystallogr. Sec. A 24, 1968, 217. 176

[9] A. S. Wills, A new protocol for the determination of magnetic structures using simulated annealing and representational analysis (SARAh), Physica B, 278, 2000, 680. 176

[10] J. Rodriguez-Carvajal, BasIreps: a program for calculating irreducible representations of space groups and basis functions for axial and polar vector properties (see FullProf site: http://www.ill.eu/sites/fullprof). 176

[11] Subrata Ghose, Cheng Wan, Fujio P.Okamura, Crystal structures of $CaNiSi_2O_6$ and $CaCoSi_2O_6$ and some crystal-chemical relations in C2/c clinopyroxenes, American, Mineralogist, 72, 1987, 375-381. 186

[12] S. V. Streltsov and D. I. Khomskii, Electronic structure and magnetic properties of pyroxenes (Li,Na)TM(Si,Ge)$_2$O$_6$: Low-dimensional magnets with 90° bonds, Phys. Rev. B 77, 2008, 064405. 168

[13] A.S. Borovik-Romanov, H.Grimmer, M.Kenzelmann, International tables for crystallography, Nonlinear magnetoelectric effects. VolD, 2013, Ch.1.5.8.2, 106-153. 180, 185

[14] O'Dell, An induced magneto-electric effect in yttrium iron garnet, Philos. Mag., 16, 1967, 487. 185

[15] M. J. Cardwell, Measurement of the magnetic field dependent electric susceptibility of yttrium iron garnet, Phil. Mag., 20, 1969, 1087. 185

[16] R.D. Shannon, Revised effective ionic radii and systematic studies of interatomic distances in halides and chalcogenides, Acta Cryst., A32, 1976, 751-767. 162, 186

[17] H. T. Stokes and D. M. Hatch, "FINDSYM: Program for Identifying the Space Group Symmetry of a Crystal." J. Appl. Cryst. 38, 2005, 237-238. 178

[18] D.G. Wickham, W. J. Croft, Crystallographic and magnetic properties of several spinels containing trivalent JA-1044 manganese, 7, 1958, 351.

188

Chapter 8

$SrMGe_2O_6$(M=Mn, Co): a new family of pyroxenes

8.1 Introduction

We have appreciated the typical topology for pyroxenes ($M2M1T_2O_6$) in chapter 1, ranging from low monoclinic ($P2_1/c$) to high monoclinic phases ($C2/c$) which being the active ground in exploring the multiferroic, magnetoelectric and ferrotoroidic properties as well as some exotic quantum spin physics. These intriguing physical properties are attributed to their relevant magnetic symmetries which depend on their unique crystal structure and orbital occupancy of magnetic cations.

The most attractive characteristics of pyroxenes is the presence of isolated zigzag edge-sharing chains of $M1O_6$ octahedra. Since the chains are bridged by SiO_4 or GeO_4 tetrahedra, the magnetic interchain interaction is considered to be negligible as compared to the intrachain interaction, therefore, the system can be considered as quasi-unidimensionnal. In the presence of interchain exchanges, the dimensionality of the system is altered and a long range magnetic ordering can appear at low temperature. The type of magnetic order, either FM or AFM, depends both on the strengths and signs of intrachain and interchain interactions.

Even though the presence of isolated $M1O_6$ chains is a common structural feature for most pyroxenes, a variety of magnetic properties have been found. Apart from the different orbital occupancies which depend on different cations on M1 sites, the chemical substitution of nonmagnetic cations on M2 and T sites also largely affects the magnetic properties of pyroxenes. For example, $NaCrSi_2O_6$ undergoes AFM transition at 2.6K while $NaCrGe_2O_6$ is a FM below 6K[1]; $NaFeSi_2O_6$ displays multiferroic properties while $LiFeSi_2O_6$ only shows linear magnetoelectric effect[2]. According to our studies and recent reports[3, 4], the magnetic ground state in $CaMGe_2O_6$ and $CaMSi_2O_6$ for M=Ni, Co, Fe, Mn is the same and it seems that the effect on magnetic properties from the chemical substitution of T cation is negligible in Ca-based pyroxenes.

However, so far, Ca-based pyroxenes are known as the only series for divalent-based pyroxenes containing transition metal cations. Although Mg-based magnetic pyroxenes have been

reported as we presented in chapter 4, Mg^{2+}cation typically occupies the M1 site instead of M2 site, as a result, divalent transition metal cations occupy the M2 sites with very weak magnetic interactions, making such systems inappropriate for displaying interesting magnetic properties Hence there are very rare choices to study the magnetostructural relationships. The chemical substitution of Ca^{2+} by Sr^{2+}may bring in new physics and structural chemistry in pyroxene family since the large cation radius of Sr^{2+} will obviously modify the unit cell parameters, in particular the b-parameter, which will make the zigzag $M1O_6$ octahedra chains more isolated. An ensuing decrease in interchain interactions and possible new magnetic properties will be expected. On the other aspect, this new pyroxene family allows us to compare the influence of chemical substitution on the magnetic properties and physical properties of pyroxenes with same transition metal cations.

Therefore, we present here the investigation of synthesis, crystal structure and magnetic properties of $SrMGe_2O_6$(M=Mn,Co), belonging to a new family of pyroxenes, by means of neutron diffraction, heat capacity and magnetic measurements. Single crystal x-ray diffraction is used to solve the crystal structure of $SrMnGe_2O_6$. A long range spin ordered state in $SrMnGe_2O_6$ is found below 4.5K and the relevant magnetic structure is determined by neutron diffraction data. It turns out that $SrMnGe_2O_6$ has cycloidal spin arrangement below 4.5K. The multiferroic properties associated with the cycloidal magnetic structure are experimentally observed and a spin-current model is used to explain the spontaneous polarization below T_N. The crystal structure of $SrCoGe_2O_6$ is determined by ab initio method from powder diffraction data. Magnetic and heat capacity measurements coincidentally reveal the presence of long-range magnetic order below 10 K. We determine the magnetic structure of $SrCoGe_2O_6$ where a FM order within chain is antiferromagnetically coupled between the nearest neighboring chains.

8.2 Experimental details

8.2.1 Sample preparation

Polycrystalline $SrMGe_2O_6$ (M=Mn,Co) were prepared by standard solid-state reaction. As starting materials, the stoichiometric mixtures of reagent-grade $SrCO_3$, MnO_2, Co_3O_4 and GeO_2 were ground in an agate mortar and pressed into pellets. The pellets of $SrMnGe_2O_6$ were placed in a platinum boat and heated in air to 1150°C at 10 °C/min, then held at 1150°C for 100 h and cooled down to room temperature. For $SrCoGe_2O_6$, to obtain the single phase sample, the pellets were calcined in air at 1100°C for 100 h.

As a congruently melting compound, single crystals of $SrMnGe_2O_6$ were grown by cooling a stoichiometric melt using self-flux method. The dark brown crystals with needle shape (about 1mm in length) were obtained by cooling the molten solution from 1150°C to room temperature.

8.2.2 X-ray and neutron powder diffraction

X-ray powder diffraction (XRPD) measurements were carried out using a D5000T diffractometer equipped by position sensitive detectors and with Cu Kα1 radiation filtered by a Ge (111) primary beam monochromator. The data were collected by step-scanning in the 2θ range of 10˜90° at a step size of 0.016°.

For $SrMGe_2O_6$(M=Mn, Co), neutron powder diffraction (NPD) experiments were performed on the two-axis diffractometer D1B at Institut Laue Langevin (ILL), from 1.5 K to room temperature. For nuclear structure refinement, NPD data were collected at 300 K with the 1.28 Å wavelength. For magnetic structure investigation, the neutron wavelength of 2.52 Å was used, with longer data collections at 2 K, 15 K, 30 K, 100 K and 300 K and a slow temperature ramp between 1.7 K and 300 K on heating process was accompanied. Both XRPD and NPD data were analyzed by the Rietveld method using the Fullprof suite programs[10].

8.2.3 Single crystal x-ray diffraction

Single crystal x-ray diffraction experiments for $SrMnGe_2O_6$ were performed at room temperature on Kappa CCD diffractometer using Ag Kα1 radiation (0.56087 Å). First a proper single crystal with needle shape was selected using a microscope with polarized light. Then the single crystal was placed on the top of quartz fiber which was then fixed on the goniometer head for centering the crystal. The data collection as carried out up to ϑ=30.0° by rotation around ω- and φ-axis with a step size of 0.5° at a speed of 20s/°. Determination of the orientation matrix and unit cell was carried out with the program Dirax[5], then EvalCCD was used for data reduction[6]. The absorption correction was applied using program SADABS[8]. Structure solution was obtained using direct methods with program SIR97[7] , followed by structure refinement with SHELXL-97[9].

8.2.4 Magnetic susceptibility measurement

The temperature-dependent magnetic susceptibility was measured with a SQUID magnetometer (Quantum Design, Magnetic Property Measurement System). The dc magnetic susceptibility measurements were performed under both zero field cooled (ZFC) and field cooled (FC) procedures over the temperature range between 2 K and 350 K in magnetic fields of 0.01, 0.1, 1 and 5 T for $SrMnGe_2O_6$, of 0.01 and 0.1 T for $SrCoGe_2O_6$. Magnetic hysteresis loops between -7T and 7 T were recorded between 10 and 90K for $SrMnGe_2O_6$. For $SrCoGe_2O_6$, the field dependence of magnetization was measured between 2 K and 50 K over a magnetic field range between 0 to 7 T.

Moreover, alternating current (ac) susceptibility for $SrMnGe_2O_6$ was also measured at fixed frequencies of 1, 250, and 500Hz over the temperature range of 2K$\leq T \leq$ 100K. A drive amplitude of 2 Oe was applied for each ac susceptibility measurement.

8.2.5 Specific heat measurement

Heat capacity measurement was carried out using a relaxation technique on a Quantum Design Physical Property Measurement System (PPMS). For $SrMnGe_2O_6$, the heat capacity was measured from 2 to 250K under applied magnetic fields of 0T and 8T. The heat capacity of $SrCoGe_2O_6$ was recorded in the temperature range of 2-300K without external field. For all the measurements, the pelletized sample was mounted on sample platform with Apiezon N-grease (applied within low temperature measurement) for better thermal contact.

8.2.6 Electrical properties

The temperature dependence of electric polarization was obtained for $SrMnGe_2O_6$ by measuring pyroelectric current under various external magnetic fields (0 T, 2 T, 4 T, 6 T, 8 T). In order to improve the grain connectivity of sample, the sample was first sintered by heating a pressed pellet at 500°C for 20 hours. Then, the pellet was coated with silver epoxy on both sides to make conducting electrodes. The magnetoelectric annealing was performed before the measurement of pyroelectric current by cooling down the sample from 50 K to 2 K with simultaneously applying both electric field E of ±512 KV/m and magnetic field μ_0H of 8 T. At 2K, the poling fields were removed. Then, the sample was heated at a constant rate of 3 K/min, and the pyroelectric current curves under various magnetic fields were recorded using a Keithley 6514 electrometer. Electric polarization was eventually obtained by the integration of the time dependence of the pyroelectric current.

8.3 Results and discussion

8.3.1 Crystal structure

8.3.1.1 Crystal structure determination for $SrMnGe_2O_6$ and $SrCoGe_2O_6$

By performing a single crystal x-ray diffraction experiment on a $SrMnGe_2O_6$ single crystal, we are able to solve its crystal structure and to refine it. XRD data of single crystal were collected with the maximum angle of θ=30.0°. Patterns with 12278 reflections were collected with -18≤h≤18, -14≤k≤16 and -9 ≤l≤9. Among them, 1544 were independent reflexions, with 1318 observed ones ($I > 2\sigma(I)$). The crystal structure of $SrMnGe_2O_6$ was solved by SIR97. It turns out that $SrMnGe_2O_6$ crystallizes into monoclinic C2/c symmetry with lattice parameters: a=10.35(1)Å, b=9.42(1)Å, c=5.51(1)Å, β=104.67(1)°. The obtained atomic coordinates and the isotropic thermal parameters are summarized in table 8.1.

The polycrystalline $SrMnGe_2O_6$ sample is dark brown in color which is similar to that of $CaMnGe_2O_6$. A starting model for structural refinement of powder XRD, can be obtained from single crystal determination, the powder XRD data were thus refined by the Rietveld method using the Fullprof program[10]. The refined structural parameters are close to those determined from single crystal XRD (not shown here). In order to check the nuclear crystal structure, the NPD data collected at room temperature with wavelength of 1.28Å were refined with the same

Table 8.1: Agreement factors and refined structural parameters for $SrMnGe_2O_6$ at 300K. Note: XRD-single crystal XRD at RT; NPD-neutron powder diffraction at RT.

Name	Method	Position	x	y	z	B(Å^2)
Sr	SC-XRD	4e	0.0	0.30814(3)	0.25	0.202(1)
	NPD	4e	0.0	0.3094(6)	0.25	0.9(1)
Mn	SC-XRD	4e	0.0	0.90707(4)	0.25	0.162(2)
	NPD	4e	0.0	0.905(1)	0.25	0.3(2)
Ge	SC-XRD	8f	0.28247(2)	0.09514(2)	0.21798(4)	0.129(2)
	NPD	8f	0.2820(3)	0.0965(3)	0.2201(6)	0.30(6)
O1	SC-XRD	8f	0.1110(2)	0.0870(2)	0.1390(3)	0.186(1)
	NPD	8f	0.11109(4)	0.0828(5)	0.1394(8)	0.72(8)
O2	SC-XRD	8f	0.3575(2)	0.2542(2)	0.3159(3)	0.274(2)
	NPD	8f	0.3559(4)	0.2551(4)	0.3155(8)	0.71(8)
O3	SC-XRD	8f	0.3535(2)	0.0218(2)	0.9807(3)	0.191(1)
	NPD	8f	0.3530(3)	0.0215(5)	0.9827(9)	0.36(8)
SC-XRD: a=10.35(1)Å, b=9.42(1)Å, c=5.51(1)Å, β=104.67(1)°						
NPD: a=10.3511(6)Å, b=9.4204(5)Å, c=5.5093(3)Å, β=104.700(2)°						
NPD: Rp=3.69, Rwp=4.90, Rexp=0.50, Chi^2=97.9, R_{Bragg}=5.96						

starting model. For both XRPD and NPD refinements: the background was modelled by a linear interpolation of selected points; to describe the profile of pattern, the Thomson-Cox-Hastings model[13] was employed; low angle peak asymmetry was taken into account using the Berart-Baldinozzi model[14]. A small amount of unknown impurity phase was detected but despite many efforts, the phase could not be identified and could not be considered in the refinements. The NPD refinement results are consistent with the single crystal XRD results, as shown in table 8.1. Table 8.2 presents the selected interatomic distances, bond angles and bond valence sums[15] derived from NPD data. The final refinement plots of XRPD and NPD are shown in figure 8.1(a) and (b), respectively.

The color of $SrCoGe_2O_6$ powder is light pink. Its crystal structure was determined from x-ray powder diffraction data. The Dicvol program[11], integrated into Fullprof suite, was used to index peaks and extract the peak information from a powder diffraction pattern (XRPD). A Lebail fit was then performed.

To solve the crystal structure from powder diffraction, the FOX program was used [12]. C2/c was obtained as the most probable space group by successive LeBail fits. Then a random atomic model was provided to the program and the global optimization process was followed to determine the positions of all atoms. Then, by performing Rietveld refinement using Fullprof Suite based on the solution provided by FOX, the crystal structure of $SrCoGe_2O_6$ was determined. We found that $SrCoGe_2O_6$ also crystallizes into monoclinic C2/c symmetry and is isostructural to $CaCoGe_2O_6$, being the typical crystal structure for divalent-metal based pyroxenes. The final Rietveld refinement plot for room temperature XRPD pattern of $SrCoGe_2O_6$ is shown in figure 8.2 (a). The only impurity phase is $Sr_3CoGe_5O_{14}$ which was taken into account in the refinement and its cell parameters and scale factor were refined.

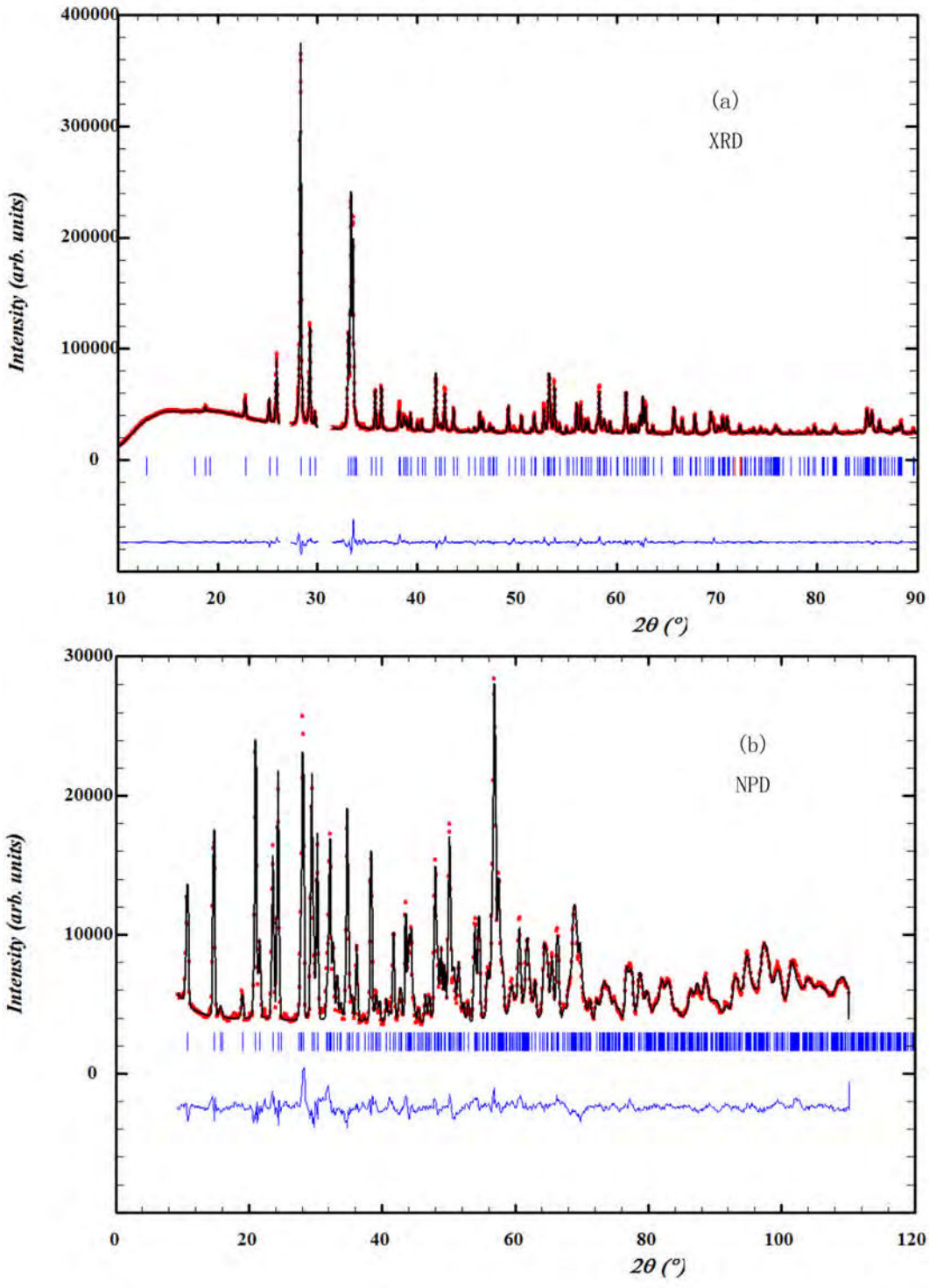

Figure 8.1: Profiles of XRPD (a) and NPD (b) patterns of $SrMnGe_2O_6$ taken at room temperature. Observed (red), calculated (black), and difference (blue) plots are shown. The vertical marks represent positions calculated for Bragg reflections of $SrMnGe_2O_6$.

Table 8.2: Principal cation-anion distances (Å) and angles for $SrMnGe_2O_6$ from NPD at room temperature.

Sr-O1	2.570(7)	Ge-O1	1.716(5)
Sr-O2	2.552(4)	Ge-O2	1.700(5)
Sr-O3	2.710(6)	Ge-O3	1.800(6)
Sr-O3	2.736(6)	Ge-O3	1.825(5)
Ave.Dist.	2.642(2)	Ave.Dist.	1.760(3)
Distortion	9.52×E-04	Distortion	9.14×E-04
BVS	1.99(1)	BVS	3.91(3)
Mn-O1	2.202(9)	Mn-Mn (J)	3.282(8)
Mn-O1	2.164(4)	Mn-Mn (NNN intra)	5.5093(3)
Mn-O2	2.152(8)	Mn–Mn(J2)	7.00(1)
Ave.Dist.	2.173(3)	Mn-Mn (J1)	5.975(7)
Distortion	0.95×E-04	Mn-O1-Mn	97.5(2)°
BVS	2.14(2)	O3-O3-O3	163.2(2)°

Table 8.3: Agreement factors and refined structural parameters for $SrCoGe_2O_6$ at 300K with NPD using wavelength of 1.28Å.

Name	position	x	y	z	B(Å^2)
Sr	4e	0.00000	0.3050(3)	0.25000	0.54(5)
Co	4e	0.00000	0.9099(9)	0.25000	0.9(1)
Ge	8f	0.2820(2)	0.0963(2)	0.2087(3)	0.34(3)
O1	8f	0.1083(2)	0.0825(3)	0.1318(4)	0.40(4)
O2	8f	0.3547(2)	0.2602(2)	0.3055(4)	0.69(4)
O3	8f	0.3553(2)	0.0191(2)	0.9788(4)	0.52(6)
a=10.2560(1)Å, b=9.2970(1)Å, c=5.4701(1)Å, β=105.588(1)°					
Rp=1.72, Rwp=2.28, Rexp=0.30, Chi^2=55.9, Rbragg=2.51					

The inital structure model for refining NPD data is similar with the XRPD refinement, except that the backgroud was described by a polynominal function with 12 parameters. The final refinement yielded a weight fraction of 0.54(3) % for the impurity phase. The nuclear structure parameters of $SrCoGe_2O_6$ were obtained by refining the NPD data measured at room temperature. Figure 8.2 (b) presents the final Rietveld refinement plot. The refinement results, main interatomic distances, bond angles and bond valence sums (derived from NPD data) calculated using the BondStr program[15] are respectively presented in table 8.3 and 8.4. Note that to have a consistent comparison in structure parameters between $SrMnGe_2O_6$and $SrCoGe_2O_6$ in the following, we only use the crystal structure parameters derived from NPD.

Since $SrMnGe_2O_6$ and $SrCoGe_2O_6$ have the same crystal structure and symmetry, we take the crystal structure of $SrCoGe_2O_6$ as a representative to illustrate the structure characteristic of this new family of pyroxenes. As shown in figure 8.3, analogous to the typical structure of clinopyroxenes, $SrMGe_2O_6$ is characteristic of almost one-dimensional chains made of the edge-sharing MO_6 octahedra and the corner-linking nonmagnetic GeO_4 tetrahedra chains (also one-

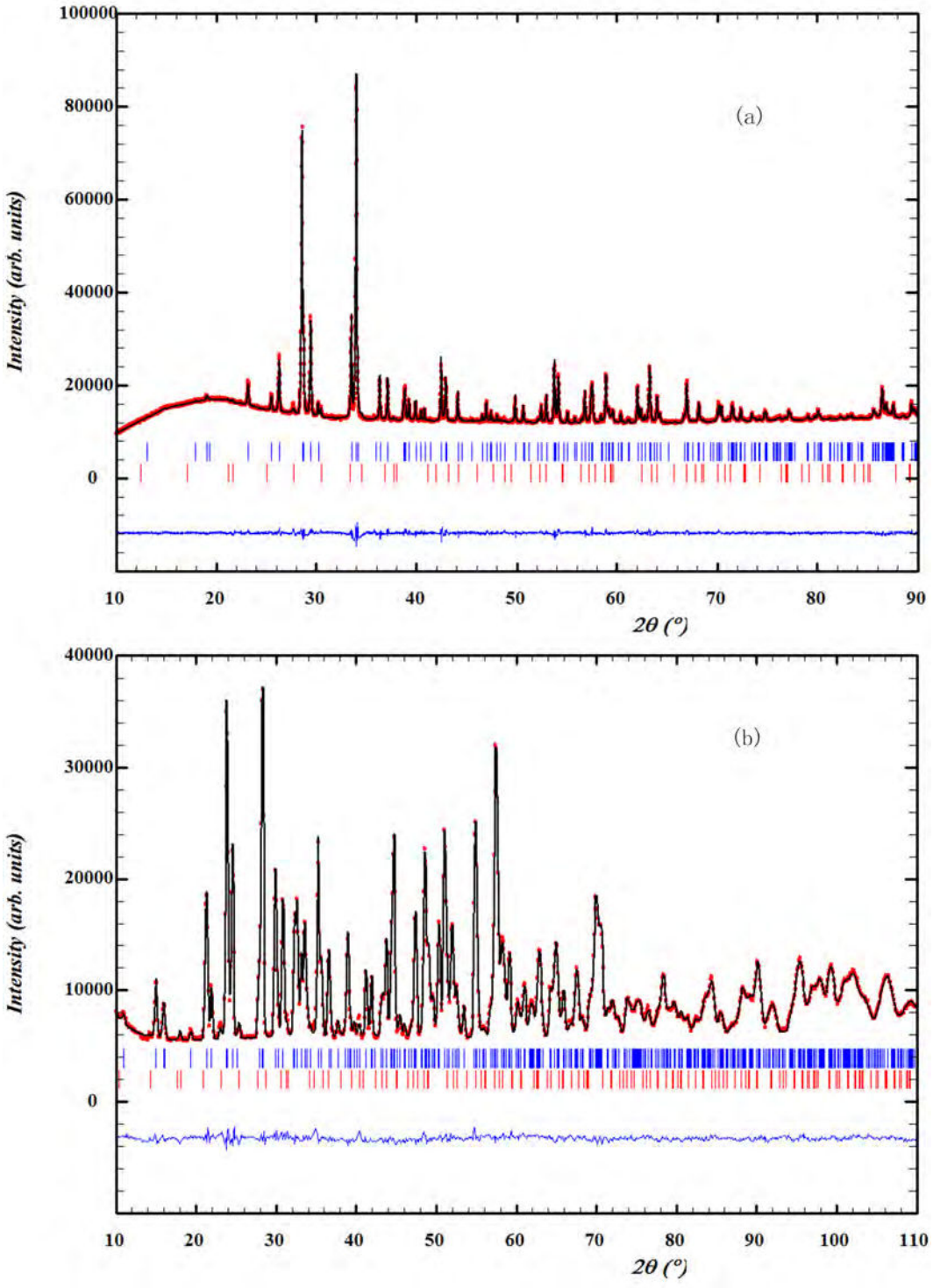

Figure 8.2: Rietveld refinement plots of $SrCoGe_2O_6$ for XRPD (a) and NPD (b) patterns taken at room temperature. Observed (red), calculated (black), and difference (blue) plots are shown. Bragg reflections from the main phase are denoted by blue tick marks. The lower set of Bragg reflections belong to a $Sr_3CoGe_5O_{14}$ impurity phase.

Table 8.4: Principal cation-anion distances (Å) and angles for $SrCoGe_2O_6$.

Sr-O1	2.513(4)	Ge-O1	1.722(3)
Sr-O2	2.5598(2)	Ge-O2	1.717(2)
Sr-O3	2.680(3)	Ge-O3	1.780(3)
Sr-O3	2.728(3)	Ge-O3	1.817 (3)
Ave.Dist.	2.620(1)	Ave.Dist.	1.759(1)
Distortion	11.01×E-04	Distortion	5.65×E-04
BVS	2.116(6)	BVS	3.91(1)
Co-O1	2.148(7)	Co-Co (J)	3.207(6)
Co-O1	2.087(2)	Co-Co (NNN intra)	5.470(1)
Co-O2	2.120(6)	Co–Co(J2)	6.921(8)
Ave.Dist.	2.118(2)	Co-Co (J1)	5.923(6)
Distortion	1.40×E-04	Co-O1-Co	98.47(9)°
BVS	1.90(1)	O3-O3-O3	165.2(1)°

dimensional) along the c-axis (figure 8.3 (a) and (c)). The Sr^{2+} cation is filled into the channels formed by MO_6 octahedra chains and GeO_4 chains. Figure 8.3(b) highlights the geometry of MO_6 and SrO_6 octahedra: a zigzag chain composed of edge-sharing MO_6 is running along the c-axis while SrO_6 octahedra fill the shoulders formed by zigzag MO_6 without connection. It is worth noting that the zigzag chain characteristic of MO_6 chains makes the M-O1-M angle close to 98° (see figure8.4). These usually provide the dominant magnetic interaction (J) between the M^{2+} nearest-neighbors (NN) due to direct interaction and superexchange. As shown in figure 8.3 (a) and (d), the chains made of MO_6 octahedra are well bridged by corner-sharing GeO_4 tetrahedra, this makes the one dimensional chains more isolated in some extent, and simultaneously gives rise to two possible magnetic coupling pathways J1 and J2 between the nearest neighboring magnetic octahedra chains (see the blue rectangle mark in figure 8.3 (a)), as schematically shown in figure 8.3(d). As presented in figure 8.5, for $SrMGe_2O_6$, J2 is formed between two M^{2+} cations sited on neighboring MO_6 chains through edge O1-O2 of GeO_4tetrahedra while J1 is formed between two M^{2+} cations belonging to neighboring MO_6 chains with shorter distance.

8.3.1.2 A structural comparison between $SrMnGe_2O_6$, $SrCoGe_2O_6$, $CaMnGe_2O_6$ and $CaCoGe_2O_6$

It is interesting to compare the crystal structure of these Sr-based magnetic pyroxenes from two points of view. The first one is the crystal chemistry of pyroxenes, looking for the effect of substituting diverse chemical species, which may be helpful in studying the relationship between crystal structure and chemical bonding in this system. On the other hand, the structural parameters which are associated with magnetic properties are of significance in understanding the magnetostructural correlations. As a result, we first evaluate the changes in global crystal structure coming from M1 site and M2 site , then, we will focus on the structural parameters which determine the magnetic properties in terms of intrachain and

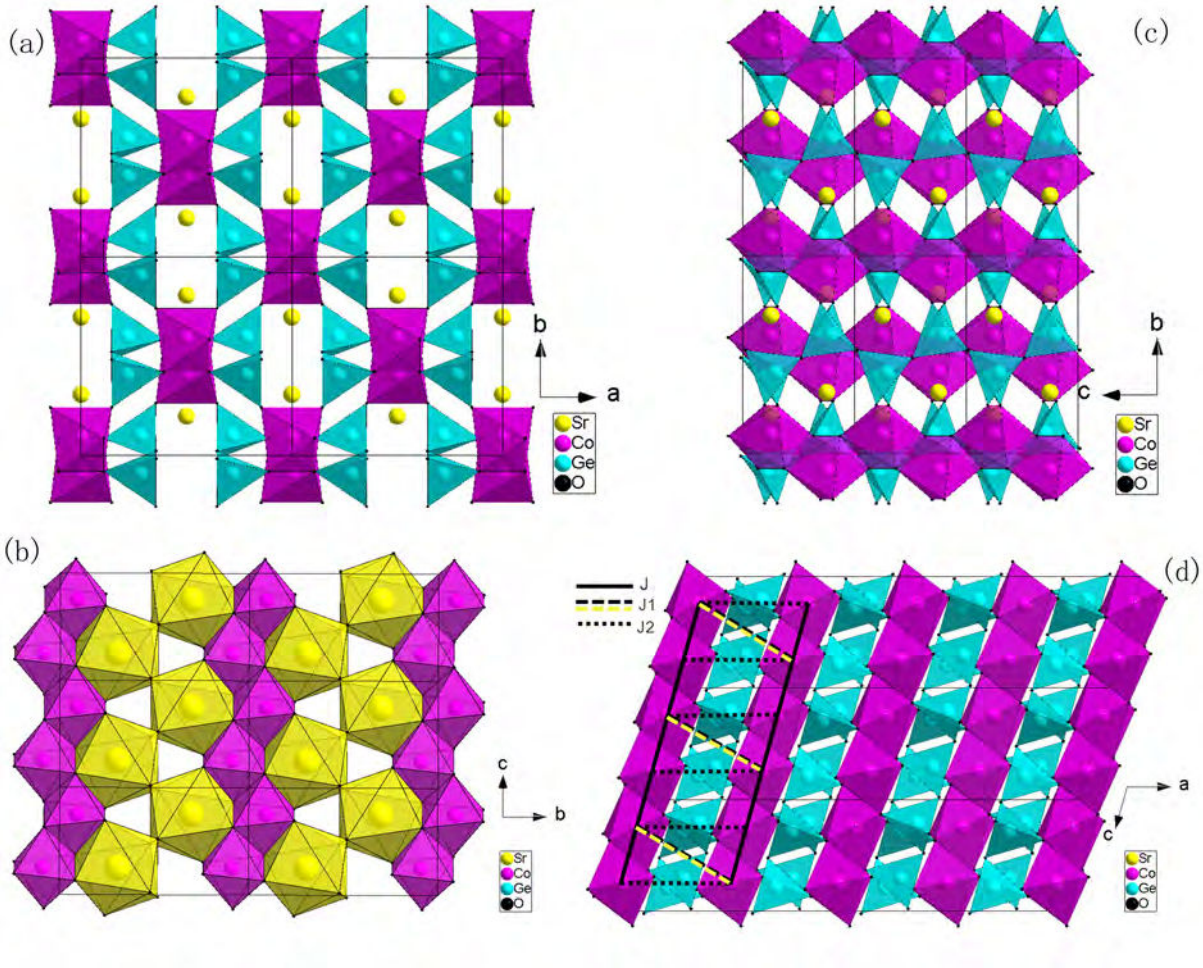

Figure 8.3: Projections of the $SrCoGe_2O_6$ structure ($SrMnGe_2O_6$ also shares similar manner) along different axes, derived from NPD at room temperature: (a) The alternate stacking of layers consist of CoO_6 octahedra and GeO_4 tetrahedra. (b) CoO_6 octahedra chains with zigzag characteristc and SrO_6 octahedra non-connected chains. (c) The corner-sharing GeO_4 tetrahedra chains characterized by O-rotation(close to E-chain). (d) The CoO_6 zigzag chains bridged by GeO_4 tetrahedra through O3-O3 edge of each tetrahedron; three possible magnetic interaction pathways J (solid line), J2 (dashed line) and J1 (dottd line) are marked; note that for J1 and J2, black line represents the coupling via GeO_4 tetrahedron in the back, and yellow line denotes the interaction via GeO_4 tetrahedron in the front.

Table 8.5: Comparison of principal structural parameters (distances in Å) for $SrMnGe_2O_6$,$SrCoGe_2O_6$, $CaMnGe_2O_6$ and $CaCoGe_2O_6$at RT.Note: change of each parameter is in %.

					For Mn	For Co	For Sr	For Ca
Parameter	$SrMnGe_2O_6$	$SrCoGe_2O_6$	$CaMnGe_2O_6$	$CaCoGe_2O_6$	Sr vs Ca	Sr vs Ca	Mn vs Co	Mn vs Co
a	10.3511(6)	10.2560(1)	10.2794(3)	10.1417(2)	0.7	1.14	0.93	1.37
b	9.4204(5)	9.2970(1)	9.1756(3)	8.9767(2)	**2.67**	**3.56**	1.33	2.21
c	5.5093(3)	5.4701(1)	5.4714(2)	5.4246(1)	0.69	0.83	0.72	0.86
β	104.700(2)°	105.588(1)°	104.244(2)°	104.885(1)°	0.44	0.68	-0.84	-0.61
V(Å^3)	519.64(5)	502.39(1)	500.20(3)	477.28(1)	3.89	5.26	3.43	4.80
M-M(J)	3.282(8)	3.207(6)	3.249(8)	3.162(5)	1.02	1.42	**2.34**	**2.75**
M–M(J1)	5.975(7)	5.923(6)	5.918(7)	5.848(5)	0.96	1.28	0.88	1.20
M-M(J2)	7.00(1)	6.921(8)	6.889(1)	6.772(7)	**1.61**	**2.20**	1.14	1.73
M-O1-M	97.5(2)°	98.47(9)°	94.0(4)°	95.66(10)°	**3.72**	**3.00**	-0.99	-1.67
M-M-M	114.1(1)°	117.02(1)°	114.7(1)°	118.15(1)°	-0.52	-0.96	**-2.50**	**-2.92**
Ge-Ge-Ge	113.1(1)°	113.60(6)°	114.5(1)°	114.01(6)°	-1.22	-0.35	-0.44	0.44

interchain interactions.

The principal structural parameters for $SrMnGe_2O_6$, $SrCoGe_2O_6$, $CaMnGe_2O_6$ and $CaCoGe_2O_6$at RT are presented in table 8.5 for the sake of comparison. For Sr vs Ca, generally, all distances get larger (relatively, modified by 1%) because the bigger cation radius of Sr^{2+}has to be accommodated in the unit cell. There are two parameters changed around 3%: (i) The angle of M-O1-M increases to about 98° which obviously deviates from the ideal 90° pyroxene, as illustrated in figure 8.4; (ii) The b parameter increases by around 3% because of the introduction of Sr^{2+} with bigger cation radius, giving rise to major modification of the zigzag MO_6 chains (as well as the tetrahedra chains) being much more isolated from each other along the b axis. The M-M distance corresponding to J2 pathway is altered by 2%, as seen in the detailed pathways, presented in figure 8.5.

As to Co vs Mn, the consequence of smaller cation radius of Co^{2+} (0.745Å) comparing to Mn^{2+}(0.83Å) in high-spin state affects mainly M-M (J1) distance. Whatever the geometry of MO_6 octahedra and GeO_4 tetrahedra does not vary from Ca to Sr. However, from Co to Mn, the M-M-M angle is modified by about 3%.

The magnetic coupling between MO_6 octahedra chains, operated by the bridged GeO_4 tetrahedra, is complex. Let's evaluate the angle parameter for these four compounds by considering the magnetic interaction pathways associated with double J1 and single J2 exchanges. The fragments of crystal structure, aiming to illustrate these pathways, are presented in figure 8.5.

From Ca to Sr: For J1, the angle M-O1-O2 substantially decreases by about 6° while O1-O2-M angle largely increases by about 10°. The sum for these two distinct tendencies is around 4° with one angle increases while another decreases. For J2, The M-O1-O2 angle increases by 4°, and O1-O2-M increases by 10°. Here, both angles increase, with a total increment amplitude of 14°.

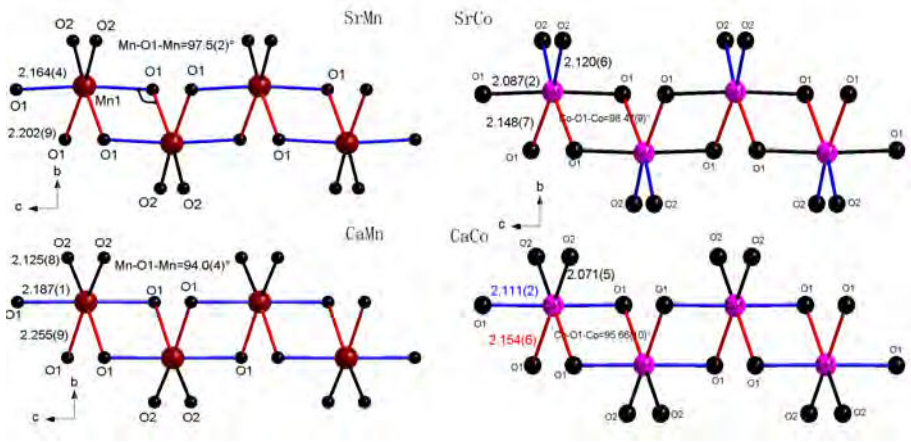

Figure 8.4: The schematic drawing of MO_6 (M=Mn, Co) octahedra along the chain direction for $SrMGe_2O_6$ and $CaMGe_2O_6$, showing up the J exchange interaction. Red line: the longest bonding distance; Blue line: intermediate bonding distance; Black line: the shortest bonding distance.

8.3.2 Magnetic properties

8.3.2.1 $SrCoGe_2O_6$

Figure8.6 (a) shows the temperature dependence of magnetic susceptibility for $SrCoGe_2O_6$. Both ZFC and FC curves reflect that $SrCoGe_2O_6$ undergoes an AFM transition at 10K, characterized by a sharp peak around 10K. In contrary to $SrMnGe_2O_6$, no deviation is found between the ZFC and FC in $SrCoGe_2O_6$ in the measured temperature range. As shown in the inset of figure 8.6 (a), the inverse magnetic susceptibility at 0.1 T was fitted using the Curie-Weiss law ($\chi = C/(T-\theta)$) between 250 K and 350 K, where C is the Curie constant, θ is Weiss temperature. The effective moment was determined to be μ_{eff} = 4.9 (1) μ_B/Co^{2+}, which is bigger than the expected spin-only value of 3.87 μ_B for Co^{2+} ($3d^7$) cations in the high spin state due to the presence of spin-orbit coupling in this system. Despite the long-range AFM ordering in $SrCoGe_2O_6$, the positive Weiss temperature of 20.7(1) K indicates that ferromagnetic interactions are predominant in the paramagnetic regime.

Field-dependent magnetization isotherms M(H) collected between 2 K and 50 K for $SrCoGe_2O_6$ are presented in figure 8.6(b). The field-induced magnetization is linear up to applied fields of 7T above T_N. However, below T_N magnetic field induces another magnetic phase transition. On the curves at 2, 4 and 6 K, a magnetic phase transition can be clearly seen at 2K at $\mu_0 H \tilde{}$3.92 T represented by peak in dM/dH vs H (inset). This is indicative of a field induced metamagnetic transition. No saturation can be achieved with the maximum field applied (M<1.5μ_B/Co^{2+} at 7T).

The characterization of the magnetic transition via the measurement of the heat capacity was carried out. Figure 8.7 shows the temperature dependence of the specific heat for $SrCoGe_2O_6$. An ordering transition is seen in the HC of $SrCoGe_2O_6$, characterized through the occurance of the sharp peak in Cp at 10K. This temperature is consistent with the Neel

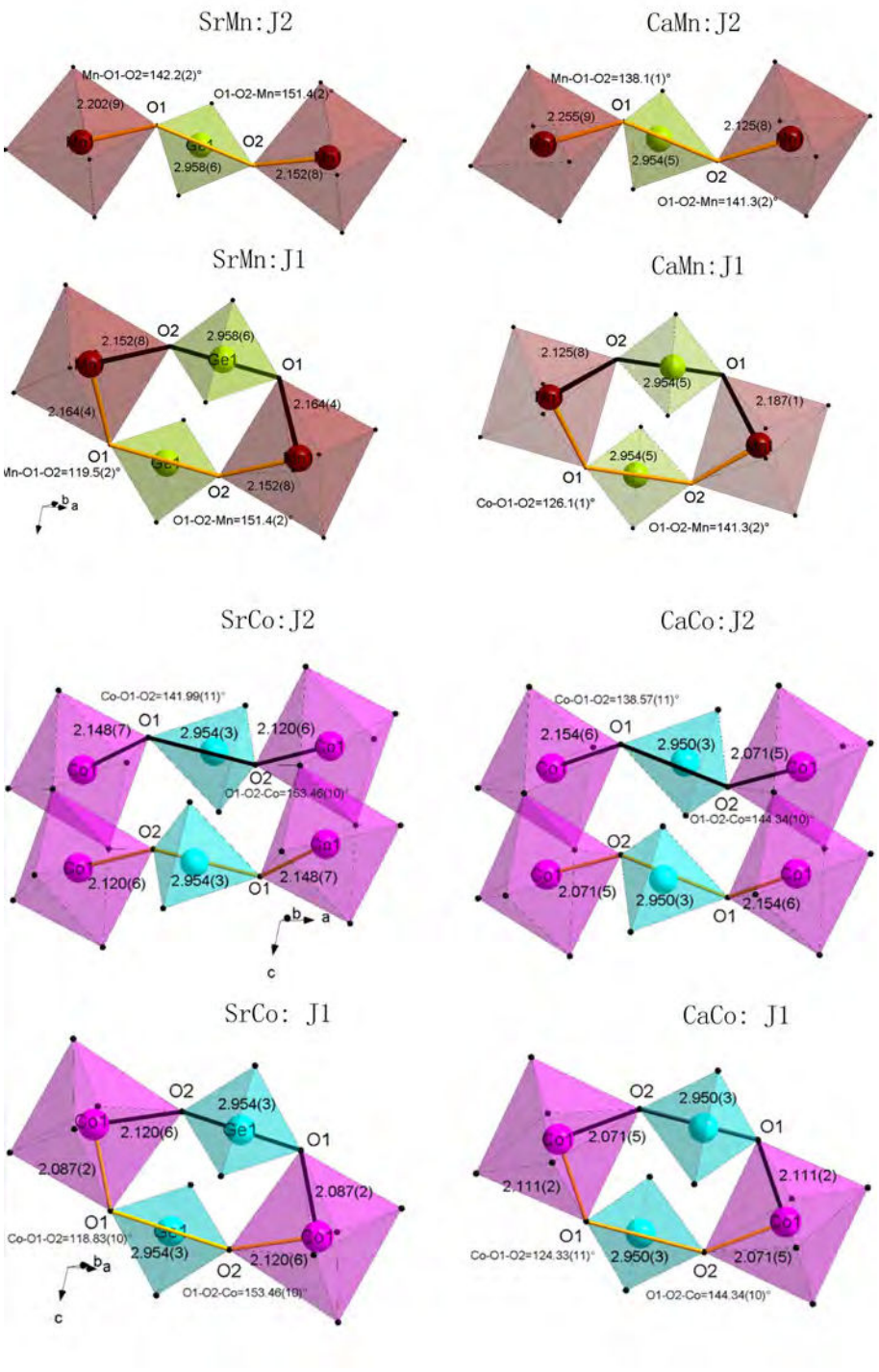

Figure 8.5: The polyhedral drawing shows the two interchain interactions J1 and J2 for $SrMnGe_2O_6$, $SrCoGe_2O_6$, $CaMnGe_2O_6$ and $CaCoGe_2O_6$, respectively.

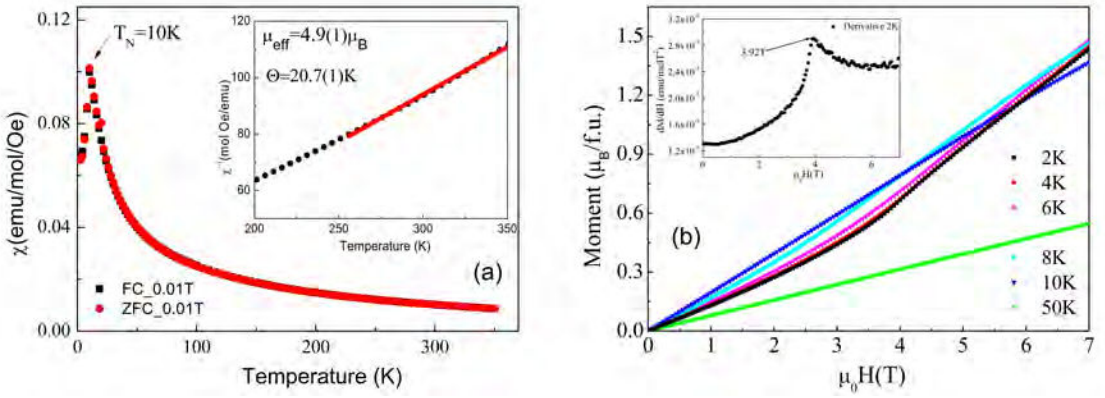

Figure 8.6: (a) Temperature dependence of the magnetic susceptibility of $SrCoGe_2O_6$. The inset shows the Curie-Weiss fit for inverse magnetic susceptibility (red line). (b) Isothermal magnetization curves of $SrCoGe_2O_6$ collected at T=2, 4, 6, 8, 10 and 50 K.

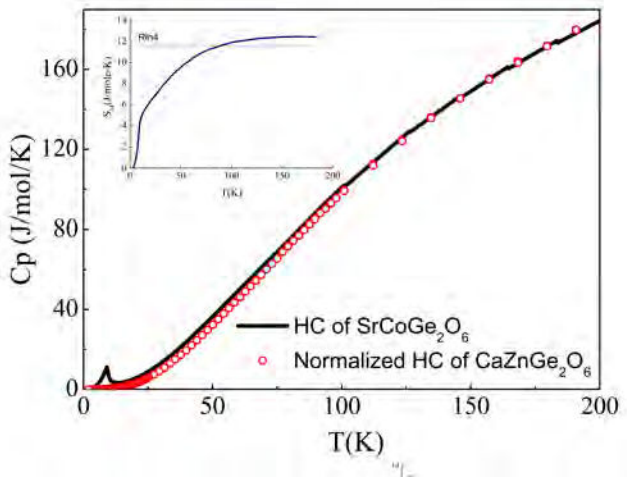

Figure 8.7: Specific heat capacities of $SrCoGe_2O_6$ and $CaZnGe_2O_6$ which is used as a lattice standard after normalizing its HC at 200K. Inset shows the magnetic entropy for $SrCoGe_2O_6$.

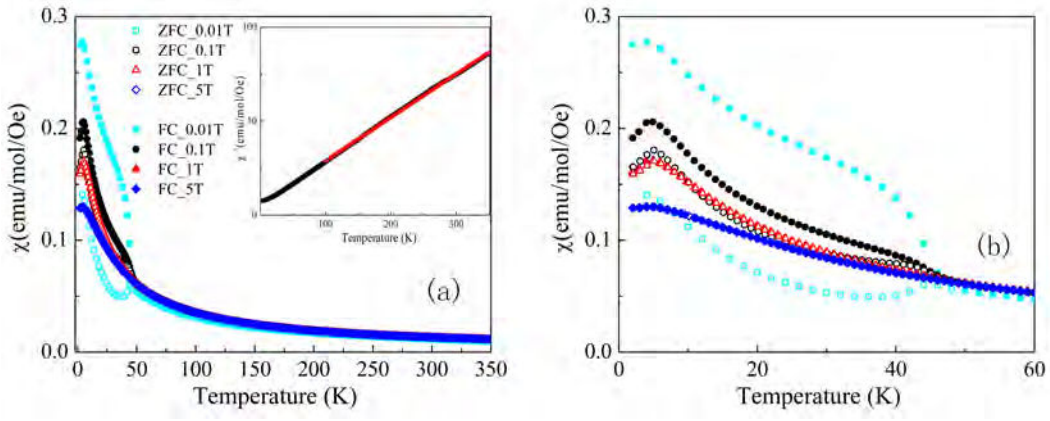

Figure 8.8: Temperature-dependent magnetic susceptibility of $SrMnGe_2O_6$ under different magnetic fields. Inset: The Curie-Weiss fit for the inverse susceptibility measured at 5T. (b) Enlarged view of the susceptibility in low temperature regime.

temperature observed in magnetic susceptibility and the appearance of the magnetic reflection peaks in neutron diffraction (see below). $CaZnGe_2O_6$ was chosen as the nonmagnetic analogue for subtraction of the phonon contribution. To estimate the phonon contribution for $SrCoGe_2O_6$, the HCs of $SrCoGe_2O_6$ and $CaZnGe_2O_6$were normalized to be equal at 200K by scaling HC of $CaZnGe_2O_6$. The magnetic component of the specific heat capacity of $SrCoGe_2O_6$ was then obtained by subtracting the phonon contribution. The magnetic entropy was estimated by integrating Cmag/T dT. The experimental magnetic entropy with S_m=12.4J/mol/K at 200 K is close to the theoretical value of 11.5 J/mol/K for the spin S=3/2 Co^{2+} ions given by Rln(2S+1). The discrepancy may arise from the lattice estimation as used $CaZnGe_2O_6$.

8.3.2.2 $SrMnGe_2O_6$

The temperature-dependent magnetization susceptibility for polycrystalline $SrMnGe_2O_6$ is shown in figure 8.8. As the enlarged view, figure 8.8(b) clearly shows the opening of bifurcation between ZFC and FC measurements recorded under 0.01 and 0.1 T below 45K. A sharp transition observed at around 4.5K signals the AFM ordering. No such derivation between ZFC and FC curves can be found under 1 and 5T but the cusp at 4.5K remains in all magnetic susceptibility curves. We take T_N to be 4.5 K based on a cusp magnetic ordering transition observed in heat capacity measurements and the appearance of magnetic reflections in neutron diffraction data. The anomalous magnetic behavior observed at 45K is quite similar to that of $CaMnGe_2O_6$ in which this transition was preliminarily explained as the existence of impurity phase Mn_3O_4.. Curie-Weiss law was used to fit the paramagnetic portion of the inverse susceptibility between 100 and 350K. The effective moment was determined to be 5.88(1)μ_B/Mn^{2+} which is close to the spin-only value expected for the Mn cation in a high-spin state (5.92μ_B). The Weiss temperature is -24.6(1)K, the negative value indicates that the predominant magnetic interaction between Mn^{2+} cations is antiferromagnetic. It is worth

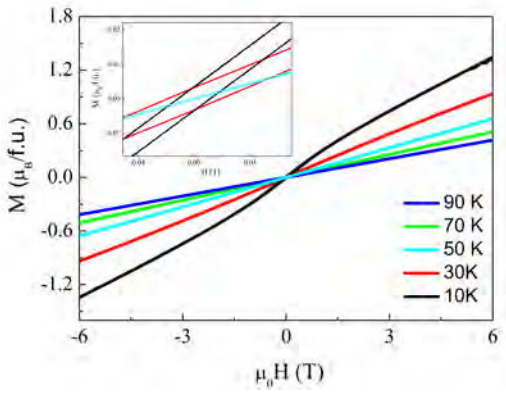

Figure 8.9: The magnetic hysteresis loops for $SrMnGe_2O_6$ at various temperatures.

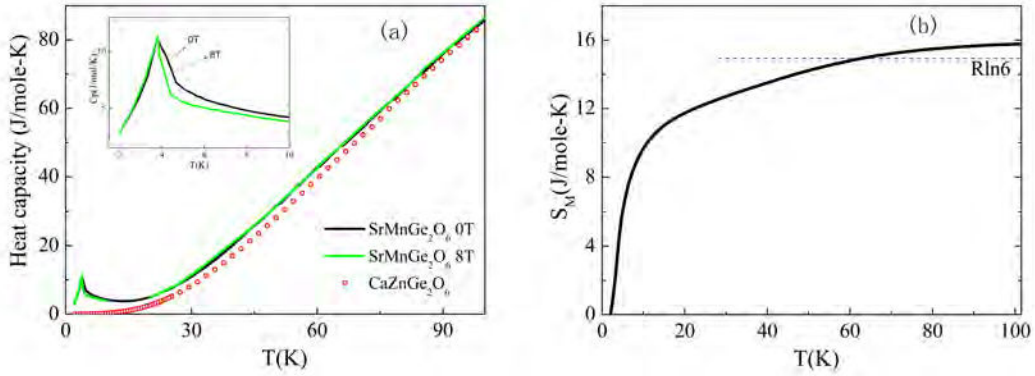

Figure 8.10: (a) Specific heat capacity of $SrMnGe_2O_6$ and $CaZnGe_2O_6$ which is employed as a lattice analog. Inset shows the comparison of HC at 0T and 8T. (b) The magnetic entropy released via magnetic ordering.

noticing that for $SrMnGe_2O_6$ the frustration index f is determined to be 5.3 which is two time larger in magnitude than that of $CaMnGe_2O_6$, suggesting that $SrMnGe_2O_6$ is more frustrated.

Figure 8.9 shows the isothermal magnetic hysteresis loops for $SrMnGe_2O_6$. It can be seen that the magnetic loops are almost proportional to the external magnetic field without apparent magnetic hysteresis above 50K. However, as shown in the inset of figure 8.9, magnetic hysteresis signal can be clearly observed below 30K. This indicates the presence of small ferromagnetic component which seems not varied with the decrease of temperature: the values at 30 and 10K are both determined to be $3.2\times10^{-3}\mu_B/Mn^{2+}$. We have measured the ac susceptibility to exclude this possibility. Figure 8.11 shows the ac magnetic susceptibility as a function of temperature at various frequencies. The real part of susceptibility is in fact frequency independent. We observed two magnetic transitions in the ac susceptibility $\chi'(T)$, indicated by two cusps: one cusp at 4.6K corresponds to the T_N seen in dc magnetic susceptibility measurement, another transition at 45K is probably due to the impurity phase Mn_3O_4.

To further study the magnetic transition of $SrMnGe_2O_6$, the heat capacity was measured

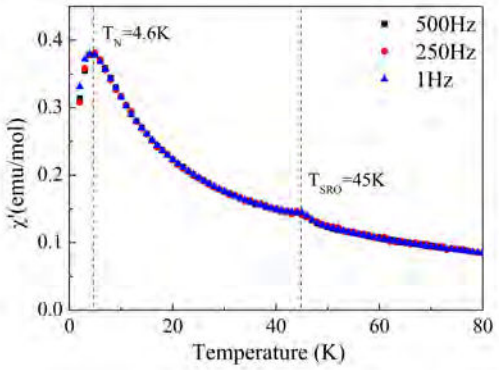

Figure 8.11: Temperature and frequency dependence of the real part of the ac susceptibility of $SrMnGe_2O_6$.

under 0T and 8T, and the heat capacity data are presented in figure 8.10(a). Only one ordering transition is seen in the HC of $SrMnGe_2O_6$, reflected by the presence of the sharp peak in Cp around 4K under both 0 and 8T. This temperature is close to the Néel temperature seen in magnetic susceptibility curves and the magnetic reflection peaks in neutron diffraction patterns. Note that on the high-temperature side of Cp, the heat capacity has negligible modification from 0T to 8T, and makes the peak around 4K more sharp. By making the difference between HC curves under 0 and 8T, we are able to estimate the decrease of magnetic entropy. It turns out that magnetic entropy with 0.82 J/mol-K is suppressed for HC from 0T to 8T. In order to estimate the magnetic entropy, $CaZnGe_2O_6$ was chosen as the nonmagnetic analogue for subtraction of the phonon contribution. Note that $SrZnGe_2O_6$ compound may be the best choice as a nonmagnetic analogue, unfortunately, several attempts for synthesizing it were unsuccessful. The magnetic HC of $SrMnGe_2O_6$ was obtained by subtracting the HC of $CaZnGe_2O_6$ compound, and then the experimental magnetic entropy S_M(T) was calculated by integrating Cmag/T dT. As shown in figure 8.10 (b), the magnetic entropy ultimately saturates at around 70K with maximum magnetic entropy of 15.6 J/mol-K, relatively bigger than the value 14.9 J/mol-K expected for Mn^{2+} with a spin-only contribution given by Rln6. The discrepancy of magnetic entropy may arise from the subtracted heat capacity from lattice contribution. Nevertheless, one sees that the magnetic entropy loss occurs in two regions on cooling: first it undergoes a gradual change from 100K to temperature close to T_N, then a sharp loss in entropy at T_N is followed. This magnetic entropy release with more than half of the total magnetic entropy is assumed to be associated with short-range spin order.

8.3.3 Magnetic structure

8.3.3.1 $SrCoGe_2O_6$

Figure 8.12 shows temperature dependent NPD patterns below 11K for $SrCoGe_2O_6$. It is obvious that the magnetic reflections appear below 10K, consistent with our magnetic susceptibility and heat capacity measurements. Figure 8.13 presents the NPD patterns collected at

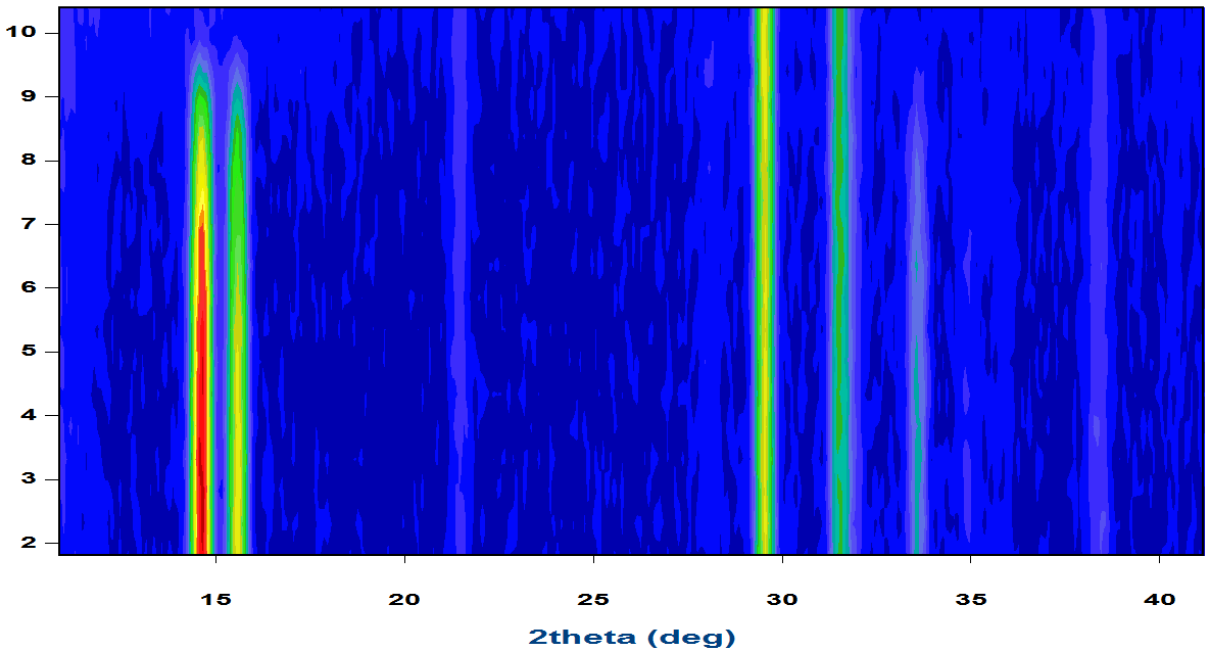

Figure 8.12: Plot of neutron powder diffraction scans showing up the magnetic transition at 10K using a wavelength of 2.52Å.

Table 8.6: Basis vectors for Co^{2+} at 4e site (Co1(0, 0.9099, 0.25), Co2(0, 0.0901, 0.75)). Notations: F=S1+S2, C= S1-S2.Space group C2:c, propagation vector k1=(1,0,0).

IR	Basis vector
Γ1	(0,Fy,0)
Γ2	(0,Cy,0)
Γ3	(Fx, 0, Fz)
Γ4	(Cx,0,Cz)

30, 15 and 2K, it is clear that no magnetic reflection for patterns at 30 and 15K, and magnetic reflections appear at 2K. At low temperature all magnetic reflections of $SrCoGe_2O_6$ can be indexed with a commensurate magnetic propagation vector k=(1,0,0). To determine all the possible magnetic structures compatible with the crystal symmetry (C2/c), the representation analysis, which is described by Bertaut, was performed[16]. Calculations were carried out using version 2 K of the programs SARAh-Representation analysis[17] and BasIreps integrated in Fullprof Suite[10, 18]. For the Co^{2+} cations on the 4e Wyckoff position of space group C2/c, the decomposition of magnetic representation is

$$\Gamma = 1\Gamma_1^1 + 1\Gamma_2^1 + 21\Gamma_3^1 + 2\Gamma_4^1. \tag{8.1}$$

The different basis vectors calculated using the projection operator technique associated with each IR are summarized in table 8.6. There are four magnetic ions in the unit cell but only two possible magnetic couplings. Because of the C center symmetry broken by the **k** vector, the magnetic moments carried by the two Co^{2+} cations correlated by C center translation are

intrinsically antiparallel. All possible models determined from the symmetry analysis were tested by Rietveld refinement. The best fit was achieved with the model described by the IR Γ3. Similar to $CaCoGe_2O_6$ $SrCoGe_2O_6$ adopts P_c2_1/c magnetic space group.

The final refinement for the 2 K pattern is present in figure 8.13. A sketch of the magnetic structure of $SrCoGe_2O_6$ is shown in figure 8.14 . The Co^{2+} magnetic moment is constrained by symmetry in the (a,c) plane, aligned mainly along the a-axis with an angle of 96.67° and 8.92° to the c-axis, with ma=0.369(170)μ_B, mc=3.184(41)μ_B. The total ordered magnetic moment refined at 2 K is Mtot=3.12(1) μ_B which is larger than the theoretical spin-only ordered value 3 μ_B for Co^{2+} and indicates that the orbital moment is not totally quenched. Consequently, the magnetic ordering of $SrCoGe_2O_6$ can be described as: FM coupling between the Co^{2+} cations within the CoO_6 octahedra zigzag chains, while the spin couplings between neighboring chains are AFM, consisting of two possible interchain superexchanges. The magnetic arrangement is the same as in $CaCoGe_2O_6$ the diffrence is in the direction of the moment. The temperature dependence of the magnetic moment is shown in figure 8.15 , it shows that magnetic moment elevates just below 10K, evidencing the magnetic ordering temperature, and in agreement with the magnetic susceptibility and heat capacity measurements.

It is worth noting that the topology of magnetic coupling in $SrCoGe_2O_6$, in principle, does not allow any geometrical frustration since all the exchange interactions are satisfied. In comparison to $CaCoGe_2O_6$, the magnetic moments of $SrCoGe_2O_6$ are mainly aligned along c-axis with vanishing moments along a-axis.

Lattice parameters as a function of temperature derived from NPD data are shown in figure 8.16. The b- and c-parameters exhibit a normal evolution of temperature over the measured temperature range. Above the Neel temperature 10K, a and beta angle parameters follow a standard evolution, but below 10K, both a- and beta parameters slightly increase with decreasing temperature.

8.3.3.2 $SrMnGe_2O_6$

Figure 8.17 shows the evolution of the NPD patterns with temperature. It can be clearly seen that additional reflections, arising from magnetic ordering, appear below 4.5K. The intensities of these magnetic reflections grow with decreasing temperature. The magnetic periodicity in reciprocal space could not be expressed by simple rational fractions of the periodicity of the crystal structure. Instead, the magnetic reflections can be indexed with an incommensurate propagation vector. After a Rietveld refinement of the nuclear structure of $SrMnGe_2O_6$, the k-search program integrated into Fullprof suite was used to find a proper propagation vector. This gives the most possible **k** vector (0.0, 0.425, 0.0), which was then refined to be (0.0, 0.42426(13), 0.0) at 2K. The position of the first magnetic satellite of reflection (1,-1,0) is modified with decreasing the temperature, as shown in figure 8.18. The refined k vector as a function of temperature from 4.5 K to 1.55K by profile refinement is presented in figure 8.18. It reveals that the magnetic propagation vector **k** is temperature-dependent, i.e., it remains along the b-axis direction and its modulus decreases with the decrease of temperature and

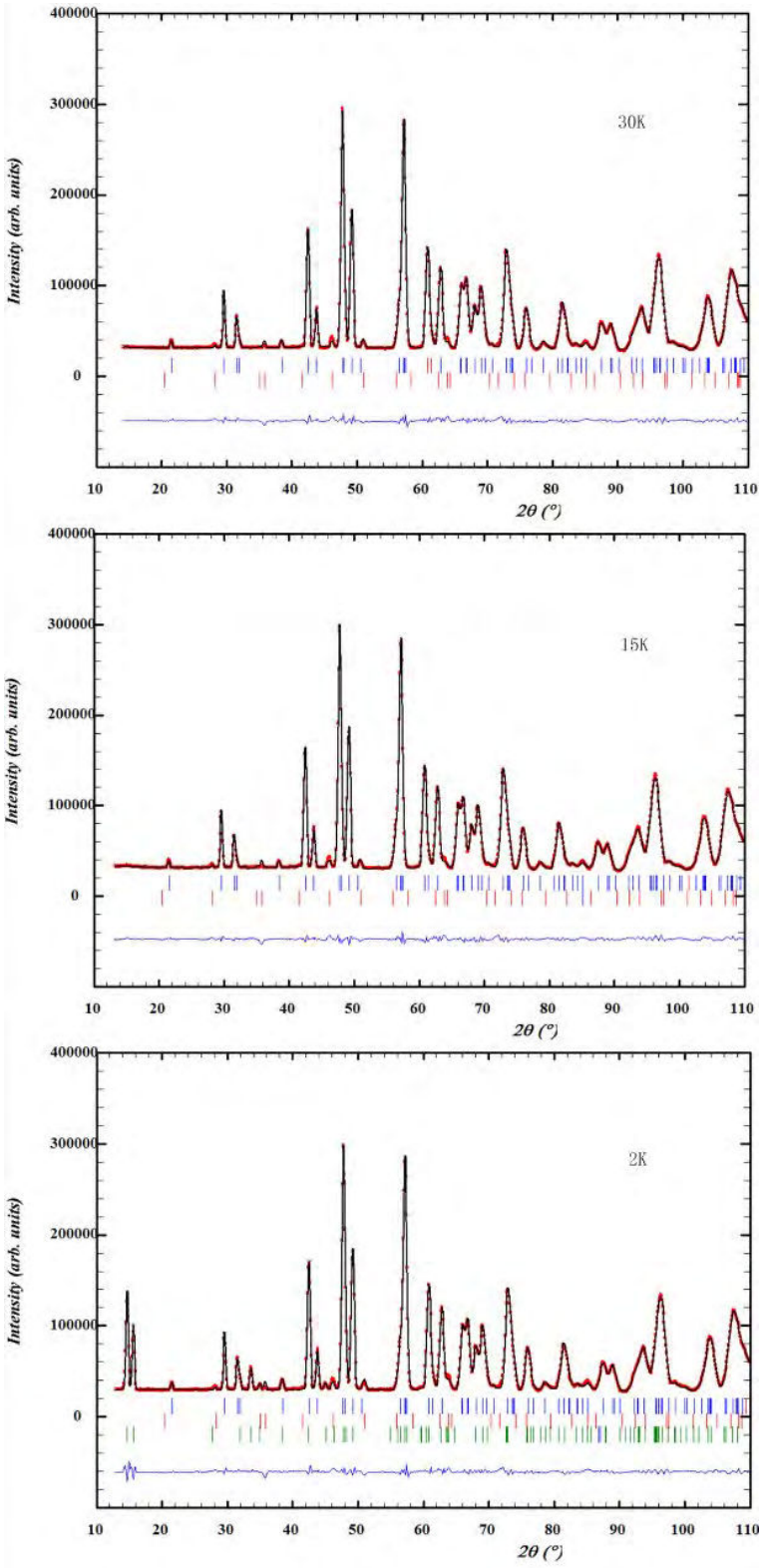

Figure 8.13: Observed (symbols) and calculated (line) powder neutron diffraction patterns for $SrCoGe_2O_6$ at 30, 15 and 2K. The green tick marks shows the magnetic reflections. The nuclear reflections of the main phase are denoted by blue tick marks. The reflections marked in red belong to a $Sr_3CoGe_5O_{14}$ impurity phase. The blue line shows the difference between the observed and calculated diffraction patterns.

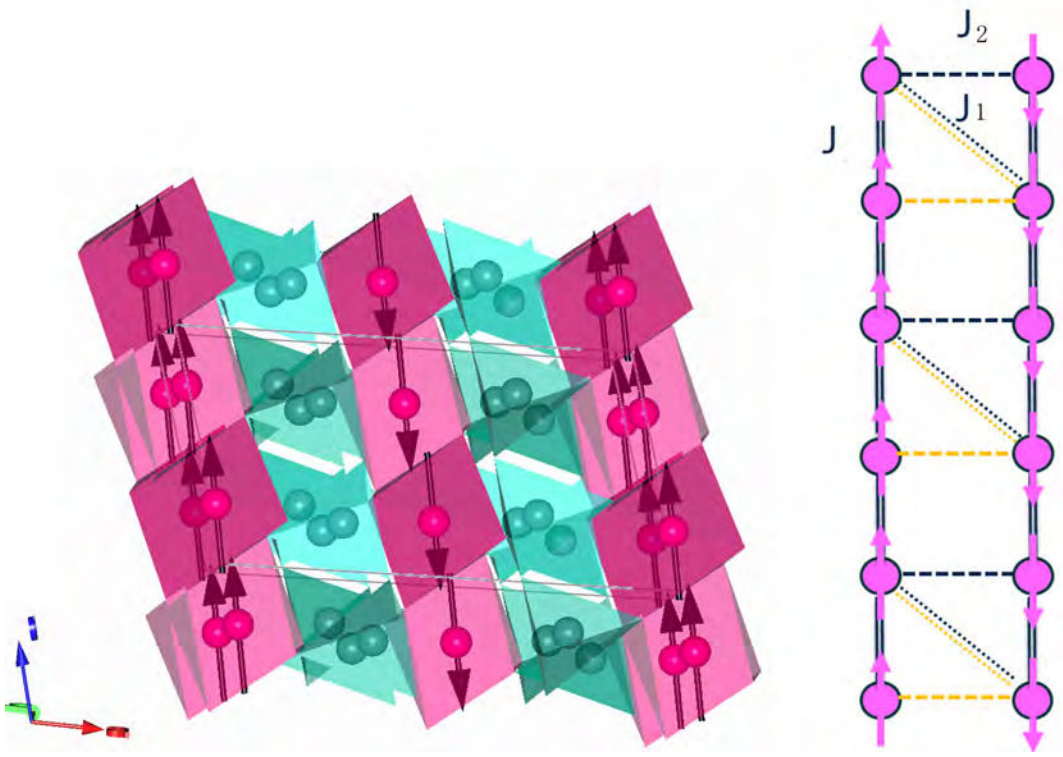

Figure 8.14: (Left) Representation of the magnetic structure of $SrCoGe_2O_6$; (Right) the schematic drawing of exchange interactions, and here magnetic moments were added arbitrarily in order better to exhibit the triangular exchange interaction.

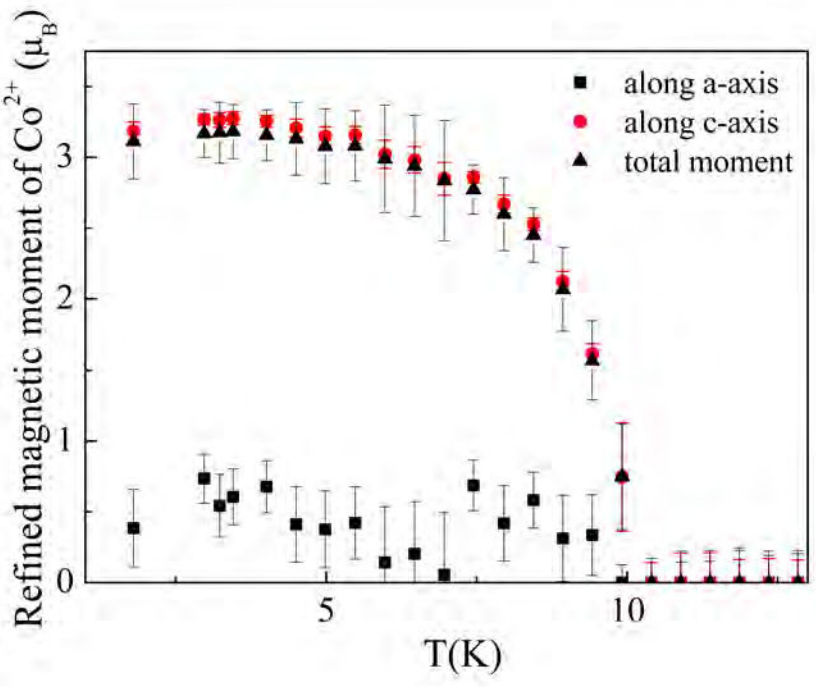

Figure 8.15: Evolution of the refined Co^{2+} magnetic moment components as a function of temperature.

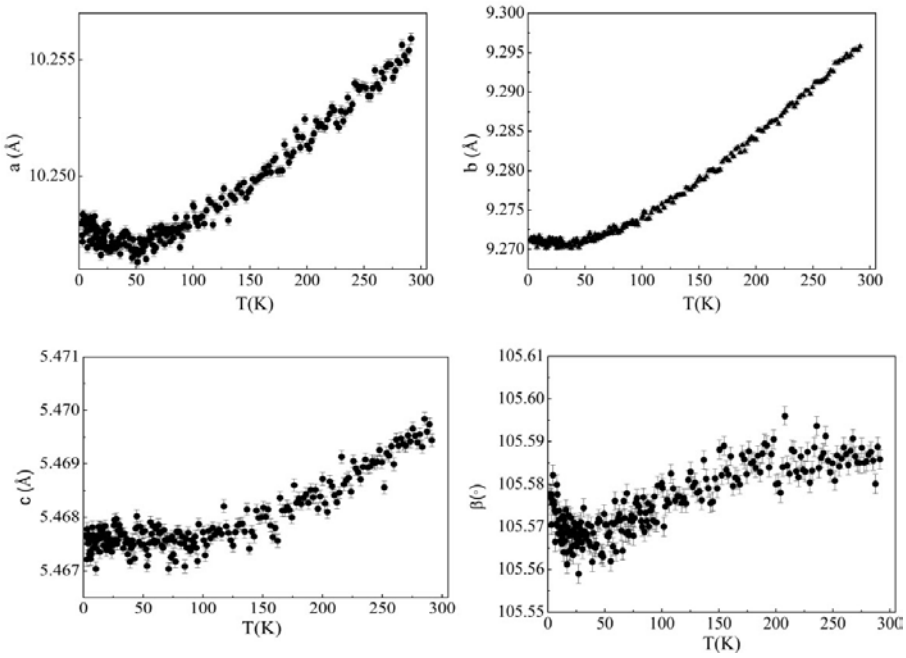

Figure 8.16: Lattice parameters of $SrCoGe_2O_6$ as a function of temperature derived from NPD data.

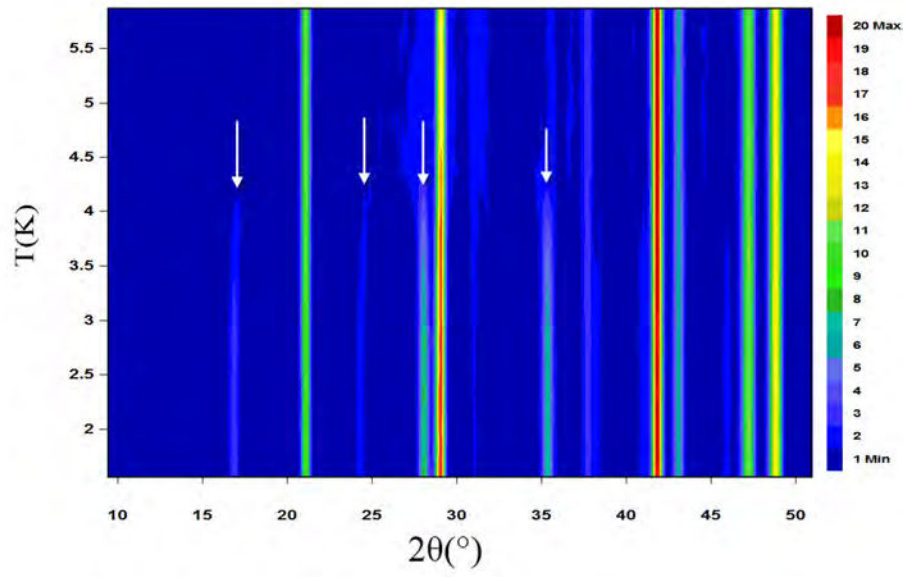

Figure 8.17: NPD patterns as a fuction of temperature showing a magnetic satellite reflections at 4.5K. Note: arrows mark the appearance of magnetic reflections.

reaches a relatively stable value at around 2K.

For such an incommensurate k vector, only a sinusoidal or a spiral magnetic structure is possible within the prediction of group theory. Actually, a sine-wave modulated structure is a just particular case of helical structures for which the irreducible representation is of one dimension. The magnetic structure of $SrMnGe_2O_6$ is assumed to be spiral based on our obser-

vation of spontaneous polarization measurements (see next section). There are indeed several kinds of spiral magnetic structures depending on the relative orientation between propagation vector and moments. These include proper screw, cycloidal, longitudinal conical and transverse conical magnetic structures. Among them, only cycloidal and transverse conical spin configurations have non-zero electric polarization. We found that the best fit to the observed magnetic reflections can be obtained with a cycloidal magnetic structure model which is in good agreement with the ferroelectricity observed in $SrMnGe_2O_6$. The cycloidal spin order is formed by the magnetic moments rotating within the (a,b) plane containing the propagation vector k_y=0.42426(13).

The distribution of magnetic moments over the different crystallographic sites of the structure can be given by:

$$m_{lj} = Re_j cos2\pi[k \cdot R_l + \phi_j] + Im_j sin2\pi[k \cdot R_l + \phi_j] \tag{8.2}$$

where Rl=n_1a+n_2b+n_3c is a lattice vector, $\phi_j$is the phase angle (in fractions of 2π), Re_j and Im_j are the real and imaginary Fourier coefficients of the magnetic moments. In order to have a circular configuration of magnetic moments, here, $\mid Re_j \mid = \mid Im_j \mid$ all j atoms have equal magnetic moments. Hence, the basis vector is determined as: For real part: (u,0,0); for imaginary part (0,v,0). The best fit between the observed and calculated patterns were obtained by Rietveld refinement with the phase angles of the four Mn atoms within one unit cell as follows:

$$\phi_{Mn1} = \phi_{Mn3} = 0, \phi_{Mn2} = \phi_{Mn4} = -0.1572(48), \tag{8.3}$$

As a result, there are two magnetic orbits even if there are four magnetic atom sites in the unit cell. Because of the C centering which is not conserved by the incommensurate k vector, the orientation of magnetic moment carried by Mn1 and Mn3 (represented as blue moments in figure 8.20) or by Mn2 and Mn4 (represented as red moments in figure 8.20) cations differ by 76° (1/2**k**).

The final refinement based on the model described above for the 2K NPD data is shown in figure 8.19(a). A total magnetic moment of $4.09\mu_B/Mn^{2+}$ was determined. We present the magnetic structure of $SrMnGe_2O_6$ with projections along c and b directions in figure 8.20. The magnetic moments are confined in the (a,b) plane, and they rotate along the b axis. Each orbit along a and c axes is identical. The temperature dependence of refined magnetic moments is shown in figure 8.19(b). The magnetic moment increases with decreasing temperature below 4.5K, confirming the long range ordering temperature T_N=4.5K, in accordance with the dc and ac magnetic susceptibility and heat capacity measurements. Referring to the transition theory introduced in chapter 1, the phenomenological power law for magnetization as a function of temperature based on the Landau theory can be described by M=a(1-$(T/T_N)^{\alpha})^{\beta}$[22], here β is critical exponent. With this equation, the temperature dependent refined magnetic moment was fitted, yielding T_N=4.73(2) K, α=-3.38(38), β= 0.378(15), in accordance with the classical Heisenberg 3D model (0.367).

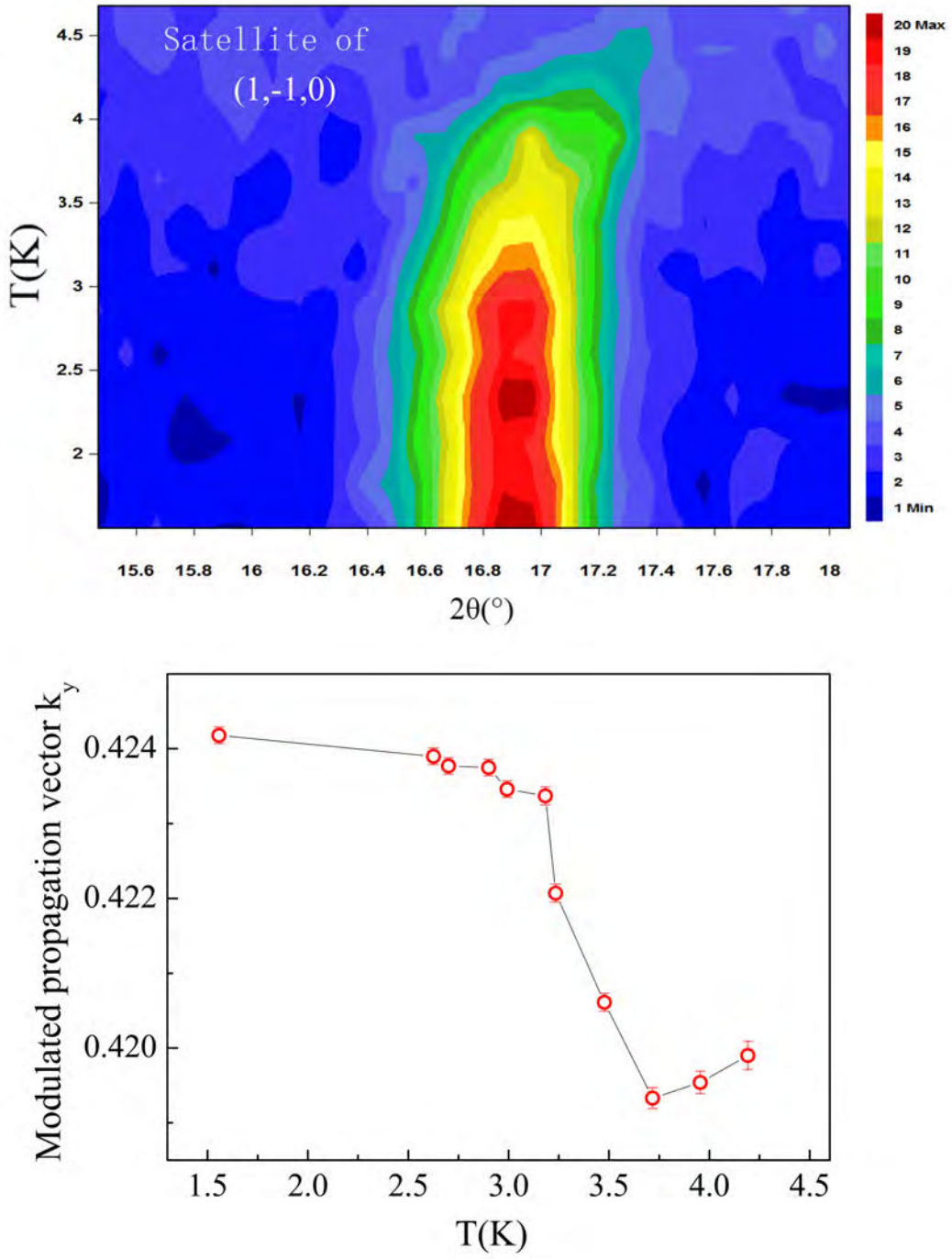

Figure 8.18: (upper) The evolution of the magnetic satellite of reflection (1,-1,0) as a function of temperature, (lower) the modulated propagation vector k variation of temperature refined from NPD data.

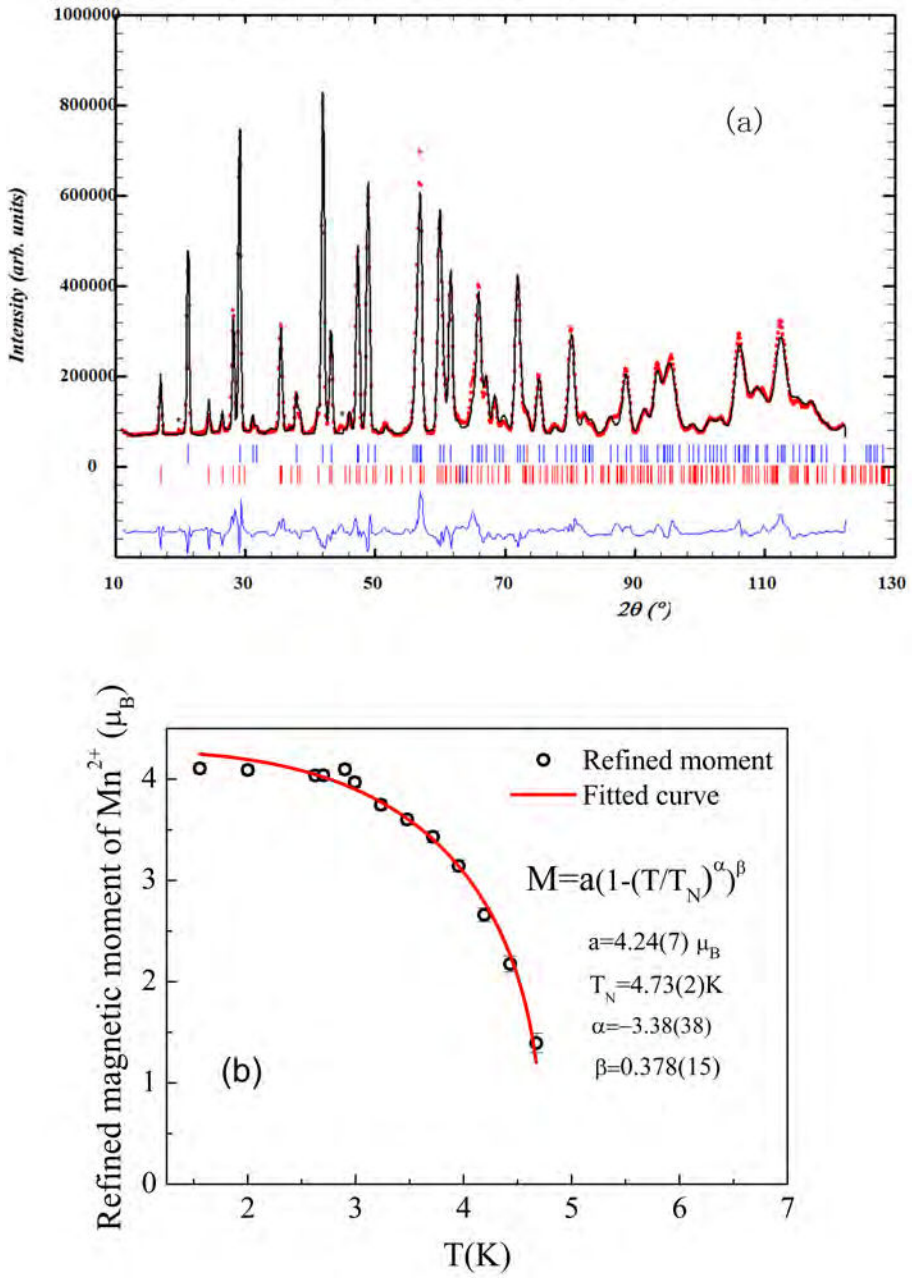

Figure 8.19: (a) Plot of refined NPD data at 2K for $SrMnGe_2O_6$. Symbols show the observed NPD pattern, and line represents the calculated one. The blue line shows the difference between them. (b) Temperature dependence of the refined Mn^{2+} magnetic moments.

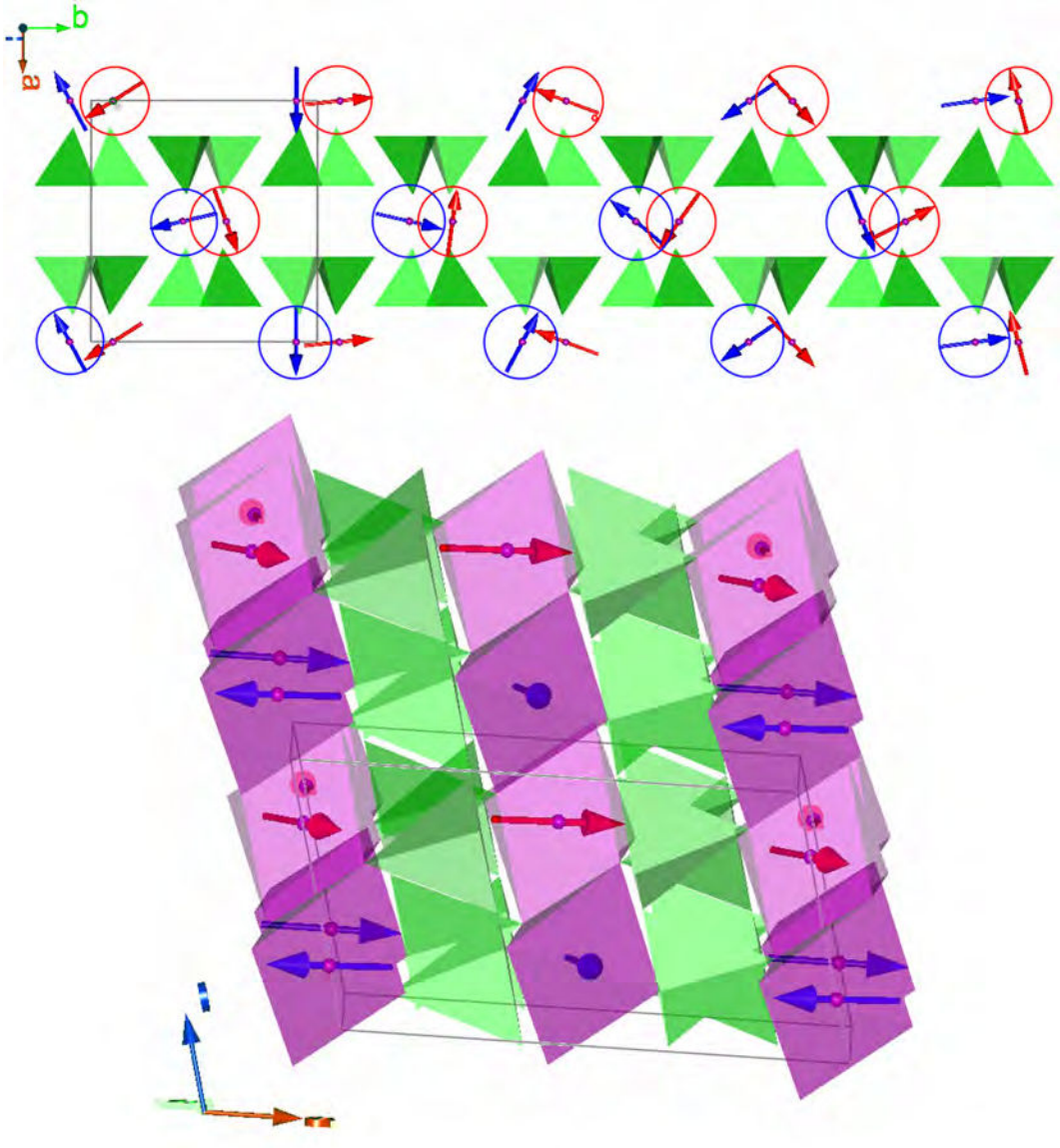

Figure 8.20: Cycloidal spiral magnetic structure of $SrMnGe_2O_6$ below T_N.

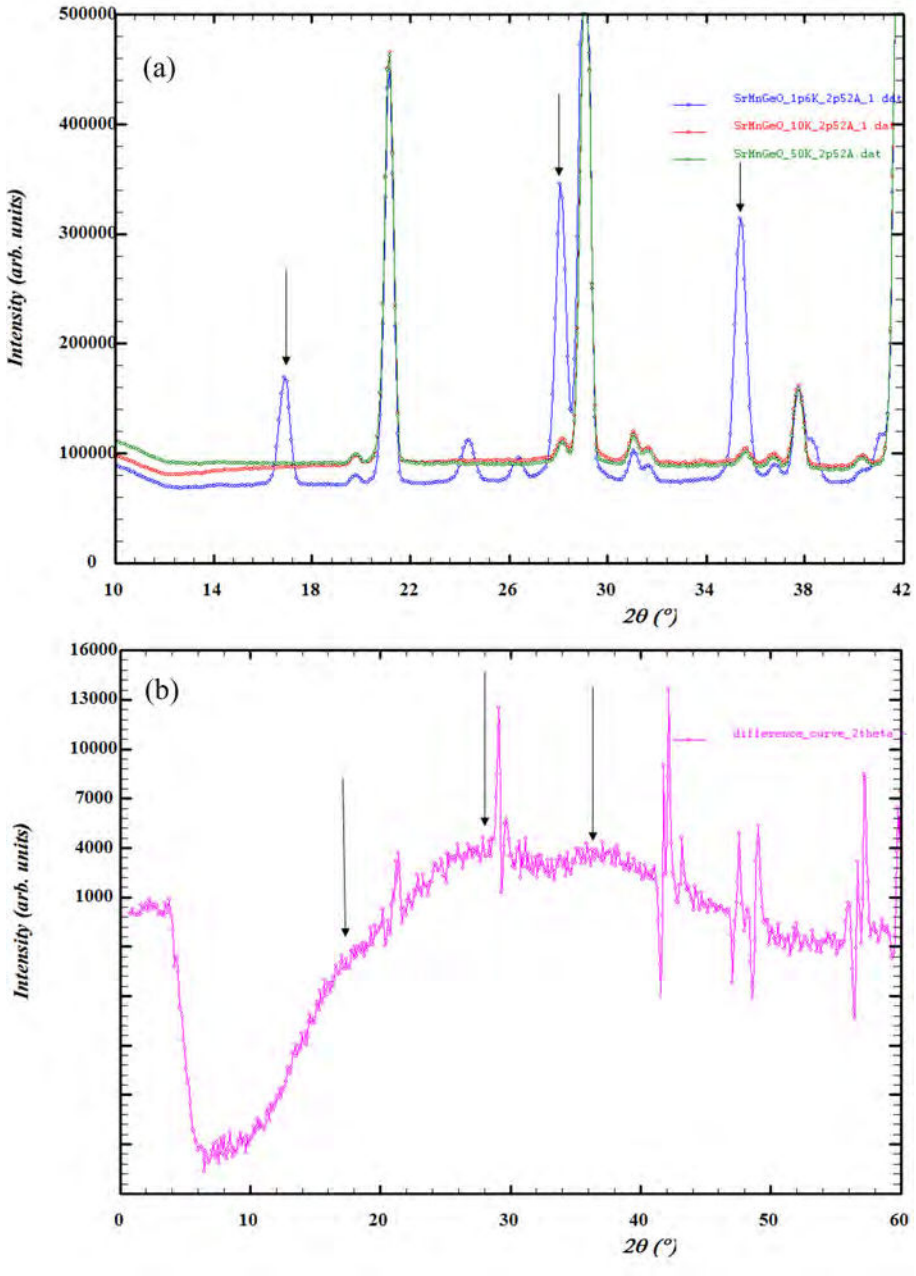

Figure 8.21: (a) NPD patterns taken at 1.6K, 10K and 50K. (b) NPD pattern difference between 10K and 50K. Note: arrows in (a) mark the strongest magnetic peaks which are also present in plot (b).

In the earlier chapters, we have evidenced that the short-range order, found in $CaMnGe_2O_6$ and $CaMnSi_2O_6$, is attributed to 1D short-range spin correlation within chains by fitting the diffuse scattering data observed well above their Néel temperatures. The diffuse scattering present in $SrMnGe_2O_6$ seems to be a pre-ordering of spins with 3D character, as shown in figure 8.21. By comparing the NPD patterns taken at 1.6K, 10K and 50K, the apparent variation of background between data at 10K and 50K reflects the appearance of diffuse scattering. The diffuse scattering data extracted from the NPD pattern difference between 10K and 50K are shown in figure 8.21(b). Three broad peaks (marked in the figure) can be seen, corresponding to the strong magnetic reflections appearing below T_N, as illustrated in figure 8.21 (a). Thus, this diffuse scattering is actually a result of the development of pre-ordering of spins, and can not be fitted by the 1D model we constructed. No anomaly can be found in the NPD pattern collected at 35K. All these features suggest that the short range spin correlations present in $SrMnGe_2O_6$ above T_N is distinct to that in $CaMnGe/Si_2O_6$.

We obtained the lattice parameters as a function of temperature by refining the NPD data in the temperature range of 1.6-100K. As shown in figure 8.16, all parameters follow a standard evolution with temperature above T_N. However, the AFM magnetic transition is accompanied by abrupt changes in a, b, c and beta parameters with respectively different manners. We found that a, c and beta parameters increase with the decrease of temperature while b parameter decreases.

8.3.4 Magnetoelectric properties

8.3.4.1

8.3.4.2 Multiferroic properties in $SrMnGe_2O_6$

To confirm the magnetically-induced ferroelectricity, we evaluated the electric polarization by measuring the pyroelectric current on polycrystalline $SrMnGe_2O_6$. The results of the pyroelectric current at 0T shown in figure 8.23 (a) demonstrate that a pyrocurrent develops below T_N. With the decrease of temperature, for current recorded at 0T, a peak with induced current of 0.9 pA is observed at around 4.2K, and with further decreasing temperature, the pyrocurrent decreases slowly to the lowest measured temperature 2K. We also confirmed that the sign reversal of pyrocurrent occurs below T_N on heating process after a poling field with reverse dc electric field. After integrating the induced pyroelectric current with respect to time, we obtained the temperature variation of electric polarization P at 0T. As shown in figure 8.23(b), a finite spontaneous polarization appears below T_N. Spontaneous polarization at 2K is about $0.63\mu C/m^2$ which is quite tiny as compared to the type-II multiferroic as-mentioned in chapter 1, this is because of the very narrow spanned temperature range but with considerable induced pyrocurrent. The spontaneous polarization P can be reversed by the dc electric field. These results evidently indicate that $SrMnGe_2O_6$ becomes ferroelectric simultaneously when the magnetic phase with cycloidal spin configuration appears.

In figure 8.23 we also show the pyroelectric current and electric polarization under different

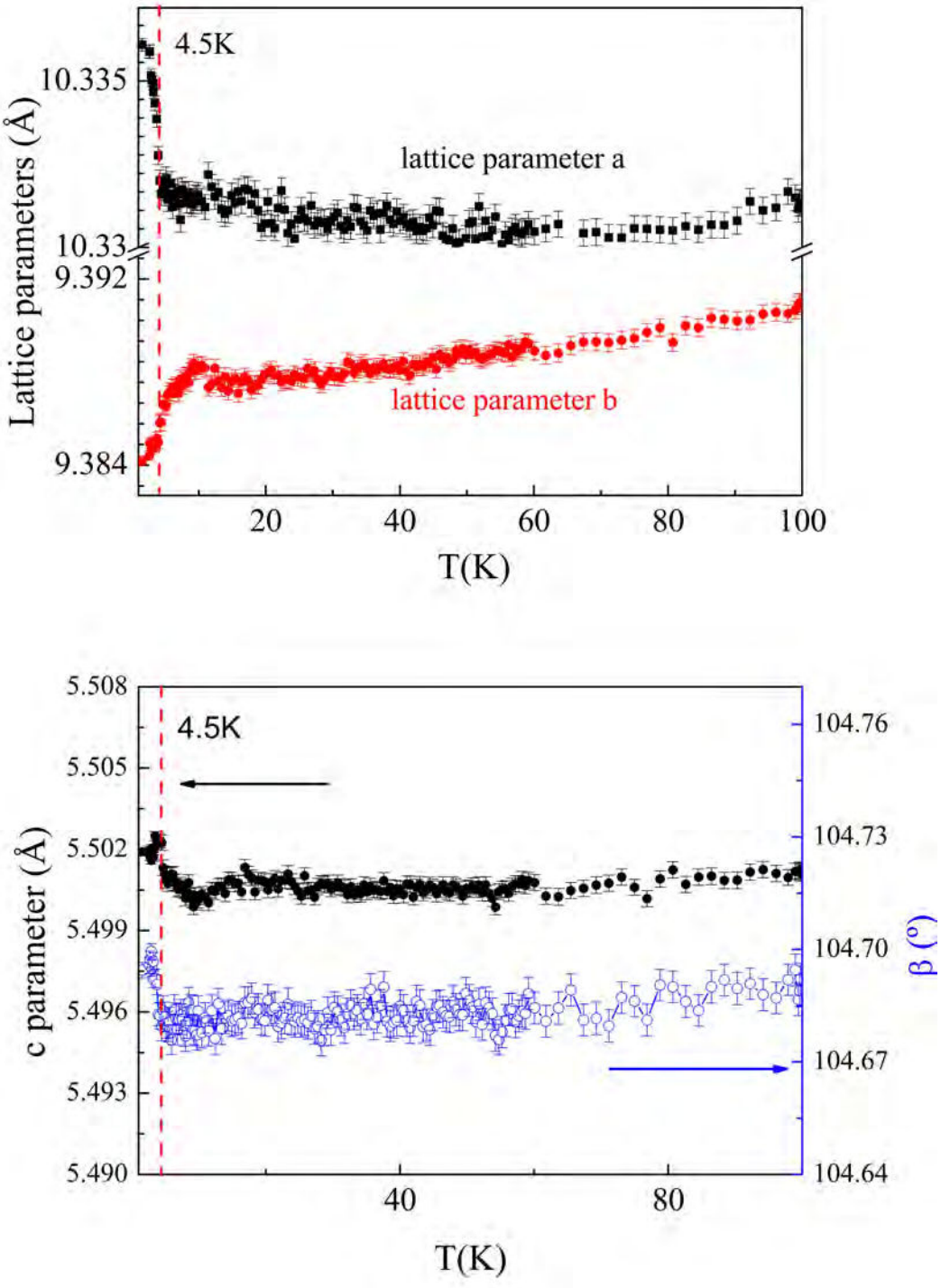

Figure 8.22: Temperature dependent lattice parameters for $SrMnGe_2O_6$.

magnetic fields. With the increase of magnetic field (below 4T), the induced pyrocurrent is enhanced, and also the electric polarization. The maximum pyrocurrent and polarization are 2.3 pA and 1.4 $\mu C/m^2$ at 4T, respectively. However, by applying magnetic field above 4T, the pyrocurrent and spontaneous polarization is gradually suppressed below T_N. As a comparison, the current and polarization are similar in magnitude at 2T and 8T. This contrast means that the magnetic field deviates the ferroelectric polarization direction from the a axis. Although the spontaneous polarization in $SrMnGe_2O_6$ is very small, the considerable current signal together with the concurrent features support the presence of ferroelectricity below T_N. Actually, $SrMnGe_2O_6$ is the first multiferroic compound in family of pyroxenes with bivalent cation occupied M2 site.

8.4 Discussion

We have compared the structural parameters beween $SrMnGe_2O_6$ and $CaMnGe_2O_6$. The apparent increment in a and b parameters in $SrMnGe_2O_6$ greatly affects the magnetic properties. According to the recent theoretical calculation of the exchange interactions in pyroxenes, the distance between the nearest neighboring Mn-Mn is a key parameter in varying the magnetic properties. This distance in $SrMnGe_2O_6$ relatively increases, although not much, but this increase may decrease the exchange strength to some extent. On the other hand, the considerably increased angles of O1-O2 pathways in between two Mn cations sitting on neighboring chains probably make the interchain interactions stronger. Given the exchange constants from interchain are comparable or at some special amount to the intrachain exchange, spiral magnetic structures with strong frustration are produced.

It seems that we are working at some specific boundaries: The appearance of 1D short-range ordering in $CaMn_2Ge_6O$ requires the promotion by magnetic frustration in a 3D magnetic exchange system, and the magnetic frustration is built up by strong intrachain interactions and relatively weak interchain ones, this is an original phenomenon; In $SrMnGe_2O_6$, the structure parameters are apparently modified, but still the C2/c symmetry remains, and this modification make $SrMnGe_2O_6$ compound being at another boundary which is the boundary of commensurate AFM coupling and incommensurate spiral state. Consequently, the magnetic properties in pyroxenes can be tuned by properly varying the structure parameters.

There exist several different microscopic mechanisms which can account for multiferroic properties. Among them, spin-current model, describing the relationship between the polarization and the canted spin sites, has been very powerful in exploring new multiferroics and explaining multiferroic properties in spiral magnetic structures[21]. In $SrMnGe_2O_6$, the spontaneous polarization is only present in the cycloidal spin structure below T_N, which is consistent with the spin-current model. Let's first make a phenomenological description of this model, and then by combining this model into the cycloidal spin configuration of $SrMnGe_2O_6$, we are able to appreciate the multiferroic properties observed in $SrMnGe_2O_6$.

The spin-current model can be simply given by[19, 20, 21]:

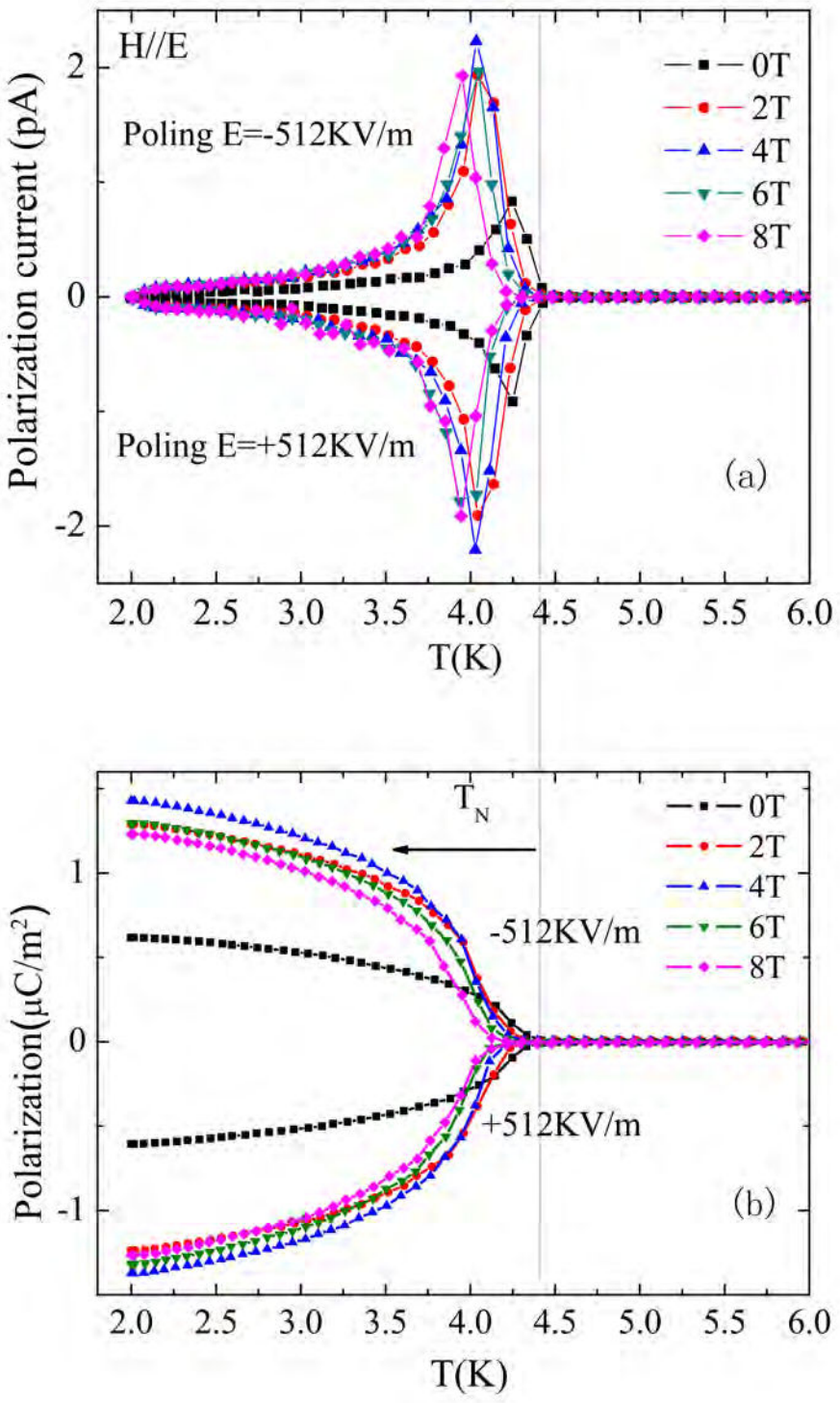

Figure 8.23: (a) Temperature dependence of pyroelectric current under various magnetic fields. (b) Electric polarization as a function of temperature in different magnetic fields.

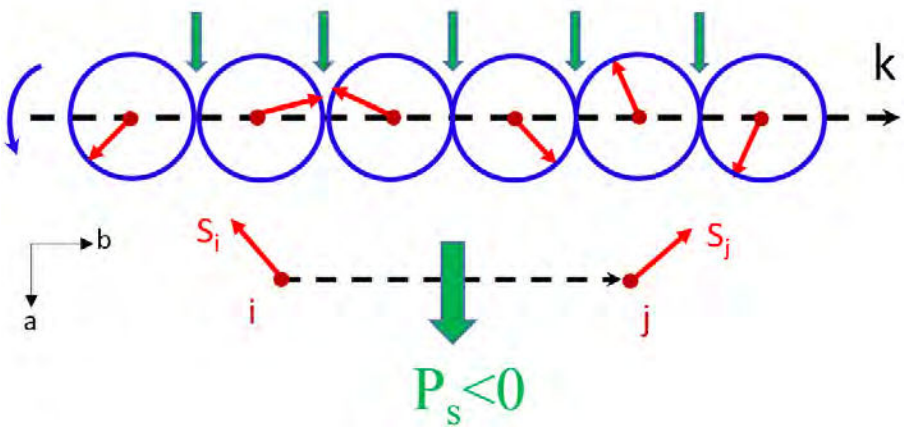

Figure 8.24: Representation of spin current model in $SrMnGe_2O_6$.

$$P = ae_{ij} \times (S_i \times S_j) \tag{8.4}$$

where a is the proportional constant depending on the spin exchange interaction and the spin-orbit coupling; and e_{ij} denotes the unit vector connecting the two canted moment sites, representing the spontaneous spin-current flow; S_i and S_j represent the canted spins on two neighboring sites. We draw schematically the spin arrangement along the b axis (i.e. the k vector direction) in figure 8.24. All the magnetic moments are confined into the (a,b) plane, and the propagation of spin leads to the counter-clockwise configuration. For any two moment sites with canted spins, the spin current flows from left to right, giving rise to the spontaneous polarization P_s along the a direction as a result of spin-orbital coupling. This is reflected by the abrupt change of the a parameter just below T_N.

The magnitude of P_s is anticipated to be proportional to the magnitude of spin-orbit coupling and also to the exchange interactions of spins. The very small polarization value observed in $SrMnGe_2O_6$ is probably attributed to the very weak spin-orbit coupling strength of Mn^{2+} cations since its orbital moment is greatly quenched.

8.5 Conclusion

We investigated the synthesis, crystal structure and magnetic properties of $SrMGe_2O_6$(M=Mn, Co) which belong to a new family of pyroxenes. Both ab initio crystal structure determination from x-ray powder diffraction ($SrCoGe_2O_6$) and single crystal diffraction data ($SrMnGe_2O_6$) reveal that these new compounds both crystallize with C2/c space group. This crystal structure is further confirmed by refining the nuclear structure using NPD .

For $SrCoGe_2O_6$, both magnetic susceptibility and heat capacity measurements show the long-range AFM ordering below 10K, and this is complemented by neutron powder diffraction experiment at low temperature. The magnetic structure of $SrCoGe_2O_6$ is determined from neutron diffraction data where magnetic moments align mainly parallel to the c-axis in

CoO_6 octahedra chains but are coupled AFM between the neighboring chains. The magnetic symmetry of $SrCoGe_2O_6$ is described by P_c2_1/c (same case as $CaCoGe_2O_6$).

The dc and ac magnetic susceptibility measurements indicate that $SrMnGe_2O_6$ undergoes an AFM phase transition at 4.5K, which was confirmed by the analysis of heat capacity and neutron diffraction measurements. A cycloidal magnetic structure is determined from neutron powder diffraction data at low temperature, for which spin moments rotate within the (a,b) plane along the b axis with incommensurate propagation vector k_y=0.424. A spontaneous polarization was observed just below T_N= 4.5K by pyroelectric current measurements, and referring to the cycloidal spin configuration, the spin-current model is used to discuss the multiferroic mechanism in $SrMnGe_2O_6$.

Bibliography

[1] G. Nénert, C. Ritter, M. Isobe, O. Isnard, A. N. Vasiliev, and Y. Ueda, Magnetic and crystal structures of the one-dimensional ferromagnetic chain pyroxene $NaCrGe_2O_6$, Phys. Rev. B 80, 2009, 024402. 193

[2] S. Jodlauk, P. Becker, J. AMydosh, D. I. Khomskii, T. Lorenz, S.V. Streltsov, D. C. Hezel, L. Bohaty, Pyroxenes: a new class ofmultiferroics, J. Phys.: Condens. Matter, 19, 2007, 432201. 193

[3] G.J. Redhammer, G. Roth, W. Treutmann, W. Paulis, et al., Magnetic ordering and spin structure in Ca-bearing clinopyroxenes $CaM^{2+}(Si,Ge)_2O_6$, M=Fe, Ni, Co, Mn, J. Solid State Chem., 181, 2008, 3163. 193

[4] G.J. Redhammer, G. Roth, A. Senyshyn, G. Tippelt, C. Pietzonka, Crystal and magnetic spin structure of Germanium-Hedenbergite, $CaFeGe_2O_6$, and a comparison with other magnetic/magnetoelectric/multiferroic pyroxenes, Z.Kristallogr., 228, 2013, 140. 193

[5] Duisenberg & Schreurs, 1989-2000. 195

[6] A.J.M. Duisenberg, L.M.J. Kroon-Batenburg and A.M.M. Schreurs, An intensity evaluation method: EVAL-14, J.Appl.Cryst., 36, 2003, 220-229. 195

[7] Angela Altomare, et al., SIR97: a new tool for crystal structure determination and refinement, J. Appl. Cryst. 32, 1999, 115-119. 195

[8] Sheldrick, G. M. 1996. SADABS. University of Göttingen, Germany. 195

[9] Sheldrick, G. M. SHELXL-97, Program for the Refinement of Crystal Structure; University of Göttingen: Germany, 1997. 195

[10] J. Rodriguez-Carvajal, Recent Advances in Magnetic Structure Determination by Neutron Powder Diffraction. Physica B, 192, 1993, 55-69. 195, 196, 210

[11] A. Boultif, D. Louër, Powder pattern indexing with the successive dichotomy method, J. Appl. Cryst. 37, 2004, 724. 197

[12] V. Favre-Nicolin and R. Cerny, FOX, 'free objects for crystallography': a modular approach to ab initio structure determination from powder diffraction. J. Appl. Cryst., 35, 2002, 734-743 197

[13] P. Thompson, D.E. Cox, J.B. Hastings, Rietveld refinement of Debye-Scherrer synchrotron X-ray data from Al_2O_3, J. Appl. Cryst., 20, 1987, 79-83. 197

[14] J.F. Bérar and G. Baldinozzi, Modeling of line-shape asymmetry in powder diffraction, J. Appl. Cryst., 26, 1993, 128-129. 197

[15] J. Rodrıguez-Carvajal, BondStr, 2010, www.ill.eu/sites/fullprof/ 197, 199

[16] E.F. Bertaut, Representation analysis of magnetic structures, Acta Crystallogr. Sec. A 24, 1968, 217. 210

[17] A. S. Wills, A new protocol for the determination of magnetic structures using simulated annealing and representational analysis (SARAh), Physica B 278, 2000, 680. 210

[18] 3J. Rodriguez-Carvajal, BasIreps: a program for calculating irreducible representations of space groups and basis functions for axial and polar vector properties (see FullProf site: http://www.ill.eu/sites/fullprof). 210

[19] M. Mostovoy, Ferroelectricity in spiral magnets, Phys. Rev. Lett., 96, 2006, 067601. 222

[20] H. Katsura, N. Nagaosa, A. V. Balatsky, Spin current and magnetoelectric effect in noncollinear magnets, Phys. Rev. Lett., 95, 2005, 057205. 222

[21] Y.Yamasaki, S. Miyasaka, Y.Kaneko, J.P. He, T.Arima, Y.Tokura, Magnetic reversal of the ferroelectric polarization in a multiferroic spinel oxide, Phys. Rev. Lett., 96, 2006, 207204. 222

[22] S. J. Blundell, C. A. Steer, et al., Detection of magnetic order in the S=1 chain compound $LiVGe_2O_6$ using implanted spin-polarized muons, Phys. Rev. B, 67, 2003, 224411.

215

Chapter 9

Summary and Outlook

9.1 Summary

The main thrust of this thesis has been the exploration for novel multiferroic materials in pyroxenes M2M1T_2O_6, and the understanding of structure-property relationships. Considering the pyroxenes as a rich playground in magnetism, some exotic magnetic properties were expected. In this work, we have presented synthesis, crystal and magnetic structures and magneto-electric properties on magnetic pyroxenes based on divalent metal cations. One aim of this work was to reveal the relevant crystal-chemical parameters which control the various magnetic ground states observed in this complex family of compounds. In chapter 4, we have first investigated the crystal structure of the $Cu_{0.8}Mg_{1.2}Si_2O_6$ clinopyroxene compound. In this case, the 3d cation is located in the M2 site, which we interpreted as due to the Jahn-Teller effect of the Cu cation, based on the analysis of strong structural distortions. Due to the isolated nature of the magnetic cations, this arrangement prevents the compound from ordering magnetically. In chapter 5, the properties of the $CaMnGe_2O_6$ compound were reinvestigated in details. An original 1D short-range spin correlation state has been revealed and explained by constructing a phenomenological magnetic model in $CaMnGe_2O_6$. The symmetry of this compound allows the existence of linear magnetoelectric effect and ferrotoroidicity. These properties were evidenced and studied experimentally and theoretically.

In order to check the response of the system to a change of size on the T site, we decided to synthesize and investigate the Si analog to the previous compound. In chapter 6, we have presented the magnetic and magnetoelectric properties on the high-pressure synthesized $CaMnSi_2O_6$ in which the magnetic ground state is similar to the Ge-based compound and 1D short-range spin order was also observed. The study of the magnetic phase diagram of $CaCo_{1-x}Mn_xGe_2O_6$ solid solution offered the possibility to study the effect of substitution on the M1 site occupied by magnetic 3d cations, with the added motivation that the end members of the solid solution were known to present different magnetic arrangements. This study, including the magnetic phase diagram, is presented in chapter 7. Finally, the effect of substitution on the M2 site was carried out by replacing the Ca^{2+} by the Sr^{2+}cation. Chapter 8 is dedicated to the study of synthesis, crystal structure and magnetic and magnetoelectric

Table 9.1: Summary of crystal structure, magnetic and magnetoelectric properties of M2M1T_2O_6(M2=Ca,Sr; M1=Mn, Co; T=Ge, Si). Distance (Å).

Parameter	$CaMnGe_2O_6$	$CaMnSi_2O_6$	$SrMnGe_2O_6$	$CaCoGe_2O_6$	$SrCoGe_2O_6$
a	10.2794(3)	9.9209(2)	10.3511(6)	10.1417(2)	10.2560(1)
b	9.1756(3)	9.1370(2)	9.4204(5)	8.9767(2)	9.2970(1)
c	5.4714(2)	5.2747(1)	5.5093(3)	5.4246(1)	5.4701(1)
β	104.244(2)	105.128(3)	104.700(2)	104.885(1)	105.588(1)
M-M(J)	3.249(8)	3.140(7)	3.282(8)	3.162(5)	3.207(6)
M-M(J1)	5.918(7)	5.740(7)	5.975(7)	5.848(5)	5.923(6)
M-M(J2)	6.889(1)	6.744(9)	7.00(1)	6.772(7)	6.921(8)
M-O1-M(°)	**94.0(4)**	**91.8(1)**	**97.5(2)**	**95.7(1)**	**98.47(9)**
T_N(K)	15	12	4.5	21	10
MSG	C2'/c	C2'/c	Cycloidal	P_c2_1/c	P_c2_1/c
Property	linear ME	linear ME	MF	-	-

properties of this new family of pyroxenes $SrMGe_2O_6$ (M=Mn, Co).

To recall the principal results obtained in this thesis in a more synthetic way, we summarize the main structural parameters, and magnetic and magneto-electric properties of M2M1T_2O_6(M2=Ca,Sr; M1=Mn, Co; T=Ge, Si) in table 9.1. From this table, we can try to extract the more salient features and relevant parameters related to the substitutions on the various cation sites.

(i) Substitution on the T site: From $CaMnGe_2O_6$ to $CaMnSi_2O_6$, the a and c parameters decrease considerably by about 3.5% and the Mn-O1-Mn angle decreases by 2.2°; The other structural parameters remain essentially unchanged. The alteration of the magnetic properties is very minor: both magnetic structures and 1D short range order are conserved except that the ordering temperature is slightly decreased. Finally, both $CaMnGe_2O_6$ and $CaMnSi_2O_6$ exhibit linear magnetoelectric effect and ferrotoroidicity. This absence of effect of the Si/Ge substitution contrasts with the case of trivalent 3d metal cation bearing pyroxenes (e.g. $LiFeSi_2O_6$ and $LiFeGe_2O_6$) for which the type magnetic ordering may be strongly modified.

(ii) Substitution on the M2 site: From $CaMnGe_2O_6$ to $SrMnGe_2O_6$, the more salient features are the increase of the b parameter by about 2.6% up to the quite large value of 9.42 Å, and of the Mn-O1-Mn angle by 3.5°. It is striking that this structural modification profoundly alters the magnetic structure which has been varied from collinear to cycloidal structure. Accordingly, the magnetoelectric property is tuned from linear ME (Ca) to multiferroic (Sr). In the case of Co, the relative change of the b parameter is even larger (about 3.5%) but the value is still smaller (9.30 Å) than for Mn. In opposition to the Mn case, here the magnetic property remains the same from Ca to Sr: only the ordering temperature decreases substantially from 21K for Ca to 10K for Sr. One can argue that the increase of the b parameter, corresponding to an increase of the chain separation, will weaken the magnetic exchange coupling between the chains. For the Co case with ferromagnetic chains, this weakening will lower T_N while essentially keeping the spin arrangement. For the Mn case where the chains are antiferromag-

netic and there is a competition between interchain interactions, this strong modification of the interchain distances leads to a complete change of the magnetic ground state.

(iii) Substitution on the M1 site: From Mn to Co, the most strongly affected structural parameter is the M-M distance which decreases by about 2.7%. However, these modifications seem to be less relevant for the complete change of magnetic behavior between the Mn- or Co-containing compounds.The dominant factor influencing their magnetic properties is rather the orbital occupancy of the 3d cation, which leads to the extremely different dominant exchange interactions, especially along the chains. For the Mn case, at least for Ca-bearing pyroxenes, the chains order antiferromagnetically which creates a competition between super-super-exchange interchain interactions. The resulting frustration leads to the existence of an original 1D short range ordered state. Among all the documented pyroxenes containing divalent transition metal cations, Mn-bearing pyroxenes, i.e., $CaMnGe_2O_6$ and $CaMnSi_2O_6$, are only ones which present such magnetic frustration resulting from a triangular-like topology, the rest share the same magnetic symmetry. Our study of the magnetic phase diagram for the $CaCo_{1-x}Mn_xGe_2O_6$ solid solution gives further indication of the key role of magnetic frustration in determining the magnetic ground state.

9.2 Perspectives

By providing new compounds and original insights into the mechanisms underpinning the magnetic properties in pyroxenes, this works opens a wealth of future investigations to be carried out, both theoretical and experimental.

The variety of magnetic behaviors observed in pyroxenes are rooted in their electronic structures. For example, the 1D short range spin correlation evidenced experimentally in $CaMnGe_2O_6$ and $CaMnSi_2O_6$ needs to be further clarified. As our studies (among others) have shown, the magnetic ground state depends strongly on the competing exchange interactions, which in turn are controlled by fine details of the structural and electronic configurations of the system. Therefore, in order to complete our qualitative understanding of the magnetic behavior of these compounds, it will be crucial to determine the values of exchange interactions. This can be done both by ab initio calculations, or by carrying out inelastic neutron scattering experiments.

In order to gain further insight into the magnetoelectric behavior of these pyroxene compounds, several types of experiments will also need to be carried out. The main issue is to perform direction-dependent measurements on large single crystals. This comprises magnetoelectric measurements as a function of the direction of the applied magnetic and electric fields. Such experiments are required to obtain a full description of the linear magnetoelectric effect . In addition, polarized neutron measurements could allow the observation of the ferrotoroidic order in the linear magnetoelectric compounds.

Complementary neutron diffraction experiments on single crystals could allow to elucidate the nature of the metamagnetic transition observed at moderately high fields.

As can be seen, all of these future directions rely on the obtention of high quality and large

size single crystals. In the literature, the synthesis of pyroxene compounds is often reported as the growth of crystals via long duration experiments at high temperatures. However, the samples obtained are of sufficient size for crystallographic studies and sometimes magnetic characterization, but are generally too small for single crystal neutron diffraction and even more for inelastic neutron scattering. Magnetoelectric measurements on single crystals also require large samples to be cut along special direction and onto which electrodes can be attached. Preliminary experiments are carried out in collaboration with the pôle Cristaux Massifs of Institut Néel and Pascal Lejay to grow such large high quality crystals using an image furnace. Positive results have been recently obtained in the $SrMnGe_2O_6$ system, which is very encouraging for the continuation of these studies.

Synthèse et étude structurale et magnétoélectrique de composés multiferroïques de la famille des pyroxènes

Résumé

Cette thèse traite de la synthèse, et de l'étude des structures cristallines et magnétiques et des propriétés magnéto-électriques d'un système magnétique non trivial: la famille des composés pyroxène $M2M1T_2O_6$ (M2 = métal mono- ou bivalent, M1 = métal de transition di- ou trivalent, T = Si ou Ge). L'objectif réside dans l'étude de leurs propriétés magnétiques et multiferroïques sur la base de la compréhension de leurs structures. Cinq systèmes sont présentés, visant à comprendre comment la variation des structures affecte les propriétés magnétiques et magnéto-électriques qui en découlent.

Nous avons synthétisé le pyroxène $Cu_{0.8}Mg_{1.2}Si_2O_6$ qui cristallise avec la structure de type bas-clinopyroxène, avec Cu^{2+} localisé sur le site M2 en raison de sa nature Jahn-Teller. Cela rend $Cu_{0.8}Mg_{1.2}Si_2O_6$ paramagnétique à toutes températures en raison de l'arrangement isolé des cations magnétiques.

Les propriétés de $CaMnGe_2O_6$, ont été réétudiées par mesures de susceptibilité magnétique, chaleur spécifique et diffraction de neutrons. Des corrélations de spins unidimensionnelles à courte portée ont été attestées par l'ajustement par un modèle phénoménologique de mesures de diffusion diffuse magnétique de neutrons. L'effet magnéto-électrique linéaire et la ferrotoroïdicité concomitante autorisés par la symétrie magnétique, ont été mis en évidence expérimentalement et théoriquement. Le composé $CaMnSi_2O_6$ a été synthétisé à haute pression et à haute température et étudié pour évaluer l'effet de la modification de taille sur le site T sur les propriétés magnétiques du système. Il apparaît que $CaMnSi_2O_6$ présente des propriétés magnétiques très similaires à celles de son homologue Ge: la symétrie magnétique et les propriétés magnéto-électriques sont conservées.

Pour étudier l'effet de la substitution sur le site M1 occupé par des cations 3d magnétiques, nous avons étudié le diagramme de phase magnétique de la solution solide $CaCo_{1-x}Mn_xGe_2O_6$, pour laquelle les deux membres extrêmes présentent des états fondamentaux magnétiques différents. Tous les composés présentent une transition de phase magnétique vers un ordre AFM. Jusqu'à x = 0.75, l'ordre AFM correspond à celui du composé x = 0. Pour les valeurs de x plus élevées, l'état fondamental correspond à l'ordre AFM du composé x = 1 (pur Mn). Un ordre magnétique à courte portée observé au-dessus de la transition AFM pour $x>0.75$ est attribué à des corrélations de spin unidimensionnelles induites par la frustration. Pour x voisin de 0.75, les deux types d'ordre AFM coexistent dans des domaines de compositions légèrement différentes.

En outre, une nouvelle famille de pyroxènes à base de Sr, $SrMGe_2O_6$ (M = Mn, Co) a été synthétisée et étudiée, rendant accessible l'étude des relations magnéto-structurales liées à la substitution de cations sur le site M2. Nos mesures magnétoélectriques et les données de NPD indiquent que $SrMnGe_2O_6$ est un multiferroïque de type II avec un ordre magnétique caractérisé par une configuration de spins cycloïdale, tandis que $SrCoGe_2O_6$ présente une structure magnétique identique à celle de son homologue au Ca.

Mots clés : Multiferroïsme, Structure, Magnétisme, Synthèse

Synthesis, structural and magneto-electric properties of compounds belonging to the pyroxene family

Abstract

This thesis deals with the synthesis, crystal and magnetic structures and magneto-electric properties of a non-trivial magnetic system: the family of pyroxene compounds $M2M1T_2O_6$ (M2 =mono- or divalent metal, M1=di- or trivalent transition metal, T=Si or Ge). The focus of this thesis lies on multiferroic and exotic magnetic properties based on the understanding of their structures. Five systems have been investigated and presented aiming to understand how the structural variation affects the magnetic properties, and the ensuing magneto-electric properties.

We have synthesized a copper-bearing pyroxene $Cu_{0.8}Mg_{1.2}Si_2O_6$ which crystallizes with the low-clinopyroxene structure, with Cu^{2+} located in the M2 site due to its Jahn-Teller nature. This makes $Cu_{0.8}Mg_{1.2}Si_2O_6$ paramagnetic at all temperatures due to the isolated arrangement of the magnetic cations.

The properties of $CaMnGe_2O_6$, were re-investigated by means of magnetic susceptibility, heat capacity and neutron diffraction measurements. One dimensional short-range spin correlations were evidenced by fitting a phenomenological model to diffuse magnetic neutron scattering. The linear magnetoelectric effect and concomitant ferrotoroidicity allowed by the magnetic symmetry, were evidenced experimentally and theoretically. High pressure and high temperature synthesized $CaMnSi_2O_6$ was investigated to evaluate the effect of size modification of the T site on the magnetic properties of the system. It turns out that $CaMnSi_2O_6$ displays quite similar magnetic properties to its Ge counterpart: both the magnetic symmetry and magneto-electric properties are conserved.

To study the effect of substitution on the M1 site occupied by magnetic 3d cations, we investigated the magnetic phase diagram of the $CaCo_{1-x}Mn_xGe_2O_6$ solid solution, for which the two end members display different magnetic ground states. All compounds undergo a magnetic phase transitions to AFM ordering. Up to x=0.75 the low T AFM order corresponds to that of the x=0 (pure Co) end member. For higher x values, the ground state corresponds to the AFM order of the x= 1 pure Mn end member. Magnetic diffuse scattering observed above T_N is attributed to one-dimensional short range spin correlations induced by frustration. For x close to 0.75, both types of AFM order coexist in domains of slightly different compositions.

Moreover, a new family of Sr-based pyroxenes $SrMGe_2O_6$ (M=Mn, Co) was synthesized and investigated, making the study of magneto-structural relationships accessible for the substitution of cations on the M2 site. Magnetoelectric measurements and NPD data indicate that $SrMnGe_2O_6$ is a multiferroic of spin origin with a magnetic order characterized by a cycloidal spin configuration, while $SrCoGe_2O_6$ should display the same magnetic structure as its Ca counterpart. The comparison between Sr- and Ca-based pyroxenes from a structural viewpoint has been performed, and the relevant structural parameters for the magnetic ground states are also appreciated.

Keywords: Multiferroism, Structure, Magnetism, Synthesis